ABSTRACT

Title of Dissertation: Metal hydrides as a platform for reconfigurable photonic and plasmonic elements

Kevin J. Palm
Doctor of Philosophy, 2021

Dissertation directed by: Professor Jeremy N. Munday
Department of Physics

Metal hydrides often display dramatic changes in optical properties upon hydrogenation. These shifts make them prime candidates for many tunable optical devices from optical hydrogen sensors and switchable mirrors to physical encryption schemes. In order to design and fabricate optimized devices for any of these applications, we need to determine the optical and structural properties of these materials. In this dissertation, we design and implement an apparatus that dynamically measures the gravimetric, stress, calorimetric, and optical properties of metal hydrides as they are exposed to H_2. We use this apparatus to measure the properties of 5 different pure metal hydrides (Pd, Mg, Ti, V, and Zr) and then use these properties to design tunable color filters and switchable perfect absorbers, among other devices. To widen our parameter space and to combine desirable characteristics of different metal systems, we use the same apparatus to investigate the properties of different metal alloy hydride systems including Pd-Au, Mg-Ni, Mg-Ti, and Mg-Al. We demonstrate many improved nanophotonic designs with these materials, including

a thin film physical encryption scheme with Pd-Au and a switchable solar absorber with Mg-Ti.

Many of these photonic devices can be further enhanced by tailoring the substrate of the device along with the metal hydride. In this dissertation, we also investigate combining the switchable optical properties of metal hydrides with near-zero-index substrates to further enhance the optical device changes. Near-zero-index materials are ones where the refractive index is below 1 and can lead to a variety of interesting optical effects, including high absorption in surrounding materials and enhanced non-linear effects. By combining an ITO substrate with a near-zero-index resonance at $\sim$1250 nm with a thin Pd capped Mg film, we demonstrate a switchable absorption device with $>$76% absorption change at 1335 nm illumination. To further explore the possibility of large-scale fabrication of these devices, we survey the properties of commercially available near-zero-index materials and report the range of attainable optical properties, showing its feasibility.

METAL HYDRIDES AS A PLATFORM FOR RECONFIGURABLE PHOTONIC AND PLASMONIC ELEMENTS

by

Kevin J. Palm

Dissertation submitted to the Faculty of the Graduate School of the
University of Maryland, College Park in partial fulfillment
of the requirements for the degree of
Doctor of Philosophy
2021

Advisory Committee:
Professor Jeremy N. Munday, Chair/Advisor
Professor James Williams
Professor Daniel Lathrop
Professor Edo Waks
Professor Thomas Murphy

Dedication

I dedicate the following thesis to Rachel for her unwavering support throughout this journey.

Acknowledgments

There are many people to thank for their contributions to this thesis along with my development as a scientist. First, I would like to thank my committee for attending my defense: Professors James Williams, Daniel Lathrop, Edo Waks, and Thomas Murphy. I would like to thank my advisor Professor Jeremy Munday for supporting me throughout my graduate studies and always making time to discuss either research or personal issues, editing many manuscripts and fellowship applications, and aiding in my development as a researcher and as a person. I owe a special thanks to Joe Murray and Tarun Narayan for mentoring me as a young graduate student working on my first research project. They taught me to never stop asking questions and how to persevere through the tough times in a project when it seems like nothing will ever work properly. I would not be the scientist I am today without their teaching and friendship. I'd also like to thank all of my fellow Munday Lab members for their guidance, assistance, and camaraderie along the way: Joe Garrett, David Somers, Lisa Krayer, Sarvenaz Memarzadeh, Tristan Deppe, and Jongbum Kim.

I would like to thank other professors I have worked with throughout my Ph.D., including Professors Marina Leite, Yet-Ming Chang from MIT, and Curtis Berlinguette from UBC. I also want to give a special thanks to Thomas Schenkel at LBNL along with Matt Trevithick, David Fork, and Ross Koningstein from Google. Working with these researchers helped to broaden my scientific horizon and hone my skepticism when analyzing data.

I'd like to thank the staff of IREAP for all of their help. Judi Gorski, Nancy Boone, Taylor Prendergast, Dottie Brosius, and Leslie Delabar made sure that I was fully equipped and supported throughout my studies. None of my research would have been possible without all of the help that I received from the Fablab staff. Tom Loughran, John Abrahams, Mark Lecates, and Jon Hummel all spent many hours teaching me how to use all of the various tools in the cleanroom and helping me to develop and perfect all of the fabrication and measurement methods for my samples.

Finally, I would like to thank my family and friends. My parents and siblings have been supporting me and pushing me in my schooling since the very beginning. I would like to thank my Grandma and Grandad whose support has allowed me to come this far in my schooling. I wouldn't have survived my time as a graduate student without the fun and shenanigans with my housemates during my years living at the 7 Seas: Antony Speranza, Chris Flower, Jon Curtis, Jaron Shrock, Zach Eldridge, and Zack Castillo. Lastly, I want to thank Rachel who has been by my side through all the ups and the many downs of creating this dissertation.

Parts of the work in this thesis were supported by grants from Google LLC and the National Science Foundation. I was personally supported by a National Defense Science and Engineering Graduate Fellowship for the final 3 years of my studies.

Table of Contents

List of Tables

List of Figures

List of Abbreviations

ADC	Analog to Digital Converter
AFM	Atomic Force Microscopy
AZO	Aluminum-doped Zinc Oxide
CSID	Calorimetry System Identification
EDX	Energy-dispersive X-ray Spectroscopy
EELS	Electron Energy Loss Spectroscopy
EMA	Effective Medium Approximation
ENZ	Epsilon-Near-Zero
FDTD	Finite-Difference Time-Domain
FTO	Fluorine-doped Tin Oxide
HEA	High Entropy Alloy
ICP-OES	Inductively Coupled Plasma - Optical Emission Spectroscopy
IREAP	Institute for Research in Electronics and Applied Physics
ITO	Indium Tin Oxide
IR	Infrared
LSPR	Localized Surface Plasmon Resonance
MFC	Mass Flow Controller
MSE	Mean-Squared-Error
NIR	Near-Infrared
NZI	Near-Zero-Index
PECVD	Plasma Enhanced Chemical Vapor Deposition
PWM	Pulse Width Modulation
QCM	Quartz Crystal Microbalance
RMS	Root Mean Square
RTD	Resistance Temperature Device
TCO	Transparent Conducting Oxide
TE	Transverse Electric
TM	Transverse Magnetic
TMM	Transfer-Matrix Method

List of Publications

Portions of this thesis have been drawn from the publications listed below:

J. B. Murray, **K. J. Palm**, T. C. Narayan, D. K. Fork, S. Sadat, J. N. Munday. "Apparatus for combined nanoscale gravimetric, stress, and thermal measurements" Review of Scientific Instruments 89, 085106 (2018)

K. J. Palm, J. B. Murray, T. C. Narayan, J. N. Munday. "Dynamic optical properties of metal hydrides" ACS Photonics 5, 4677-4686 (2018)

K. J. Palm, J. B. Murray, J.P. McClure, M. S. Leite, J. N. Munday. "In situ optical and stress characterization of alloyed Pd_xAu_{1-x} hydrides" ACS Applied Materials and Interfaces 11, 45057-45067 (2019)

K. J. Palm, L. J. Krayer, J. N. Munday. "Highly switchable absorption in a metal hydride device using a near-zero-index substrate" Submitted (2021)

Other publications co-authored during the course of the thesis include:

J. L. Garrett, L. J. Krayer, **K. J. Palm**, J. N. Munday. "Effect of lateral tip motion on multifrequency atomic force microscopy" Applied Physics Letters 111, 043105 (2017)

D. A. T Somers, J. L. Garrett, **K. J. Palm**, J. N. Munday. "Measurements of the Casimir torque" Nature 564, 386-389 (2018)

L. J. Krayer, **K. J. Palm**, C. Gong, A. Torres, C. E. P. Villegas, A. R. Rocha, M. S. Leite, J. N. Munday. "Enhanced near-infrared photoresponse from nanoscale AgAu Alloyed films" ACS Photonics 7 (7), 1689-1698 (2020)

S. Memarzadeh, **K. J. Palm**, T. E. Murphy, M. S. Leite, J. N. Munday. "Control of hot-carrier relaxation time in Au-Ag thin films through alloying" Optics Express 28 (22), 33528-33537 (2020)

T. Gong, P. Lyu, **K. J. Palm**, S. Memarzadeh, J. N. Munday, M. S. Leite. "Emergent opportunities with metallic alloys: From material design to optical devices" Advanced Optical Materials, 2001082 (2020)

J. M. Howard, **K. J. Palm**, Q. Wang, E. M. Tennyson, B. Roose, E. Lee, A. Abate, J. N. Munday, M. S. Leite. "Water-induced photoluminescence dynamics in triple-cation metal halide perovskites" Submitted. (2021)

Finally, I plan to submit several sections of this thesis to academic journals:

K. J. Palm, C Shelden, L. J. Krayer, J. N. Munday. "Investigation of physical properties of commercial near-zero-index materials" In Preparation (2021)

K. J. Palm, M. S. Leite, J. N. Munday. "Optical tunability characterization of Mg-Ni, Mg-Ti, and Mg-Al alloys" In Preparation (2021)

Chapter 1: Introduction

1.1 Overview of metal hydride systems

Metal hydrides have a long history of discovery and application. Pd, the most commonly studied and used metal hydride, was discovered to absorb large amounts of hydrogen in 1866 [1]. Since this discovery, there have been numerous applications of these materials including membranes to extract or purify hydrogen [2, 3], hydrogen gas sensors [4, 5], hydrogen storage devices [6, 7], and rechargeable batteries [8], amongst many others. All of these applications take advantage of one or more of the physical property changes of certain metals upon hydrogenation, including changes in electrical resistivity, optical properties, lattice expansion, and thermal conductivity. Many metal hydrides are non-stoichiometric compounds, where the amount of hydrogen in the material is dependent on the driving force (pressure or electrochemical voltage) of the hydrogen on the lattice [9]. Thus, these material changes are on a dynamic spectrum and allow for a broad range of intermediate properties between the fully metallic and hydride states. In this thesis, we will use novel methods to more precisely characterize these dynamic properties to inform the design of nanophotonic and plasmonic devices to further propel applications of metal hydrides.

First, we begin with a physical picture of the hydrogenation reaction. The two common ways of hydrogenating metals are gas-phase loading and electrochemical loading. The hydrogen loading value is a measure of how many H atoms are located within the metal lattice, and is measured in the units of H/M, or the number of hydrogen atoms per metal atom in the lattice. For gas-phase loading, as certain metals are exposed to H_2 gas, the diatomic hydrogen molecule can adhere to a surface site on the metal and subsequently dissociate into individual hydrogen atoms. These hydrogen atoms can then diffuse into the bulk of the metal, occupying interstitial sites within the metal lattice. In many metals, this gas-phase reaction is not spontaneous at room temperature and reasonable H_2 pressures. These metals require a catalyst to split the diatomic hydrogen molecule, which then the atomic hydrogen atoms can diffuse through the catalytic film into the lattice sites of the substrate metal. The most common catalyst is Pd, which also has the added benefit of protecting the substrate film from oxidation when it fully encapsulates the substrate. Electrochemical loading occurs when the metal is placed in an aqueous (usually acidic) medium and hydrogen is driven into the lattice with an applied voltage. This process generally allows for higher hydrogen loadings to be achieved, because a relatively small applied voltage in an electrochemical cell is chemically equivalent to a very high H_2 gas pressure [10]. For example, a Pd loading of H/Pd $= 0.96$ has been achieved with electrochemical loading, when gas phase loadings can generally only achieve H/Pd ≈ 0.75 even at high pressures [10, 11]. The applications of this process are limited to devices that can operate in an aqueous cell, thus in this thesis, we will focus solely on the gas phase loading reaction.

As small amounts of hydrogen enter the interstitial sites of a metal lattice, the hydrogen initially occupies the α material phase describing very low hydrogen concentrations. As the lattice fills with more hydrogen, the material enters a mixed-phase ($\alpha + \beta$), which is caused by H-H interactions becoming more dominant [4]. The β phase continues to grow in the lattice as more hydrogen is added until it becomes the only phase in the material. As this phase transition occurs, a significant amount of stress is introduced into the lattice as each hydrogen interstitial causes displacements of the metal atoms from their usual lattice sites. This displacement causes a distortion of the crystal lattice. A significant volume expansion occurs during this process, with Pd achieving a 14% expansion under 1 atm H_2 [12], while other materials have an even greater expansion, such as Mg, which has a 30% expansion [13]. Taking into account these stresses, especially in constrained systems, is very important, as they are connected with spurious phase formations. High stresses beyond the critical yield stress of the material can also result in the formation of dislocations in the lattice, which further affect its optical and structural properties [12]. Ways to mitigate these high stress values include nanoscaling the active materials to have fewer constraints on the system and alloying the active metals with other transition metals in order to suppress the α to β phase transition. This mitigation is essential for systems that desire repeatable switchable responses, as dislocations and deformations to the lattice can significantly degrade device response over many H_2 cycles.

1.2 Tunable optical properties and applications

In this thesis, we focus most of our attention on the dynamically tunable optical properties of metal hydrides, compared with their other dynamic properties. Metal hydrides started to draw significant attention for their tunable optical properties in 1996 when Huiberts et al. discovered that yttrium and lanthanum demonstrate a metal-insulator transition when exposed to H_2 gas [14]. This transition caused a dramatic change in the materials' optical properties as the metallic YH_2 and LaH_2 transitioned to the semiconducting YH_3 and LaH_3. Further work was continued investigating the optical changes in thin-film metal hydrides and how these changes can be applied to different devices, such as for smart windows [15], switchable solar absorbers [16], hydrogen sensors [17], and switchable mirrors [18] using metal hydrides including Y, Mg, Pd, and Mg-Ni alloys respectively.

Beyond thin film applications, as nanofabrication techniques improved and nanostructuring metals became more commonplace, many groups began to study nanoscaled metal hydrides. Nanoscaling allows for finer control of the optical response of a device by tailoring the light-matter interaction. One common way of doing this is to create a localized surface plasmon resonance (LSPR) on the metal structures. The LSPR occurs when the oscillating electric field from incident light causes the conduction electrons in the metal to coherently oscillate. This process allows for high absorption at the LSPR resonance wavelength. By exposing this plasmonic metal structure to H_2, you can then either shift or eliminate this resonance, as has been demonstrated using Y [19] and Nb [20] nanorods and Mg [21]

and Pd-Au [5] nanodisks.

Recently, the primary application for these optical metal hydride devices has been for optical hydrogen sensing. H_2 gas is an ideal clean energy source candidate because when burned, it emits no greenhouse gases and can be easily transported to regions where high-voltage power lines cannot reach. With the increase in H_2 usage, high-quality sensors are needed to regulate the flammability risks. In particular, optical H_2 sensors are ideal due to a decreased risk of sparking in a flammable H_2 environment, as opposed to electrical sensors that utilize metal hydrides' change in resistance upon hydrogenation. They are also much less energy and space-intensive than combustive H_2 sensors that section off and combust a portion of the chamber gas and analyze the resulting atomic spectra. Optical H_2 sensors can be implemented in many different forms. The most common current design utilizes the LSPR resonance of nanostructured metal hydrides. By fitting the peak of the LSPR resonance, the amount of hydrogen in the atmosphere above the sensor can be determined [5, 22, 23]. Another common way of implementing an optical H_2 sensor is to use a coating on an optical fiber that either uses a thin metal hydride layer at the end of the fiber to detect changes in back-reflected light [24] or uses a full coating of a metal hydride that expands or contracts with the hydrogen content of the atmosphere, changing the effective optical path length of the fiber [25, 26]. Simpler designs for hydrogen sensors have also been proposed that utilize resonances in thin-film devices by creating a cavity effect [17].

Beyond adjusting the optical properties of these materials by only changing the H loading, alloying metals has the added benefit of a wider parameter space

for potential optical properties. Alloying allows for the tuning of the initial optical properties of the metal, along with its response to hydrogenation. In the case of the Mg-Ni system, alloying has been used to tune the final properties of the hydride to be more clear for switchable window applications [15]. Alloying also has the potential to solve many other issues with metal hydride devices. Many pure metal H_2 sensors suffer from intracycle hysteresis, which causes a large ambiguity in the H_2 pressure reading depending on whether the sensor is loading or unloading. These sensors can also suffer from surface poisoning from various trace gases in the atmosphere, such as CO. Surface poisoning occurs when a molecule binds to a H dissociation site on the H_2 sensor and blocks any further hydrogen splitting at this site. In particular, Pd-based sensors suffer from this, where the C atom in the CO molecule chemisorbs to H splitting sites [27, 28]. One example of an alloying system that begins to solve these issues is Pd-Au, which has been shown to eliminate hysteresis with high enough Au atomic fractions and has shown a significant reduction of surface poisoning [5, 23]. To offer an even higher resistance to poisoning, ternary systems like Pd-Au-Cu have been explored and have shown a complete elimination of this poisoning effect [22]. Finally, some metal hydrides are too stable in their fully hydrogenated state and must be heated in order to unload the hydrogen from the metal lattice. MgH_2 in particular suffers from this effect, and much work has been done to investigate ways to destabilize the lattice for switchable room temperature desorption for hydrogen storage purposes [29, 30, 31]. Alloying has the potential to solve all of these issues by retaining the large optical changes upon hydrogenation while introducing other positive effects by alloying with other transition metals.

1.3 Outline of this thesis

Before we can take advantage of the wide parameter space of tunable optical and structural properties of metal hydrides, we first need to build and qualify an apparatus that can characterize these systems. In Chapter 2, we describe the custom measurement system designed to measure the gravimetric, optical, thermal, and stress properties of thin-film and nanoscaled metal hydrides. This system is based around a Quartz Crystal Microbalance (QCM) that is used to measure the mass of hydrogen entering the metals under investigation. The stress of thin-film samples is measured using an adopted Michelson-Morely interferometer with the QCM acting as one of the interferometer mirrors. By measuring the change in interference spacing, the curvature change of the substrate can be calculated, which can then be converted to the stress of the film. To measure thermal signals from reactions on the film, we designed on-chip Resistance Temperature Devices (RTD) whose outputs are fed into a one-state nonlinear lumped element model. Finally, multi-angle optical ports are available in the system to incorporate dynamic optical property measurements with variable angle spectroscopic ellipsometry. This chapter is based on the published manuscript "J. B. Murray, K. J. Palm, T. C. Narayan, D. K. Fork, S. Sadat, J. N. Munday. "Apparatus for combined nanoscale gravimetric, stress, and thermal measurements" Review of Scientific Instruments 89, 085106 (2018)".

With the demonstrated ability to measure the properties of these metal hydrides, we then investigate the structural and optical properties of 5 pure metals, Pd, Mg, V, Zr, and Ti, in Chapter 3. We find a range of different optical responses

upon hydrogenation from the different metals, and we use these measured dynamic optical properties to propose different thin film and nanophotonic designs including switchable perfect absorbers and color filters utilizing the metal hydride transition. This chapter is based on the published manuscript "K. J. Palm, J. B. Murray, T. C. Narayan, J. N. Munday. "Dynamic Optical Properties of Metal Hydrides" ACS Photonics 5, 4677-4686 (2018)".

In Chapter 4, we take a brief detour from metal hydride systems to explore commercially available Near-Zero-Index (NZI) materials. NZI substrates can greatly enhance optical effects in the wavelength range around the NZI resonance, and we are interested in the range of potential properties of these materials for eventual combination with a metal hydride system. We investigate the range of properties that can be obtained with three different types of Transparent Conducting Oxides (TCO): indium tin oxide (ITO), fluorine-doped tin oxide (FTO), and aluminum-doped zinc oxide (AZO). We find positive correlations between the locations of the NZI resonances and the strengths and bandwidths of those resonances. This chapter is based on a manuscript currently in preparation "K. J. Palm, Calum Shelden, L. J. Krayer, J. N. Munday. "Investigation of Physical Properties of Commercial Near-Zero-Index Materials" In Preparation (2021)".

Utilizing the unique properties of these NZI materials, in Chapter 5 we use an NZI substrate under a Pd/Mg stack to create a switchable thin-film absorber. The device can be switched from a high reflectivity to a high absorption state by exposure to H_2 gas. We show that the NZI substrate is essential to obtaining the extremely high absorption change and that the high absorption is created by a

destructive interference effect with the light reflecting off the Mg/NZI boundary. We experimentally demonstrate this device with a 350 nm ITO film coated with 25 nm Mg and 3 nm Pd, which shows an absorption change >76%. This chapter is based on a recently submitted manuscript "K. J. Palm, L. J. Krayer, M. S. Leite, J. N. Munday. "Highly switchable absorption in a metal hydride device using a near-zero-index substrate" Submitted (2021)".

Although pure metals have a wide range of uses in optical metal hydride devices, there are a limited set of materials to choose from, and many of these metals suffer from deleterious effects such as intracycle hysteresis, degradation over multiple cycles, and surface poisoning from atmospheric gases such as CO. In order to limit these negative effects and exactly tune our optical properties to the desired results, we can alloy our metal hydrides with other transition metals. In Chapter 6, we investigate the optical and structural properties of the Pd-Au alloy system and demonstrate their use as H_2 gas sensors and physical encryption devices. By alloying Pd with Au, we reduce sensor hysteresis and increase chemical resistance, while still maintaining a measurable optical signal. This chapter is based on the published manuscript "K. J. Palm, J. B. Murray, J.P. McClure, M. S. Leite, J. N. Munday. "In situ Optical and Stress Characterization of Alloyed Pd_xAu_{1-x} Hydrides" ACS Applied Materials and Interfaces 11, 45057-45067 (2019)".

Mg alloys are another material system of interest due to their ability to increase the H absorption and desorption kinetics when compared to pure Mg and still maintain large optical changes. This increase in kinetics is caused by the hydride state being destabilized when different transition metals are introduced into

the Mg lattice. In these systems, a large range of potential optical properties can be obtained. In Chapter 7, we investigate the optical properties of three different Mg alloy systems, Mg-Ti, Mg-Ni, and Mg-Al, to determine the effects of different atomic percentages on the optical and loading properties of the system. We show that the Mg-Ti system in particular works well as both a switchable mirror and broadband switchable light absorbers. This chapter is based on a manuscript currently in preparation "K. J. Palm, M. S. Leite, J. N. Munday. "Optical tunability characterization of Mg-Ni, Mg-Ti, and Mg-Al alloys" In Preparation (2021)".

Finally, Chapter 8 concludes this thesis with closing remarks about the impact of the work and future directions. In this chapter, we discuss further research areas in different optical metal hydride systems, including high entropy alloys. We also go through future applications of metal hydrides beyond optical sensors and devices, specifically for use in plasmonic beam targets for enhancing light element nuclear reactions.

Chapter 2: Experimental Apparatus Design and Qualification

In this chapter, we present the design and qualification of the apparatus that will be used to characterize various metal hydride systems throughout the rest of this thesis. This apparatus allows for the simultaneous measurement of mass change, heat evolution, and stress of thin-film samples deposited on QCMs. We show device operation at 24.85 $\pm$ 0.05 °C under 9.31 $\pm$ 0.02 bar of H_2 as a reactive gas. Using a 335 nm palladium film, we demonstrate that our apparatus quantifies curvature changes of 0.001 m^{-1}. Using the QCM curvature to account for stress-induced frequency changes, we demonstrate the measurement of mass changes of 13 ng/cm^2 in material systems exhibiting large stress fluctuations. We use a one-state nonlinear lumped element model to describe our system with thermal potentials measured at discrete positions by three RTDs lithographically printed on the QCM. By inputting known heat amounts through lithographically defined Cr/Al wires, we demonstrate a 150 μW calorimetric accuracy and 20 μW minimum detectable power. We also show that by switching out the chamber lid and coupling our environmental chamber with a variable angle spectroscopic ellipsometer, we can combine our dynamic mass measurement with in-situ dynamic optical property measurement. The capabilities of this instrument allow for a more complete characterization of reactions occurring

in nanoscale systems, such as the effects of hydrogenation in various metal films and nanostructures, as well as for direct stress compensation in QCM measurements.

2.1 Introduction to QCM sensing

Chemistry in nanoscale systems is increasingly important in a wide variety of fields from energy and information storage to catalysis and sensing [32, 33, 34, 35, 36, 37, 38, 39]. The shift away from the macroscale allows for dimensional reduction and dramatic changes in surface-to-volume ratios, which in turn present opportunities to tailor the thermodynamics and kinetics. Despite the small amount of material present in a nanoscale system, reactions can still produce significant amounts of heat and stress that can change the chemical and physical properties of the material. As such, it is crucial to quantify the mechanical, optical, and thermal properties of these systems to inform the design of devices exploiting these chemical processes.

QCMs are commonly used to observe nanoscale chemical reactions. A QCM is a quartz wafer (typically a disc) with its crystal orientation cut to produce a shear displacement in the presence of an electric field normal to its face. Applying an oscillating electric field between two electrodes on opposite sides of the QCM excites a shear wave in the quartz disc due to its piezoelectric response. The resonance frequency of this oscillation is very sensitive to the material attached to the surface of the resonator, which causes a change in the acoustic impedance of that interface. This frequency changes (very nearly) linearly with added rigid mass, such as a thin metal film, and can thus be used to detect changes of mass due to chemical

or physical processes [40, 41]. This mass sensitivity lends itself to a number of applications as far reaching as protein sensing and electrochemical degradation [42].

The QCM resonance frequency also has a pronounced dependence on a number of other parameters including pressure, density and viscosity of the medium surrounding the QCM, temperature, and stress (e.g. from mounting or from stress in an adhered thin film) [43, 44, 45]. In order to compensate for these myriad effects when performing a mass measurement, it is necessary to couple multiple measurement techniques to independently determine the other parameters to which the QCM is sensitive. Doing so, however, not only results in a more accurate determination of the mass change (e.g. by accounting for stress effects) but also simultaneously provides a greater understanding of a chemical or physical process than a QCM measurement alone could by leveraging the knowledge of sample stresses. As such, QCM samples can be integrated into a modular experimental apparatus to not only correctly determine mass changes, but also a range of complementary processes in a chemical reaction.

Our system combines the QCM platform in a pressure and temperature controlled environmental chamber with optical access, which allows in situ, high-speed, stress measurements to properly characterize mass change. It also includes optical, calorimetric, and electrical measurements for a more complete picture of chemical reactions on nanoscale structures. Here we capitalize on the planar nature of these devices to be used as interferometric mirrors, for measurement of stress by means of sample curvature, as well as substrates for photolithographically defined RTDs that can be used for sensing or introducing known amounts of heat for calorimetry

modeling. All of these measurements are made in a temperature controlled, variable pressure reaction chamber. Below, we describe the components of this system and demonstrate the system's stability and precision. We then apply this apparatus to a palladium hydrogenation reaction as an example of operation.

2.2 Background

Each of the disparate measurement capabilities is motivated by the need to form a complete picture of nanoscale chemical reactions. The particular choices of techniques are driven by constraints of integration into our system. Below we provide background and context for these individual measurements.

2.2.1 Stress measurement

In some of the earliest work measuring film stress on QCMs, EerNisse showed that quartz wafers cut along different crystal axes have significantly different relationships between resonance frequency and film stress [46, 47]. A measurement of the frequency changes on differently-cut quartz wafers during hydrogenation of a palladium film deposited on the QCM, assuming the same hydrogen absorption, thickness, and stress level in both films, yielded a change in both stress and mass associated with the reaction. However, preparing two identical films is complicated by the fact that samples grown at slightly different locations within an evaporator or with slightly different currents by electrochemical means could result in variations of film thickness and defect density. Further, mass and stress do not necessarily scale

linearly with the sample thickness, as thermodynamic and kinetic properties often change at small length scales. Thus, in our system, we perform simultaneous mass, stress, and thermal measurements on a single sample to control for sample-to-sample variation.

Measurements of stress not only allow for corrections in QCM measurements, but can also yield significant insight into material systems beyond quantification of mass changes. For example, a combined stress and optical transmittance study on the hydrogenation of 10 nm palladium films on glass slide substrates revealed a gradual removal of a surface oxide layer that is often not evident in studies of hydrogen content in palladium [48]. A curvature measurement of electrochemical lithiation of silicon has shown that the chemical potential of lithium in silicon is heavily governed by the stress present in the material [49]; the joint measurement scheme also clearly delineates the extent to which the reaction can proceed before the film undergoes plastic deformation, which can inform further engineering of the Li/Si system.

2.2.2 Optical properties measurement

A number of studies have been conducted that combine optical measurement techniques with a QCM to extract unique insights into a system, surpassing what either technique could provide individually. Many of these studies focus on nanostructured samples that have a plasmonic response that depends on the chemical reactivity within the environment. For example, a study of the corrosion of copper

and aluminum nanoparticles was able to distinguish between two primary oxidative corrosion mechanisms [50, 51]. Taken separately, neither the optical nor the QCM measurements could have distinguished between the different processes. By allowing optical access to the sample, our apparatus retains the ability to distinguish these processes.

2.2.3 Calorimetry

The most sensitive QCM-based calorimetry relies on heat conduction calorimetry [52]. This technique detects heat using a thermopile that is thermally grounded on one side. The generated heat flows through the thermoelectric plate creating a voltage by the Seebeck effect. This calorimeter has been shown to accurately measure heat from thin-film reactions. The main drawback is that heats arising from different locations on a sample are treated equally. As such, it is challenging to distinguish between local and global events. Local photochemical processes occurring upon laser illumination can have heat conduction pathways that differ from those that homogeneously arise from the film, complicating the calorimetric analysis. Thus in our apparatus, we chose to perform calorimetry with multiple RTDs in order to allow for the localization heat effects as opposed to the global heat conduction calorimetry. Optical calorimetry is another way to achieve this localized measurement [53], but due to its low resolution of approximately 1 K and its dependence on a multitude of environmental factors (e.g. not only the refractive index changes but changes in size, shape, environment, etc.), we found the RTDs were a

superior measurement scheme in this context.

2.3 Instrument design and description

Table 2.1 outlines our system specifications. Our instrument design allows us to perform on-chip calorimetry with QCM substrates in order to simultaneously resolve changes in curvature of 0.001 m^{-1} (corresponding to a stress of 0.006 MPa per micron of film thickness), changes in mass of 13 ng/cm^2, and changes in optical reflectivity of 0.3%, as well as measurement of heat with 150 μW accuracy. This system has pressure capabilities up to 9.3 bar and a temperature range of 15 to 35 °C with stabilities of ± 0.02 bar and ± 0.05 °C, respectively. Our approach compensates for sample to sample variation by performing gravimetric, stress, and thermal measurements simultaneously on a single QCM. Calorimetry is achieved by modeling the outputs of lithographically printed Cr/Al resistance temperature devices on the sample substrate. We use sample curvature, measured by an interferometer integrated into our microscope, to measure in-plane stress. This non-contact method allows for accurate mass measurements by accounting for frequency changes due to stress effects. The optical access also allows for an external optical source such as a laser, ellipsometer, or spectrometer to be incorporated into the system. Figure 2.1 shows a systems overview of our apparatus. Below we describe, in turn, each of the subsystems: environmental control, optical excitation, interferometry, mass measurement, and calorimetry.

The reactions occur in an environmental chamber capable of achieving and

Parameter	Characteristic Values
Typical steady state minimum detectable power[i]	20 μW
Measured Power Accuracy[ii]	150 μW
Approximate minimum detectable temperature change in film[i]	$\sim$1 mK
Minimum detectable concentration of H	$\sim$0.1 H/M in a 5 nm film
Operation temperature	15 °C to 35 °C
Temperature stability	50 mK over 1 hour 150 mK over 24 hours
Differential temperature stability[iii]	$\sim$ 4 mK
Operating pressure[iv]	1 - 10 atm
Illumination wavelength range	250 nm to 26,000 nm
Minimum detectable Δ (curvature)	0.001 m^{-1}
Stress sensitivity	0.006 MPA per micron of film thickness
Optical excitation laser wavelength	660 nm
Typical absorbed laser power	1-8 mW
Optical excitation laser repetition rate	100 Hz to 500,000 Hz

[i]Defined as the RMS noise about the mean
[ii]Accuracy is defined as the power equivalent to the typical 10 hour drift of RTDs
[iii]Based on typical temperature coefficients. Calorimetry is performed without reference to a temperature
[iv]Can reach 40 atm without optical access

Table 2.1: Apparatus Specifications

maintaining pressures up to 9.3 bar. The sample substrates are 25.4 mm diameter, 5 MHz polished Cr/Au QCMs (Maxtek ®). The piezoelectric resonant frequency of the QCM is measured by a QCM Driver (Stanford Research Systems Model QCM200) using a 10 MHz Rb frequency standard (Stanford Research Systems SIM940). In our system, samples consist of either a 12.7 mm-diameter film or a nanoparticle array of the same area deposited on the center of the QCM. Samples are mounted on custom machined Macor stages with electrodeposited Au contacts to make electrical connection with the QCM. A custom circular array of

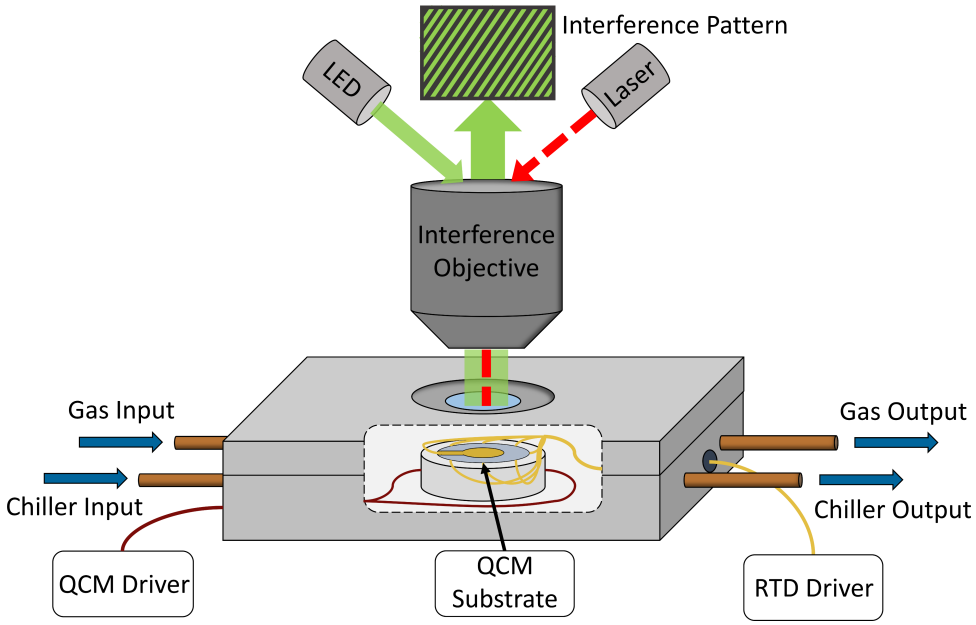

Figure 2.1: Systems overview. The samples are deposited onto a QCM substrate. This QCM sits in an environmental chamber that controls the pressure, temperature, and gas composition. The QCM also has RTDs deposited on its surface that are electrically driven, and the reflective top surface of the QCM is used as a mirror in an adapted Michelson-Morley interferometer with a bandpass filtered LED used as a partially coherent source (see Figure 2.5 for further details). The created interference pattern is used to calculate the curvature of the sample. This setup allows for the introduction of outside optical sources, such as the 660 nm diode laser depicted here. Note that the actual chamber incorporates an additional reference QCM, which we have excluded in this image for clarity (see Figure 2.2).

clip springs (Ted Pella 16399) is used to clamp the sample to the stage and provide in situ electrical contacts for devices such as RTDs. The springs are contacted to a custom-designed flexible printed circuit board that is fed through a tube, which is hermetically sealed with epoxy (3M Scotch-Weld DP125 Translucent). Figure 2.2 depicts the full environmental chamber. The sample under investigation is placed on one of the stages, while a QCM without the active film is mounted on the second stage. This blank QCM allows for any ambient effects in the chamber, such as vibrations or environmental changes, to be calibrated out from the active sample

data.

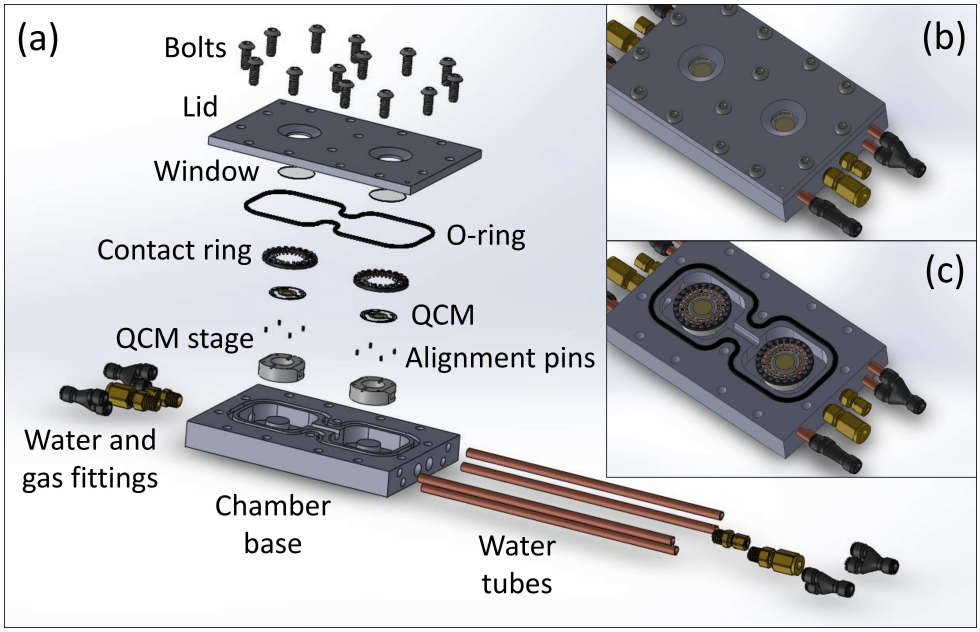

Figure 2.2: (a) Exploded schematic of the environmental pressure chamber. The QCM samples are centered on a Macor stage with Teflon pins and held in place with a circular spring array. A Buna-N O-Ring provides the gas seal for the chamber. The glass window, serving as the optical port, is affixed to the chamber lid with epoxy, creating a hermetic seal. Gas, fluid, and wire feedthroughs are on the sides of the chamber. (b) Lid on and (c) lid off schematic images of the assembled sample chamber.

Figure 2.3 outlines the gas flow system of the apparatus. The gas flows into the system through 1/4" high pressure nylon tubing (McMaster-Carr 5173K43) with high pressure fittings (Swagelok Ultra-TorrTM) to minimize leaks. The chamber is kept gas-tight with a Buna-N O-Ring. For an experiment, the flow rate of the Ar gas is regulated with a mass flow controller (MFC) (Alicat MC Series) and the reactive gases are controlled by high pressure MFCs (Bronkhorst EF-Flow Select). The Alicat MFC can operate at pressures up to 10 bar, so we choose to run experiments at slightly lower pressures to avoid damaging the unit. The 3 MFCs combine into a single gas line and are run through a heat exchanger that is temperature controlled

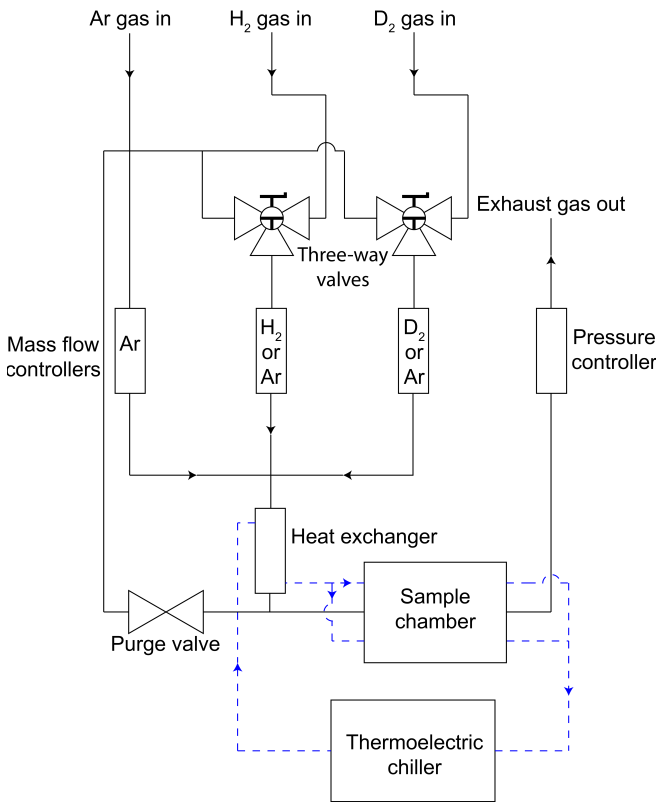

Figure 2.3: Instrument Gas Flow System. Black lines represent gas flow with dashed blue lines representing water flow from the thermoelectric chiller.

with an Oasis Three thermoelectric chiller (Solid State Cooling Systems 10-12684-1C). This chiller also regulates the temperature of the chamber by flowing water through copper pipes embedded in the chamber, as shown in Figure 2.2. The heat exchanger, shown in Figure 2.4, is necessary in order to ensure that the gas is at the same temperature as the sample chamber when it enters the system. The main tube of the heat exchanger is a 1" hollow copper pipe. The gas is wound through this main pipe in a 1/8" flexible copper pipe with 3-5 turns per inch. Water from the thermoelectric chiller enters and exits the exchanger through 1/4" copper pipes, creating a thermal bath around the gas line. Both the water and gas lines that exit the heat exchanger are run directly to the chamber through insulated tubing.

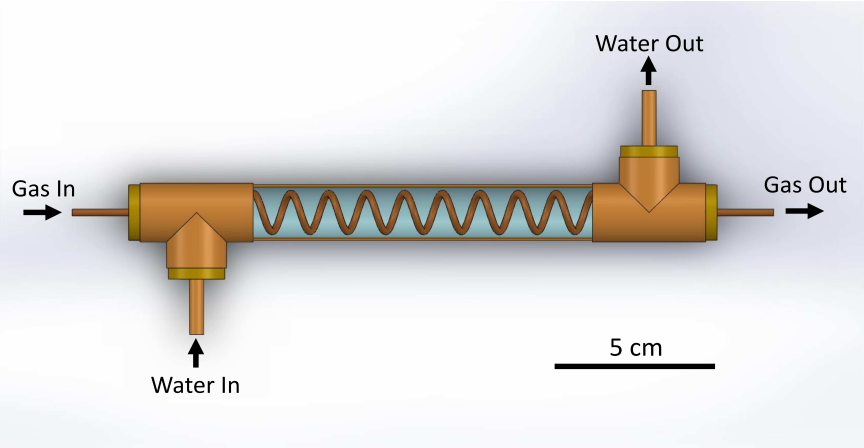

Figure 2.4: Gas heat exchanger design. Before entering the chamber, the gas is flowed through a copper pipe coiled inside a hollow copper tube filled with the temperature controlled glycol/water solution from the thermoelectric heat exchanger. The chamber and the exiting gas tubing are all thoroughly insulated.

The pressure of the chamber is regulated with a digital pressure controller (Bronkhorst P-702CV-21KA-AAD-22V). The temperature is monitored with a thermistor (Omega ON-402-PP) embedded in the bottom of the chamber, which is read out with a digital panel meter (Omega DP32PT-C24). In order to provide the option of resetting the system to an inert environment, a set of valves allow purging of all reactive gases from the chamber and gas lines. During a purge, the 3-way valves (Swagelok SS-42GXS4) are switched to the Ar input, and Ar is flown through all MFCs at 20 sccm each. The 2-way purge valve (Swagelok SS-41GS2) is opened so Ar can flow directly to the chamber at ∼200 sccm, bypassing the MFCs, with the flow rate regulated by a precision needle valve (McMaster-Carr 45585K85).

Figure 2.5 depicts the optical setup of the apparatus. In our system, stress is determined using the curvature of the sample, which is monitored by measuring the distortion of the interference pattern images produced using an adapted Michelson-

Morley interferometer. A 520 nm LED is passed through a bandpass filter (Thorlabs, 520 ± 10 nm), fed into the microscope (Nikon Eclipse LV 100ND), and focused with a modified 5x interferometric objective (Nikon CF IC Epi Plan TI Interferometry Objective) incorporating a 50:50 beamsplitter. Half of the light is reflected off the sample with the other half directed to a flat, tiltable reference mirror. The tilt of this mirror allows the user to compensate for sample tilt, with the acceptable amount of tilt determined by the coherence length of the illumination (∼2 degrees for our light source). In this case, our filtered LED has an approximately square spectral density that results in a fringe amplitude that is roughly a sinc function of sample height. Thus, for ease of analysis, we typically set the tilt to ∼0.1-0.25 degrees. This setting avoids the antinodes of the fringe amplitude and results in a monotonic change in phase of the fringe pattern which simplifies the analysis by including no points of ambiguous phase change, characterized visually by rings or crosses.

Note that the difference in optical path length for the sample and reference beams should be significantly less than the coherence length of the illumination (∼20 μm in our system). To that end, a compensating window cut from the same wafer used to form the window of the chamber is inserted in the path of the reference beam. Further, the length of the reference arm is adjusted with stainless steel spacers to account for the change in focal length introduced by the windows, ensuring that the image focus plane coincides with the interference focus plane. The beams are recombined at the beam splitter to form an interference pattern that is recorded with the microscope camera (Nikon DS-Fi2).

Our setup allows for other light sources to illuminate the QCM either for mea-

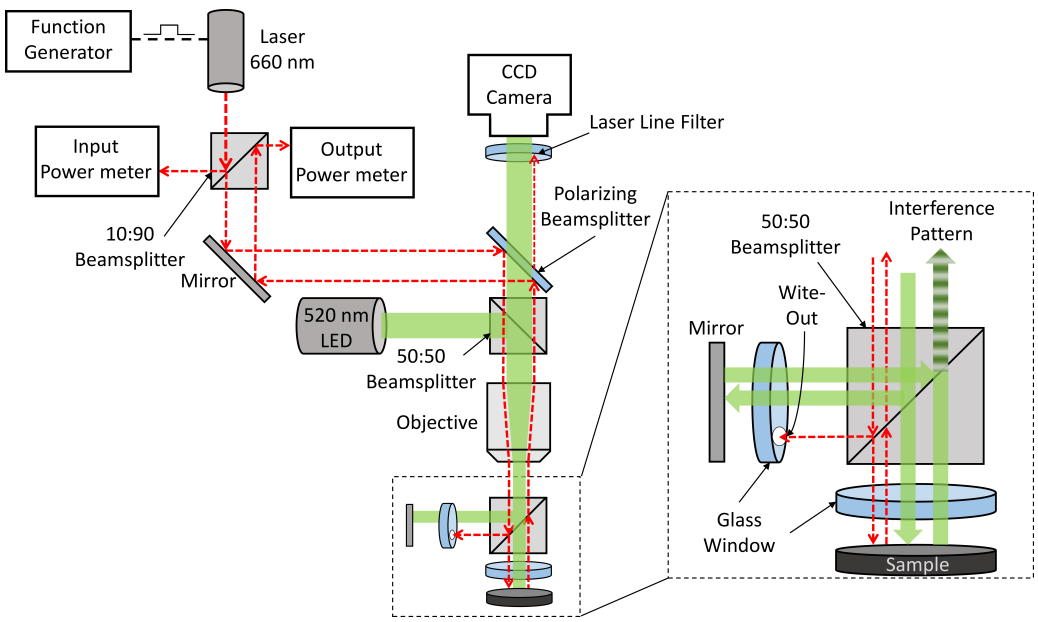

Figure 2.5: Instrument Optical System. Curvature measurements are obtained by collecting the interference patterns from the adapted Michelson-Morley interferometer setup with the sample acting as one of the mirrors. A 660 nm laser is fed into the system with its input and output power values recorded with optical power meters, allowing for the absorption within the sample to be calculated. The laser is blocked from entering the interference arm of the setup with a spot of Bic Wite-Out to prevent interference effects in the reflected beam.

surements of reflectivity, spectrometry, ellipsometry, or for other optical excitations of the sample. In the current apparatus, a 660 nm laser diode (Vortran Stradus 660-100) is used to illuminate the sample for optical excitation or reflectivity. The incident and reflected optical powers are recorded with Si power detectors (Edmund Optics 89-309) connected to power meters (Edmund Optics 89-307) for data collection. The laser beam is reflected onto the sample with a broadband polarizing plate beamsplitter (Edmund Optics 48-545). The section of the glass window in the interference arm intersecting the laser is blocked with a white scattering coating (Bic Wite-Out) to eliminate any interference effects of the laser. A 658 nm notch reflective filter (Thorlabs NF658-26) is placed before the camera to prevent the laser from

saturating the interference image. The output of the laser is controlled with a pulse width modulation (PWM) signal from an arbitrary function generator (Tektronix AFG1062).

To perform calorimetry, heating elements and temperature measurement devices are integrated into the QCM device. For measuring temperature, three ∼300 Ω Cr/Al RTDs are lithographically printed onto the QCMs, with the patterning shown in Figure 2.6. The central and midway RTDs have intertwined heating elements that are used to add known quantities of heat to the localized points (i.e. the location of the RTDs) on the QCM by passing current through the elements. In addition to the RTD elements and localized heaters, the system incorporates contact pads composed of 400 nm thick Ag with a 50 nm thick Au capping layer, which connects to the sample film (see Figure 2.6d). These connections allow us to pass known amounts of current through the film to simulate distributed power sources such as chemical reactions. In the case of discontinuous samples, such as nanoparticle arrays, a 50 nm Cr film is deposited below the active sample to retain the capability of simulating distributed power. The electrically-generated localized heat from the central heating element and the distributed heat from the film are used for calibration purposes in the calorimetry model, as elaborated upon in the Calorimetry section.

To fabricate these RTDs, each QCM sample is initially rinsed with acetone, methanol, isopropyl alcohol, and then water to clean the initial substrate. The substrate is then further cleaned with a 100 W plasma in 1 torr of O_2 for 30 min. Immediately following this clean, 600 nm of SiO_2 is deposited using plasma enhanced

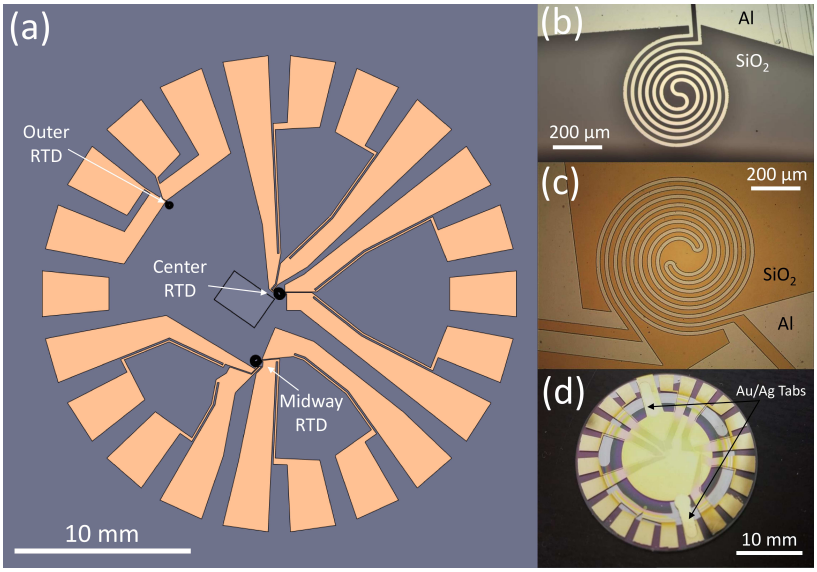

Figure 2.6: (a) Mask design for samples' RTD pattern. The RTDs are located at the center of the QCM, 4 mm from the center (midway RTD), and 8 mm from the center (outer RTD). Each RTD is measured with 4-point contacts for improved accuracy. The center and midway RTDs consist of two RTDs intertwined, with one acting as a heater and the other as a sensor. The outlined box near the center of the QCM is used for consistent alignment within the microscope. (b) Outer and (c) intertwined center RTD images. (d) Sample with complete fabrication of RTDs and Ag/Au contact tabs.

chemical vapor deposition (PECVD) (Oxford Instruments). The RTDs are then patterned on the SiO_2 using standard contact photolithography, and 50 nm Cr and 120 nm Al are deposited using electron beam evaporation (Angstrom). The excess metal is lifted off overnight and then sonicated the following morning for 2 min to finish the lift-off process. Another 600 nm of SiO_2 is PECVD deposited on the center of the sample using a shadow mask that excludes the RTD contact tabs. Next, 400 nm Ag and 50 nm Au are e-beam deposited using a shadow mask for the film contact tabs. The active film is then e-beam deposited on the center of the sample using a separate shadow mask. A schematic of each step of this process is shown in Figure 2.7.

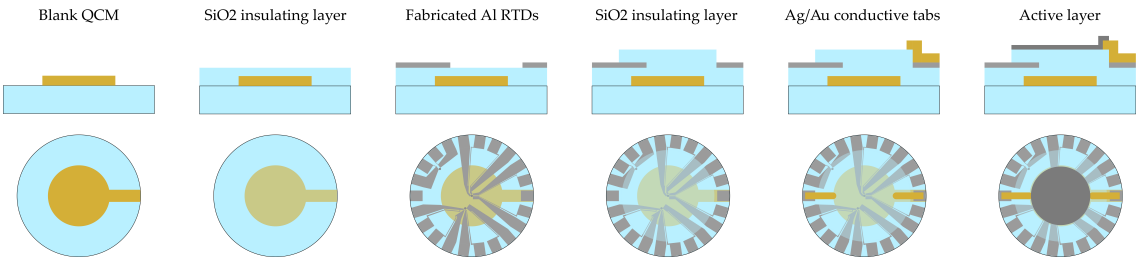

Figure 2.7: Outline of each step of the sample fabrication process. Top row: cross-sectional view. Bottom row: aerial view

To quantify the sensitivity of the lithographically printed RTDs to the temperature of the entire system, as controlled by the thermoelectric chiller, we recorded the measured resistances of the RTDs while sweeping the temperature of the chamber from 15 to 35 °C. The actual temperature of the chamber was monitored with the thermistor embedded in the bottom of the chamber. The resistances from all three RTDs on a QCM without an active sample were recorded throughout the sweep. Normalizing to the 25 °C resistance of each RTD, we find that the RTDs have an average temperature coefficient of 0.0028 ± 0.0001 $(\Omega/°C)/\Omega$. Results of this temperature sweep are found in Figure 2.8.

The RTD sensing system driver is an Analog Devices AD7124-8 integrated circuit, implemented here via an AD7124-8 evaluation board. This driver was chosen because it met our requirements of customizability, sensitivity, noise, speed, and integrability into our custom measurement software. The AD7124-8 uses a multiplexed set of input/outputs, which can be internally connected to a differential amplifier and analog to digital converter (ADC) or output to peripherals such as the precision variable current source in use here. See Figure 2.9 for full wiring diagram. Each of the three sensing RTDs are connected in a four-point probe configuration.

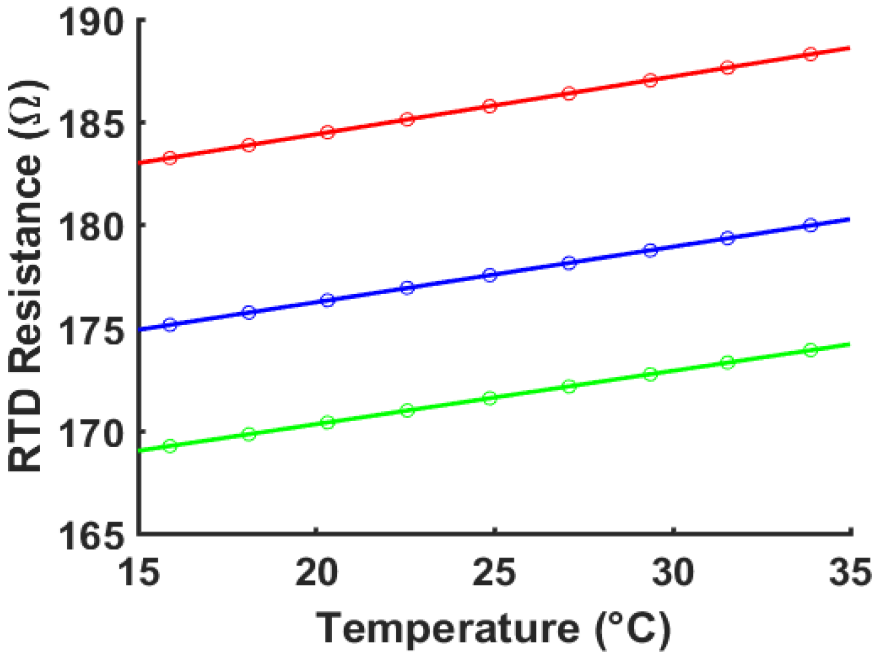

Figure 2.8: RTD resistances as a function of measured chamber temperature. The average temperature coefficient is 0.0028±0.0001 (Ω/°C)/Ω. The RTD resistances shown correspond to the center (red), 4 mm from the center (blue), and outer (green) RTDs.

The voltage drop across each RTD is compared to that across a reference resistor in a ratiometric scheme, as seen in Figure 2.10. We use two 470 Ω bias resistors to ensure that the inputs to the ADC meet the absolute voltage requirements (0.1 V from the rails of 0 and 3.3 V). The AD7124-8 incorporates several digital filter options, which allow the user to define the tradeoff between speed and noise. We use a sinc^4 filter with first zero at 60 Hz (primary source of noise), which results in a sampling time of 62 ms per channel. Our applications use 4 channels: 3 RTD ratiometric measurements and a voltage measurement of the reference resistor (compared to the on-chip 2.5 V precision voltage source). Communication with the chip is accomplished via the SPI interface on a Teensy 3.2 development board, which also transmits data on-demand with a USB COM port. The data exchange between

the controlling computer and the 4 inputs takes ∼270 ms for a single measurement. Our typical sampling period in the custom-built Windows user application is 350 ms; this leaves sufficient time for the ∼270 ms required for acquisition and 80 ms for other tasks such as saving data. The currents through the center intertwined heating element and the center disk are driven by Keithley 2450 sourcemeters in order to model known heating effects in the sample.

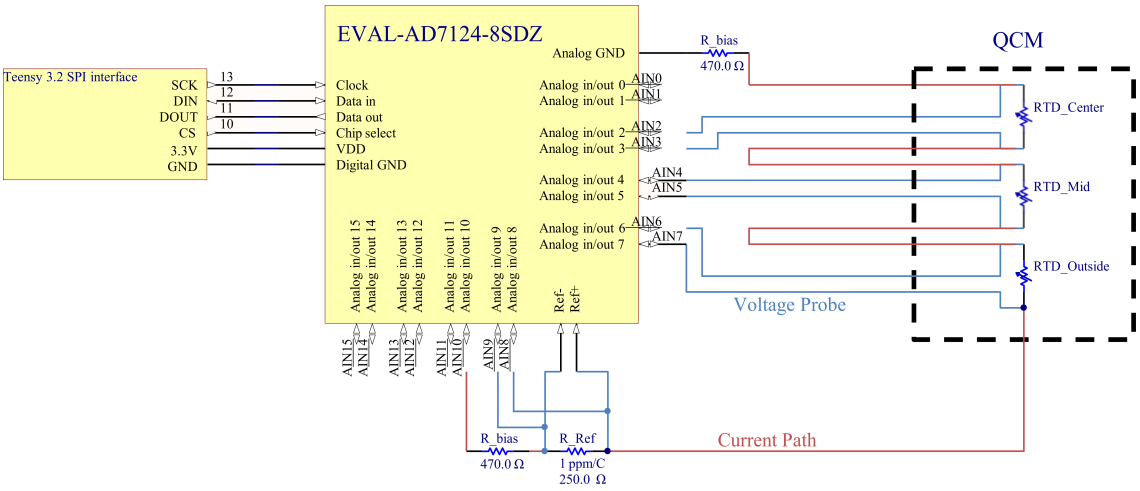

Figure 2.9: RTD and current sensing schematic. The current (path shown in red) flows through all of the RTDs and reference resistors. The voltage drops (blue paths) across each of these resistors is probed and compared to the drop across the reference resistor. Note that the voltage probes do draw non-zero current. However, the current is typically < 1 nA resulting < 1 ppm offset for a 1 mA excitation current.

Lastly, in order to properly perform the calorimetry measurements, we need to estimate the thermal conductivity of the gas and how it changes with time. Eq. 2.8 in our calorimetry section assumes that thermal dissipation to the gas environment can be approximated by a quadratic equation with respect to partial gas pressure. Below we demonstrate the accuracy of this approximation. The thermal conductivity is related to the mole fraction of argon as shown in Figure 2.11a. This

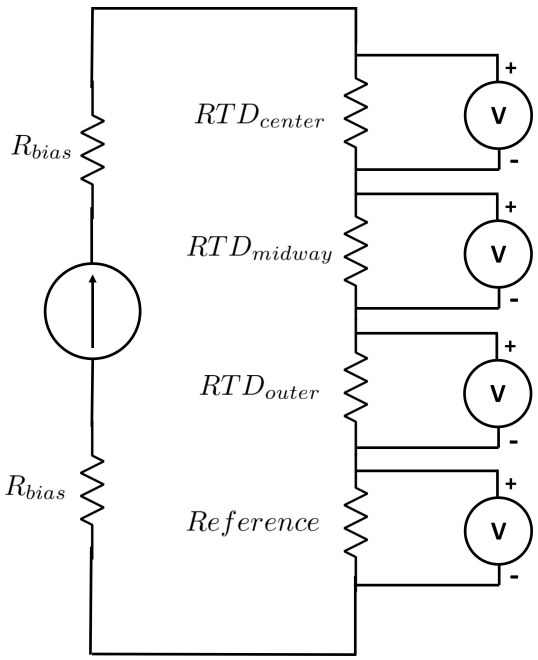

Figure 2.10: Schematic for the RTD current source and voltage measurement system. The RTD resistances are ~300 Ω, the reference resistance is 500 Ω, and the R_{bias} resistances are 470 Ω

plot suggests that the relationship is nearly linear, but has small deviations from linearity. Another metric would be preferable to better capture the effects of heat loss through gaseous conduction. Fortunately, the resistance of a QCM is linearly related to the change in thermal conductivity. For a QCM in a viscous medium, the resistance can be expressed as [54]:

$$R = \left(\frac{\omega_s L_u}{N\pi}\right)\sqrt{\frac{2\omega_s \rho_L \eta_L}{\bar{c}_{66}\rho_q}} \tag{2.1}$$

where N is the overtone number, ω_s is the resonant frequency, L_u is the inductance of the QCM in vacuum, ρ_L is the density of the fluid, η_L is the viscosity of the fluid, ρ_q is the density of quartz, and $\bar{c}_{66}$ is the piezoelectrically stiffened quartz elastic constant. N, L_u, ρ_q, and $\bar{c}_{66}$ are all constant upon a change of atmosphere,

thus they do not factor into ΔR. The resonant frequency is constant to four significant digits during a standard hydrogenation experiment, thus can also be ignored. Larger frequency changes result in nonlinear behavior and are outside the scope of this correction scheme. Thus this expression can be approximately written as:

$$\Delta R \propto \sqrt{\rho\eta} \tag{2.2}$$

Where the L subscripts have been dropped for clarity. Figure 2.11b shows that the square root of the product of density and viscosity for the Ar-H_2 system, and thus the QCM resistance, scales linearly with thermal conductivity for Ar mole fractions greater than ~0.1 [55]. When plotted against time, with the H_2 partial pressure modeled as a decaying exponential, Figure 2.11c shows that assuming a linear relation between mole fraction and thermal conductivity will only slightly underestimate the thermal conductivity of the gas atmosphere. Given the small discrepancy, we assume that partial pressure is proportional to thermal conductivity which allows us to perform calorimetry while a new gas is introduced. This assumption would cause for a maximum error of 1.5% to our calorimetry model (given by the error in the conductance that this partial pressure error would create), well below our noise level.

Fortunately, the QCM resistance is not very sensitive to changes in mass or stress, so it serves as a good proxy for changes in thermal conductivity of the environment [56]. Accordingly, we fit the QCM resistance in the region surrounding a change in gas content to an exponential. Using the time constant from this fit and

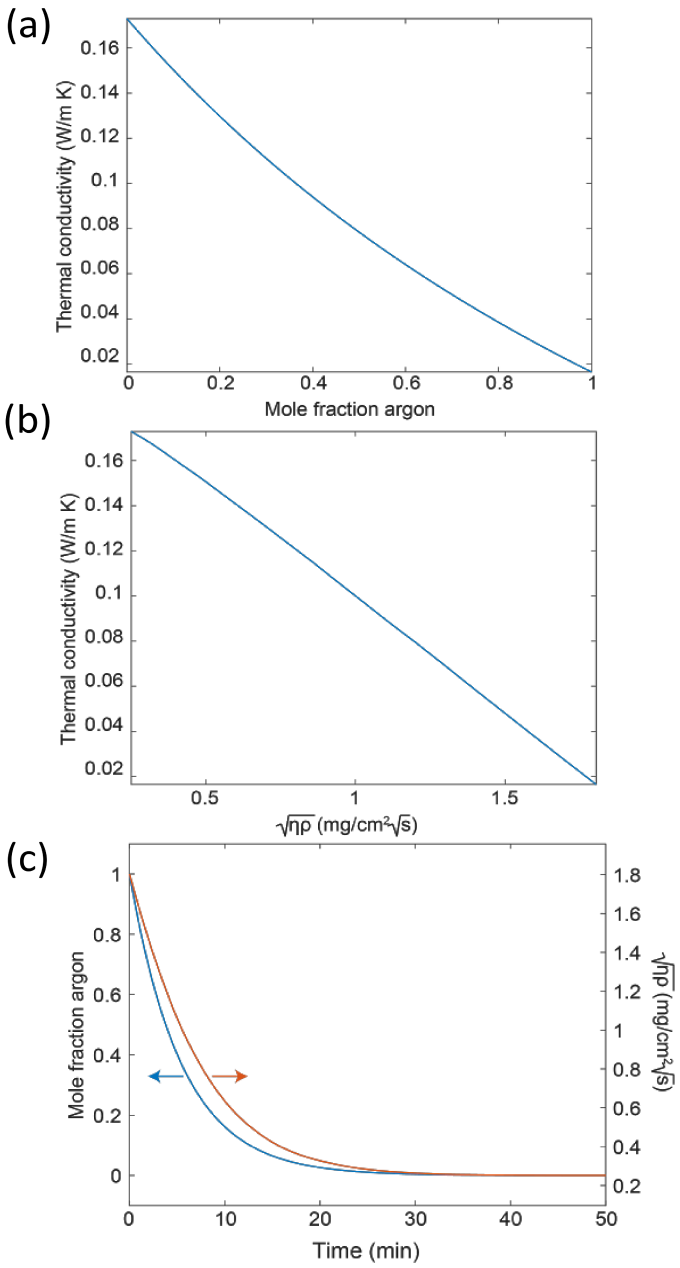

Figure 2.11: (a) Plot of thermal conductivity of an Ar-H_2 mixture at 9.3 bar as a function of the mole fraction of argon. (b) Plot of thermal conductivity of an Ar-H_2 mixture at 9.3 bar as a function of the product of the square roots of the density and viscosity. This parameter serves as a proxy for the change in resistance of the QCM. (c) Plot of both the mole fraction of argon and change in resistance proxy as a function of time when the H_2 MFC is opened at time 0 and flowing at 20 sccm. The initial atmosphere is assumed to be pure argon at 9.3 bar in a chamber with a volume of 13 mL.

the initial partial pressures (as determined by the ratios of the MFC flow rates), we generate approximate partial pressures.

2.4 Demonstration of operation and stability

To demonstrate the stability of the apparatus, a control experiment was performed on a blank QCM sample with RTDs. The sample was pressurized in Ar up to 9.3 bar, switched to H_2 at 9.3 bar for 4 hours, switched back to Ar for 4 hours, and finally returned to H_2. During the run, the 660 nm laser was pulsed and incident on the sample while in H_2 and Ar to test how well the calorimetry model fit the heating induced by laser absorption. The data of this run are reported in Figure 2.12 and show the stability of the system. The partial pressure of H_2 gas is calculated using the method described in the previous section. The leak rate of the system at 9.3 bar is measured to be 2 sccm.

2.5 Example of stress and mass change measurements

The stress in the sample is characterized by the curvature of the substrate. The curvature is determined by converting the optical phase change measured by the interferometric images into a sample height change, with the process depicted in Figure 2.13. The curvature is then directly converted into a corresponding frequency change that is linearly independent of the frequency change due to mass under the thin-film approximation (i.e. the film mass is much smaller than the QCM mass). First, the image is bandpass filtered and normalized so that spatial variations in

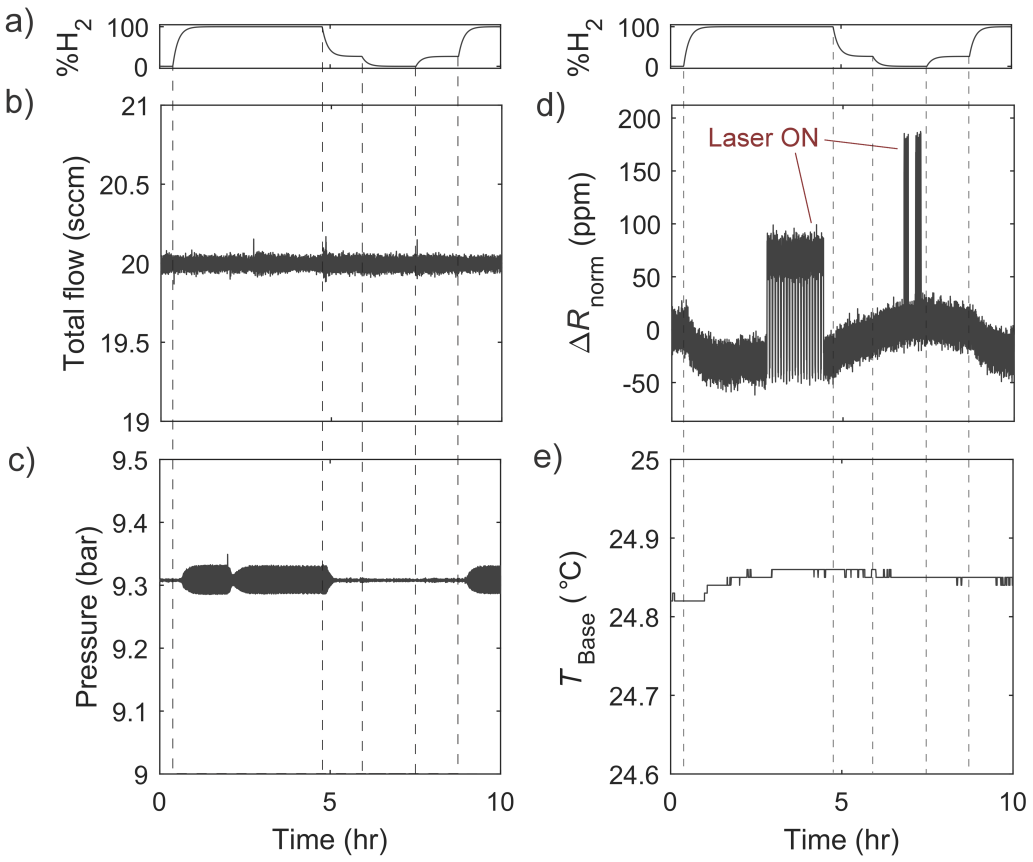

Figure 2.12: Apparatus stability for a control experiment including changes in gas composition and laser excitation. Vertical dashed lines indicate a change in H_2 flow rate set point. (a) Calculated H_2 partial pressure. (b) Total flow rate over the course of a 10 hour experiment. (c) Pressure of the chamber for a fixed pressure set point. (d) Normalized differential RTD resistances through a run. The spikes in the resistances correspond to the temperature increases from the absorption of laser light. (e) Temperature of the environmental chamber, as measured by the interior thermistor.

image brightness and fringe sharpness are reduced. Greater fidelity to the original sample surface can be achieved by removing some artifacts and by utilizing the very narrow bandwidth of the signal. The first artifact is simply brightness variation in the image. This is removed by high-pass filtering the image with the cutoff frequency one-fifth of the fundamental frequency. The second artifact is given by the finite coherence length of the filtered LED light. This results in a fringe amplitude

variation with sinc dependence on the sample surface height. To normalize this variation, the image is then rectified and low-pass filtered. The high-pass filtered image is divided by this amplitude envelope. Finally, we low-pass filter this image to reduce noise. This filtering process is graphically shown in Figure 2.14.

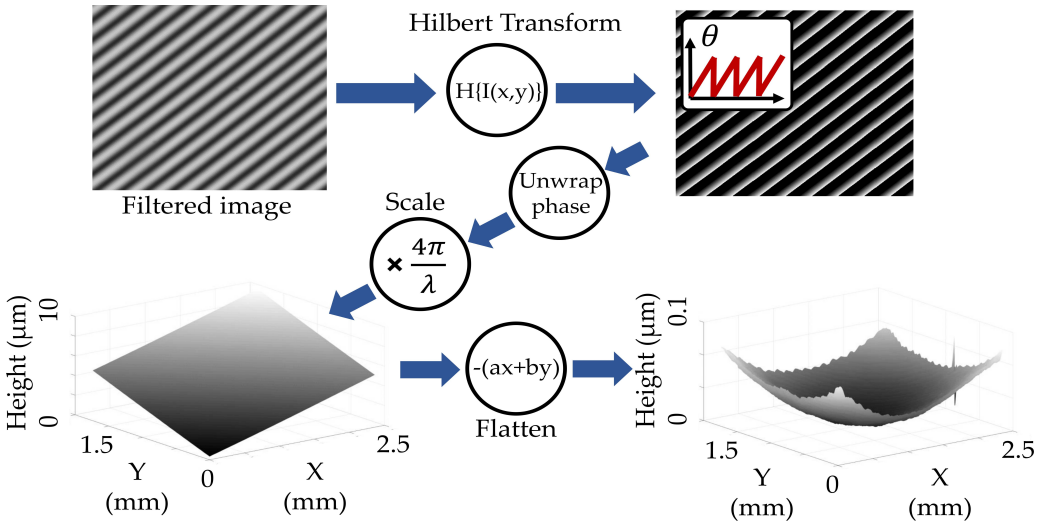

Figure 2.13: Image processing flow to extract curvature measurements from interference image. The image is filtered and normalized (Figure 2.14). The instantaneous phase is then extracted from the Hilbert transform. The phase is converted to height and flattened to give the sample topography. The curvature is extracted from the second derivative of a 2D polynomial fit to the sample height.

After the image is filtered, it is Hilbert transformed and the phase angle of the now-complex signal is extracted. The phase angle, which varies from only 0 to 2π in a sawtooth pattern, is then unwrapped by stitching together steps in a phase of 2π to produce a smooth phase surface. This phase surface can then be converted to sample height by dividing by the phase change per change in height, $2\pi/(\lambda/2)$, where λ is the central illumination wavelength ($\lambda = 520 \pm 10$ nm for our LED). Finally, a 2D polynomial is fit to this phase surface and the curvature can be directly extracted as the second spatial partial derivatives of the surface.

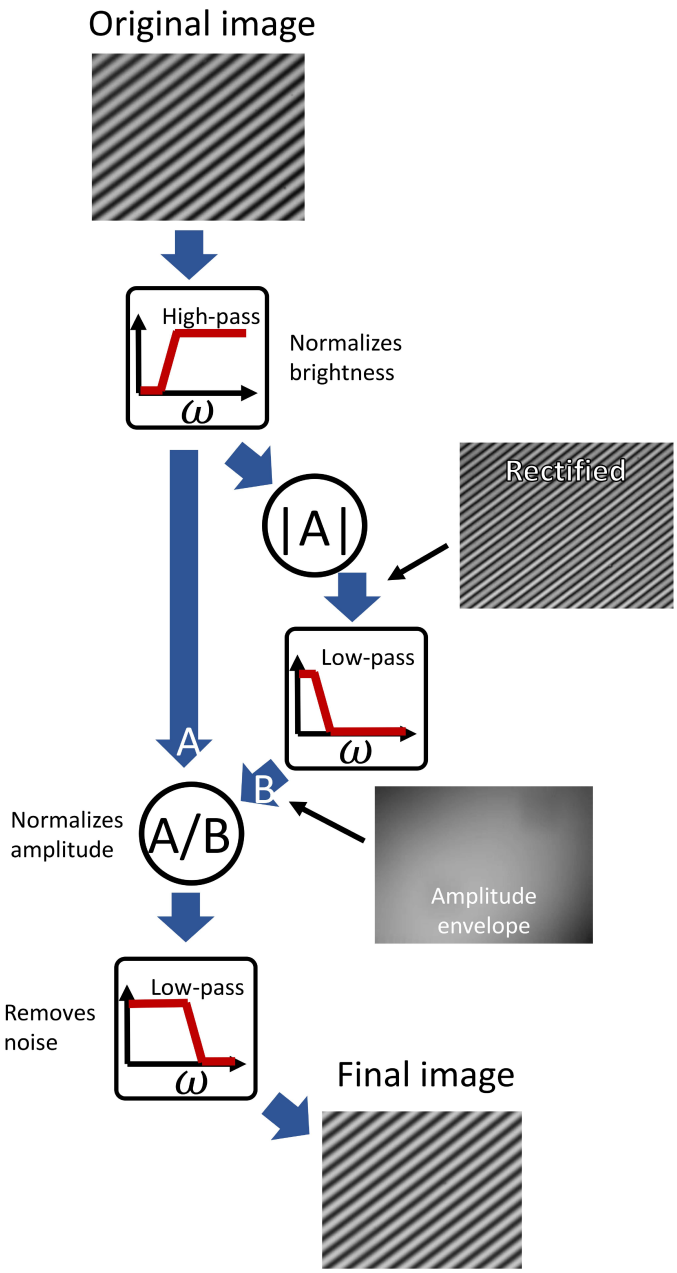

Figure 2.14: Image processing flow. The process removes variation in brightness and interference fringe amplitude. Noise is then removed with a low-pass filter.

The hydrogen mass loading of the active sample is an important factor when characterizing a reaction on a film. To determine this loading, we begin with a precise measurement of the mass of the active material deposited on the sample. To accomplish this goal, we fabricate an additional, sacrificial sample that consists

of a lithographically defined 1 cm x 1 cm square of the material we are characterizing on a polished Si wafer during each sample film deposition. We dissolve this film using 4 mL of either aqua regia or boiling hydrochloric acid and dilute to 100 mL as determined by film composition. We then use inductively coupled plasma atomic emission spectroscopy (ICP-OES) to determine the metal mass per area of the sample deposition. We assume that the areal mass density of the metal on the sample is the same as it is on the calibration piece (note that areal mass density is expected to be constant even if other properties such as grain size change sample to sample), as the deposition occurs on both pieces concurrently. Knowing the area of the active film on the QCM allows us to determine the exact mass of the active material. This method is robust to multi-layer samples, where the individual layers of each sample cannot be easily measured. If the sample is only a single layer, an alternative method of finding the sample thickness is to use a step height measurement using Atomic Force Microscopy (AFM) over one of the lithographically defined edges of the Si wafer. Once the mass is known, we determine loading in the film by the QCM frequency change less the portion due to stress and environmental effects (frequency compensation discussed below).

To calculate the contribution of stress to the frequency shift measured by the QCM, we use a combined technique of numerical and analytical calculations. First, we numerically calculate in COMSOL the amount of stress-induced in the QCM due to curvature changes. In the simulation, we bound the system to be immobile at the edges to match our conditions of the spring ring holding down the QCM. Using these numerical stress values, we can calculate the relationship between frequency and

stress analytically by calculating the propagation speed of the shear wave through the crystal and then integrating over two times the length of the crystal to get the frequency. The final output of our derivation gives

$$\Delta f_\sigma = \alpha \Delta \kappa \tag{2.3}$$

where α is the calculated curvature to frequency conversion factor equal to -777 Hz m and $\Delta\kappa$ is the change in curvature. See Appendix A for a full derivation of the stress to frequency equations. For a typical thin metal film (0 - 1 μm) on a QCM, the curvature measurement has an uncertainty of 0.001 m^{-1} which corresponds to a stress uncertainty of 0.006 MPa per micron of film thickness from this calculation. An example of the contribution of stress to the total frequency change can be seen in Figure 2.15. Here we use a 335 nm palladium film, which has a well-known hydrogen loading fraction to confirm the equations above. The gas pressure and composition of the chamber also contribute to the frequency change and these effects are calibrated out using the measured frequency of the QCM on the secondary control stage caused solely by environmental effects. The frequency from the mass change of the sample can be calculated from the total frequency change using the following equation:

$$\begin{aligned} \Delta f_m &= \Delta f_{tot} - \Delta f_{gas} - \Delta f_\sigma \\ &= \Delta f_{tot} - \Delta f_{secondary} - \alpha \Delta \kappa \end{aligned} \tag{2.4}$$

where Δf_m is the frequency change due to a mass change, Δf_{tot} is the total frequency change, Δf_{gas} is the frequency change due to environmental effects, Δf_σ is the

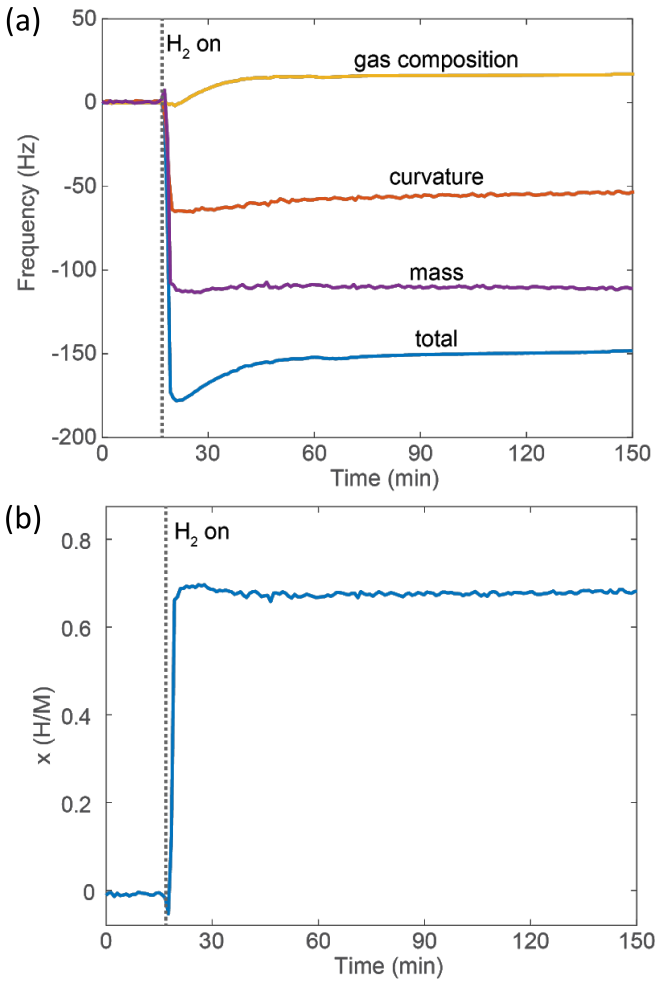

Figure 2.15: a) Plot of QCM frequency change during hydrogen loading of a 335 nm thick Pd film. The blue curve is the measured frequency of the active QCM, the yellow curve is the measured frequency of the secondary blank QCM, and the orange curve is the frequency contribution from the stress in the active QCM, as calculated from the curvature. By subtracting the stress and gas composition contributions from the total measured frequency, we obtain the frequency change due to the added mass of the hydrogen within the Pd lattice (purple curve). b) Mass loading fraction x upon introduction of H_2.

frequency change due to stress, and$\Delta f_{secondary}$ is the measured frequency of the blank QCM on the secondary control stage. The mass-induced frequency change can then be converted to the hydrogen loading with the equation:

$$\Delta x = \frac{\Delta f_m A_M}{\rho_M t_f A_H C_f} \tag{2.5}$$

where Δx is the change in hydrogen atoms in the lattice per metal atom, A_i is the atomic mass of species i (either M, the metal host or H, hydrogen), ρ_M is the density of the unloaded metal M, t_f is the film thickness, and C_f is the Sauerbrey coefficient from the literature relating a frequency change to a corresponding mass change. The uncertainty of the mass change measurement in our system is 13 ng/cm^2, which is dominated by the uncertainty in curvature. It should be noted that the extra mass and varied impedance associated with RTDs, insulating layers, and the film under test result in a correction to the Sauerbrey coefficient of $< 2\%$ (determined by full transmission line simulation as per C. Steinem and A. Janshoff [41]). However, this correction factor lies within the uncertainty for a typical gas-phase loading experiment and can generally be ignored. The measured loading fraction of 0.7 agrees with the well-known value for palladium at this pressure (9.3 bar) [57, 58].

2.6 Calorimetry

We use a one-state nonlinear lumped element model to describe our system (i.e. the state is described by a single variable) with thermal potentials measured at discrete positions by our RTDs [59]. This model takes the difference of the normalized resistances of the outer and center RTDs as the independent variable (i.e. state variable of the single floating node), τ, which is a function of the differential temperature between the center and outside of the QCM. Thus, all that is needed

is a measure of relative temperature during a system calibration, which may then be used to infer the input power (from any source) during an experiment. The thermal power input sources are the powers from the RTDs, P_{RTD}, the laser or laser-induced reactions, P_{Laser}, the heat from running a current through the sample thin-film or thin-film reactions, P_{Disk}, and the heat from running current through the central heating element, P_{Heater}. Figure 2.16 shows a schematic of the lumped element model with the thermal resistor and capacitor driven by the inputs and tied to a thermal ground. While only two RTDs are utilized in the one-state model, we have included a third RTD on the QCM. This third (midway) RTD presents an opportunity for a two-state model (using τ and a second state variable), which could offer higher precision as well as additional information about heat localization, but would require more development and an extended calibration process. Thus, a two-state model is left as a future refinement.

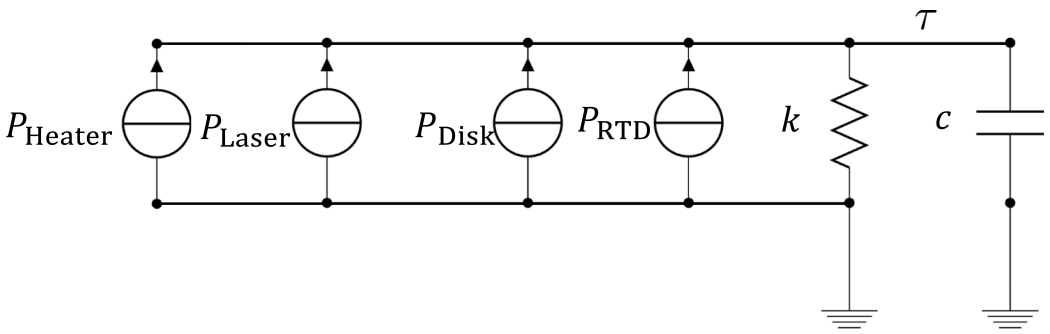

Figure 2.16: The four source, one-state lumped-element calorimetric model diagram. The four contributing powers measured into the sample are the input powers from the RTDs, P_{RTD}, the laser or laser induced reactions, P_{Laser}, the heat from running a current through the sample thin film or thin film reactions, P_{Disk}, and the heat from running current through the central heating element, P_{Heater}. The state variable, τ, is the relative thermal gradient of the system defined by the difference between normalized (to equilibrium resistance) center and outer RTD resistances. k and C are the thermal conductance and thermal capacitance of the system respectively.

This one-state system can be modeled with a first order differential equation described by a single independent state variable τ and is given by:

$$P_{In}(t) = k\tau + C\frac{d\tau}{dt} \tag{2.6}$$

with

$$\tau \equiv \frac{R_{Center}(t)}{R_{Center,0}} - \frac{R_{Outer}(t)}{R_{Outer,0}} \tag{2.7}$$

Here P_{In} is the total effective input power (i.e. the sum of the individual input powers weighted by power distribution scaling factors, see below), $R_i(t)$ is the measured resistance of RTD i at time t, and $R_{i,0}$ is the measured near-equilibrium resistance of RTD i (i.e. the resistance when the only input power to the system is the small RTD sensing current). The non-linear thermal conductance, k, and capacitance, C, depend on the state variable and the partial gas pressures. These values are given by:

$$k = k_0 + k_\tau\tau + \sum_{n=0}^{N} k_{\rho_n}\rho_n + k_{\rho_n,2\rho_n^2} \tag{2.8}$$

$$C = C_0 + \sum_{n=0}^{N} C_{\rho_n}\rho_n + C_{\rho_n,2\rho_n^2} \tag{2.9}$$

where ρ_n is the partial pressure of gas species n. Note that when the system is operated at a constant total pressure and with a mix of two gases, as is often the case, the partial pressure terms can be collapsed to a single term. With all the constants

above known, the total input power may be inferred. However, these constants must first be determined during the calibration process (i.e. system identification), when known powers are input into the system and the constants are fit using Eq. 2.6. The effective total input power during the system identification process is given by:

$$P_{In}(t) = P_{RTDs}(t) + P_{Disk}(t)\left(A_{Disk} + \sum_{n=0}^{N} A_{Disk,\rho_n}\rho_n\right) + P_{Laser}(t)A_{Laser} \quad (2.10)$$

where P_i and A_i are respectively the input power and the power distribution scaling factor of power type i, with $A_{i,\rho n}$ being the proportion due to the change in partial pressure n. These power distribution scaling factors are a result of the differences in the spatial distribution of the heat sources and are also fit during the calibration process. The terms that include partial pressures represent the differences in effective power due to the spatial distributions. As noted above in the case of a constant total pressure composed of two gases, the sum can collapse to a single term.

A complete calorimetry measurement of a sample is composed of three sections: experiment where we measure the heat of a reaction, calibration where we fit a system model, and prediction where we confirm the accuracy of the model. After each experimental section, a system identification cycle is run where various known power inputs are applied at higher powers and frequencies than expected in the experimental run. The results of these excitations are used to fit the parameters defined above (A's, k's, and C's). While this system identification step could theoretically be conducted before the experiment, it requires changing the reactive gas

partial pressure, which in the case of irreversible gas-based reactions would cause the sample to be fully reacted before the experimental section. While the equations above present a comprehensive system, generally the calibration should be tailored to the experiment, which may allow for reduced dimensionality of the fit. The fitting process uses Matlab System Identification Toolbox together with the freely available Calorimetry System Identification (CSID). This Matlab toolbox takes a set of user-defined differential equations with unidentified constants (A's, k's, and C's) and uses a calibration dataset (known inputs with measured outputs) to fit these constants. The CSID adds additional functionality and gives examples specific to the identification of calorimetric systems.

In order to fully probe the dynamics of the apparatus, it is important to excite with a wider bandwidth and with greater amplitude than the heat pulses expected during the course of the experiment, as well as with all possible power sources. In our experiments, we use a set of square pulses of increasing power at a constant total pressure of 9.3 bar and 3 different partial pressures of the reactive gas (see Figure 2.17). Note that the calibration routine only calibrates for a limited range of the system's capabilities and thus limits the scope of experiments. However, by reducing the scope of the experiment and tailoring the calibration to the actual use of the instrument, we can reduce the number of fit parameters in our model. Table 2.2 shows the reduced set parameters actually employed in a typical experiment. The calibration portion is followed by a prediction section. During this phase, the system is excited more gently in an attempt to simulate run data. The data from this section can then be used to derive error bars and help assess overfitting during

the calibration phase.

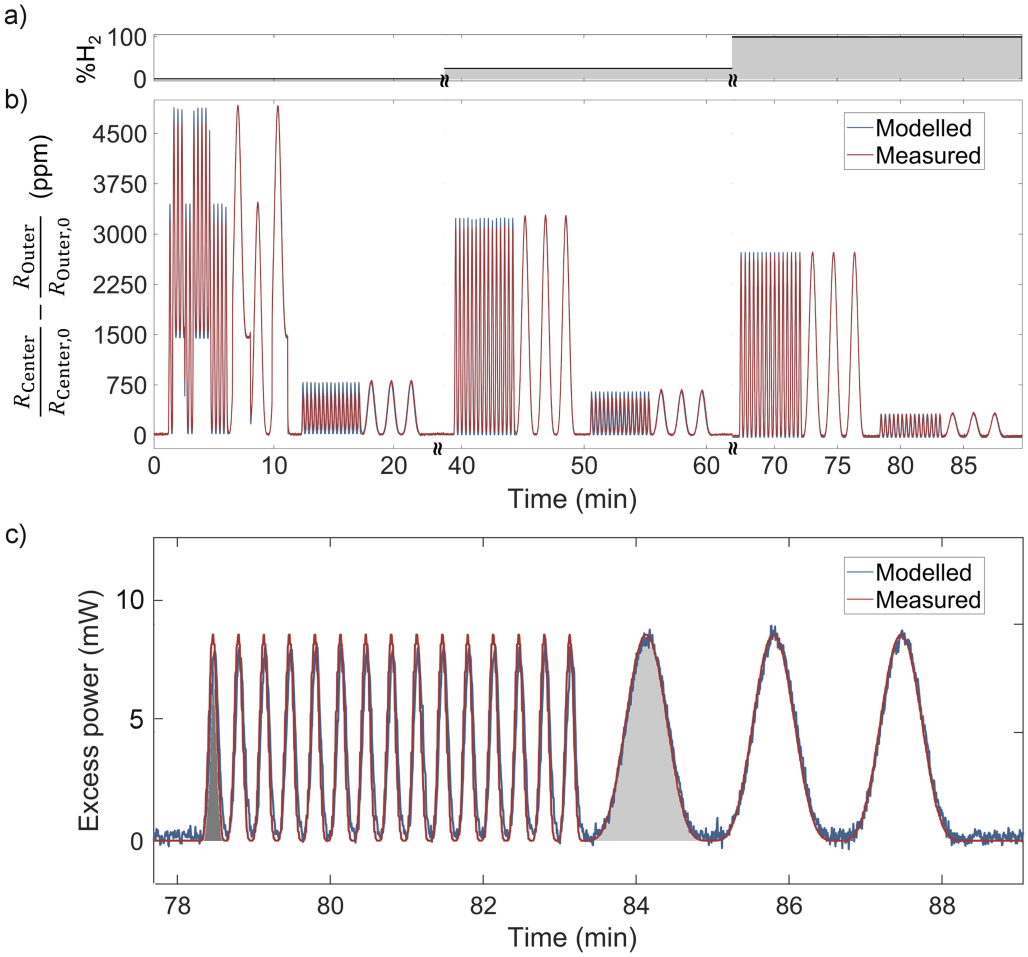

Figure 2.17: Modeled and measured calorimetry data for a thin Cr film during the prediction portion of a run in which the accuracy of the calibration is assessed. (a) Calculated H_2 partial pressure of the system. (b) The system is excited with each of the power sources. The red line is the state variable measured by the apparatus and the blue line is the output of the model of this data. (c) Modeled and measured excess powers due to pulses of the disk heating power during the final portion of the prediction section. The system is thermally excited by flowing current through the film. This portion corresponds to the integration region used to calculate the accuracies of the energy pulses. Here the integration is represented by the shaded areas with dark grey for the short 65 mJ pulses and light grey for the larger 325 mJ pulses.

With the fit complete, we first check the parameter values and the accuracy of the model. Table 2.2 shows some typical fitted calorimeter values for a standard

experiment using one total pressure and two gases. The parameters are scrutinized to verify that they are physical (e.g. no negative temperature coefficients for our quartz-based system). The fit is tested by using a prediction run with sinusoidal excitation at two different frequencies.

Parameter	**Value**[i]
k_0	$2.7W\Omega/\Omega$
k_τ	$4.2W\Omega^2/\Omega^2$
C_0	0.017 $J\Omega/\Omega$
C_{pH_2}	-0.028 $J\Omega/\Omega$ Bar
$C_{pH_2,2}$	0.012 $J\Omega/\Omega$ Bar^2
k_{pH_2}	-0.054 $J\Omega/\Omega$ Bar
$k_{pH_2,2}$	-0.00056 $J\Omega/\Omega$ Bar^2
A_{Disk}	0.11
A_{Laser}	0.72
A_{Disk,pH_2}	-0.0052 1/Bar
Stress sensitivity	0.006 MPA per micron of film thickness

[i]Note that the state variable, τ, is unitless but the unit of τ, Ω/Ω, are shown here to make dimensional analysis clear.

Table 2.2: Example fit parameters for a calorimetry calibration run

The quality of the fit is then tested with another set of more gentle excitations of the various power sources in a prediction run that immediately follows the calibration cycle. Data recorded from a typical prediction run is compared to the output of the calibrated model in Figure 2.17. This run shows a normalized (by the mean value) root mean squared (RMS) error between measured and modeled data of 8%. We also compare the energy calculated from the disk power in a single pulse to that of the energy modeled. This comparison gives the accuracy of the energy inferred from a potential chemical reaction on a similar timescale and power to that

of the pulse, assuming that P_{Disk} is an analog to the power of the reaction. Here we define our metric as the difference between the integrated excess calculated power (difference between quiescent power and pulse power) and integrated excess effective input power (P_{In}) divided by the integrated modeled power over the pulse region. In the run shown, we find this average error to be 4% for the short 65 mJ pulses and 2% for the larger 325 mJ pulses in 100% H_2. The improved accuracy compared to the error for the total run arises from sensor drift. Finally, to put bounds on the instantaneous power accuracy and resolution of our system, we consider the sensor drift over the course of a 10-hour experiment. The typical sensor drift on this time scale is 75 ppm which corresponds to 150 μW of apparent power drift.

There are several sources of error in our current calorimetry system. The primary source of error in our measurements is instrument drift. The typical drift of our state variable τ is $\sim$75 ppm over 12 hours, which sets our accuracy at 150 μW. While the sources of the drift are unknown, several possibilities provide avenues for better fits. The range of potential causes is narrowed by the fact that our drift is both non-monotonic and does not appear to be improved by burn-in or aging. The most likely candidate is temperature non-uniformity, which would be evidenced by drift in the state value (differential relative resistance). This is made more likely by the differences in equilibration time between the outer RTD and the center and midway RTDs patterned above the Au electrode. Note, however, that while the drift creates apparent inferred power offsets (representing a constant additional power sink or source), the timescale is on the order of hours which still permits the determination of shorter time scale events by subtracting observed background power caused by

this drift. To potentially resolve this the chamber and gas lines could have improved insulation and additional temperature sensors could be added to the chamber. This would allow us to mitigate and account for non-uniformities which may be the source of our sensor drift.

Another source of error is the use of a single state lumped element model, which only approximates the distributed heat source produced by the disk power or a chemical reaction of a film on the QCM. By modeling this heat source in the same way as the other point sources, we neglect the larger thermal capacitance and differences in temperature across the film which affect the determination of the nonlinear terms of the above equations. However, fitting suggests the former, while non-zero, is a minor effect (e.g. for the run shown in Figure 2.17 the difference in normalized RMS error between when the system is excited by the heating element vs. when the system is excited by the disk power is 4% during the high-frequency oscillations where the fit is least accurate). As to the latter, the actual nonlinear components are negligible in our experiments (e.g. a typical k_0 is 2.7 WΩ/Ω with the typical maximum product of $k_\tau \tau$ is 0.00005 WΩ/Ω, where the units originate from the unitless state value τ). Lastly, our data suggest that stress results in an apparent power source due to a combination of the piezoresistance and linear expansion of the RTD, which can cause a stress induced change in the resistance. This is estimated to result in a $\sim$50 ppm change in resistance for a typical change in curvature but measuring this effect is difficult and it is not currently incorporated in the model.

These errors suggest potential improvements. First, a two-state model may improve the modeling accuracy by incorporating the additional data taken by the

midway RTD. This would also allow for a better simulation of the distributed power arising from film reactions or the disk heater. This approach has not yet been pursued as it would require a more in-depth calibration. Second, we can begin to incorporate the changes in input power due to stress into our system model.

2.7 Optical property measurement

By taking the system fully defined above and switching out the chamber lid with a specifically designed ellipsometry lid, we can incorporate optical property measurement into our system. We measure the optical properties via variable angle spectroscopic ellipsometry (Woollam M-2000). Spectroscopic ellipsometry can be used to calculate optical properties by shining linearly polarized light on the sample of interest and measuring the change in magnitude (Ψ) and phase (Δ) of the resulting elliptically polarized beam. By modeling these values at multiple angles across a spectrum of wavelengths, the optical properties of the measured material can be determined. This method can also be used for measurements of thin-film and roughness thicknesses. In our system, in order to accommodate in situ measurements, we designed a chamber lid, shown in Figure 2.18, with windows at 4 incident angles (48°, 55°, 70°, 75°) so that light would be normally incident on the chamber windows. It is important that the measurement beam is normal to the windows to avoid spurious Fresnel effects in the measurement. By allowing for 4 separate incident angles, a high-quality, multi-angle fit can be achieved. One requirement in this system is to incorporate the calorimetry scheme with the optical property

measurement, the sample measured must be optically thick so that the RTDs do not interfere with the optical measurement.

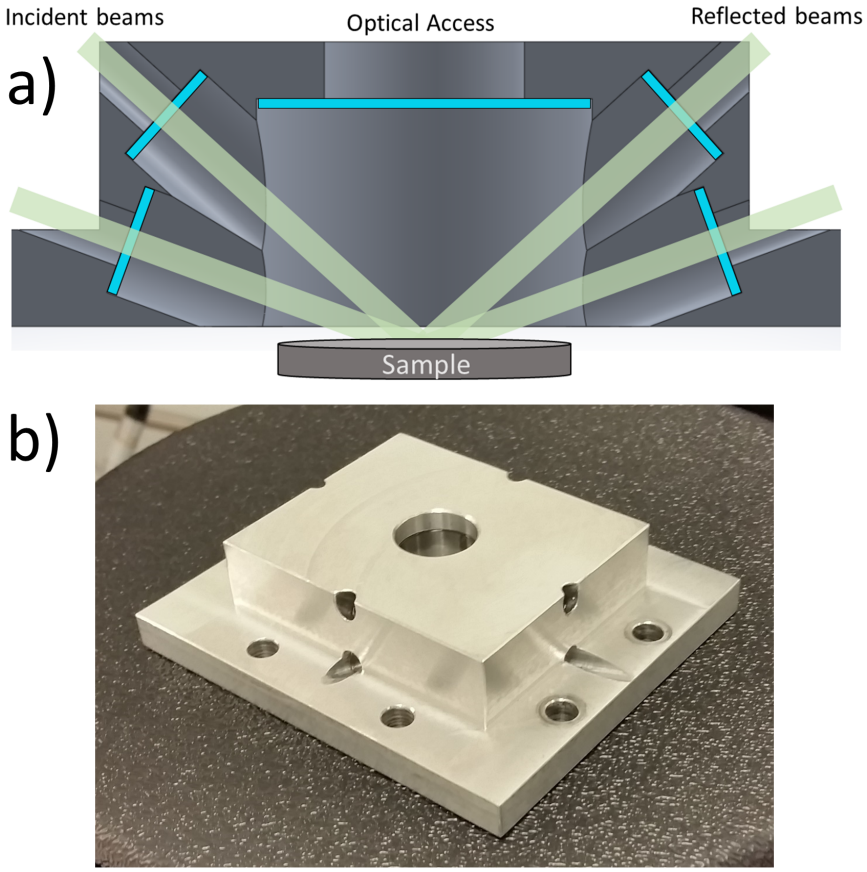

Figure 2.18: a) Cut-through drawing of ellipsometry chamber lid. This cutout shows two of the possible incident angles. The other two angles are in the plane of the screen. This lid still allows for optical access through the top of the lid. b) Picture of the manufactured chamber lid with the 4 incident angles (output ports are on the other side of the lid).

This system setup allows for dynamic optical property measurement under changing environmental conditions. For the most precise dynamic optical measurement, the optical properties of the sample under consideration need to be measured prior to being placed in the chamber. In our system, the spectral range of the ellipsometer is 193 - 1690 nm and we take this ex situ measurement with angles varied

from 50° to 75° in steps of 5°. Once these initial properties are obtained, the sample is then mounted on the QCM stage in the environmental chamber and the chamber is closed and brought to the desired experimental pressure in Ar. The optical properties are then recorded at the 4 separate inlet angles of the environmental chamber (48°, 55°, 70°, 75°). These results are compared to the initial ex situ measurement to determine the change in the phase difference between TE and TM polarizations as light passes through the chamber windows (ellipsometric retardation effects). The origin of this retardation is the birefringence in the glass produced by anisotropic window stress when mounting the chamber lid. A dynamic ellipsometric measurement is then taken through the 75° window (∼10 data points per minute) and the chamber flow rate is set to 20 sccm H_2. This method could also be used with other reactive gases other than H_2, but in this thesis, we will only focus on the effects of H_2 on metallic systems. The dynamic measurement is stopped when both the optical properties and the measured QCM frequency have stabilized, meaning that the full reaction has completed. While still under H_2 flow, ellipsometric measurements are taken of the metal hydride using all 4 inlet angles.

2.7.1 Optical fitting

All ellipsometric data is fit using the Woollam CompleteEASE fitting software. The fitted optical parameters are created using a Kramers-Kronig consistent B-spline to minimize the difference between the modeled ellipsometric data and the measured data. In order to decrease the number of fit parameters, the surface roughness of each

measured sample is recorded before and after a loading run using AFM. The RMS surface roughness from these experiments is input into the optical model for that metal. For samples that require a Pd capping layer to catalyze the hydrogenation reaction, the capping layer thickness in the fit is constrained between 2 - 4 nm, with the thickness value being a fit parameter. The optical data used for the Pd capping layer is from our measurements, which we will go into further detail in Chapter 3.

To determine the ellipsometric retardation phase effects (given by the added TE/TM phase difference) of the environmental chamber windows, the pure metal model found above is fixed and the difference between the measured phase through each window and the phase of the pure metal model is fit using the following equation:

$$\Delta(f) = f\left(C_1 + C_2 f^2\right) \tag{2.11}$$

where Δ is the frequency-dependent retardation effects input to the model, f is the optical frequency of the spectroscopic beam, and C_1 and C_2 are the fit constants. Note that each set of windows has a different retardation due to different stresses present in the windows, thus each set has to be calibrated separately. These effects do not change during the course of an experiment, so they are held constant at these values for the duration of the run. These values do vary from run to run due to slight differences in clamping stresses of the chamber, thus they must be calibrated individually for each run. Because these stresses have an amplified effect at shorter wavelengths, we generally lower bound the wavelength of our fits to 250

nm to eliminate extra errors introduced by these window stresses.

The final hydride optical properties are also fit using a Kramers-Kronig consistent B-spline to the measured data of the 4 angles recorded after the dynamic run (including the set delta offsets found above). In some experiments, there can be unusually high stresses in one set of windows causing a distortion in the data. In these cases, the data from that angle is excluded from the model. The surface roughness for the hydride is input into the model from the AFM measurement, and the Pd thickness found in the pure metal fit is held constant. We note that there is lattice expansion from hydrogenation that would cause the PdH_x thickness to be slightly thicker ($\sim$12% for unbounded Pd) than the original Pd capping layer, however this is within the error bars for the thickness determination [60]. The experimental PdH_x data for the Pd sample run is used for the capping layer optical properties.

The dynamic fit uses two Bruggeman effective medium approximations (EMA): one for the metal under investigation and one for the Pd capping layer. The two materials input into each EMA are the pure metal model and the hydride model found above. The three fit parameters in the model are the EMA % of the metal under investigation, the EMA % of the Pd capping layer, and the surface roughness, which is bounded by the defined roughnesses of the metal and the hydride measured with AFM.

One extra note with this added optical setup, with the increased height of the ellipsometry lid, the stress compensation microscope cannot be integrated with the optical property measurement due to the length of the interference arm. This

requires for two samples to be deposited at the same time, close to each other in the deposition chamber to make as identical films as possible. One sample is then measured in the optical setup, with the other measured in the regular apparatus defined above. The QCM frequency changes in each of the chambers can be compared to ensure that they are having identical responses to hydrogenation. Then, the loading value obtained from the main apparatus can be used to scale the frequency data from the optical sample QCM so that it can be converted to loading data. The dynamic optical data can then be temporally aligned with the loading data from the QCM to correlate the optical changes of the material with its loading at that point.

2.8 Conclusions

In this manuscript, we have presented a novel apparatus with the combined capability to measure stress, mass, and heat while pressurized under a reactive gas and retaining optical access to the sample. The incorporation of stress compensation allows for the accurate determination of mass loading. Prior studies on QCMs have neglected this important factor, likely resulting in anomalous mass determinations. We have demonstrated the ability of our chamber to hold pressure at 9.31 ± 0.02 bar of H_2 at 24.85 ± 0.05 °C with a leak rate of 2 sccm. On a 335 nm thin-film palladium sample, we demonstrated a measurement sensitivity of 0.001 m^{-1} of curvature, corresponding to a stress sensitivity of 0.006 MPa per micron of film thickness, and a mass measurement sensitivity of 13 ng/cm^2. Using a one-state lumped-parameter

heat transfer model, the heat creation of a reaction can be measured with 150 μW accuracy. The on-chip calorimetry scheme allows for a very flexible system where small heats can be detected in thin films, which might be overwhelmed by base noise if the temperature measuring elements were located farther from the sample.

This instrument enables the study of phenomena including the ellipsometric determination of optical properties at varied metal hydride compositions, measurement of interfacial energies between metals and various substrates, spectroscopic measurement of nanoparticle resonance frequency for optical analysis of chemical processes or optical calorimetry, and the direct quantification of heat and stress from coupled plasmonic excitations. Many of these phenomena have not been thoroughly explored because of the inability to collect all of the necessary data simultaneously throughout a reaction. The combination of these measurements will lead to new insights into nanoscale reactions. Further, the integration of optical access with the other capabilities already described offers interesting possibilities for expanding the scope of this apparatus.

Throughout the rest of this thesis, we will use this apparatus to measure the dynamic optical and structural properties of various pure metal and metal alloy hydride systems. The measurement of these switchable properties will allow us to design, propose, and fabricate various nanophotonic structures for different applications ranging from optical hydrogen sensors to switchable high absorption devices.

Chapter 3: Dynamic Optical Properties of Pure Metal Hydrides

Metal hydrides often display dramatic changes in optical properties upon hydrogenation. These shifts make them prime candidates for many tunable optical devices, such as optical hydrogen sensors and switchable mirrors. While some of these metals, such as palladium, have been well studied, many other promising materials have only been characterized over a limited optical range and lack direct in situ measurements of hydrogen loading, limiting their potential applications. Further, there have been no systematic studies that allow for a clear comparison between these metals. In this chapter, we present such a systematic study of the dynamically tunable optical properties of Pd, Mg, Zr, Ti, and V throughout hydrogenation with a wavelength range of 250 - 1690 nm. These measurements were performed utilizing the apparatus defined in Chapter 2, which allows for us to correlate these dynamic optical changes with the mass loading of the metal hydride. In addition, we demonstrate a further tunability of the optical properties of Ti and its hydride by altering annealing conditions, and we investigate the optical and gravimetric hysteresis that occurs during hydrogenation cycling of palladium. Finally, we demonstrate several nanoscale optical and plasmonic structures based on these dynamic properties. We show structures that, upon hydrogenation, demonstrate

five orders of magnitude change in reflectivity, resonance shifts of >200 nm, and relative transmission switching of >3000%, suggesting a wide range of applications.

3.1 Introduction to metal hydride optical properties

Materials with tunable optical properties are critical to the development of novel active nanophotonic devices ranging from plasmonic light absorbers and biosensors to switchable mirrors [14, 61, 62, 63, 64, 65, 66, 67]. The ability to change the resonances of a structure in situ allows for increased functionality and enables new device architectures. One particular class of materials well-suited for tunable applications is metal hydrides. A number of metals have been shown to strongly absorb hydrogen, resulting in hydrogen to metal atom ratios approaching or even exceeding 1:1 [12, 57, 58, 68, 69, 70, 71]. These metals typically undergo crystalline phase transitions, altering their crystal and electronic structures. The large changes to the crystal structure, the additional electrons, and the additional resonances associated with the binding energy of the hydrogen to the lattice can create dramatic shifts in the metal's optical properties.

These metal hydrides are of great interest for switchable photonic devices, particularly for applications involving optical hydrogen sensors and switchable mirrors. Palladium and palladium alloys have been widely used for such sensors, structured as both thin films and nanoparticles [72, 73, 74, 75, 76, 77, 78, 79]. Yttrium and lanthanum have been investigated for their use as switchable mirrors due to their metal to dielectric transition upon hydrogenation[14, 66]. Magnesium has seen re-

cent interest for use in reversible color filters due to its optically dramatic shift from metal to dielectric upon hydrogenation [80]. Hafnium has been introduced as an optical hydrogen sensor that can span six orders of magnitude [81]. Niobium nanorods were recently investigated as a new material for high-temperature plasmonics with switchable properties upon hydrogenation [20].

While work has been done on the optical properties of metals and their hydrides, these previous studies have a variety of limitations (see Table 3.1 for a summary of previous data), including: narrower wavelength ranges (250 - 1690 nm in this work), lack of any dynamic or intermediate hydride data, or temperature ranges that prevent comparison across different studies. On top of these limitations, varied fabrication conditions and procedures alter the optical properties of a metal in a given experiment, furthering the difficulty of comparison. No systematic work has compared a wide range of materials (here Pd, Mg, Zr, Ti, and V) prepared and tested under identical broadband illumination and time-dependent hydrogenation conditions. Further, none of the referenced studies include direct in situ loading measurements (Azofeifa et al. indirectly infer loading in situ via resistivity and transmission spectra) [82].

By addressing all of the above issues in this work, we present a complete, uniform set of measurements that can be used to compare the optical properties of five different metal thin-films (Pd, Mg, Zr, Ti, and V) before, during, and after hydrogenation. We pair this data with simultaneously recorded measurements of the hydrogen loading using a custom environmental chamber incorporating a QCM [95]. We also investigate the effects of annealing on the optical properties of Ti and TiH_x

Material	Wvl range (nm)	Temp (K)	Dynamic?	Reference
MgH_x	$\sim$ 80-200	293	No	van Setten 2007 [83]
MgH_x	190-1240	293	No[i]	Isidorsson 2003 [84]
ZrH_x	240-1040	293	No[i]	Azofeifa 2017 [85]
VH_x	350-950	20, 140	No	Azofeifa 2013 [82]
PdH_x	380-1650	293	Yes	Yamada 2009 [86]
PdH_x	250-1200	293	No	Vargas 2014 [87]

[i]Data is offered for multiple partial pressures

Table 3.1: Previously published work on the measured optical properties of metal hydrides. Here we show only references offering data for the pure metals and ones which derive optical constants. There are several manuscripts on Pd alloy hydrides [74, 76, 88, 89] and Mg alloy hydrides [89, 90, 91]. There are also some references which offer transmission data only which are not shown above such as for MgH_2 [92] and for TiH_x [93]. Also not shown here are measurements of Titanium deuteride [94].

to quantify its strong dependence on preparation conditions, which offers another knob for optical response tunability. We perform a cycling experiment on Pd to study the hysteresis between hydrogenation cycles and to determine the correlation of the loading value with cycled optical properties. Finally, we demonstrate the applicability of the tunable optical properties of these metal hydrides in dynamically controlled nanostructures and thin-film cavities. We find that the dramatic changes in the optical response of these materials with the hydrogenation reaction present a wealth of possibilities for practical devices.

3.2 Optical, loading, and stress characterization of pure metal hydrides

In this section, we use the optical apparatus setup defined at the end of Chapter 2 to measure the optical, loading, and stress properties of 5 different pure metal hydrides. Figure 3.1 presents the dielectric functions of the five metals (Pd, Mg, Zr, Ti, and V) as they hydrogenate over the entire visible to near-infrared (NIR)

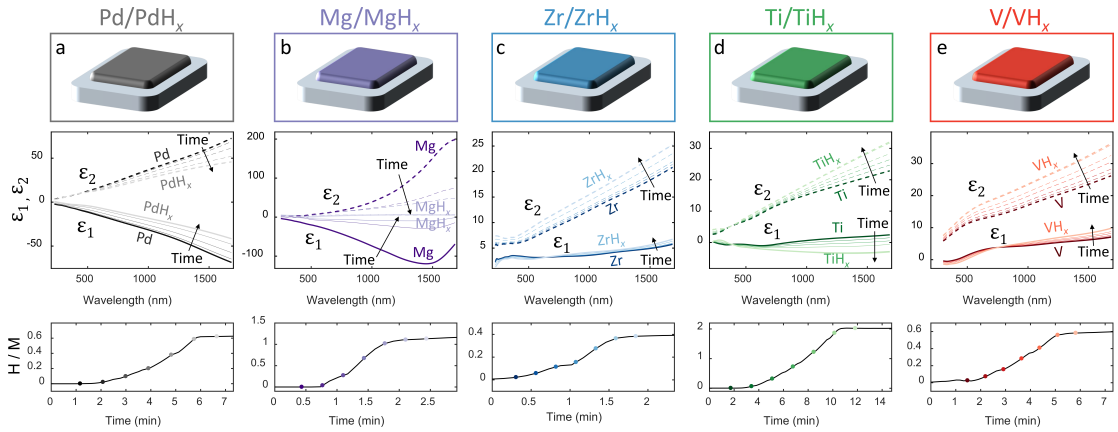

Figure 3.1: Dynamic optical properties and loading measurements of Pd, Mg, Zr, Ti, and V metals and their hydrides. The top panel shows schematics of the thin metal films used for the measurements (note: the 3 nm Pd capping layer used in the experiment is not shown). The middle panel displays the dielectric function of each metal and its hydride, as well as the intermediate loading states. The dynamic loading data is shown in the bottom panel where H/M is the number of hydrogen atoms per metal atom in the metal lattice. The colored dots indicate the times corresponding to the optical measurements in the graphs. ϵ_1 is shown as solid lines and ϵ_2 as dashed lines. As time progresses, the shading of the lines gets lighter.

spectral range, 250 to 1690 nm. For those who prefer viewing the optical properties in terms of the index of refraction, see Figure 3.2. The bottom panels show the hydrogen loading (i.e. number of hydrogen atoms per metal atom in the lattice) as a function of time, and the colored dots represent points in time where the optical properties are recorded (bottom plots in each panel). Measurements were taken on ∼200 nm thick metal films capped with 3 nm of Pd that were annealed for 2 hours at 350 °C under $<$ 1 mtorr vacuum (with the exception of Mg, which had a thickness of 25 nm). During Mg hydrogenation, the Mg closest to the Pd capping layer hydrogenates, turning primarily to MgH_2. This MgH_2 layer is a poor proton conductor and acts as a blocking layer for more hydrogen to penetrate into the film, causing the time scale for total, bulk hydrogenation to be several days [96]. Because

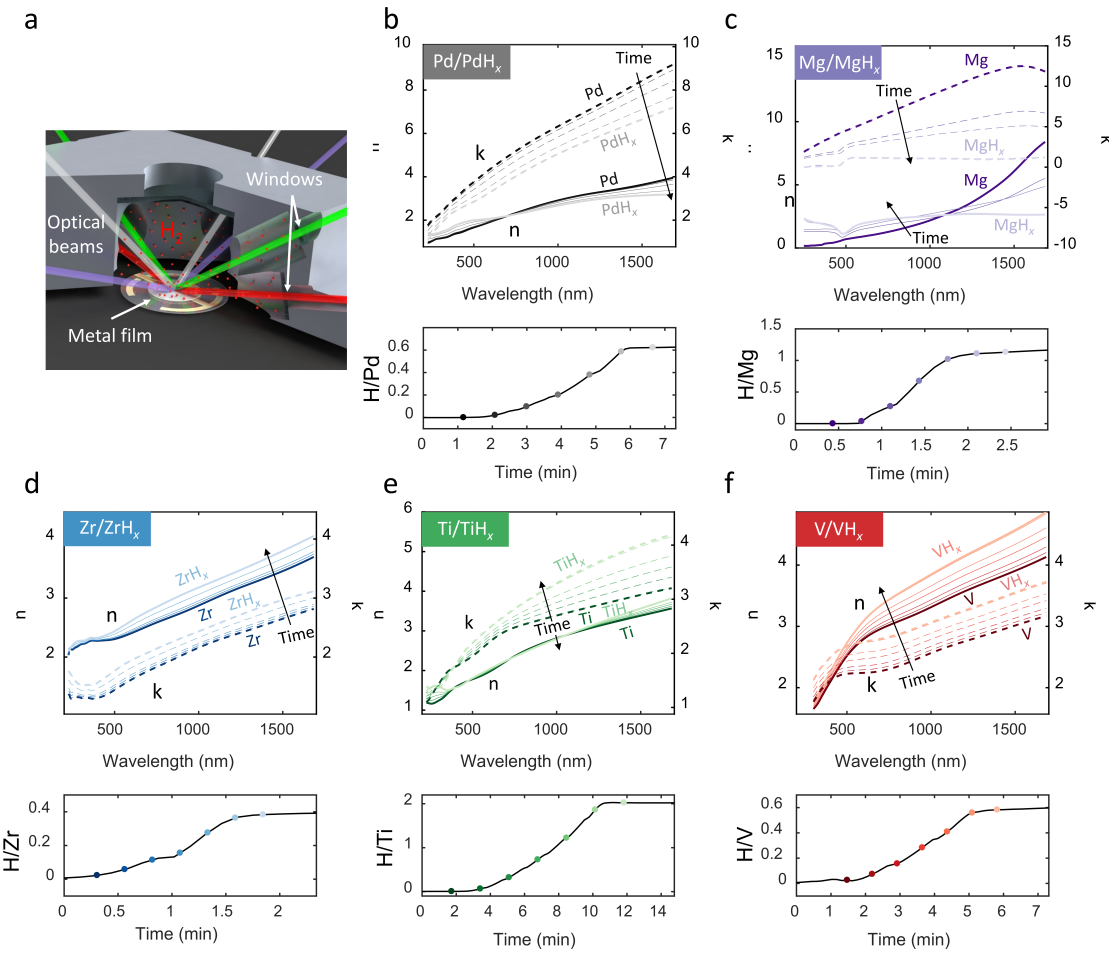

Figure 3.2: Dynamic index of refraction upon hydrogenation of Pd, Mg, Zr, Ti, and V (a) Schematic of ellipsometric measurement on a QCM substrate through windows in the environmental chamber at 48°, 55°, 70°, and 75°. (b-f) n and k of each metal and its hydride, as well as the intermediate loading states. The dynamic loading data is shown on the bottom panel where H/M is defined as the number of hydrogen atoms per metal atom in the metal lattice, with the points of the optical measurement delineated by points of the corresponding color in the graph above. n is shown as solid lines and k as dashed lines. As time progresses, the shading of the lines get lighter.

of this phenomenon, we performed measurements on a 25 nm Mg thin film (the thickness of the formed blocking layer) in order to fully hydride the sample. The Pd capping layer is necessary for each metal (other than Pd itself) in order to reduce the activation energy of H_2 splitting and allow for diffusion into the bulk [97]. This

capping layer also prevents oxidation of the underlying film, keeping it pristine. Note that in the case of the V/VH_x data, wavelengths below 300 nm are not available due to high stress-induced ellipsometric retardation (i.e. polarization-dependent phase change of the transmitted light) in the windows during this measurement.

Figure 3.3 shows the dependence of the optical properties on the measured loading values of the metals. Two main points can be drawn from this data. First, Mg's dramatic change in optical properties is clearly evident in its dependence on the loading values. Second, Ti has the most interesting relationship because the real part of the dielectric function has a different slope depending on the wavelength of illumination. This feature could enable a resonance to shift to longer or shorter wavelengths upon hydrogenation depending on the incident wavelength.

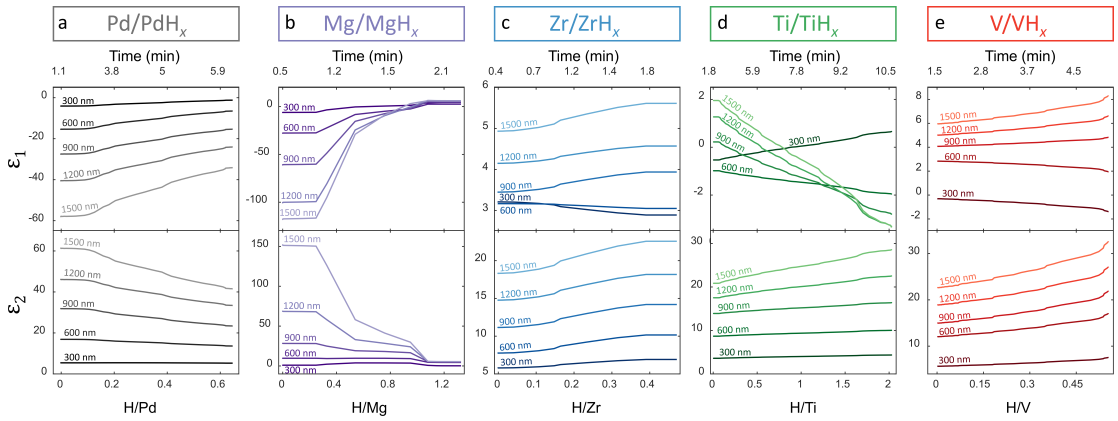

Figure 3.3: Optical properties of the metal hydrides as a function of hydrogen to metal ratio. Ti is of particular interest because the slope of the real part of the dielectric function with hydrogen loading depends on the wavelength investigated. This may present a new scheme for optical detection of hydrogenation in Ti. Note that the upper time axis is not linearly spaced.

Finally, during our loading measurement, we also recorded the total stress change in these metals as they hydrogenated. We measured these values by mea-

suring the curvature change in the samples interferometrically and then converting this curvature change to stress, as outlined in Chapter 2. In Figure 3.4, we show the total amount of stress change in each of these films compared to the total final loading in the film. In this data, we expected to see a larger stress change in the films with higher loading, but we do not see any strong relationship with final loading amount and total stress change across material systems.

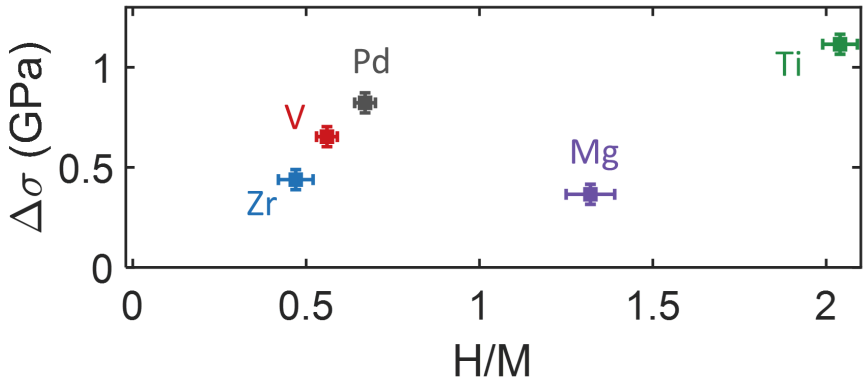

Figure 3.4: Stress change upon hydrogenation for pure metals. Stress values plotted are the total stress change of the thin films after the hydrogneation is complete compared with the total final loading number of the material. We do not find any strong trends between the hydrogen induced stress change and the total loading amount.The stress values here are defined to be positive.

The results of all of the optical and loading measurements for the five different metals and their hydrides are discussed in turn below.

3.2.1 Pd/PdH$_x$

The optical properties of both the pure Pd metal and the PdH$_x$ films agree well with literature values across the measured range, which serves as a standard for this measurement technique [86, 87]. There are no clear peaks or inflection points in the Pd film's optical properties within the wavelength range under investigation. Upon

hydrogenation, Pd becomes distinctly less metallic at a fairly uniform rate with the real part of the dielectric function increasing by up to 39% in the near-infrared, and the imaginary part decreasing by similar percentages. The film reaches a final loading value of 0.67 ± 0.12, where the loading value is defined as the number of hydrogen atoms per metal atom in the lattice, in agreement with previous results [57, 58].

3.2.2 Mg/MgH_x

Of the metals investigated, Mg has the most dramatic optical changes. The optical properties of the metal, which matches well with reported data over the previously studied wavelength region [98, 99], is the most lossy, with the imaginary part of the dielectric function three times greater than that of the next metal, Pd. During hydrogenation, it can be seen that while mass loading proceeds continuously, the optical properties change abruptly from a metal to an insulator, which is consistent with previous electrical measurements [100]. When comparing the dielectric function of MgH_x with those reported in the literature, we find that our measured film appears more metallic (characterized by a decrease in the real part and increase in the imaginary part of the dielectric function with wavelength). One likely cause for this discrepancy is that Mg and Pd readily form an alloying layer [101, 102]. This alloy does not become entirely a dielectric, as we expect for MgH_2, which would cause our film to appear more metallic than the pure MgH_2. After accounting for apparent oxide formation (see 3.7 Experimental Methods), the Mg

demonstrated loading of 1.3 ± 0.5, which is lower than the expected 2.0 loading value. The alloying layer discussed above could account for this lower measured value. Another potential cause could be that the bottom few nm of the film did not fully hydrogenate due to the blocking layer.

3.2.3 Zr/ZrH_x

Zirconium has the smallest change in optical properties of the metals being investigated. The real part of the dielectric function exhibits very small changes during the loading process, but the imaginary part increases significantly. The Zr film also exhibited the lowest amount of loading amongst the films, only reaching a value of 0.47 ± 0.05. The Zr and ZrH_x optical data shown here differ from the values reported by Azofeifa et al. [85] (note that those values also greatly deviate from previous data for Zr [103]). Thus, there appears to be an important factor in sample preparation yet to be fully described. However, the magnitude of our measured shift in the dielectric function upon hydrogenation agrees very well with the data presented by Azofeifa et al. over the wavelength range they explored [85]. The difference in initial properties could be attributed to metal preparation conditions, as the grain size of the metal has an effect on the optical properties of the hydrides [87]. We also observe that at 640 nm, our data shows that there is zero change in the real dielectric function upon hydrogenation. Points like these may be useful as reference points in a differential measurement scheme.

3.2.4 Ti/TiH$_x$

The derived optical properties of the initial, pristine Ti metal are in good agreement with previously reported data over the same wavelength range measured here [104]. The local maxima in the real part of the dielectric function at ∼400 nm and ∼800 nm, typically ascribed to d-band transitions [105, 106], are also clearly visible. After hydrogenation, these undulations disappear and the TiH$_x$ appears to become more metallic, characterized by a decrease in the real part and an increase in the imaginary parts of the dielectric function with wavelength. However, the previous studies have not observed an increase in Ti conductivity upon hydrogenation, which would have explained this behavior [107]. This phenomenon may simply be due to the elimination of the above mentioned d-band oscillations. Also, a small, broad peak at ∼250 nm is visible in the data, which is characteristic of the metal-hydrogen bond [108]. Ti loads to the highest value of any metal measured in this experiment, achieving a value of 2.04 ± 0.12.

3.2.5 V/VH$_x$

Over the visible wavelength range previously reported, our V metal data exhibits similar trends [82]. Band structure theory predicts that there should be two absorption peaks in the data centered at 406 and 708 nm [109]. In the literature, it has been observed that thermal broadening merges these peaks into one broad peak. Azofeifa et al found this peak to be at 520 nm, and we find this peak at a similar location of 510 nm. The broadening of this peak is attributed to large

electron lifetimes in the excited states [110]. Upon hydrogenation, we find that V has a small change in the real part of the dielectric function with a much more significant change to the imaginary part, which increases by more than 38% in the near-infrared region. Further, we find that at 750 nm, there is no change in the real part of the dielectric function even though the imaginary part changes significantly upon hydrogenation, showing that the imaginary part of the dielectric function can be controlled independently from the real part through hydrogenation over this bandwidth. This phenomenon was also observed previously, but near 500 nm. We attribute this difference to sample preparation and the resulting difference in the grain size of the metal. The V film achieves a loading of 0.56 ± 0.03.

3.3 Effect of annealing Ti on TiH_x hydrogenation

We found that the Ti and TiH_x optical properties were quite sensitive to preparation conditions. To further explore this phenomenon, we varied the annealing conditions. Ti samples were either not annealed, annealed at 200 °C for 2 hours, or annealed at 350 °C for 2 hours, with each anneal occurring in under $<$1 mtorr vacuum. These samples were then characterized using the same process described above. Figure 3.5 shows the measured dielectric functions. This experiment revealed two interesting characteristics of Ti. When not annealed, the oscillations associated with d-band transitions mentioned above are clearly visible and become less prominent with increased annealing temperature. The hydrogen loading generally reduces the impact of annealing, as the hydrides exhibit a smaller optical property change

from annealing than the pure metals. There are a few possible explanations for this effect. First, the very large stresses involved in creating the hydride may be producing enough dislocations that it is partially undoing the impact of annealing. Second, it is known that the effect of defects on resistivity is reduced with higher hydrogen concentration and perhaps this is the effect we observe; however, additional studies are needed to understand the root cause [107]. Nevertheless, it is clear that annealing offers an additional opportunity for modifying how hydrogenation affects the optical properties of Ti.

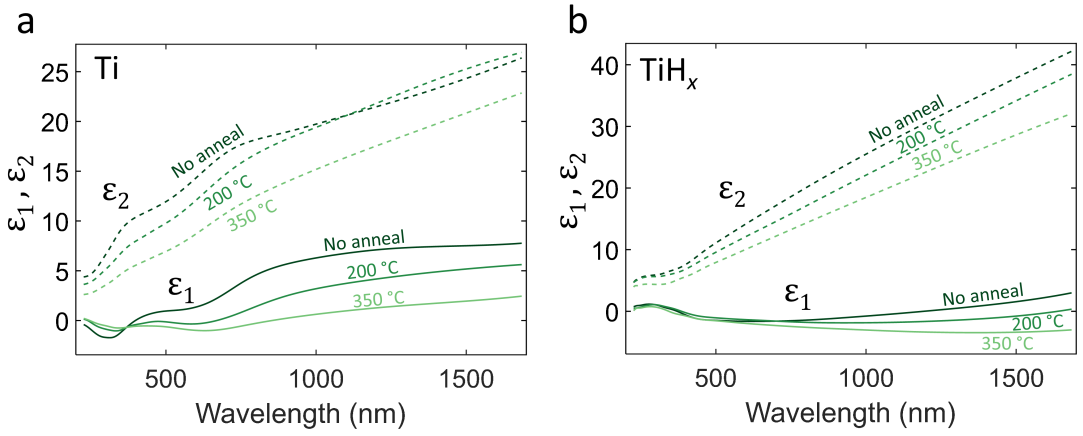

Figure 3.5: Effects of annealing on the optical properties of Ti and TiH_x. (a) Dielectric function of Ti with different levels of annealing. (b) Dielectric function of TiH_x measured on the same samples.

3.4 Characterization of Pd hysteresis

Some devices, such as hydrogen sensors, require the ability to cycle the metal between a hydrogenated and unhydrogenated state. Palladium is unique compared to the other metals because it unloads at room temperature with easily realizable, low hydrogen partial pressures, allowing cycling by simply varying the H_2 gas content

in the chamber. We use this process to measure the optical properties and the loading of the Pd through three consecutive loading cycles, shown in Figure 3.6. The red shaded regions in Figure 3.6a indicate when H_2 is flowing into the chamber at 20 sccm and hydrogen is loading the metal film. The blue shaded regions indicate unloading phases where Ar fills the chamber, displacing the H_2, and the metal film desorbs.

We can see in Figure 3.6b that there is a clear hysteresis in the optical properties of the Pd metal between the first loading cycle and the subsequent measurements. However, after the Pd had been loaded once, there is no discernible difference in optical properties between the Pd after the first and the second unload, eliminating further hysteresis. Note that there is no discernible hysteresis in the optical response of the hydride, as demonstrated in Figure 3.6c. More data would be needed to determine performance over a longer timescale (or number of cycles), but the data imply the optical hysteresis of Pd can be greatly reduced with an initial treatment of the metal with H_2. Note that the above refers only to the inter-cycle hysteresis. The well-known intra-cycle hysteresis where the α to β phase transition happens at a different hydrogen partial pressure than the β to α phase transition would still be present [12]. This inter-cycle phenomenon is most likely attributed to deformations formed in the Pd lattice upon the first hydrogen loading. We observe that the loading value for each PdH_x state remains consistent throughout all three cycles, although we observed an increase in unloading time between the first and the second cycles.

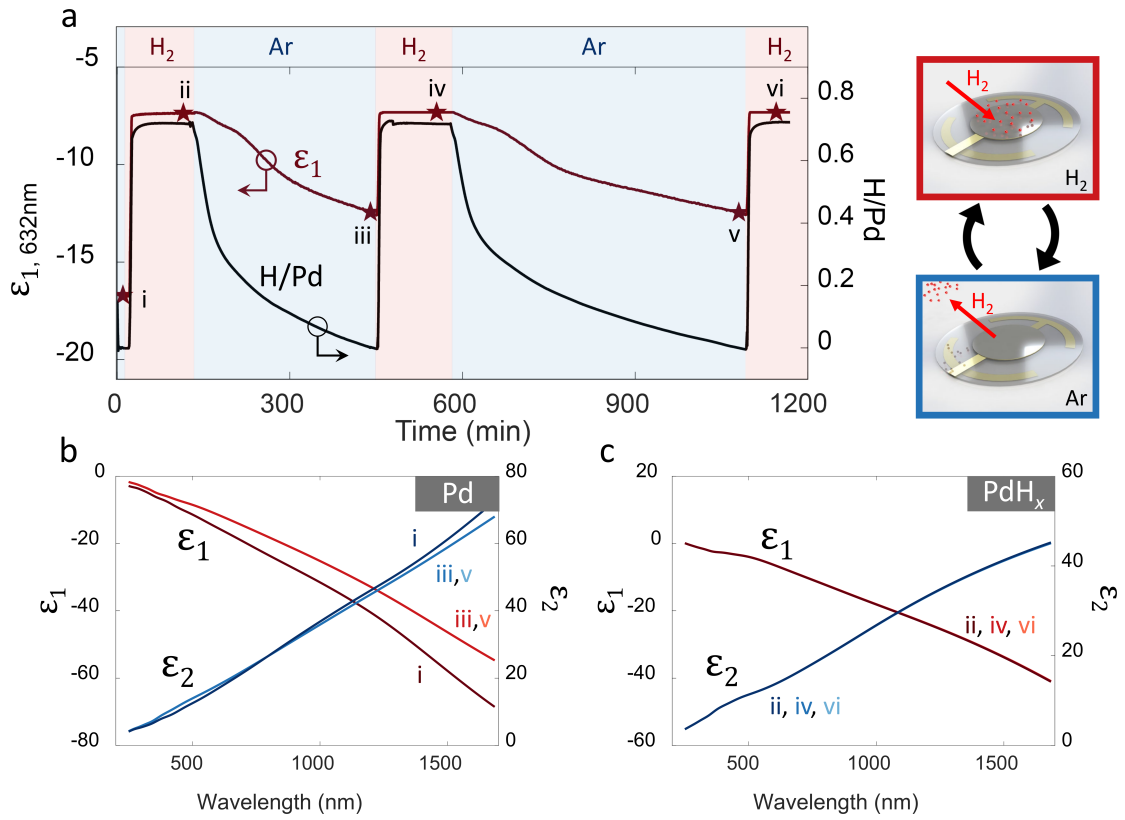

Figure 3.6: The optical and loading response of Pd during hydrogen cycling. (a) Dynamic loading data (black) and the real dielectric permittivity (red) at 632 nm plotted over three loading cycles of a 200 nm Pd film. The red shaded areas indicate periods of loading during which H_2 is flowing into the chamber, while the blue shaded sections depict times during which Ar is flowing to flush out the H_2. The stars on the plot indicate the times at which the ellipsometric measurements shown in (b) and (c) were made. (b) shows the Pd metal data and (c) shows the PdH_x data. Note for the second two Pd measurements (iii and v) and all three PdH_x measurements (ii, iv, vi) that the measured dielectric functions are indistinguishable and, thus, overlap each other in these plots.

3.5 Tunable nanophotonics with metal hydrides

There are many potential applications presented by the tunable optical properties of the metal hydrides investigated in this work. In this section, we detail four examples of the potential uses of these materials: nanoparticles with variable scattering cross-sections, nanorod arrays with tunable transmission, thin-film resonators

with adjustable color filtering, and hydrogen switchable perfect absorbers.

We begin with the simplest of these examples, showing the ability to tune the cross-section of nanoparticles in free space by hydrogenating the sample. The top panels in Figure 3.7 show a schematic of the configuration with the plane wave source being scattered by the metal and its hydride, depicting whether they primarily increase or decrease in total scattering upon hydrogenation. The bottom panels show the difference in the simulated finite-difference time-domain (FDTD) scattering cross sections between the metal and its hydride. Figure 3.8 shows the total scattering cross sections for both the metal and the hydride. First, a clear distinction can be made between two types of the metals: Pd and Mg particles primarily decrease total scattering upon hydrogenation, while Zr, Ti, and V particles show mostly increased scattering. This effect is caused by opposite responses of the metal's index of refraction, with Pd and Mg decreasing and Zr, Ti, and V increasing. Mg clearly has the largest differential response to hydrogenation, having an order of magnitude larger change than the other metals. This was expected due to its dramatic metal to insulator transition. The Pd nanoparticles have the next largest differential response and behave similarly to Mg, having a large change in response in the visible to ultraviolet range.

Ti demonstrates wavelength-dependent regions of both increased and decreased scattering cross-section – increasing near-ultraviolet scattering while decreasing NIR scattering. It also is the only metal under investigation that has its largest scattering change in the NIR range (400 nm particle diameter), presenting applications that the other metals could not provide. However, Ti did exhibit a fairly small

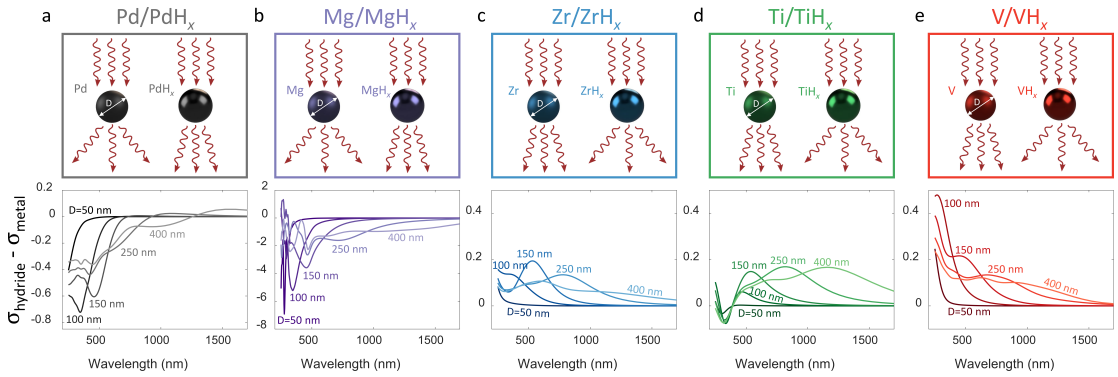

Figure 3.7: Differential scattering cross sections for nanoparticles in free space composed of different metals. The top panels show schematics illustrating the heuristic change in the nanoparticle cross section resulting from the change in the dielectric response. The bottom panels show the differences in the scattering cross sections of metals and their hydrides for multiple particle diameters ranging from 50 - 400 nm. For Pd and Mg, hydrogenation causes decreased scattering, as opposed to Zr, Ti, and V where the scattering increases.

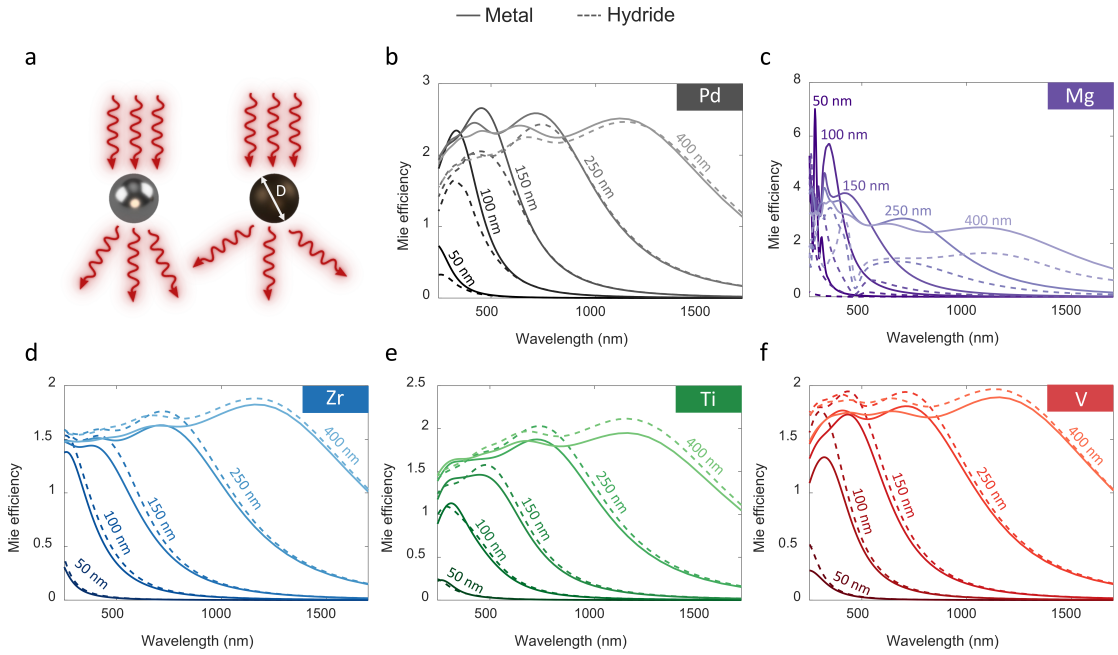

Figure 3.8: Relative scattering cross sections (Mie efficiency) of metal nanoparticles and their hydrides in free space. Solid lines indicate metal scattering cross sections and dashed lines indicate metal hydrides. Line shading indicates particle diameter.

differential scattering response compared to the other metals. V primarily has its largest scattering changes in the ultraviolet. The exact magnitude and location of

many of these peaks cannot be determined because the simulation was limited to the experimentally measured wavelength range ($>$ 250 nm), which cut off these peaks. As expected, Zr has the smallest differential response because of its small change in optical properties upon hydrogenation. The response is on the same order as Ti, with its maximum responses spanning a wider range of wavelengths than the other materials, beginning in the ultraviolet and continuing to the NIR.

Next, we simulate periodic arrays of nanorods on a glass substrate, showing large resonance shifts and changes in transmission upon hydrogenation. The relative change in transmission upon hydrogenation for these metals is shown in Figure 3.9. The arrays have a 500 nm period in both the parallel and perpendicular directions, a rod width of 100 nm, and a length that varies from 150 to 400 nm (the electric field is parallel to the length of the rods). The total transmission spectra can be seen in Figure 3.10. Once again, Mg and Pd behave differently than the other metals in terms of responses upon hydrogenation: Mg and Pd have an increase in transmission upon hydrogenation, while Zr, Ti, and V exhibit a decrease in transmission.

Mg has the strongest relative response, exhibiting a full 3800% relative transmission increase for the 400 nm rods. Pd shows the next highest response, with a 190% relative increase in transmission at the 400 nm length. Mg and Pd have the narrowest peaks, causing for a more spectrally localized response upon hydrogenation. Zr and V have very similar resonant response locations in the visible and NIR, with V exhibiting stronger changes in transmission. These materials have their peak changes in the visible and NIR. Ti has transmission magnitude shifts similar to Zr, but with its responses spanning further in the IR, allowing for a wider usable

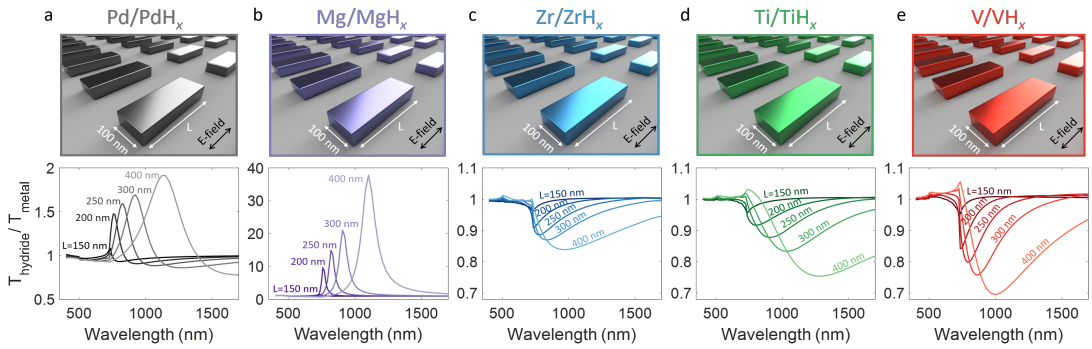

Figure 3.9: Relative change in transmission upon hydrogenation of periodic nanorod arrays. The top panels show schematics of a nanorod array on a glass substrate. The rods are spaced 500 nm apart in both the parallel and perpendicular directions and are 100 nm wide. The rod length is varied from 150 to 400 nm. The polarization of the electric field is parallel to the length of the rods. The bottom panels show the relative difference of the transmission spectra between the metals and their hydrides. The transmission for Mg and Pd nanorods increases upon hydrogenation for most of the spectrum, while those made of Zr, V, and Ti decrease.

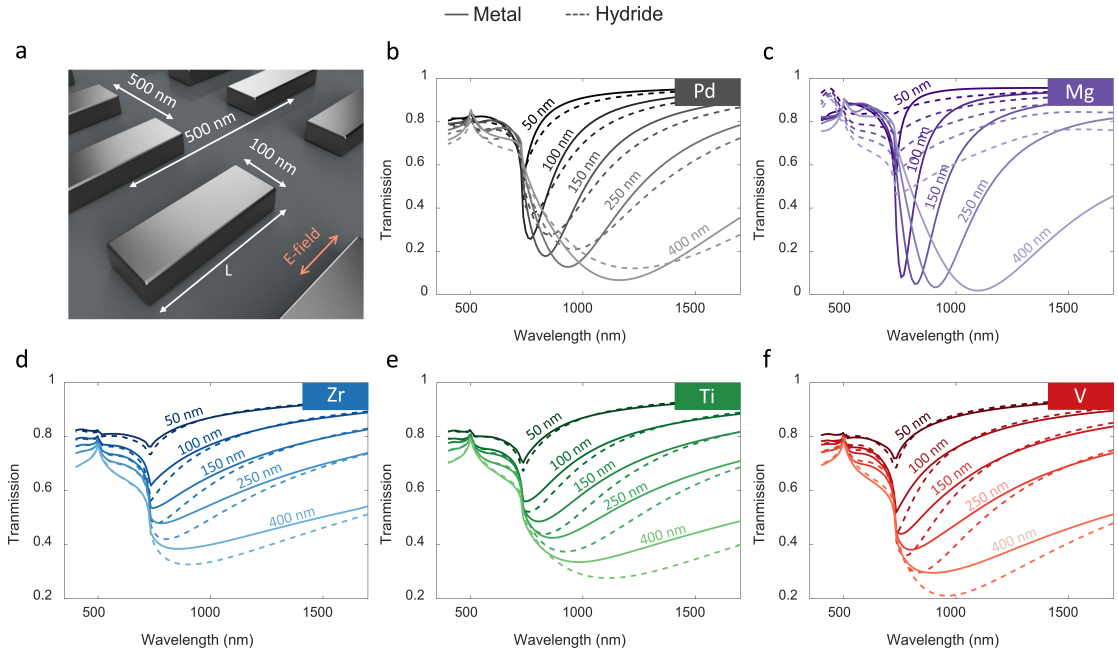

Figure 3.10: Full transmission spectrum of periodic nanorod array. Solid lines indicate metal scattering cross sections and dashed lines indicate metal hydrides. Line shading indicates length of individual nanorod.

bandwidth. These transmission differences allow for in situ tunability of optical responses for various wavelength ranges without having to physically move any piece

of the structure or electrically activate any part of it.

The dynamic optical properties demonstrated above suggest themselves to two potential thin-film applications: tunable color filters and switchable perfect absorbers. Figure 3.11 and Figure 3.12 depict two embodiments of these devices: a Fabry-Perot cavity with the metals acting as both the top (partial) mirror and the bottom mirror separated by a dielectric and a thin film Si absorber with the metals acting as a lossy bottom mirror. For each metal, several representative thicknesses of the Si or SiO_2 layers are shown. Note that tunable color filters and switchable perfect absorbers are not mutually exclusive and differ only in their figure of merit, allowing a single structure to act as both. In all respects, the Fabry-Perot cavity has better performance. However, the Si systems are of interest due to their simplicity and because a Si-based perfect absorber is useful for several applications, such as in a Si/metal photodetector [111]. In Figure 3.11, we present the materials that function well as both tunable filters and switchable perfect absorbers in either structure: Mg, Pd, and Ti.

Tunable color filtering is characterized by shifts in the wavelength of the resonance [80]. In each case shown, hydrogenation of the metal produces an easily measurable and generally visible change in the resonant wavelength. The largest shifts in the Fabry Perot modes shown are 360 nm (or 1 eV), 100 nm (or 0.4 eV), and 50 nm (or 0.1 eV), for the Mg, Pd, and Ti, respectively. The largest shift in the resonances of Si on metal are 40 nm (or 0.24 eV), 50 nm (or 0.17 eV), and 70 nm (0.04 eV) for the Mg, Pd, and Ti, respectively. These values compare well with Duan et al. which demonstrated wavelength shifts of $\sim$150 nm in a Mg nanoparticle

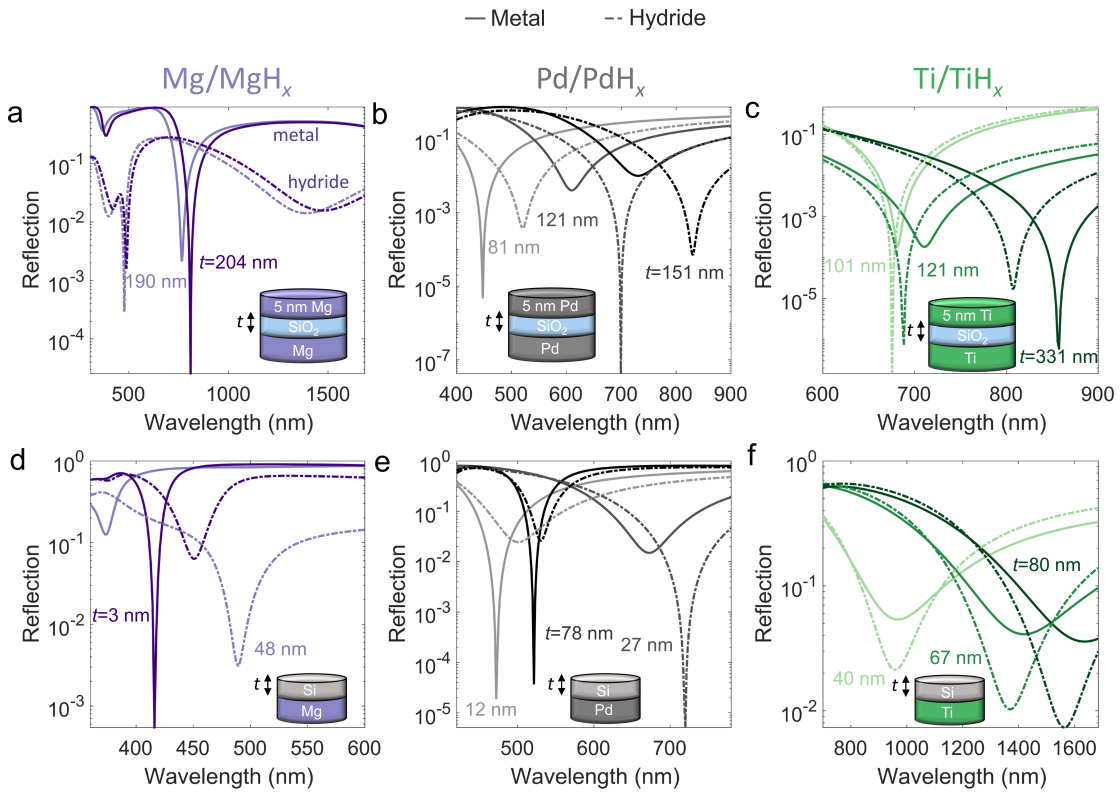

Figure 3.11: Switchable perfect absorbers and tunable color filters using thin-film structures containing the three metals that offer the largest optical response to hydrogenation: Mg, Pd, and Ti. The thickness of either the Si or SiO_2 layers are labeled on the charts for each colored curve, and the bottom metal is considered bulk. The pure metal is denoted with a single solid line and the metal hydride with dashed lines. (a-c) Fabry-Perot cavities comprised of Mg, Pd, and Ti, respectively, for top and bottom mirrors separated by SiO_2. (d-f) Si thin-film structures on Mg, Pd, and Ti, respectively, undergoing hydrogenation. All of these structures perform well as either switchable perfect absorbers (>100x changes in reflectivity) or tunable color filters (a minimum of 40 nm resonant wavelength shift).

system or wavelength shifts of ∼150 nm for Pd nanorings presented by Zorić et al. [80, 112].

On the other hand, the figure of merit for the switchable perfect absorbers is the difference in maximum absorption or reflection [113, 114, 115]. The six structures shown here also demonstrate excellent performance as switchable perfect absorbers. In fact, all of the systems in Figure 3.11 have resonances that have more than

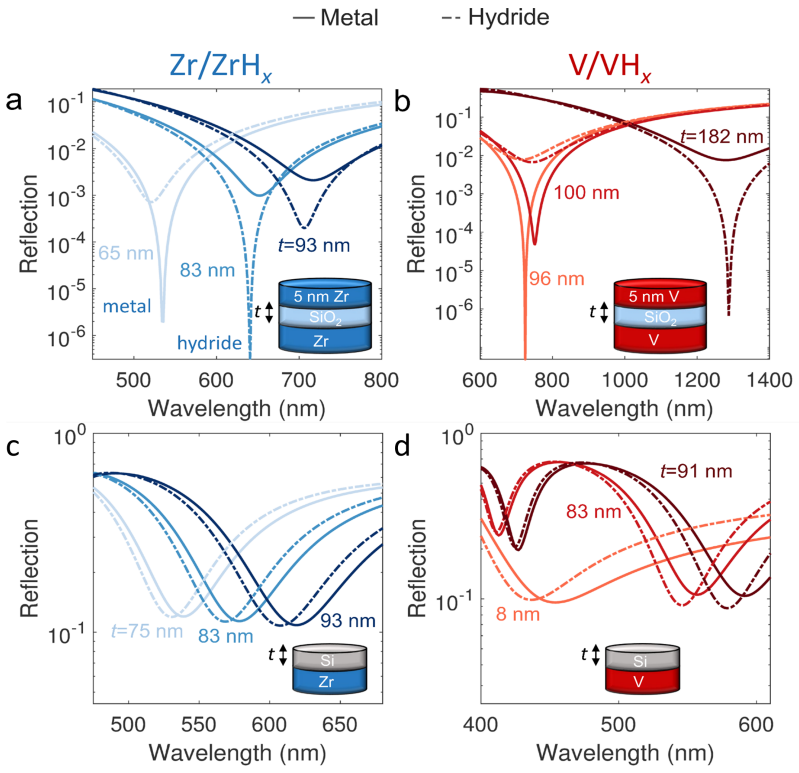

Figure 3.12: Switchable perfect absorbers and tunable color filters using Zr and V. The thickness of either the Si or SiO_2 layers are labeled on the subplot for each colored curve. The pure metal is denoted with a single solid line and the hydride with a dashed line. (a,b) Fabry-Perot cavities comprised of Zr and V respectively for top and bottom mirrors and SiO_2 centers. (c,d) Less complex Si on metal structures for Zr and V respectively.

2 order of magnitude of switchability, including extreme cases like the Pd Fabry-Perot structure with 121 nm of SiO_2, which changes absorption by more than five orders of magnitude, or the Mg Fabry-Perot structure with 204 nm of SiO_2, which switches by more than four orders of magnitude. This offers significantly improved performance compared to Walter et al. who presented reflection changes in Pd nanodiscs or Tittl et al. who demonstrated perfect absorbers in Pd gratings, who both reported reflection ratios of <1000 [114, 115]. As above, it is interesting to note that the structures involving Ti exhibit unique behavior amongst the materials

we investigated. The resonances in the Ti devices shift to shorter wavelengths after the hydrogenation reaction due to the increase in refractive index, in contrast to the redshifts demonstrated with the other two metals. Using this effect, it may be possible to combine layers of, for example, Pd and Ti to exaggerate resonant shifts. These types of simple resonant structures show the great promise for these materials as a part of tunable optical systems.

In Figure 3.12, we show the same structures with Zr and V. In these systems, the Fabry-Perot cavity structure can still obtain large reflection changes for switchable perfect absorbers, but have much smaller resonance shift, making them poor tunable color filters. The Si devices show poor absorption and resonance shifts for these metals as well, thus for future device design, we will focus our attention primarily on Mg, Pd, and Ti.

3.6 Conclusions

In summary, we have mapped the dynamic optical properties of the hydrogenation reaction of five different metal films and have simultaneously recorded the real-time hydrogen loading data. We have shown that the optical properties can be tuned for the different metals, with the largest changes exhibited in Mg and the smallest changes in Zr. We demonstrated further potential tunability for Ti structures by determining the effect of annealing on optical property changes in the metal and its hydride. Pd was shown to have a large hysteretic optical response on the first cycle, and then very consistent optical properties between the second and

third cycles, while having no hysteresis in the hydride state. Four different nanostructured geometries were studied based on the measured optical properties, which demonstrated several potential applications for the tunability of these metals. Mg was shown to have the largest response for all structures due to its extreme change in optical properties upon hydrogenation. Mg and Pd structures exhibited a redshift in their resonances, while Zr, V, and Ti systems are characterized by blue shifts. Ti, Mg, and Pd were all found to be excellent candidates for perfect absorbing devices, making them widely applicable for such designs. This work acts both as a point of comparison between these materials and to demonstrate their usefulness as tunable optical materials for novel dynamically switchable photonic devices.

3.7 Experimental methods

3.7.1 Sample fabrication

The substrate for each of the samples is a 5 MHz Inficon QCM. Before sample deposition, each QCM is cleaned with acetone, methanol, isopropyl alcohol, and water to remove any particles or organics on the surface of the Au electrode. The 12.7 mm diameter thin-film disks are defined by a machined Al shadow mask. Each metal is deposited as part of a stack using electron beam evaporation (Angstrom NEXDEP). First, a 3 nm Cr adhesion layer is deposited, followed by 200 nm of the metal under test (25 nm for Mg), and finished with a 3 nm Pd capping layer. This final layer acts as a semi-transparent and permeable surface to split the H_2 molecules. For each deposition, at least two QCMs are included: the first for the

optical and in situ loading measurement and the second for a more precise and complete loading measurement in a separate environmental chamber which incorporates stress compensation (see Chapter 2 for details) [95]. Having the samples deposited in the same run ensures the similarity of the metals on each QCM for comparison of loading. With each deposition, a lithographically defined 1 cm x 1 cm square is included for determining the sample height via AFM (Cypher, Asylum Research). Immediately after sample deposition, the samples are annealed in < 1 mtorr vacuum at 350 °C for 2 hours with the exception of the Ti samples used in the annealing study.

3.7.2 Optical measurement

The optical properties for each of the materials are measured via in situ spectroscopic ellipsometry as outlined in Chapter 2. Each sample is measured immediately after annealing in order to avoid contamination of the sample or excessive oxidation. Before an optical measurement, the sample chamber is purged with Ar at $\sim$200 sccms for a minimum of 1 hour to remove any trace hydrogen left in the system. Assuming complete mixing, this brings the H_2 partial pressure in the 45 cm^3 chamber to $<10^{-5}$ bar. Dynamic optical measurement and window compensation are then performed as outlined in Chapter 2. During the Pd cycling measurements, the H_2 is flushed from the chamber by flowing 60 sccm of Ar during the unloading steps. The metal and final metal hydride are fit using and Kramers-Kronig consistent B-spline and the dynamic data is fit using two Bruggeman EMAs: one for

the metal under investigation and one for the Pd capping layer. The two materials input into each EMA are the pure metal model and the hydride model. For full modeling details see Chapter 2.

3.7.3 Loading measurement

In a separate environmental chamber, the second QCM sample from the deposition is run under identical environmental conditions to the original sample. The loading is calculated as outlined in Chapter 2, where the stress of the QCM amongst other extraneous effects are corrected for in the loading calculation [95]. To obtain the loading data of the optically measured sample, we first subtract away the frequency change due to the changes of gas partial pressures in the chamber. We then offset and normalize the recorded frequency change. The baseline frequency before H_2 is introduced to the chamber is defined to be zero (offset), and the stabilized frequency after the hydrogen loading is complete is defined to be the calculated loading value from the duplicate sample (normalize). During the Pd hysteresis study, a concurrent hysteresis in stress required that each cycle be normalized independently. The loading cannot be directly calculated in the optical measurement chamber because the stress cannot be properly characterized interferometrically due to the geometry of the setup when taking ellipsometric data.

There were two cases where we had to add extra processing to the loading calculations of the metals: Mg and Pd. For Mg, the loading data was normalized in a slightly different process due to the possibility of a thin MgO layer existing at the

beginning of the experimental runs. Once hydrogen was introduced to the chamber, the QCM frequency sharply increased, indicating mass loss from the system, before the usual reduction in frequency due to loading. We expect that this effect is due to a MgO layer that is being reduced upon the introduction of the H_2. To account for this effect, we normalized the frequency to the top of this peak, defining it as the baseline value. For Pd, the duplicate sample was run in a D_2 environment instead of H_2. We added the known conversion factor of 0.07 to the final loading value to convert to the proper H_2 loading [12].

Chapter 4: Investigation of Physical Properties of Commercial Near-Zero-Index Materials

In this chapter, we take a brief detour from metal hydrides and investigate commercial NZI materials to potentially be incorporated into our metal hydride designs. TCO materials have been found to be ideal NZI materials, with strong NZI resonances with low losses in the NIR. In this chapter, we investigate the optical properties of 51 TCO materials and report the strength and bandwidth of their NZI resonances. We find positive correlations between $|n|$ and the NZI bandwidth, as well as between the resistivity of the film and $|n|$.

4.1 Background of NZI materials

Near-Zero-Index materials are becoming essential in nanophotonic designs and optical manipulation. As the name suggests, NZI occurs when the index of refraction of a material approaches zero over a certain wavelength range. This is achieved when a conductive material has the real part of its permittivity cross zero combined with low Drude damping in the material (low loss). These properties allow for many extreme optical effects that stem from the phase velocity and wavelength approaching infinity as the index approaches zero, along with massive electric field

enhancements within the material. Since the original seminal works on NZI materials [116, 117, 118], there have been countless applications utilizing these novel properties. These applications range from creating various near-perfect absorption or transmission devices [119, 120, 121, 122, 123, 124, 125], supercoupling light into narrow waveguides [126, 127, 128], enhancing of optical nonlinearities [129, 130, 131, 132], and increasing plasmonic control [133, 134], among many others.

Transparent conducting oxides have become the most common NZI materials due to their broad NZI region located in the telecom wavelength range, low losses at the dielectric cross-over-point (where the real part of the dielectric function crosses zero), and tunability of the NZI wavelength based on deposition conditions. In particular, indium-tin-oxide [129, 132, 133, 135, 136, 137, 138], aluminum-doped zinc oxide [119, 123, 134, 136, 139], and fluorine-doped tin oxide [140, 141] have been well-studied for their NZI properties and applications. While being a benefit in some cases, the large dependence of the optical properties of these materials on their deposition parameters can introduce difficulty in experimental replication, due to materials being deposited using different fabrication tools and methods across different institutions. As an example, the NZI resonance of ITO varies from 1260 to 1920 nm depending on the carrier concentration in the material [142]. The difference in properties between the two ends of this region could completely change the performance of a device.

Recently, there have been many commercial companies that sell TCO materials on substrates that can be used for NZI applications. By being able to purchase from one of these suppliers, the fabrication issues from batch to batch along with

comparisons across different tools are eliminated. In this chapter, we investigate the optical properties of various commercial TCO samples and report the existence, strength, and width of their NZI resonances. We focus on three different types of commercially available TCO samples, ITO, FTO, and AZO, from a total of 12 different suppliers. Beyond their optical properties, we also report the thickness and resistivity for all of the measured samples. Using these measured properties, we find general correlations relating the optical and electrical properties of the materials. We find that both the strength and the bandwidth of an NZI resonance are correlated with the location of the resonance and that the strength of the resonance is loosely correlated with the resistivity of the TCO film. We hope that these results provide a resource for future fabrications of repeatable and comparable NZI devices.

4.2 Measurement and optical modeling scheme

To measure the optical properties of these samples, we use variable-angle spectroscopic ellipsometry (Woollam M-2000). We take measurements of each sample at 65°, 70°, and 75°, and we use the same tool to take transmission intensity measurements. The raw optical data is fit using a general oscillator model with one Drude oscillator [143] and up to three Tauc-Lorentz oscillators [144]. The number of Tauc-Lorentz oscillators is determined by only adding a further oscillator to the model if this addition causes a $>10\%$ decrease in the mean-squared-error (MSE) of the fit. This method was used to avoid over-fitting the data with spurious resonances. For each sample where the company provided a bare substrate without the

TCO deposited, the optical properties of the substrate were measured separately, and these properties were input into the model fitting the TCO data. For companies that did not provide a substrate, we used the material properties from the Woollam database for the substrates (soda-lime glass, float glass, or glass slide dependent on what substrate the company stated they used) as the substrates in our fits. Our fits also accounted for reflections from the backside of the substrate. The thickness of the TCO films was determined from the optical fitting, with the transmission intensity data allowing us to unambiguously determine the value.

Many of the FTO samples had to have a slightly adjusted fitting model. Instead of having a single layer of TCO, many of the FTO samples provided were multi-layer structures. On top of the glass substrates, a thin layer of SnO_2 was deposited, followed by a thin SiO_2 layer, and then finally the active FTO layer. In this chapter, we only report the optical properties of the top active FTO layer. In our optical model, we define the optical properties of the SnO_2 with a Cauchy model and define the properties of the SiO_2 layer with experimental found data from sputtered SiO_2. In the model fit, we fit the thicknesses of these two intermediary layers and the thickness of the top FTO layer, along with the oscillator values defining the properties of the FTO. These two added fit parameters add extra variance to our fits, causing a larger error in the reporting of these FTO properties. Two of the FTO samples, sourced from Biotain Crystal and MSE Supplies, were both single-layer samples and were fit using the same process as the ITO and AZO samples detailed above.

4.3 Properties of TCO films

Typical results for the optical properties of ITO, FTO, and AZO are shown in Figure 4.1. Although there can be a fairly large variation from sample to sample, data from each material generally follows the same general shape and trends. ITO normally displays a strong NZI resonance in the NIR with a higher index of refraction in the visible and higher attenuation further into the infrared (IR). FTO usually shows a much weaker resonance than ITO, and this NZI resonance is located further into the IR. This same trend holds with AZO. In the short wavelength range, AZO also exhibits a peak in attenuation. For the individual optical properties, company names, and nominal resistances for each of the 51 samples reported in this chapter, see Appendix B.

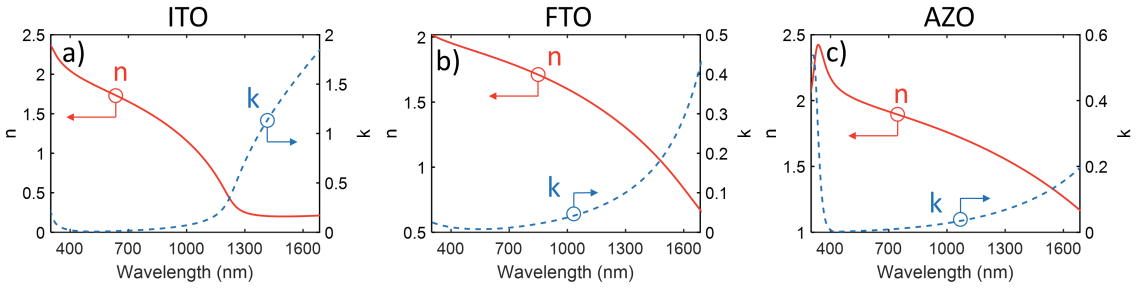

Figure 4.1: Characteristic optical properties of a) ITO, b) FTO, and c) AZO. These properties are representative of the general trends in optical properties for each of the materials. ITO samples exhibit a strong NZI resonance between 1100 -1400 nm, while FTO and AZO have resonances beyond our experimental measurement range.

With the measured properties of this multitude of samples, we explored various correlations in the NZI resonance data. In Figure 4.2, we plot the minimum magnitude of the refractive index, $|n| = \sqrt{n^2 + k^2}$, versus the wavelength where that minimum is found. In the plot, the grey shaded region denotes extrapolated data

as the range of our optical measurement ends at 1690 nm. For data in this region, we extrapolate the optical properties using the oscillators defined from fitting the ellipsometric data. We note that if there are additional phononic resonances or additional bound electron resonances in this region, it could further affect the optical properties in unaccounted for ways, adding a higher error for values in this region. The further away the resonance is from the measurement wavelength maximum of 1690 nm, the higher the uncertainty in the resonance strength and location. For two ITO samples that we measured, we did not include the data in the plots in this chapter because the extrapolated NZI resonances were too far in the IR to conclude anything about their properties in that region. Their measured optical data are reported with the other samples in Appendix B.

We see two general trends in the NZI resonances from our measurements. The first is that for these samples, the location of the NZI resonances is segmented by material. The center wavelength for the ITO NZI resonance occurs in the ∼1100 – 1400 nm range, with one outlier. As we traverse further into the IR, we find the region containing the FTO resonances ∼1500 – 1900 nm, and finally the region where the AZO can be found ∼1950 – 2100 nm. The second trend that we find is that the stronger (lower $|n|$) NZI resonances occur at shorter wavelengths. As the wavelengths extend further into IR, the resonances become slightly weaker. We fit a linear trendline to this plot as a guide to the eye to show this relationship ($R^2 = 0.68$).

The magnitude of an NZI resonance is not the only important characteristic of the material. The bandwidth of the resonance (hereby defined as the width

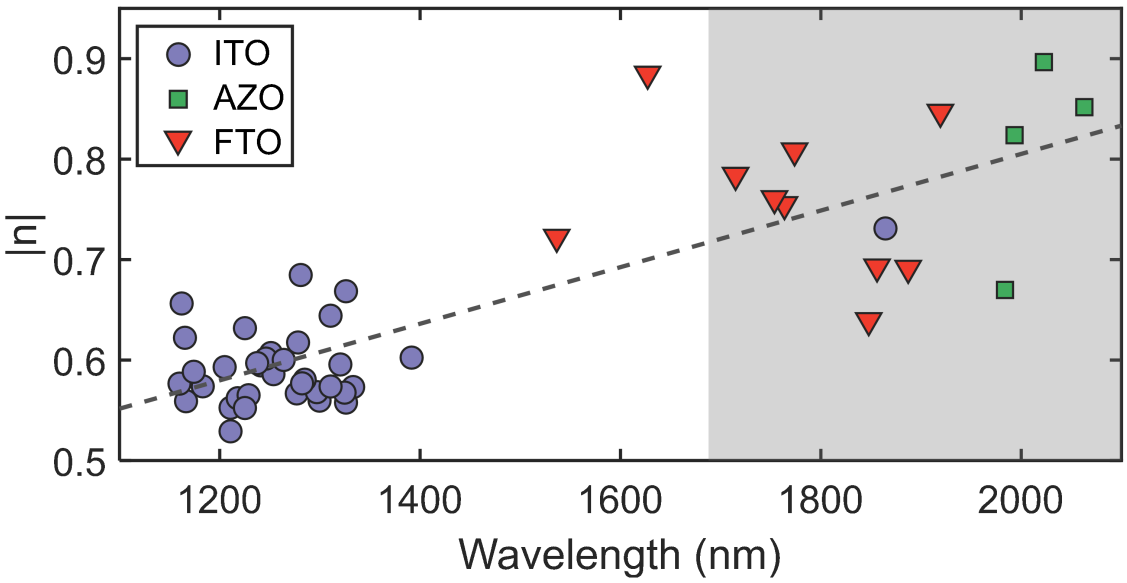

Figure 4.2: Strength of NZI resonance vs the wavelength at which the resonance occurs. For each TCO sample, the magnitude of the index of refraction, $|n| = \sqrt{n^2 + k^2}$, is plotted against the wavelength where this minimum occurs. Our experimental measurement only goes up to 1690 nm, thus the grey shaded region beyond this wavelength shows extrapolated data of the oscillator fits in the experimental region. Added Lorentz resonances in this region could affect these values. ITO samples are shown as purple circles, AZO as green squares, and FTO as red triangles. The dashed grey line is a linear fit to the data to guide the eye.

of the spectral region where $|n| < 1$) is also of vital importance for broadband devices required to perform at many wavelengths. In Figure 4.3, we plot the bandwidth of the NZI resonance for each of our measured materials versus the location of the center wavelength of the NZI resonance (location of the minimal $|n|$ value). We find that as the location of the resonance moves further into the IR, the bandwidth increases. The grey shaded region in this figure depicts the region where the center wavelength of the NZI resonance is found by extrapolation. We also note that in this figure, the two FTO samples whose center wavelengths are located in the measured region also involve some extrapolation, as the region where $|n| < 1$ extends beyond our measurement maximum of 1690 nm. For the materials

that do involve extrapolation, we find a much wider range in results deviating from our linear trendline. In this study, we cannot determine whether this high variance effect is caused by additional error from the extrapolation, difference in material responses (as most of these materials are FTO and AZO), or if materials with NZI resonances in this regime behave differently. In all likelihood, it is some combination of these three factors. Figure 4.3b shows the same plot with only the data with no extrapolation, which happens to entirely consist of ITO samples. This trend is positive with a few outliers ($R^2 = 0.58$), with most of the data points supporting the conclusion that materials with NZI resonances at longer wavelengths have a broader bandwidth of this resonance.

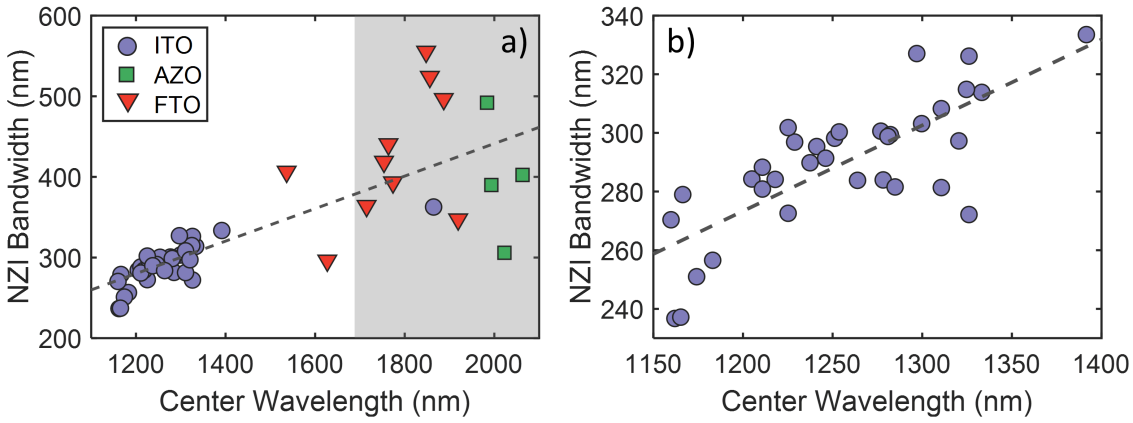

Figure 4.3: Bandwidth of NZI resonance vs the center wavelength of the resonance. We find that as the NZI minimum wavelength moves further into the IR, the bandwidth of the NZI region increases. Bandwidth is defined as the size of the spectral regime where the $|n| < 1$. They grey shaded region depicts extrapolated data. ITO samples are shown as purple circles, AZO as green squares, and FTO as red triangles. The grey dashed line is a linear fit to the data to guide the eye of the reader. b) A plot of the samples that involved no extrapolation in the bandwidth.

This positive correlation between the location and the bandwidth of the NZI combined with the correlation between the strength and location creates a trade-off

in device design. By choosing a sample with a resonance closer to the visible regime, you can achieve a stronger resonance, but at the cost of a smaller bandwidth. Thus for some applications, the ideal material might occur further into the IR where a strong resonance can still be achieved and a more broadband effect is possible.

For each sample, we also took 4-point probe resistivity measurements to characterize the electrical properties of the TCO films. We used a Signatone 4-point probe device readout with a Keithley 2400 sourcemeter. The dimensions of each sample measured were large enough that no size compensation had to be applied to the sample measurement. Each sample was measured in 3 different orientations near the center of the sample and the results reported are the averages of these measurements. In Figure 4.4, we report the resistivity of each TCO film vs $|n|_{min}$. We find that as the resistivity of the films increase, $|n|_{min}$ also increases. This correlation is in agreement with the literature, where it has been found that higher carrier concentrations in ITO samples lead to stronger NZI resonances with these resonances located at shorter wavelengths [142]. We find that FTO and AZO films have higher resistivities than the ITO films, requiring their films to be much thicker to obtain similar sheet resistance values. For samples where a thin coating is required with a high conductivity, ITO seems to be the only available commercial option of the three materials we investigated. In Figure 4.4b, we isolate the unextrapolated ITO samples and find a similar correlation over a smaller scale, with all of the resistivities of these samples located between 1.2 and 2 $\Omega - \mu$m.

We summarize the complete findings of our optical and electrical measurements in Appendix B for reference. These include the minimum $|n|$ achieved, the location

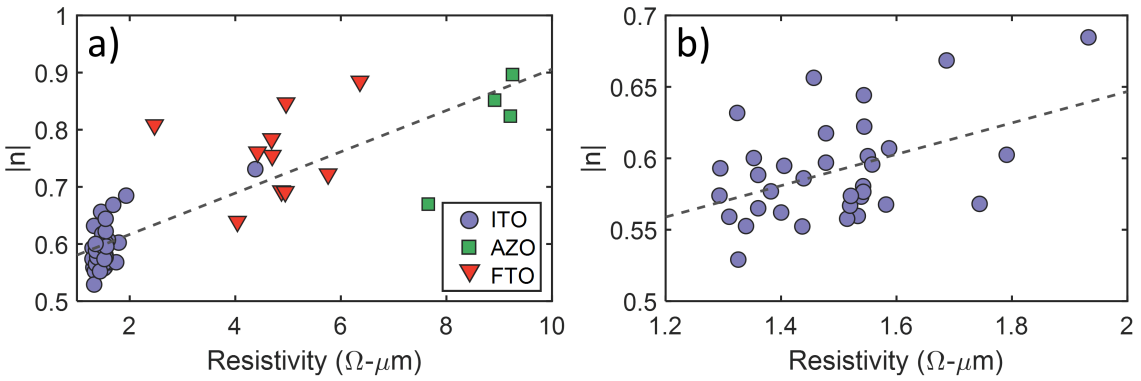

Figure 4.4: Strength of NZI resonance vs the resistivity of the film. We find that generally as the resistivity of the film increases, so does the minimum magnitude of the index of refraction. ITO samples are shown as purple circles, AZO as green squares, and FTO as red triangles. The grey dashed line is a linear fit to the data to guide the eye of the reader. b) A plot of the samples that require to extrapolation in the optical properties.

of the minimum, the NZI bandwidth, the measured thickness t of the TCO, and the measured resistance R.

In conclusion, we have surveyed the optical and electrical properties of 51 different TCO samples and found a wide range of potential NZI properties. We find that ITO is the most readily available NZI material, with many different samples having a $|n| < 0.6$. We also find a correlation between the location of the NZI resonance and the strength and bandwidth of that resonance, with shorter wavelengths leading to stronger resonances with a smaller bandwidth and longer wavelengths leading to weaker resonances with a wider bandwidth. We also find a loose correlation between the strength of the NZI and the resistivity of the TCO films, with a lower resistivity leading to a slightly stronger NZI. We hope that these results inform the consistent device design of future NZI materials, showing the breadth and availability of different TCO materials.

Chapter 5: Highly Switchable Absorption in a Metal Hydride Device Using a Near-Zero-Index Substrate

Optical switchability is an important functionality for photonic devices, which allows them to accommodate a wide range of applications. In this chapter, we propose a switchable absorption device consisting of a Pd-capped Mg thin film deposited onto a near-zero-index substrate. By utilizing Mg's extreme optical changes upon hydrogenation and combining it with the high optical contrast of the NZI substrate, we can create a device that is fully switchable from a highly reflective state to a broadband absorbing state. When modeling the substrate as a Drude material with a plasma wavelength of 600 nm, we calculate an absorption change of >70% from 650 – 1230 nm, with a peak total absorption of 78% at 905 nm. We experimentally demonstrate this effect using 25 nm of Mg with a 3 nm Pd capping layer deposited onto an ITO-coated glass substrate. This device achieves an absorption change of 76% at 1335 nm illumination, with a maximum absorption of 93% in the hydride state, utilizing ITO's NZI region in the NIR. By tuning the NZI region of the substrate, this effect can be extended from the visible through the infrared.

5.1 Background and introduction

Switchable absorption across the electromagnetic spectrum is a highly desirable functionality for applications from thermography to solar absorbers and color displays [80, 145, 146, 147]. Different absorption bandwidths are necessary for these different applications, with solar applications requiring high functionality in the visible, while telecom sensors require the sensitivity to be in the near-infrared. Specifically, absorption in thin metal films has found wide application in hot carrier photodetection and solar cells, where hot carriers created in the metallic thin film can be harnessed [111, 148, 149, 150, 151, 152, 153]. By adding a switchable functionality to this effect, devices can be turned on and off with an external stimulus, allowing a wider range of applications, such as switchable solar windows or solar cells [16, 154].

There are multiple ways to achieve switchable absorption for these various applications. One common method is to electrically trigger the optical change, whether by applying a voltage across a diode structure [155, 156], by electronically aligning a liquid crystal array [157], by actuating a micro-electro-mechanical system [158], or by electrostatically doping an active optical material, such as graphene [159]. Another method is to thermally activate a phase change in the device, such as with VO_2, which goes through a phase transition at 68°C [160, 161, 162, 163]. Alternatively, these optical changes can be triggered by atmospheric changes, such as H_2 gas exposure. Metal hydrides have recently been utilized for their switchable optical properties in the visible and NIR for various purposes including H_2 sensing and physical encryption [20, 23, 80, 115, 164, 165, 166]. Mg in particular exhibits

a dramatic optical change upon H_2 exposure, transitioning from a lossy metal to a dielectric MgH_2 [13, 165, 167]. This change upon hydrogenation can be utilized to switch a device from a highly reflective metallic state to an absorbing state. Many other switchable absorption designs are based on metamaterials that require complex fabrication procedures. In contrast, devices based on thin-film Mg only require a thin film deposition and no lithographical processing.

To further increase the functionality of thin-film devices, the optical properties of the substrate can be tuned to create a Fabry-Perot-like resonance within the active layer [111, 120, 168, 169]. By optimizing the reflection at the thin film/substrate interface, strong destructive interference can be engineered, causing high absorption in the film. For many thin metal films, this effect can be strongly enhanced in the presence of a NZI substrate where the real part of the index of refraction approaches zero [119, 120, 123]. Unlike traditional Fabry-Perot resonances that require the thickness of the thin film to be a quarter of the wavelength of the incident light, utilizing this effect allows for interference effects in films 10-100x thinner. Recently, NZI materials have been utilized for a wide range of applications, from light funneling to perfect absorbers, amongst many others [124, 128, 170].

In this chapter, we propose a thin film device structure for switchable absorption that can be tuned across the visible into the NIR spectrum by adjusting the NZI resonance of the substrate, achieving >90% absorption experimentally. The structure consists of a 25 nm Mg layer capped with 3 nm of Pd on an NZI coated glass. By utilizing the extreme optical properties change of Mg upon hydrogenation, we can switch the device from a highly reflective metallic state to a light-absorbing

hydride state. Simulations show this effect can create a $> 70\%$ change in absorption over a range of 650 -1230 nm when the substrate is modeled as a Drude material with a plasma resonance $\lambda_p = 600$ nm and a damping factor $\gamma = 10^{13}$ Hz, with a peak absorption change of 78% at 905 nm. We experimentally demonstrate this structure on an ITO substrate with an NZI resonance in the NIR and find a peak absorption change of 76% at 1335 nm, where the absorption in the hydride state is 93%.

5.2 Concept and design

Our switchable absorption structure is depicted in Figure 5.1. It consists of a SiO_2 base coated with 350 nm of NZI (labeled substrate), 25 nm Mg, and 3 nm of Pd. The Pd capping layer is necessary for this design to catalyze the H_2 dissociation reaction on the top of the structure [97, 167]. The Pd also acts as a protective layer above the Mg, preventing oxidation into MgO [171, 172]. Exposure to H_2 gas switches the device from a reflective metallic state into an absorbing hydrogenated state. The H_2 dissociates into H atoms at the Pd surface and diffuses through the thin Pd layer into the Mg to form MgH_2. As Pd hydrogenates into PdH_x, it becomes less conductive, but remains in a metallic state. Meanwhile, Mg transforms entirely into a dielectric upon hydrogenation. In this dielectric state, the light is now able to pass through the MgH_2 and interact with the substrate, as opposed to being almost entirely reflected by the Mg layer in the metallic state. Figure 5.2 shows the simulated reflection and transmission plots for each state.

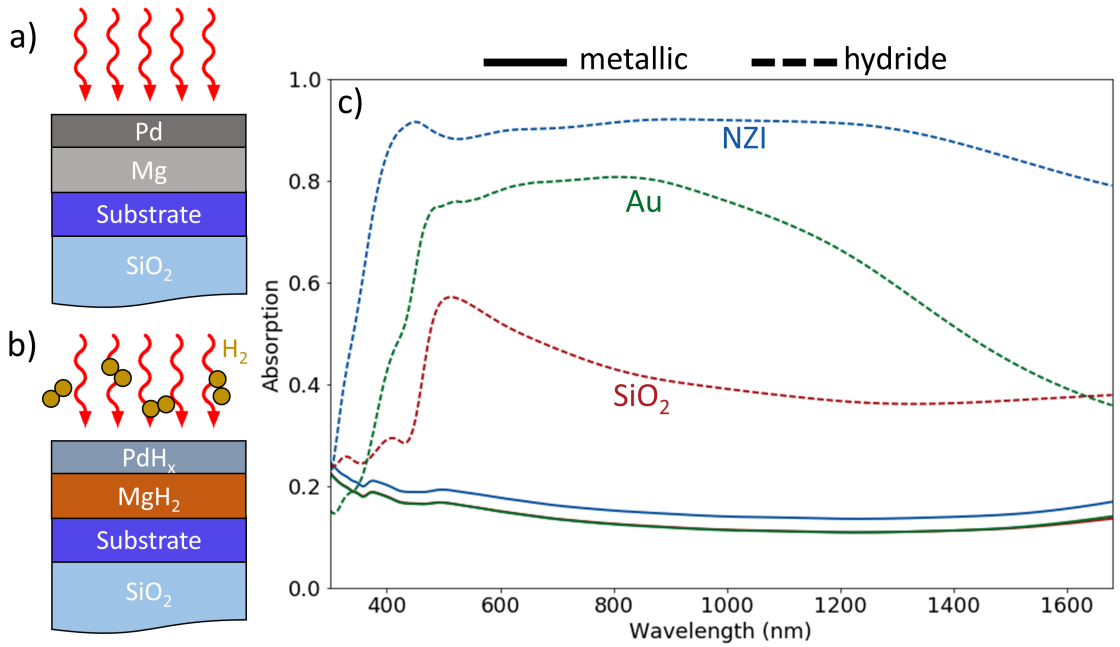

Figure 5.1: Device design and simulated absorption spectra for various substrates. a) Device architecture in the inert, metallic state, and b) when exposed to H_2. For each substrate (SiO_2, Au, or NZI), the thicknesses of the Mg and Pd layers were optimized between 3 - 50 nm for maximum absorption change. For the NZI substrate, the thicknesses used were t_{Pd} = 3 nm and t_{Mg} = 25 nm. For both the Au and SiO_2 substrates, the thicknesses were t_{Pd} = 3 nm and t_{Mg} = 50 nm. The substrate for each case was kept constant at 350 nm. c) Absorption spectra of the metallic layers (Pd + Mg) with SiO_2 (red), Au (green), and NZI (blue) substrates. The solid (dashed) lines are the spectra in the metallic (hydride) state. The absorption curves for SiO_2 and Au substrates are almost completely overlapping in the metallic state. The NZI substrate is defined to have an index of $\tilde{n} = 0.01 + 1i$ across the spectrum. These simulations account for the 30% volume expansion of Mg upon hydrogenation (e.g. 25 nm metallic Mg becomes 32.5 nm MgH_2).

In Figure 5.1c, we compare our proposed structure to other physical substrates by simulating the absorption spectra using the transfer-matrix method (TMM) found in the literature [173]. Optical properties for the Mg, Pd, and their hydrides are taken from Palm et al. [164], Au from Johnson and Christy [174], and SiO_2 from Gao et al. [175]. The index of the NZI material was defined to be $\tilde{n} = 0.01 + 1i$ (effects of dispersion are discussed and modeled below). In the simulations,

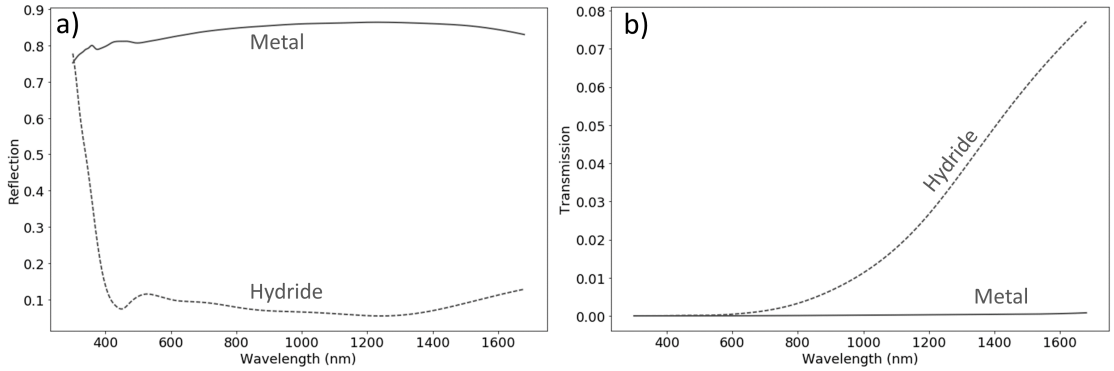

Figure 5.2: Simulated a) reflection and b) transmission plots for device with 350 nm NZI substrate. Solid lines indicate response in the metallic state and the dashed lines indicate response in the hydrogenated state. In the metallic state most of the light is reflected, as opposed to little reflection in the hydride state. In neither case is there appreciable transmission through the NZI layer.

the SiO_2 base was considered to be semi-infinite and each substrate was defined to be 350 nm. For the Au substrate, 350 nm is optically thick, so that the device can be practically thought of as an infinite Au substrate, and because the SiO_2 substrate layer is on a SiO_2 base, the defined thickness does not affect the results as the substrate is continuous with the base layer. For the NZI material, we find that as the substrate thickness increases, we achieve a greater absorption change in the material. Once the substrate becomes greater than ~300 nm, this effect begins to level off. We chose 350 nm to achieve this high absorption change, while still having a thin enough layer that is reasonably achieved in common NZI materials, such as TCOs [134, 139]. Figure 5.3 shows the complete spectral dependence of the NZI substrate thickness on the absorption change.

For each different substrate, we optimized the Mg and Pd thicknesses that would create the largest absorption change upon hydrogenation. We define the total

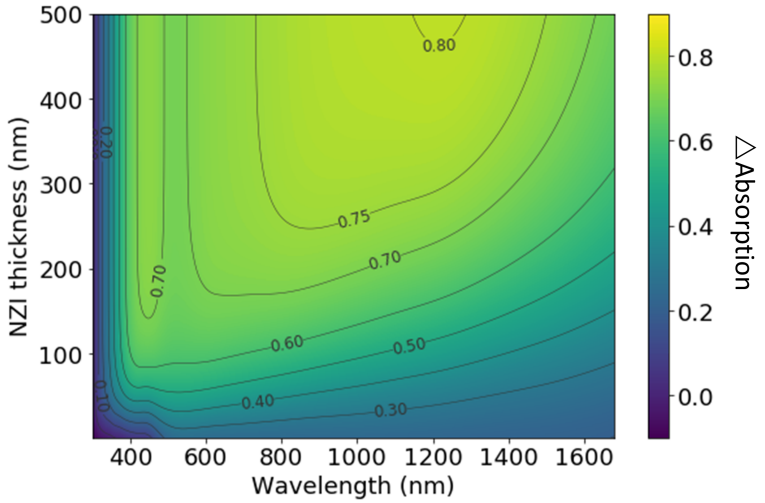

Figure 5.3: Thickness optimization of NZI substrate. Change in absorption defined as absorption of the Mg and Pd in the metallic state subtracted from their absorption in the hydride state. We can see that the absorption change is greater for thicker films of the NZI, but with diminishing returns as the film gets larger than ∼300 nm. For this optimization the Mg layer thickness was set to 25 nm and the Pd thickness to 3 nm. The NZI optical properties refractive index was defined to be $\tilde{n} = 0.01 + 1i$.

absorption as the combined absorptions in the Pd and Mg layers (note: absorption in the substrate and SiO_2 are negligible, see for example Figure 5.5). In our thickness optimization, we applied the maximum thickness of Mg as 50 nm. The full Mg film would not hydrogenate if it were greater than 50 nm due to the formation of a well-documented MgH_2 hydrogen blocking layer [13, 176]. We applied a lower thickness bound of 3 nm on the Pd layer to ensure a uniform film and complete coverage of the Mg. Expansion of the metal hydrides also needs to be taken into account, as the lattice expands as hydrogen enters the material. The Mg lattice is found to expand by 30% upon hydrogenation [13] (e.g. 25 nm metallic Mg becomes 32.5 nm MgH_2), and this effect was included in all simulations. Pd has a much smaller lattice expansion, about 12% [60], which ended up being negligible in our simulations since

the optimized Pd thicknesses were very small. We found the optimized thicknesses for each layer were $t_{Pd} = 3$ nm and $t_{Mg} = 25$ nm for the NZI substrate and $t_{Pd} = 3$ nm and $t_{Mg} = 50$ nm for both the Au and SiO_2 substrates. Figure 5.4 shows the full absorption change as a function of the Mg and Pd thicknesses at 6 different wavelengths.

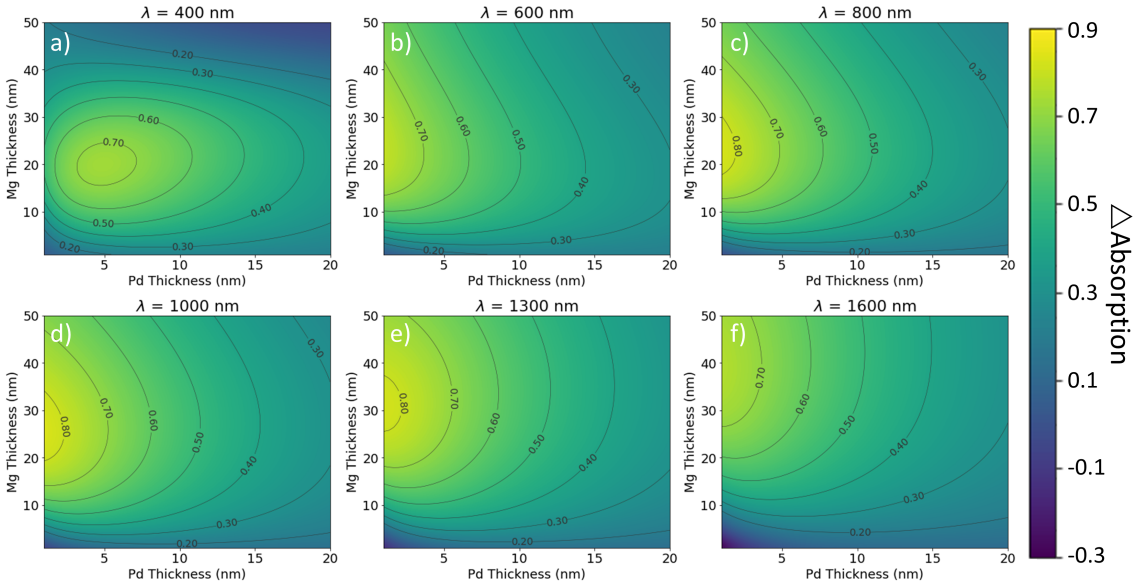

Figure 5.4: Thickness optimization for Mg and Pd thin film layers. For most wavelengths, the absorption change is maximized for thinner Pd. In order to get the catalytic and sealing effect of the Pd in the device, at least a 3 nm coating is necessary, so it was set as our lower bound for the optimization. For 400 nm illumination, the maximum falls at 5 nm, but still has strong absorption at 3 nm. The Mg is maximized between 20 and 30 nm depending on the illumination wavelength. We found that a Mg thickness of 25 nm caused for the best maximization across all of the shown wavelengths to create the most broadband effect. The thicknesses of these plots are the thickness of the metal layers and the simulations take into account the 30% Mg expansion upon hydrogenation.

In the metallic state, Mg is optically opaque at a thickness of 50 nm, so the absorption curves for the SiO_2 and Au substrates almost entirely overlap. In the NZI material case, the light slightly penetrates the Mg layer at 25 nm but is still mostly reflected with little measured absorption, under 20% for most of the

spectrum. Upon hydrogenation, we see a dramatic increase in absorption for each substrate. The extremely reflective Mg becomes a partially transmitting MgH_2. We see that the choice of substrate greatly affects the absorption in the metal hydrides, as the light now interacts at the MgH_2/substrate interface. For the SiO_2 substrate, we see the smallest increase in absorption, mostly due to the increase in path length of the light in the metal hydrides as the light transmits through it, with little added benefit from the reflection off the substrate interface. The Au substrate shows a much higher absorption increase by creating a cavity effect within the MgH_2, with light reflecting between the Au substrate and PdH_x capping layer. The largest attainable absorption change is found for the NZI substrate. In this case, a strong Fabry-Perot-like cavity is created within the MgH_2, creating high absorption due to the destructive interference effects. With these defined optical properties, we can achieve an absorption of >80% from 400 – 1650 nm and >90% from 625 – 1300 nm in the hydride state. We note that the large broadband result depicted by the NZI substrate in Figure 5.1c is not possible with a realistic substrate, because a constant complex index of refraction over this entire wavelength region does not obey Kramers-Kronig consistency. Instead, this result shows the potential for this high switchable absorption response across the visible spectrum and into the infrared if the substrate's index of refraction has a low real part with the imaginary part close to 1 for any span of these wavelengths. We also note that there will be some alloying between the Pd and Mg layers upon deposition [167]. To avoid this alloying in thin-film stacks, it is common to use a Ti interlayer between the Mg and Pd layers. The optical properties being used for these simulations were taken on a thin film stack

without this Ti interfacial layer, thus the properties being used are accurate for these simulations and account for this interfacial layer.

The absorption of the light in the hydride layers is split between the PdH_x and MgH_2. The PdH_x layer is responsible for the majority of the short-wavelength absorption up to ~500 nm. At this point, the MgH_2 begins to absorb more light, with the absorption in the Pd tapering off. The reason for this delineation is that PdH_x still behaves optically like a metal with higher attenuation for shorter wavelengths. It gets a large increase in absorption from the cavity effect, with the path length of light traveling through it increasing dramatically from the multiple reflections within the MgH_2. The MgH_2 has higher attenuation beginning in the upper visible region, which is where it begins to dominate the absorption. The combination of the absorption in these two layers allows for the near-constant absorption change observed in Figure 5.1c. Figure 5.5 shows the full breakdown of absorption between each layer in the stack across the spectrum for both the metallic and hydrogenated states.

Having found this strong absorption effect for the structure with a tailored index of refraction $\tilde{n} = 0.01 + 1i$, we now explore in-depth how the optical properties of this substrate layer affect the total absorption change in the metal films and how robust this effect is. Figure 5.6 shows the relationship of the complex index of refraction of the substrate, $\tilde{n} = n + ik$, with the change in absorption of the metal films. ΔAbsorption is defined as the absorption of the metal layers (Pd and Mg) subtracted from the absorption in the metal hydrides after hydrogen exposure (PdH_x and MgH_2). The first trend that is evident with these plots is that the

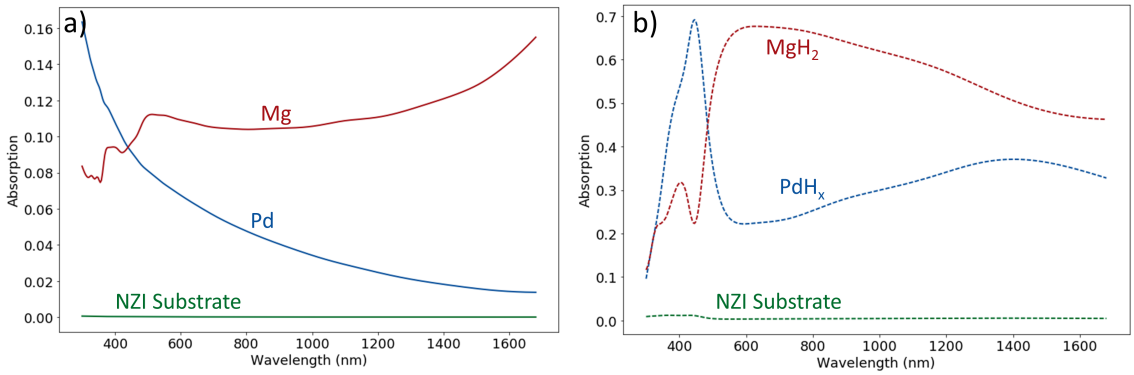

Figure 5.5: Simulated absorption by layer in the device stack in the a) metallic state and b) hydride state. In the metallic state, neither Mg (red) or Pd (blue) have very high absorption, with Mg absorbing more from the mid-visible through the IR. In the hydride state, both Mg and Pd begin absorbing significantly more. Pd has a high sharp absorption peak at ∼450 nm with Mg having a peak at ∼600 nm that broadly tails off into the IR. The combination of the absorption in these two layers allows for the high broadband absorption seen in the combined structure. In neither the metal nor the hydride state does the NZI (green) substrate have any significant absorption.

absorption change increases with decreasing n for each wavelength, showing the necessity of using an NZI substrate. A more interesting trend occurs with the imaginary part of the index. Upon first consideration, we would expect that the absorption in the metal hydrides would be maximized with a maximum reflectivity at the MgH_2/substrate interface. We find through our simulations that this is not the case, because the reflectivity R is maximized when $k = 0$ for the substrate for all investigated wavelengths (see Figure 5.7) and that the absorption is maximized for $k \approx 1$ for incident wavelengths $\lambda = 800$, 1200, and 1600 nm and $k \approx 2$ for $\lambda = 400$ nm. This analysis shows that the absorption increase in the metals is not solely from an increased path length from a perfect reflection off the NZI substrate, but from creating an additive destructive interference condition within the metals. We can see that the value of the imaginary part of the index has the largest effect on

the absorption change when the real part of the index is < 0.25. If the real part of the index is > 0.25, the absorption change becomes comparatively fairly constant for longer visible and NIR wavelengths. The 400 nm result tells a different story, where a higher k is necessary for high absorption change regardless of the value of the real part of the index.

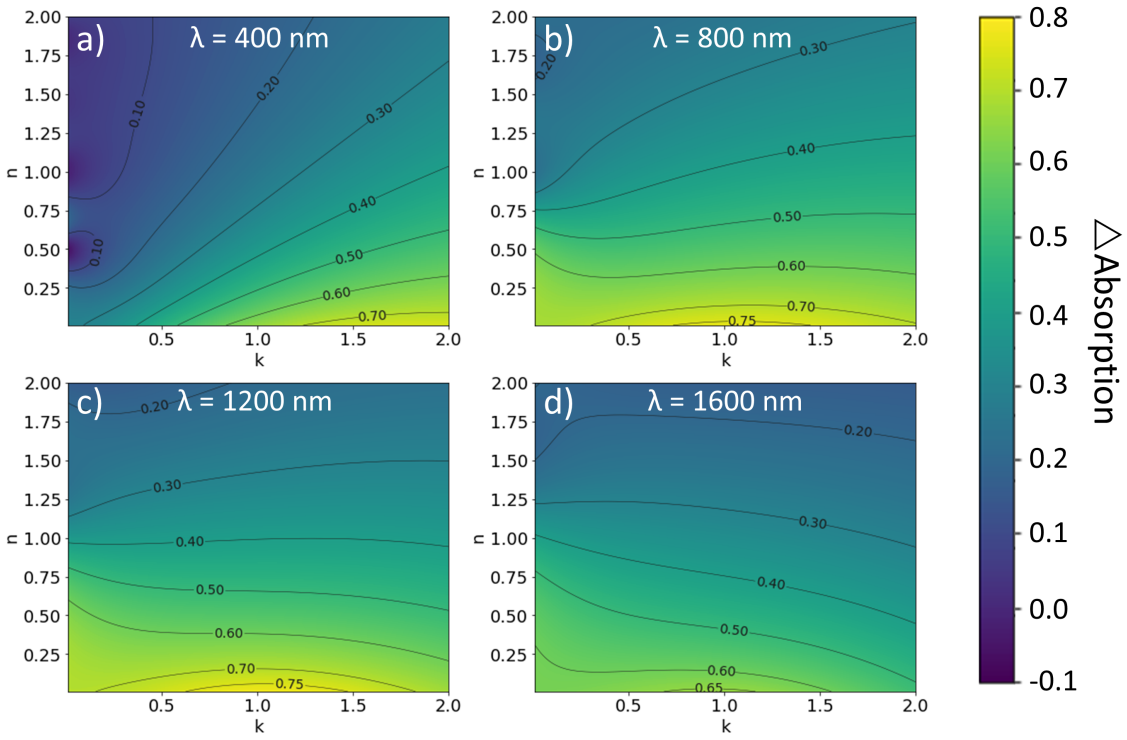

Figure 5.6: Effect of the substrate's optical properties, $\tilde{n} = n + ik$, on device absorption change. Absorption change is defined as the absorption of the device in the metallic state subtracted from the absorption in the hydrogenated state. λ represents different incident wavelengths of illumination, here showing a) $\lambda = 400$ nm, b) $\lambda = 800$ nm, c) $\lambda = 1200$ nm, d) $\lambda = 1600$ nm.

5.2.1 Modeling substrate as Drude material

So far our consideration for this structure has used specifically chosen refractive indices, but a real material has to obey causality across the spectrum. To apply a

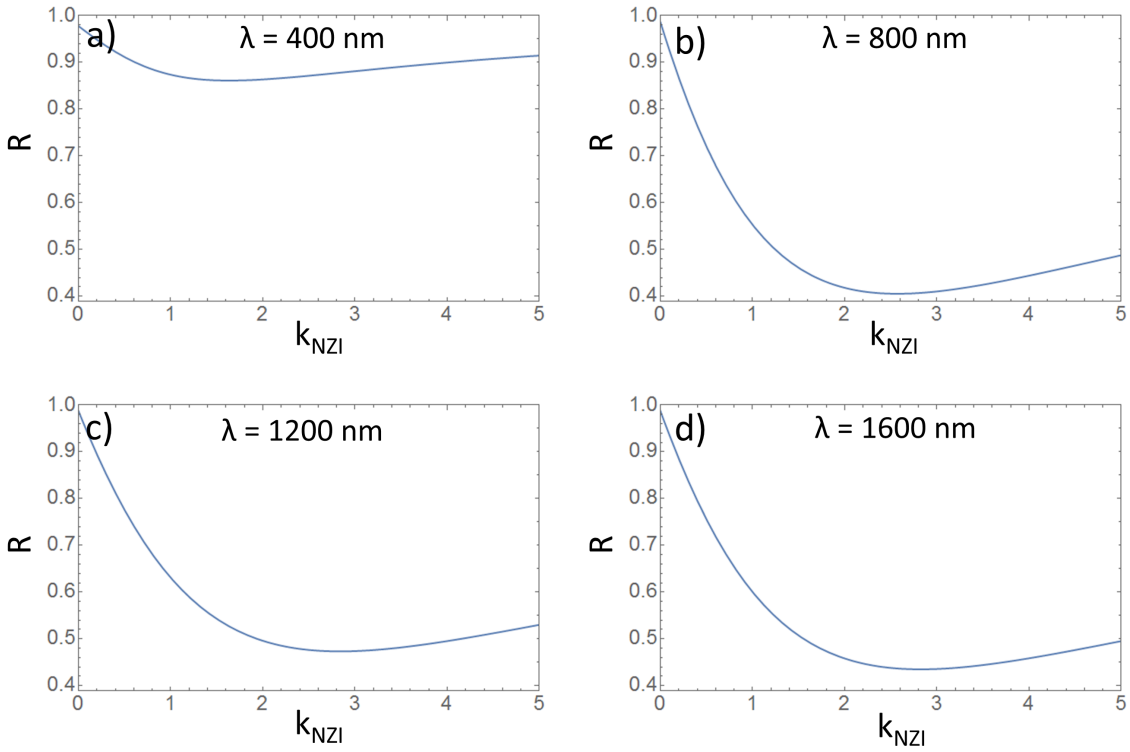

Figure 5.7: Fresnel reflectance R versus the imaginary part of the index of refraction of the NZI substrate k_{NZI} at the MgH_2/NZI interface for an illumination wavelength of a) 400 nm, b) 800 nm, c) 1200 nm, and d) 1600 nm. The real part of the index has been set to 0.01. We can see that the reflectance is maximized at $k_{NZI} = 0$. In our simulations, we find that the absorption change in the device is maximized at $k_{NZI} \approx 1$, which combined with this finding shows that the increase in absorption is from destructive interference effects and not from pure reflection intensity.

model that obeys Kramers-Kronig consistency, we modeled our substrate as a Drude material with properties:

$$\tilde{n} = \sqrt{\epsilon(\omega)} = \sqrt{\epsilon_\infty - \frac{\omega_p^2}{-\omega^2 + i\gamma\omega}} \tag{5.1}$$

where $\tilde{n}$ is the complex index of refraction, ϵ is the dielectric function, ϵ_∞ is the permittivity as $\omega \to \infty$, ω_p is the plasma frequency, and γ is the damping constant. This equation models the free-electron response of a metal without any interband

transitions, but provides for a realistic, yet simple, model of an NZI material.

Figure 5.8 shows the results of modeling the properties of the substrate layer with a Drude model. For these simulations, we have set ϵ_∞ to 1 (for effects of ϵ_∞ on the absorption change, see Figures 5.9 and 5.10). We immediately see that with this physical model, we can still achieve very high absorption changes, >75% for some incident wavelengths. The absorption is maximized for smaller γ, although this effect begins to plateau for $\gamma < 10^{14}$ Hz. This effect is what we would expect, as a higher damping term in the substrate causes an increased real part to the index of refraction. The increased damping eliminates the cavity effect in the MgH_2 exploited by the device structure. The $\gamma < 10^{14}$ Hz range is easily achievable, as many TCOs have been found to have a damping coefficient between 10^{13} and 10^{14} Hz [136].

The Drude simulations also show a very strong dependence on the plasma wavelength $\lambda_p = 2\pi c/\omega_p$ where c is the speed of light. The resonance effect occurs for plasma wavelengths slightly lower than the illumination wavelength. This occurs because, as we saw in Figure 5.6, the absorption effect is maximized for $k \approx 1$. In the Drude model, k increases for wavelengths below the plasma frequency, and the effect is greatest when k is large enough to create the phase matching in the MgH_2 and n remains low enough to harness the NZI effect. For 400 nm illumination, we can achieve >70% absorption change for a Drude material with $\lambda_p \approx 150$ nm and $\gamma < 3{*}10^{14}$ Hz. A real material that could fulfill these values would be Pt with $\lambda_p = 144$ nm and $\gamma = 1.088{*}10^{13}$ Hz [177]. For longer wavelengths in the spectrum, we see the continued potential for strong effects, with regions > 75% absorption change for $\lambda = 800$ nm and $\lambda = 1200$ nm. As we continue into the infrared, we find that

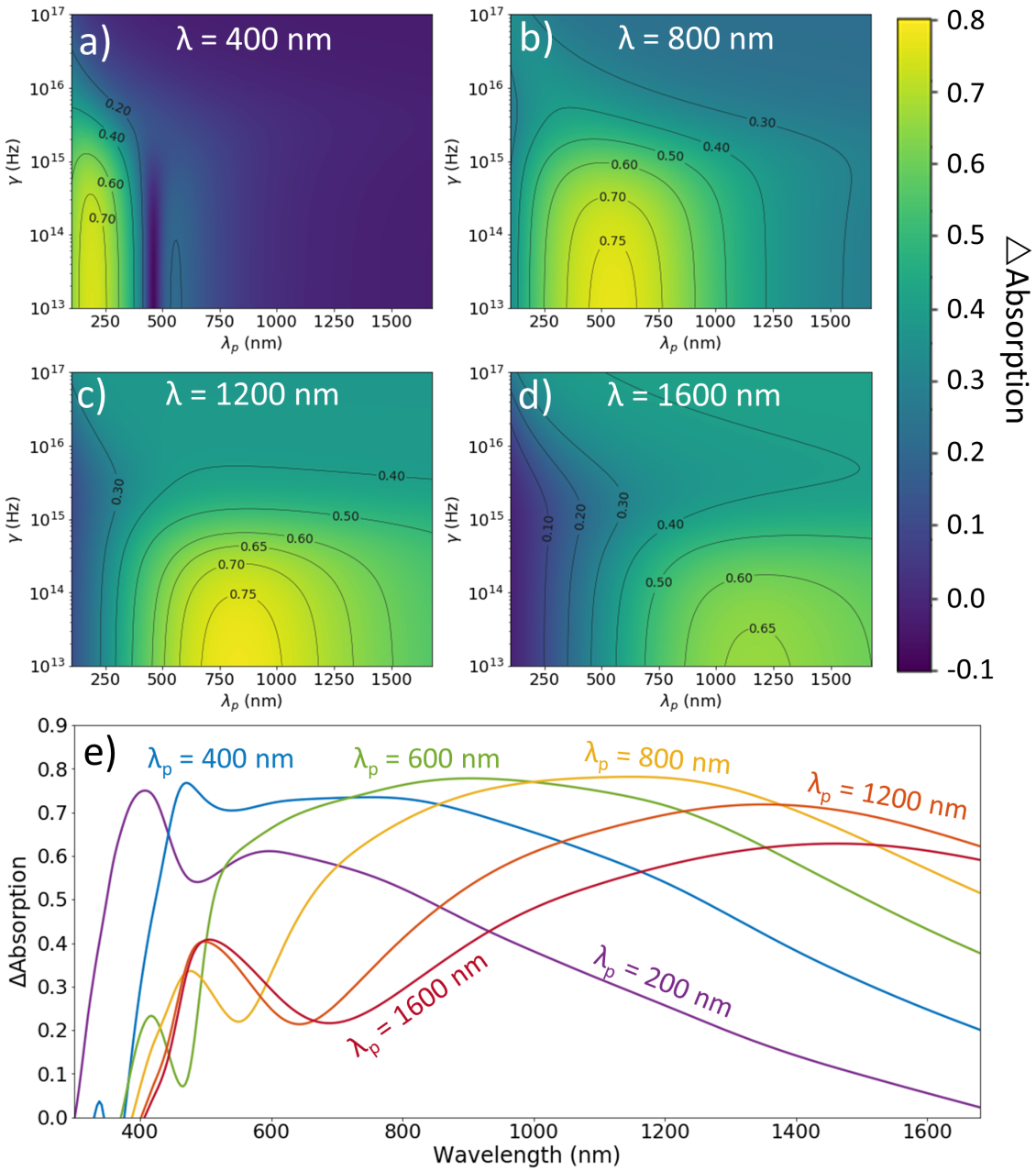

Figure 5.8: Change in absorption upon hydrogenation using a Drude model for the NZI material. λ_p is the plasma wavelength of the Drude substrate ($\lambda_p = 2\pi c/\omega_p$) and γ the damping term in the Drude model. λ represents different incident illumination wavelengths, here with a) $\lambda = 400$ nm, b) $\lambda = 800$ nm, c) $\lambda = 1200$ nm, d) $\lambda = 1600$ nm. e) Absorption change vs illumination wavelength for 6 different λ_p with $\gamma = 10^{13}$ Hz, showing how broadband the switchable effect can be with a physical model.

the high absorption change effect begins to taper off.

In Figure 5.8e, we find that even when using a Drude model for the NZI material, we still can get a broadband result. In these simulations, we defined $\gamma = 10^{13}$ Hz. For λ_p in the long-wavelength portion of the visible regime, we can see the bandwidth of the response is the greatest. We find that for $\lambda_p = 600$ nm and $\lambda_p = 800$ nm, we can achieve a region of $> 70\%$ absorption change for over a 580 nm range (650 – 1230 nm for $\lambda_p = 600$ nm and 825 – 1405 nm for $\lambda_p = 800$ nm). If we lower our absorption change threshold to 60%, then our bandwidth widens to 835 nm. Both of these cases reach a peak absorption change of 78%, at 905 nm for $\lambda_p = 600$ nm and at 1145 nm for $\lambda_p = 800$ nm. If we further increase λ_p, we still see a broadband result, but the magnitude of the peak of the absorption change begins to decrease. Conversely, if we lower λ_p, we can still achieve a high peak absorption switchability, but begin to lose the large broadband effect as the resonance narrows.

5.2.2 Angular dependence of device

To test the robustness of this effect to non-normal incidence illumination, we simulated the same structures depicted in Figure 5.1 for illumination angles varying from 0° - 85°, with the angle θ being defined from the normal. Figure 5.11 shows the dependence of the absorption change of the metals on the incident angle. We immediately notice that the NZI substrate remains the best choice for maximum absorption change as the angle increases when compared to the Au and SiO_2 substrates. The only exception to this is at very high incident angles in the

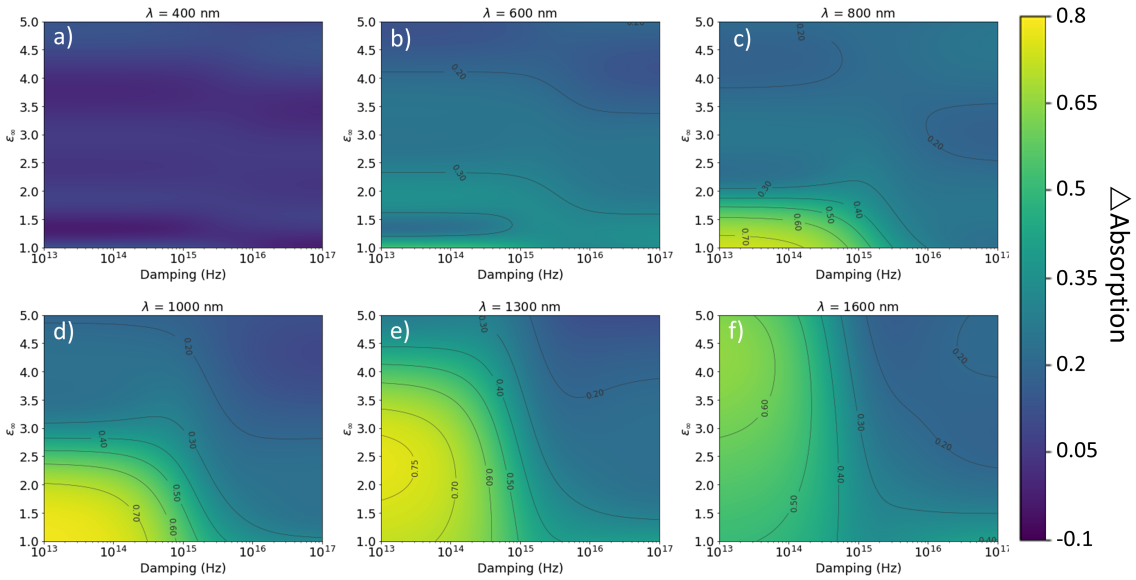

Figure 5.9: Effect of ϵ_∞ parameter in Drude model on absorption change when compared with the damping. Illumination wavelength λ is varied from 400 – 1600 nm from a) – f). The plasma wavelength λ_p was set to 700 nm. For this λ_p, we do not see any singificant absorption change until $\lambda = 800$ nm, where this change is maximized for $\epsilon_\infty = 1$. As we increase the illumination wavlength beyond this point, the maximum abosprtion change is achieved for increasingly high ϵ_∞.

long-wavelength visible and the NIR regions, where for TM polarization the Au begins to slightly outperform the NZI. In all other cases, the NZI remains strongly superior.

With the exception of 400 nm illumination, we find that the absorption change stays fairly robust (constant) for TM polarization from a 0° incident angle all the way to 60° (for 800 nm and 1200 nm illumination the absorption change remains above 70% in this entire region). For infrared illumination, we find that the absorption change for TM polarization actually slightly increases for larger angles, until 35° for 1200 nm illumination, maxing out at ΔAbs = 80%, and until 39° for 1600 nm illumination, maxing at ΔAbs = 71%. For TE polarization, we find that the absorption change drops off quicker with increasing illumination angle, where ΔAbs

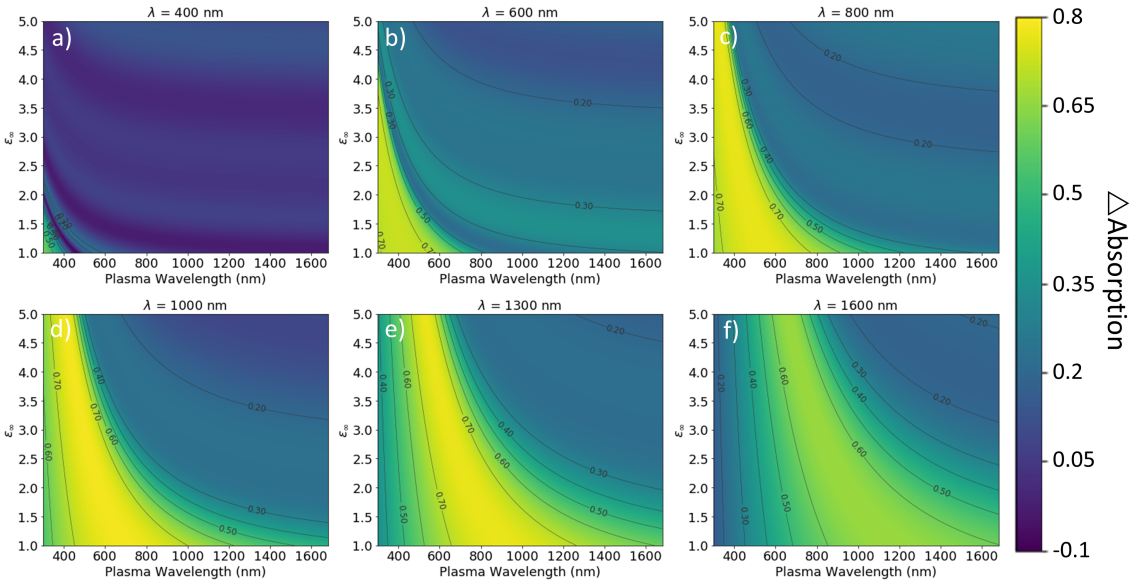

Figure 5.10: Effect of ϵ_∞ parameter in Drude model on absorption change when compared with the plasma wavelength. Illumination wavelength λ is varied from 400 – 1600 nm from a) – f). The damping term γ was set to 10^{13} Hz. For this γ, we begin to see a large absorption change for $\lambda = 600$ nm for low plasma wavelengths. As we increase the illumination wavelength, we get broader regions of high absorption that extend from $\epsilon_\infty = 1$ to $\epsilon_\infty = 5$. The high absorption change region is broadest for lower ϵ_∞ and blue shifts and narrows as ϵ_∞ increases.

drops below 60% at 58°, 60°, and 43° incident angles for 800 nm, 1200 nm, and 1600 nm, respectively. Again, the exception is when we look at 400 nm illumination where we actually see a dramatic increase in the absorption change, with a peak of ΔAbs = 88% at 59°. The 400 nm behaves differently than the other wavelengths shown here because, for this wavelength, the absorption mainly occurs in the PdH_x as opposed to the MgH_2. This difference causes different conditions for the destructive interference in the device, causing very different responses to different polarizations.

We also note that with these increasing angles, the pure absorption in the hydride state can reach almost perfect absorption. Figure 5.12 shows the absorption for the hydrogenated state for the device structure at different angles of illumination.

For TE illumination at 400 nm, the hydride absorption reaches 99.2% at 53°. For TM illumination at 800 nm and 1200 nm, the hydride absorption peaks at 99.3% at 56°and 98.1% at 49°respectively. These perfect absorption effects begin to trail off as we continue further into the IR.

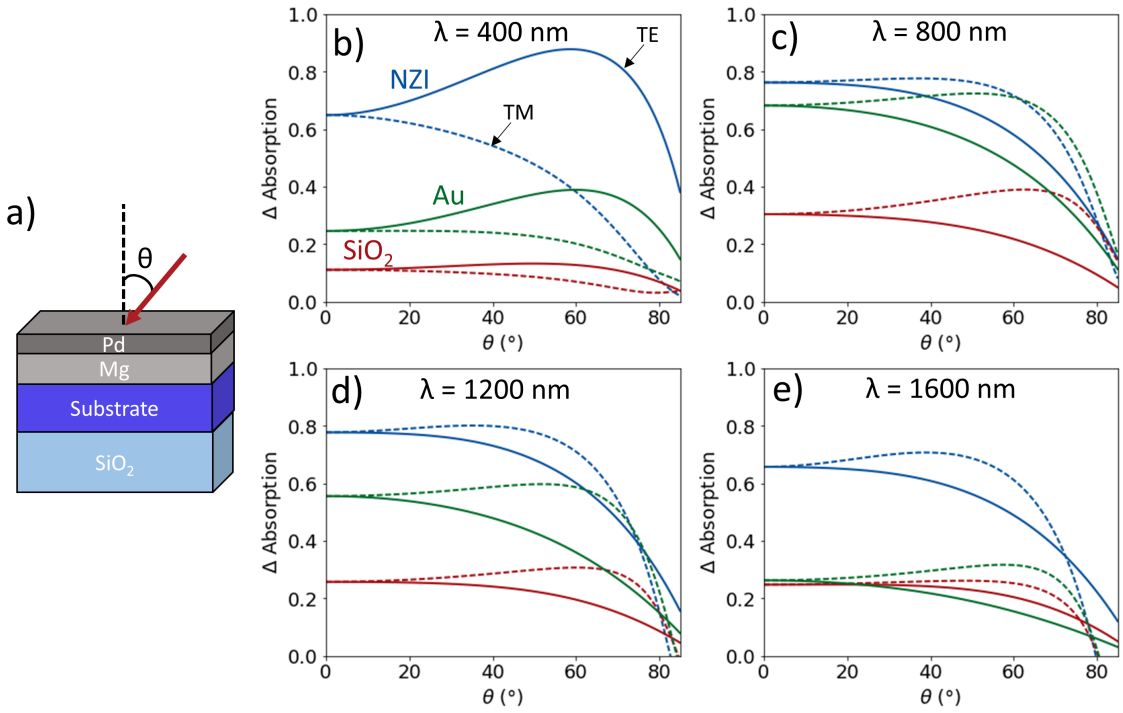

Figure 5.11: Angular dependence of incident light on absorption change. a) Diagram of the device. θ defined as angle incident light makes with the normal. b-e) Plots showing the change in absorption of the structure with increasing θ for four different incident wavelengths b) 400 nm, c) 800 nm, d) 1200 nm, e) 1600 nm. Blue lines represent NZI substrates, green lines represent Au substrates, and red lines represent SiO_2 substrates. Solid (dashed) lines are TE (TM) illumination.

5.3 Experimental demonstration

To demonstrate this effect in practice, we used a film of ITO deposited on a soda-lime glass substrate as our NZI substrate (MSE Supplies). The optical properties of the ITO were measured with spectroscopic ellipsometry (J.A. Woollam

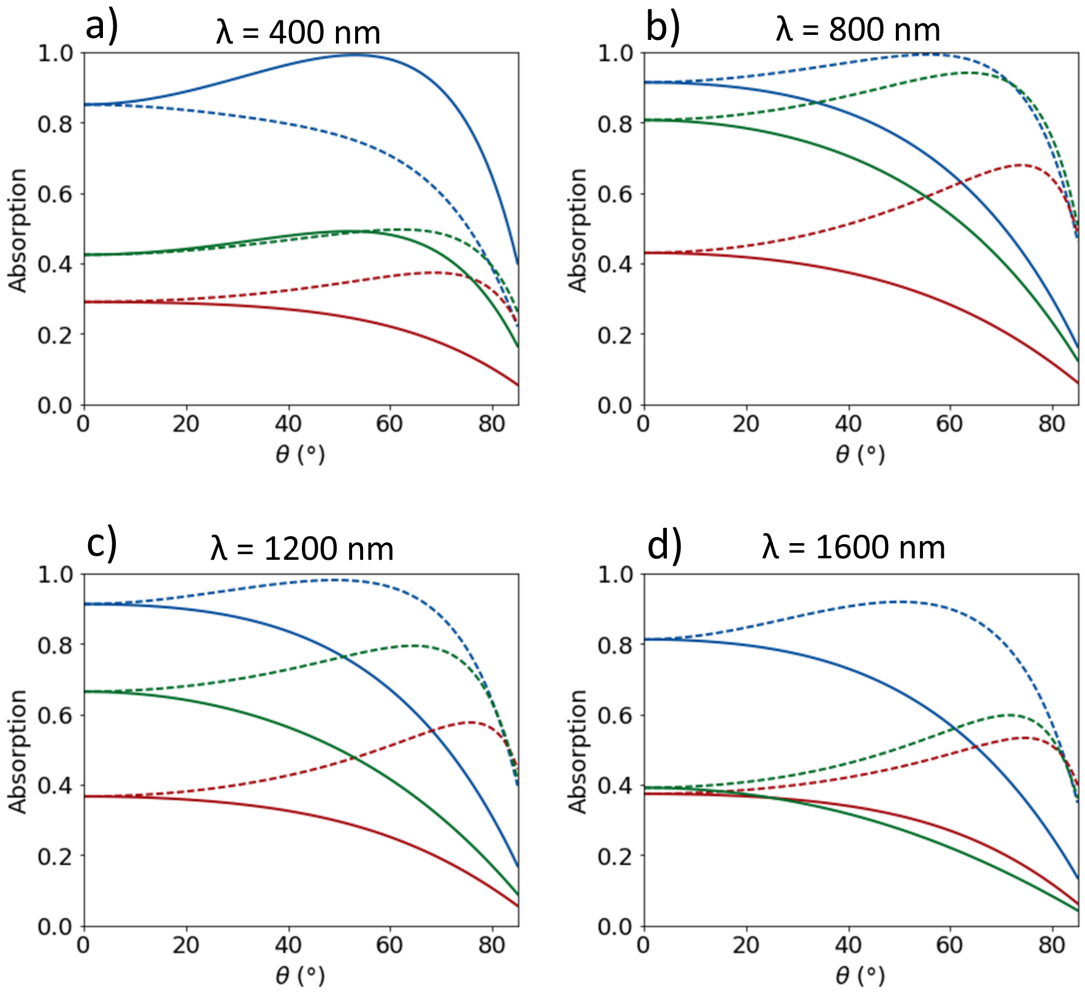

Figure 5.12: Angular dependence of absorption of device in the hydride state for different illumination wavelengths a) 400 nm, b) 800 nm, c) 1200 nm, and d) 1600 nm. Blue lines represent NZI substrates, green lines represent Au substrates, and red lines represent SiO_2 substrates. Solid (dashed) lines are TE (TM) illumination.

M-2000) and fit with a Drude-Lorentz oscillator model. Figure 5.13 shows the experimentally measured ITO optical properties. The Pd/Mg metal stack was deposited using electron-beam evaporation with a vacuum pressure of $< 3*10^{-6}$ torr (Denton Vacuum). 25 nm of Mg was deposited followed by a 3 nm Pd cap without breaking chamber vacuum. Immediately after deposition, we measured the transmission and reflection intensities of the device. Reflection measurements were

taken at 20° incident angle and transmission measurements were taken with normal illumination. Using a custom-designed environmental chamber, we then exposed the device to 1 bar of H_2 gas while dynamically measuring the transmission intensity. Once the sample had completely loaded, determined by the stabilization of the transmission intensity, we removed the sample from the transmission chamber and measured the reflection intensity. After this measurement, we remeasured the transmission intensity. This intensity spectrum exactly matched that of the in-situ measurement, showing that the sample had not had any appreciable unloading of hydrogen during the brief time outside of the environmental chamber. We repeated this process with the Pd/Mg deposited on a plain glass slide as a control sample.

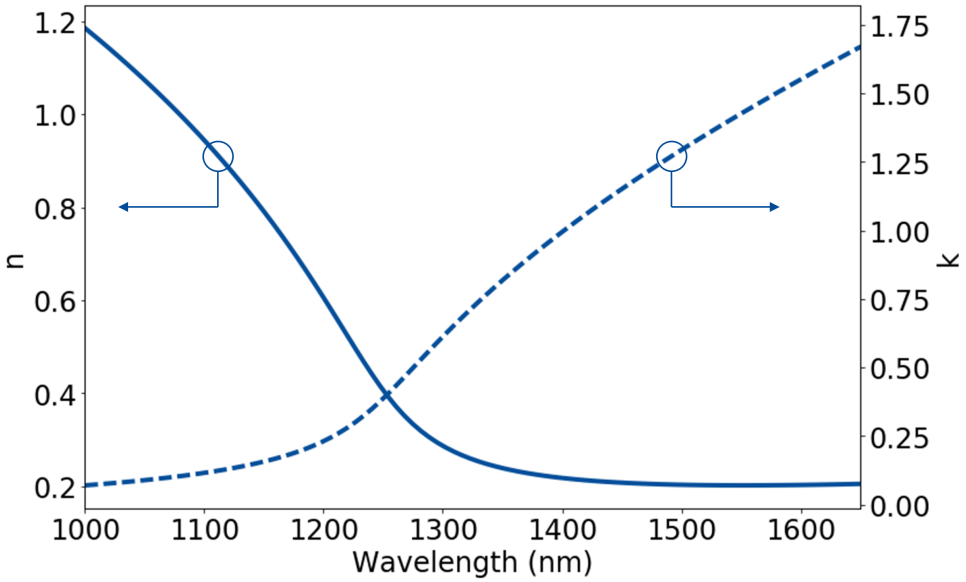

Figure 5.13: Measured optical properties of ITO used in experiments. Optical properties were determined using spectroscopic ellipsometry and fit using a Drude-Lorentz model.

The experimental absorption changes are shown in Figure 5.14 and are in good agreement with simulations. Absorption changes are calculated by using $A = 1 -$

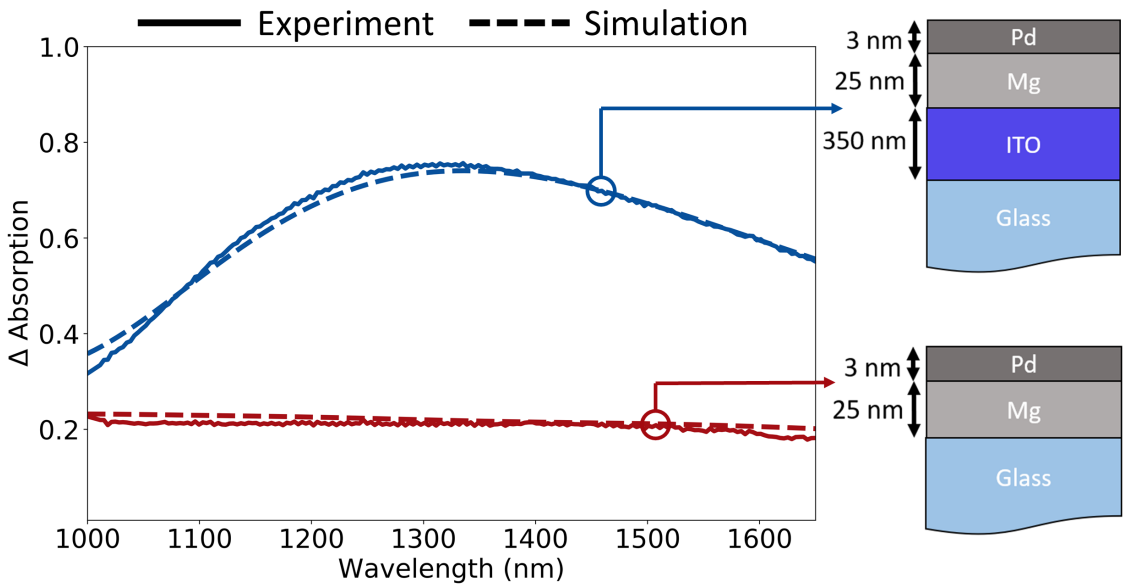

Figure 5.14: Experimental demonstration of device performance. Solid lines are experimental data, while dashed lines are simulation data. Blue lines represent the device on an ITO substrate (Top Right), while red lines are on a plain glass substrate (Bottom Right). The experimental data shows good agreement with that expected from simulations. The ITO device reaches a max absorption change of 76% at 1335 nm illumination, while the plain glass device never has an absorption change higher than 21%.

$R-T$, where A is the absorption, R the reflection intensity, and T the transmission intensity. In this formula, scattering is disregarded. This is a reasonable assumption in our experiments because the RMS roughness of our samples is < 3 nm, thus there will be negligible scattering off the surface. We compare this experimental data to transfer matrix method simulations and see strong agreement for both the ITO and glass substrates. The simulated data uses an incident angle of 20° to match the angle the reflection intensity data was taken. The experimental transmission intensity measurements were taken with normal illumination, but the difference in simulated transmission intensity of this device between normal and 20° illumination is $< 2\%$ over the reported wavelength range, so we can assume that this difference

is negligible on the scale of the effect shown. Figure 5.15 shows this simulated transmission difference.

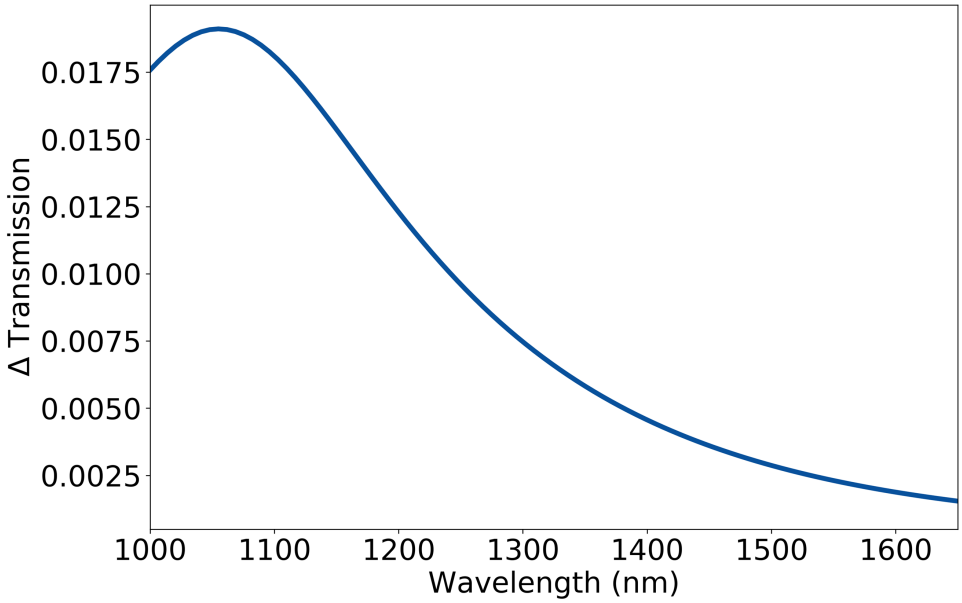

Figure 5.15: Simulated transmission intensity difference between normal and 20° illumination for the experimental device. Difference is defined as simulated transmission intensity of 20° incidence subtracted from normal incidence. At no point is this difference above 2% in the investigated wavelength range.

The ITO device resonance is maximized in the NIR at 1335 nm, near ITO's NZI resonance at 1250 nm. The device resonance is red-shifted from the NZI resonance as expected from the simulations because of the necessity of a higher k for the full absorption effect. The maximum experimental absorption change was found to be 76%, with a maximum total absorption in the hydrogenated state of 93%. This slightly outperforms the simulated maxima of 74% and 87% respectively. Reasons for this discrepancy can be attributed to the slight differences in optical properties of thin films when deposited on different substrates, or small amounts of scattering that were included in the absorption. The effect is relatively broadband, with an

absorption change $> 60\%$ from 1140 nm to 1595 nm for a bandwidth of 455 nm for this criteria. The time of loading of the sample, as determined from the dynamic transmission intensity data, was found to be 27 min (see Figure 5.16). This experimental demonstration shows the promise of this device architecture with a relative ease of fabrication.

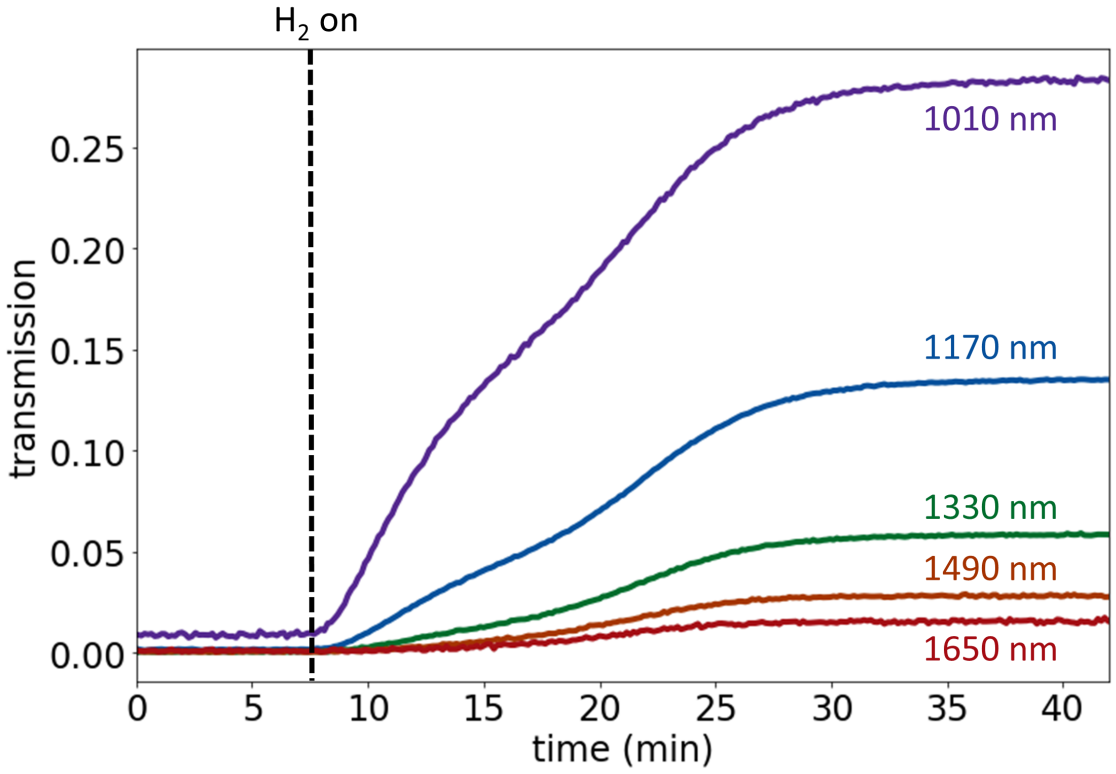

Figure 5.16: Dynamic transmission data for Mg/ITO device. Transmission intensity for Pd/Mg/ITO device taken through the device loading. Hydrogen gas was introduced to the chamber at 8 min. Transmission intensity levels off for all wavelength at 35 min, for a total loading time of 27 min.

As expected, when the metal stack is deposited on a plain glass substrate, there are no resonance effects, because the glass does not have an NZI region. There is still an absorption change in the material due to the hydrogenation of the Pd/Mg stack, but experimentally we find that it is fairly small and constant across the

near-infrared at 21%.

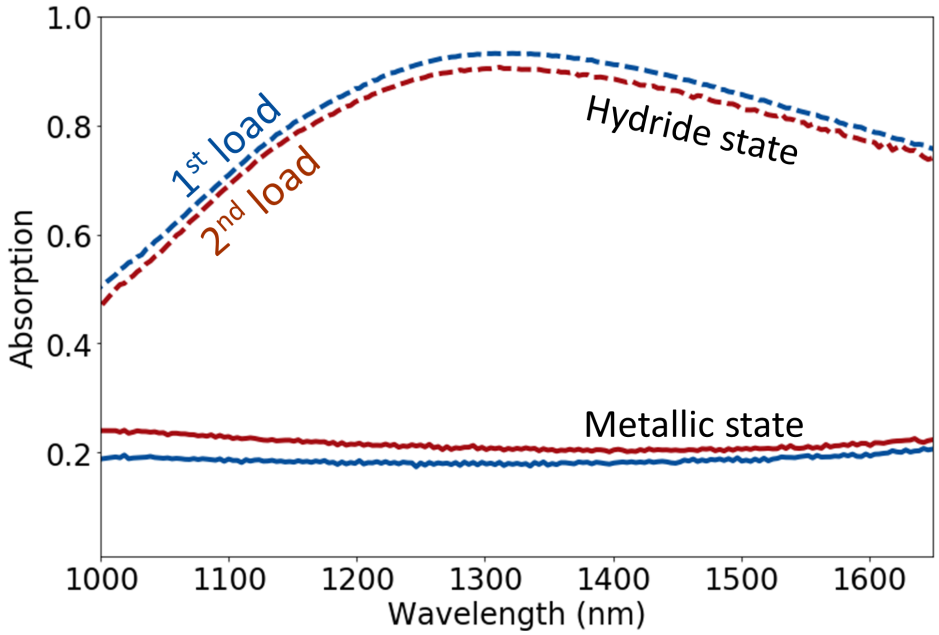

Figure 5.17: Reversibility of the Mg/ITO device switchable absorption. Solid lines are the device in the metallic state and dashed lines represent the device in the hydride state. The blue lines are the data from the original load, while the red lines indicated the second load. The data shows that the absorption change is reversible, but with a slight decrease in the magnitude of the effect on the second cycle.

Lastly, we demonstrate the reversibility of this device. To unload the MgH_2, we place the device on a hot plate at 85°C in the ambient atmosphere for 30 min. During this unloading, the device visibly turns back into a metallic state. After the unload, we retake the optical measurements and repeat the loading procedure outlined above. Figure 5.17 shows the results of this second cycle compared to the original loading. We can see that the effect is mostly reversible on the second cycle, but that the magnitude of the effect is slightly diminished. The metallic state after the unload has slightly higher absorption than the pristine metallic state, which can be attributed to dislocations formed in the Mg lattice upon the original loading.

The second loaded state still reaches a high total absorption of 91%, compared to 93% on the initial run, demonstrating that the process is reversible.

5.4 Conclusions

In summary, we have proposed and experimentally demonstrated a thin film stack of Pd/Mg can achieve switchable high absorption changes by exposure to H_2 gas. By utilizing ITO's NZI resonance in the near-infrared, our device achieves a maximum absorption change of 76%, with a maximum total absorption of 93% at 1335 nm illumination. This device has an absorbing change $> 60\%$ over a 455 nm bandwidth. This is a significant improvement when compared to a control sample consisting of a plain glass slide without the ITO layer, which only achieves an absorption change of 21% over this spectral region. We show that this process is reversible, with only a slight deprecation in total absorption change upon a second cycle. Our simulations varying the optical properties of the substrate show the potential of expanding this device to other wavelength regimes by using materials with NZI resonances in those frequency bands. We showed that this effect can create a $> 70\%$ change in absorption over a range of 650 -1230 nm incident wavelengths when being modeled as a Drude material with a plasma resonance $\lambda_p = 600$ nm and damping $\gamma < 10^{14}$ Hz, showing that this effect has the potential to be very broadband. This work shows the potential for switchable high absorption devices across different wavelength regions that exploit the NZI behavior of the substrate without affecting other aspects of the device's design. Future work will involve investigating

new substrates in these different spectral regions, as well as the potential of alloying Mg with other metals to retain this high absorption change while speeding up the dynamics and cyclability of the loading/unloading cycles.

Chapter 6: In situ Optical and Stress Characterization of Alloyed Pd_xAu_{1-x} Hydrides

In the next two chapters, we move beyond pure metal hydrides and explore improving the optical and hydrogenation properties by alloying a metal hydride with a secondary transition metal. The first of these that we investigate in this chapter is the Pd_xAu_{1-x} system. Pd_xAu_{1-x} alloys have recently shown great promise for next-generation optical hydrogen sensors due to their increased chemical durability while maintaining optical sensitivity to small amounts of H_2 gas. However, the correlation between chemical composition and the dynamic optical behavior upon hydrogenation/dehydrogenation is currently not well understood. A complete understanding of this relationship is necessary to optimize future sensors and nanophotonic devices. Here, we quantify the dynamic optical, chemical, and mechanical properties of thin-film Pd_xAu_{1-x} alloys as they are exposed to H_2 by combining in situ ellipsometry with gravimetric and stress measurements. We demonstrate the dynamic optical property dependence of the film upon hydrogenation and directly correlate it with the hydrogen content up to a maximum of 7 bar H_2. With this measurement, we find that the thin films exhibit their strongest optical sensitivity to H_2 in the near-infrared. We also discover higher hydrogen loading amounts as compared

to previous measurements for alloys with low atomic percent Pd. Specifically, a measurable optical and gravimetric hydrogen response in alloys as low as 34% Pd is found, when previous works have suggested a disappearance of this response near 55% Pd. This result suggests that differences in film stress and microstructuring play a crucial role in the sorption behavior. We directly measure the thin film stress and morphology upon hydrogenation and show that the alloys have a substantially higher relative stress change than pure Pd, with the pure Pd data point falling 0.9 GPa below the expected trend line. Finally, we use the measured optical properties to illustrate the applicability of these alloys as grating structures and as a planar physical encryption scheme, where we show significant and variable changes in reflectivity upon hydrogenation. These results lay the foundation for the composition and design of next-generation hydrogen sensors and tunable photonic devices.

6.1 Background of Pd-Au alloys

The alloying of different metals to finely tune optical and material properties has allowed for great advancements in a wide variety of applications from plasmonic sensors to catalysts [22, 23, 74, 113, 178, 179, 180, 181]. Alloying creates opportunities to improve the material characteristics beyond that of the pure metal components. Furthermore, one can combine the desirable optical and structural properties from different metals into a single alloy. This process is particularly advantageous when applied to metal hydrides where the optical properties, electric properties, and response to H_2 gas are all of interest.

Metal hydrides are useful for a wide range of applications including color displays, switchable mirrors and tunable plasmonics [14, 20, 21, 80, 115, 182, 183, 184]. Moreover, metal hydrides possess the capability to store and detect hydrogen. The opportunity to use hydrogen for energy storage and distribution is becoming more attractive, and with a push for a future hydrogen economy, more high-quality sensors are needed to mitigate the dangers of H_2 leaks. All-optical hydrogen sensors are the preferred method of detection due to the decreased risk of ignition. This is in contrast to more traditional electrical sensors, which have the potential to spark upon a device malfunction. These optical sensors are required to have fast response times, resistance to surface poisoning, limited intracycle hysteresis between hydrogen absorption and desorption cycles, and a large enough signal to be reliably read [185].

Pd has been the standard metal investigated for hydrogen sensing and storage because it is the only pure metal that can absorb and desorb hydrogen from its lattice at room temperature without an activation layer [186]. However, pure Pd suffers from slow response times, surface poisoning, and a large hysteresis [166, 187]. Alloying Pd with other metals has been shown as a solution to mitigate these problems, particularly alloying with Au [23, 74, 76, 188, 189, 190, 191]. In addition to these improved hydrogen sensing properties, Pd_xAu_{1-x} alloys have been of particular interest in improving catalysis reactions [178, 180, 192, 193, 194] as well as being used as a hydrogen separation membrane [195, 196]. A more complete characterization is essential to facilitate further use of these alloys.

In this chapter, we quantify the changes in the optical, mechanical, and chemi-

cal properties of seven different Pd_xAu_{1-x} thin films as a function of hydrogenation. These alloys are fabricated by physical vapor deposition co-sputtering at room temperature, a versatile process that allows for a wider variety of substrates for sensors that are not possible with fabrication methods that require high temperature annealing steps. We simultaneously investigate the dynamic optical properties and hydrogen loading amounts upon exposure to H_2 gas. We directly measure the optical responses with spectroscopic ellipsometry with wavelengths spanning from 225 to 1690 nm, and we identify changes in the complex refractive index upon hydrogenation. We use QCM measurements to determine the hydrogen sorption in the material and find higher loading quantities than previously reported for gas-phase loading experiments. For each hydrogen exposure, we also simultaneously measure the stress change and discover that the relative change in stress of the Pd_xAu_{1-x} alloys is 0.9 GPa higher than the change of the pure Pd. Upon investigating the correlation between this stress and the change in the surface roughness of the material, we find that despite the large amount of thin-film stress present in the alloys, there are no observed roughness changes for any of the films after loading. Finally, we computationally demonstrate the applicability of these alloys for enhancing light reflection in grating structures as well as demonstrate a scheme for physical encryption. Our research elucidates important material properties in Pd_xAu_{1-x} alloys that will further inform hydrogen sensor design and implementation.

6.2 Experimental methods

6.2.1 Fabrication and characterization of Pd_xAu_{1-x} thin films

The thin film Pd_xAu_{1-x} alloys are fabricated by room temperature physical vapor deposition cosputtering with Pd (99.95%) and Au (99.99%) sputtering targets. A Si chip with a lithographically defined 1 x 1 cm^2 area and two separate AT-cut 5 MHz QCMs were included as substrates for each deposition run. The film geometry on the QCMs was defined by a 12.5 mm diameter circular shadow mask centered on the top QCM electrode. The substrates were cleaned with acetone, methanol, and isopropyl alcohol rinses prior to deposition (the lithographic defining of the Si piece was performed after the solvent clean). Prior to Pd_xAu_{1-x} deposition, the base pressure in the main chamber was maintained at less than 1.8×10^{-8} Torr. The thin-film alloys were deposited at room temperature, with Ar gas introduced and adjusted to a 10 mTorr pressure. During deposition, a constant rotation of 20 rpm, a z-height of 100 mm, and a gun tilt of 7.5 mm were applied to ensure uniform chemical composition across each sample. Direct current powers ranging from 75 to 300 W were applied to alter the Pd_xAu_{1-x} composition. Two sets of samples were produced for these experiments. The first set was $\sim$100 nm thick and was deposited directly onto the substrates. The second set was $\sim$400 nm thick with a 10 nm Cr adhesion layer that was sputtered onto the substrates before the alloy deposition without breaking vacuum. The Cr was deposited with a 150 W RF source instead of a standard DC source because the only DC sources available in

the system were connected to the Au and Pd targets. The composition of each alloy was measured with energy-dispersive X-ray spectroscopy (EDX). For each sample on a Si substrate, EDX measurements were taken on four separate points to ensure uniformity. The raw EDX data is shown in Figure 6.1. The first set of depositions had the compositional fractions (Pd_xAu_{1-x}) of x = 0, 0.14, 0.34, 0.42, 0.52, 0.73, 1. For the second batch (∼400 nm thick with the Cr adhesion layer), we focused on higher Pd content samples, having the compositions x = 0.41, 0.59, 0.73, 0.77, 0.83, 0.88, 1.

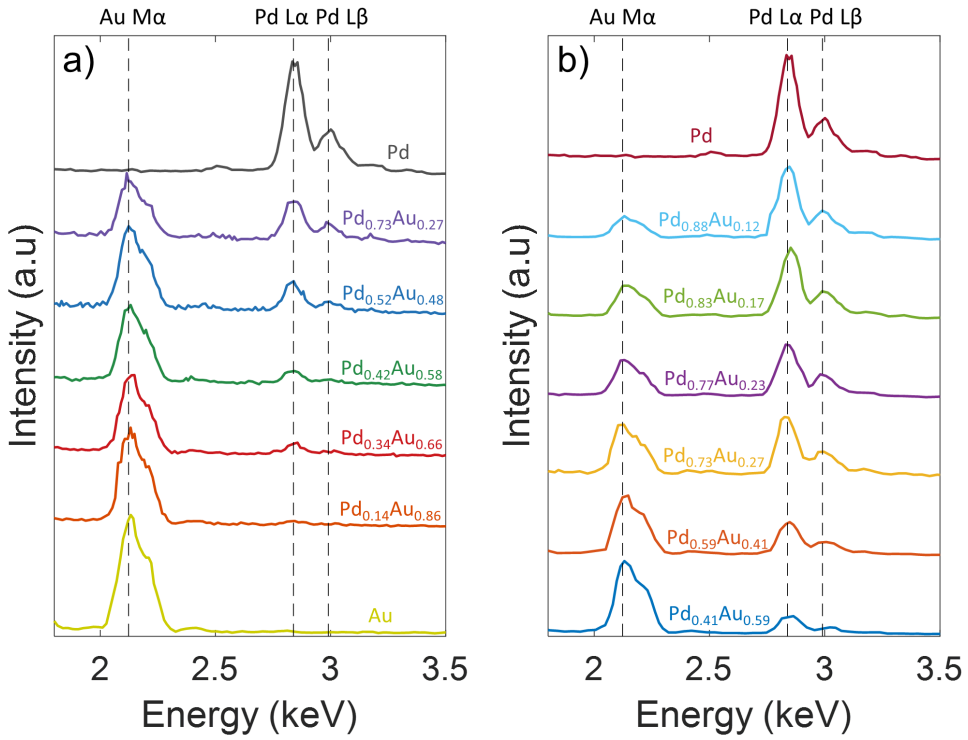

Figure 6.1: Measured EDX spectra of fabricated Pd_xAu_{1-x} alloys. a) Spectra for the 100 nm samples with x = 1, 0.73, 0.52, 0.42, 0.34, 0.14, 0 and b) for the 400 nm samples with x = 1, 0.88, 0.83, 0.77, 0.73, 0.59, 0.41. Known emission lines for Pd and Au marked with vertical dashed lines.

Film thickness and roughness measurements were taken with an AFM in an unpressurized dry air atmosphere. The roughness measurement was taken on three

distinct 2 x 2 μm^2 patches on each of the alloys. The reported roughnesses in this article are all RMS roughnesses and are calculated by taking the RMS value of each line of the AFM image and taking the median of these values. The film thickness measurements were taken on the lithographically defined Si samples. 20 x 20 μm^2 scans were taken centered on the defined edge of the metal square. The step results in a bi-modal Gaussian distribution for the histogram of the topography data. The sample height was taken as the difference in the mean of the two Gaussians. ICP-OES was used to confirm both the sample thicknesses and the chemical composition for each of the alloys. The Si squares were dissolved in boiling aqua regia and subsequently diluted to 50 mL. ICP-OES was then used to find the Pd and Au concentrations of this solution. Using the known surface area of the alloy on the Si sample, the atomic masses, and the densities of these materials, the thickness and atomic percentage of the alloys can be calculated. These calculated values agreed within the error of the results of the EDX and AFM measurements.

6.2.2 Optical property measurements

Optical property measurements were taken with a spectroscopic ellipsometer in a custom environmental chamber described in Chapter 2 and demonstrated in Chapter 3. The QCM frequency is simultaneously recorded with the optical data to correlate the hydrogen content of the sample with the optical property changes. Measurements for each alloy are made at four different angles (48°, 55°, 70°, 75°) for the pristine metal alloy before hydrogenation. The dynamic optical properties of

the alloys were then taken at 75° as the environmental chamber was switched from 7 bar Ar to 7 bar of H_2. The 75°orientation is chosen for the dynamic measurements due to steeper incident angles having a higher sensitivity to optical changes. The measurements in the hydrogenated state were then retaken at all four angles at the end of this process. The chamber was then purged with Ar with the dynamic data being recorded again at 75°. This process was repeated for a total of four hydrogen absorption steps and three desorption steps for each alloy. See Chapter 2 for further details of the ellipsometric measurement, window compensation of the environmental chamber, and the dynamic optical fitting method [164].

6.2.3 Hydrogen loading and stress measurements

The hydrogen loading and stress measurements were taken in a separate environmental chamber equipped with an interferometer using the metal alloy films on the QCM as one of the mirrors. The loading value for each alloy is calculated with the method outlined in Chapter 2 [95], which compensates the total QCM frequency change with effects from stress along with environmental effects, such as changes in gas composition.

Because the QCM substrates used in our experiments are anisotropic, the standard way of determining thin-film stress using the Stoney equation is not applicable [197]. The stress values reported in this article use an adapted method from EerNisse's double resonator model [46]. Instead of using two separate cuts of QCMs, we measure the curvature of the sample and use the curvature to frequency relation

detailed in Chapter 2 [95] to find the change in QCM frequency due to stress in the sample. The change in stress of the thin film upon hydrogenation is then

$$\Delta\sigma = \frac{\Delta f_s \tau_q}{K^{AT} \tau_f f_0} \tag{6.1}$$

where Δf_s is the change of QCM frequency due to stress, τ_q and τ_f are the thicknesses of the quartz of the QCM and the metal film respectively, f_0 is the measured QCM frequency before hydrogenation, and K^{AT} is a constant defined by EerNisse to be -2.75 x 10^{-12} cm^2/dyn for a 5 MHz AT-cut QCM [46]. Using this method, we assume that the stress is isotropic through the thickness of the film. All stresses reported in this article are compressive stresses and are defined to be positive.

6.3 Dynamic optical property measurements of Pd_xAu_{1-x} alloys

Figure 6.2 shows the optical properties for the seven different 100 nm alloys investigated in this study as well as their property change upon hydrogenation in 7 bar H_2 for the wavelength range of 225 – 1690 nm. Because metal hydrides typically have significant dislocation formation with initial loading, the data shown here are for the second hydrogenation of the alloys. Thus, the plots describe a typical loading cycle. We show the data of the initial loading of the pristine alloys Figure 6.3, and show the dielectric functions for both the first and second loads in Figure 6.4. To verify our optical fitting model for these materials, we compare our measurements to the Johnson and Christy values reported for Au and Pd, which can be found in Fig-

ure 6.5, [104, 174] and found agreement. The non-hydrogenated optical properties of Pd_xAu_{1-x} alloys have previously been inferred with modeled electron energy loss spectroscopy (EELS) data acquired on individual nanoparticles in the range of 248 - 827 nm [198] as well as with reflection and transmission measurements for a single $Pd_{50}Au_{50}$ thin film alloy in the range of 350 - 1050 nm [199]. However, the optical properties have not been directly measured with spectroscopic ellipsometry and have not been measured deeply into the NIR region. Furthermore, the optical property dependence of these alloys upon hydrogenation has not yet been investigated, which we present here.

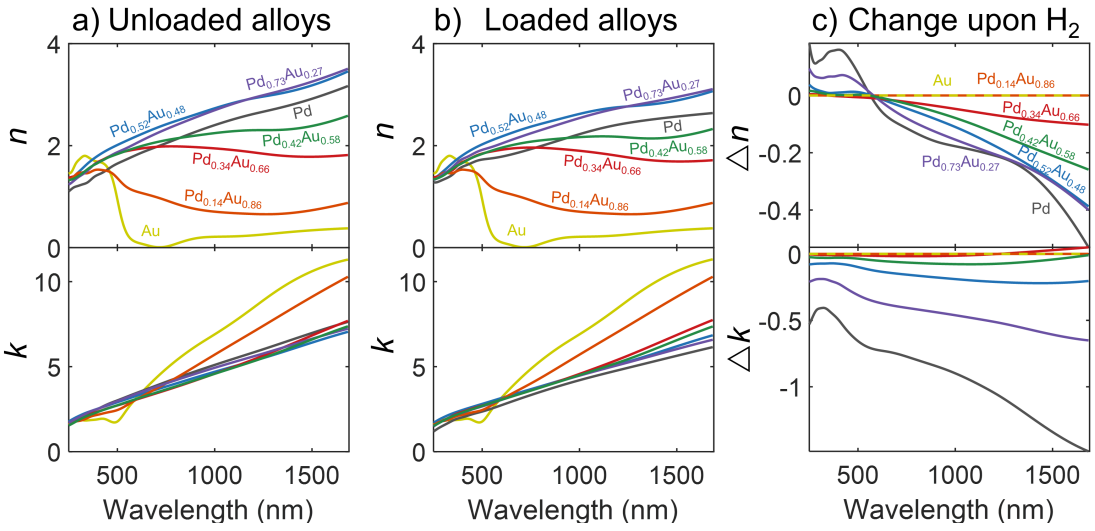

Figure 6.2: Measured optical properties of seven different Pd_xAu_{1-x} alloys. (a) Optical properties of each alloy without any hydrogen in the lattice (unloaded). (b) Optical properties of the hydrogenated alloys under an atmosphere of 7 bar of H_2. (c) Change in the optical properties for each alloy upon hydrogenation. Change is defined by the optical properties of the hydride subtracted from the optical properties of the unloaded metal.

We observe a wide range of refractive indices ($\tilde{n} = n + ik$) for the alloys as we adjust the chemical composition from pure Au to pure Pd. For the imaginary part

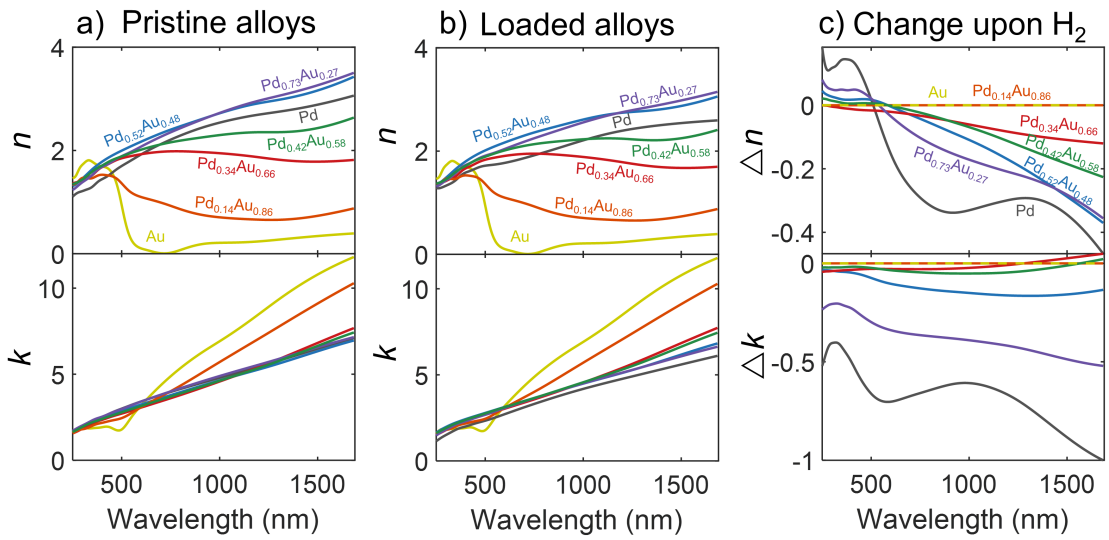

Figure 6.3: Measured optical properties of seven different Pd_xAu_{1-x} alloys for the first load of the material. The initial loading of the metals generally causes for singificant dislocation formation in the metal lattice, causing for these changes to not describe a typical loadig cycle. (a) Optical properties of each alloy without any hydrogen in the lattice (unloaded). (b) Optical properties of the hydrogenated alloys under an atmosphere of 7 bar of H_2. (c) Change in the optical properties for each alloy upon hydrogenation. Change is defined by the optical properties of the hydride subtracted from the optical properties of the unloaded metal.

of the index (k), we find that that the five alloys with the highest atomic percent Pd have similar values and trends, with the pure Au and $Pd_{0.14}Au_{0.86}$ exhibiting higher values. This is consistent with visual observation, where the five highest Pd content alloys all appear to have the same reflective grey color, with the $Pd_{0.14}Au_{0.86}$ being the only alloy with a yellow hue approaching the appearance of the Au. An interesting trend is observed in the real part of the index (n), where one may expect the intermediate alloys to monotonically increase in n from the lower Au values to the higher Pd values as the Pd composition is increased. Instead, both the $Pd_{0.52}Au_{0.48}$ and the $Pd_{0.73}Au_{0.27}$ alloys have a higher n than that of pure Pd across the entire wavelength range investigated. The nonlinearity of the optical properties

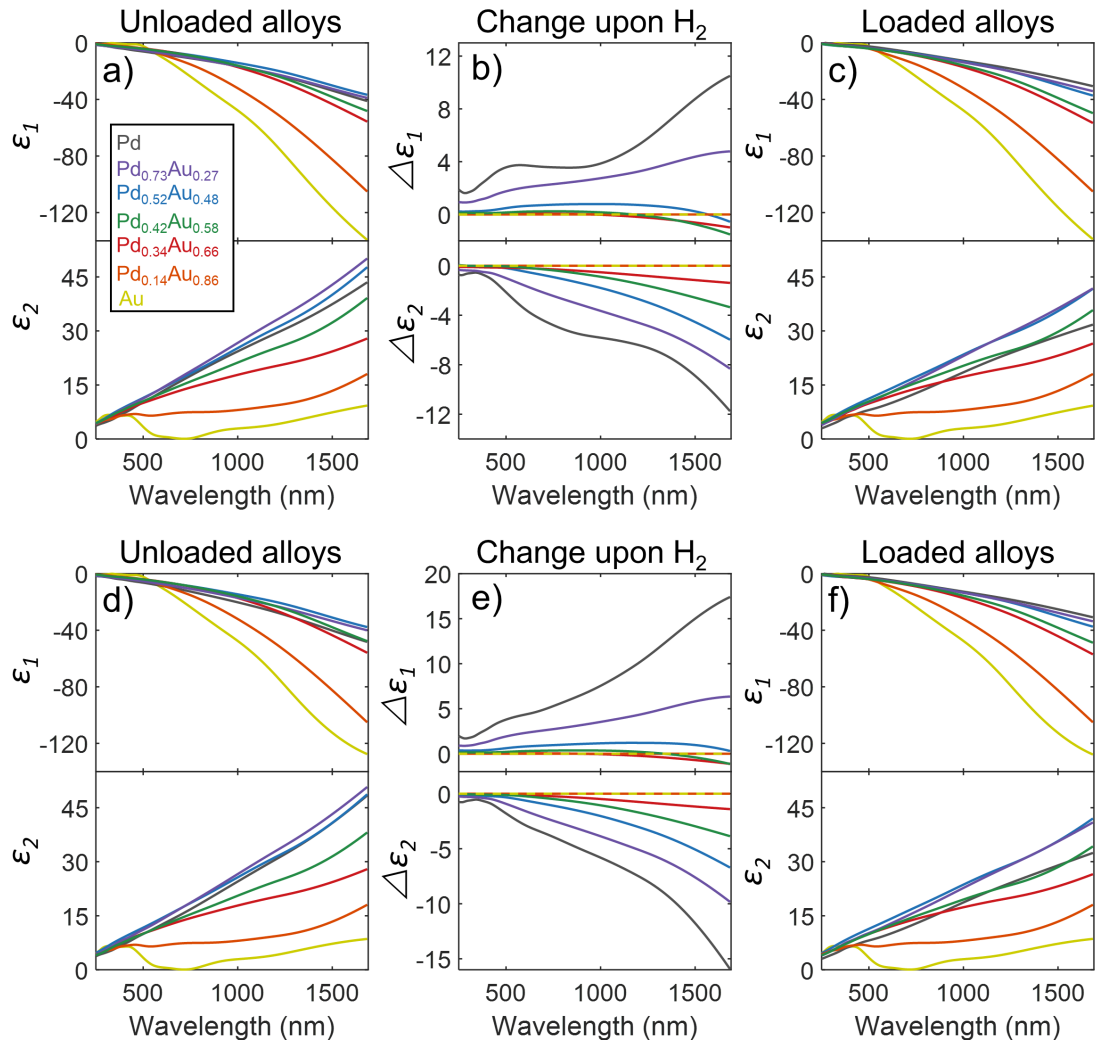

Figure 6.4: Change in dielectric functions upon hydrogenation. a-c) Dielectric functions and dielectric function change for the initial hydrogen exposure. d-f) Dielectric functions and dielectric function change for the second load of the alloys. Dielectric function change defined as the dielectric function of the hydride subtracted from the dielectric function of the metal.

with composition is not unique to the Pd_xAu_{1-x} system, but is also present in the properties of other noble metal alloys [181]. The addition of Pd to Pd-Au results in a nonmonotonic and dramatic increase of the valence band at the Γ point [178]. The additional electronic states below the Fermi level resulting from the break in degeneracy of the band structure are likely responsible for extra interband transitions

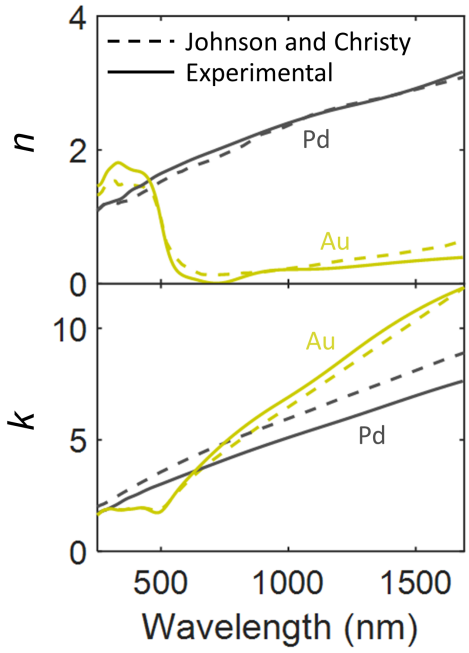

Figure 6.5: Comparison of modeled Pd and Au optical data with literature. Johnson and Christy data [104, 174] for pure Au and pure Pd plotted in dashed lines show good agreement with our measured values of Au and Pd recorded in our experiment, showing the validity of our model.

in these alloys and, ultimately, to the higher values of n observed.

Upon hydrogenation, pure Pd has the largest optical change in both n and k, as expected. The magnitude of the change decreases as the Pd content in the alloys is decreased. The x = 0.34 sample is the smallest atomic percent Pd in an alloy that we observe a measurable optical change, showing a slight decrease in n, but very little change in k. For both the Au and $Pd_{0.14}Au_{0.86}$ we observe no measurable response when H_2 is introduced to the system. For the pure Pd, the addition of H_2 causes a decrease in k across all wavelengths investigated, a decrease in n for wavelengths above 565 nm and an increase below 565 nm, which agrees with literature [86, 164]. These trends are all observed in the next three highest Pd content alloys. The zero change intercepts in the real part of the index occur between 550 – 580 nm for Pd

and the next three highest Pd composition alloys. The results also demonstrate that for all alloys (and the pure Pd film), the largest response to hydrogenation occurs in the NIR region of the electromagnetic spectrum. This higher response at longer wavelengths has been observed with other nanostructures and metal hydrides [23, 164, 189]. By shifting to longer detection wavelengths, Pd_xAu_{1-x} alloys with lower x become more detectable because of their increase in responsivity. This allows for the use of higher Au concentration alloys as sensors with their increase in anti-hysteresis and anti-poisoning benefits. For the full time-dynamic changes of the optical properties, see Figure 6.6.

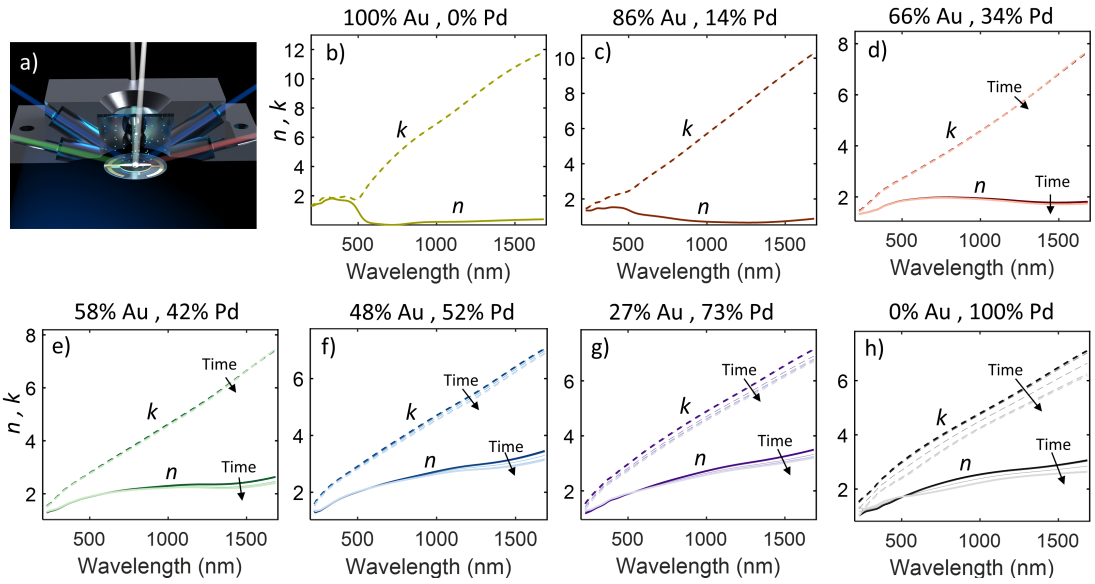

Figure 6.6: Dynamic optical properties of Pd_xAu_{1-x} alloys upon hydrogenation. a) Image depicting ellipsometry apparatus setup. b-h) Dynamic optical properties of the seven 100 nm alloys upon exposure to H_2. Line color gets lighter as time increases (and partial pressure of H_2 rises in the chamber. n plotted in solid lines and k plotted in dashed lines.

In addition to the optical properties, the amount of hydrogen in the metal lattice was simultaneously monitored. Figure 6.7 shows the dynamic behavior of

the refractive index versus hydrogen loading. We specify the amount of hydrogen by H/M, which is the number of hydrogen atoms per metal atom in the lattice (including both Pd and Au). Figure 6.7 excludes the pure Au and $Pd_{0.14}Au_{0.86}$ alloy because they have no measurable reaction with H_2 either optically or gravimetrically. All other alloys share similar dynamic relationships. Each alloy has a monotonic change in optical properties with respect to loading, with the largest changes occurring in the near-infrared. For the relationship of n and k at 1500 nm with the Pd composition of the alloy and the final H/M ratio, see Figure 6.8. The change in optical response is nearly linear with loading for each of the alloys, with the Pd film appearing to have an inflection point around H/M $\approx$ 0.25. This behavior could be attributed to the α to β phase transition in the Pd that does not occur in the lower Pd content alloys [200].

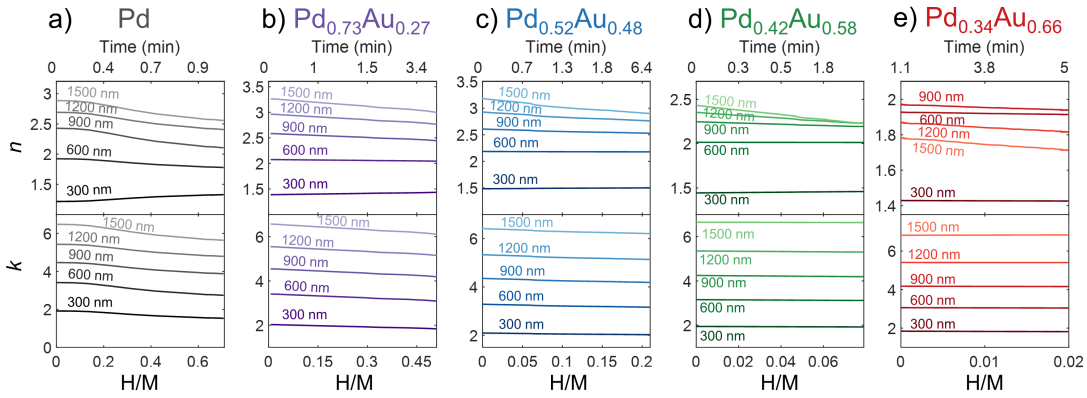

Figure 6.7: Optical response versus hydrogen loading. (a-e) Relationship of the optical properties (n and k) with the hydrogen content for each of the five alloys that have an interaction with H_2. Note that the top time axis has nonlinear spacing with each top tick corresponding to the time that the alloy reached the stated H/M amount. Time = 0 min is defined as the time that hydrogen is first introduced into the system.

We next consider the repeatability of the optical and gravimetric responses

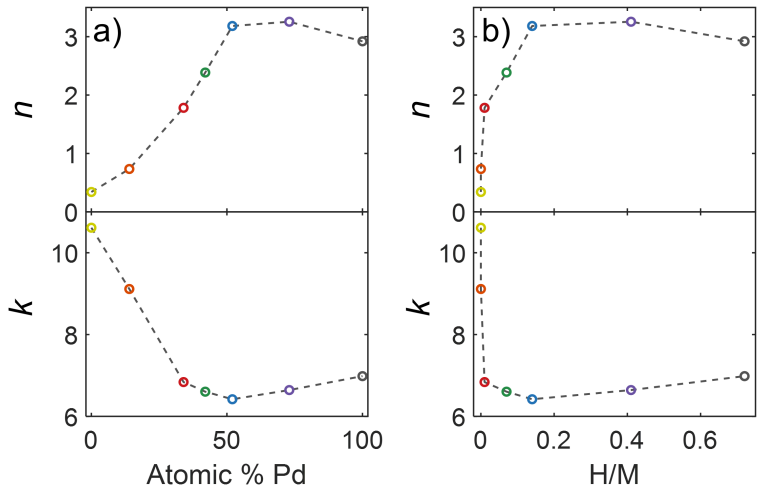

Figure 6.8: Relationship of n and k at 1500 nm illumination with (a) the atomic percent Pd of the alloy and (b) with the final hydrogen to metal atom ratio in the lattice at 7 bar H_2. The grey dashed line directly connects the points and is meant as visual guide to the reader.

upon hydrogen cycling, which is essential for any practical device. Figure 6.9a-e depicts the changes in n and k for the five 100 nm-thick alloys that react with H_2 for their second through fourth H_2 exposures. As stated above, the first hydrogenation causes a slightly different optical response than the subsequent loads due to lattice defects and dislocations as it first expands [12]. After this initial disturbance, the subsequent loads cause much less degradation of the lattice, allowing for more consistent results. For subsequent exposures (after the first), the response is very consistent for Pd as well as the alloys. Figure 6.9f shows the maximum hydrogen content at 7 bar H_2, where the amount of hydrogen in the lattice is also very consistent from load to load after the initial exposure. As expected, these results imply that any device based on Pd_xAu_{1-x} should still be pretreated with H_2 before any attempted operation. Overall, the alloys provide more consistent optical changes than the pure Pd because less hydrogen enters the lattice, causing fewer dislocations.

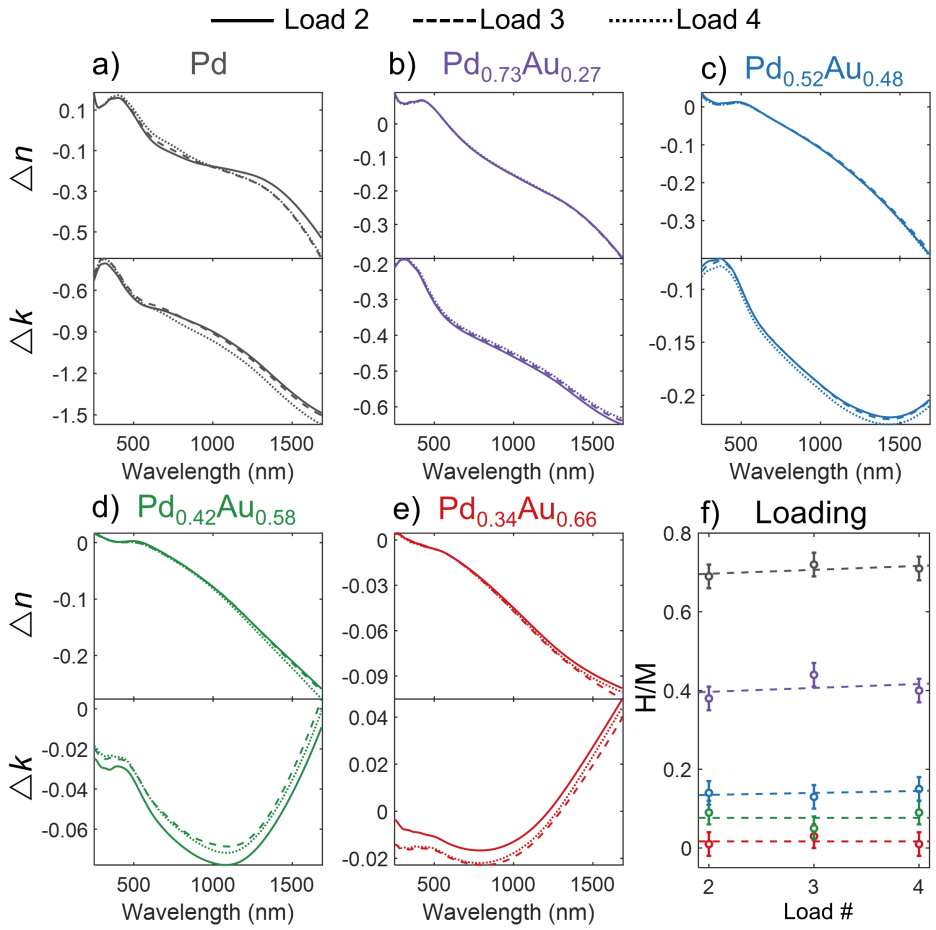

Figure 6.9: Hydrogen cycling properties of alloys. (a-e) Comparison of the change in optical properties for each of the five alloys that interact with hydrogen. n and k are plotted for the second through fourth loads with the first load excluded. n and k are defined by the optical properties of the current hydride state subtracted from the values of the previously unloaded state. (f) Calculated hydrogen loading values for the second through fourth loads. Dashed lines are linear fits for each alloy. Alloy colors match those shown in a-e with the highest (lowest) H/M ratio corresponding to Pd ($Pd_{0.34}Au_{0.66}$).

6.4 Material property measurements

To determine the exact amount of hydrogen absorbed into the metal lattice, we used a separate QCM sample in an environmental chamber that accounts for extraneous effects from stress and environmental (gas composition, pressure, tem-

perature, etc.) changes. Figure 6.10 shows the relationship of the hydrogen content of the alloys at 7 bar H_2 with the atomic percent Pd in the alloy. We can see from these measurements that the relationship follows a linear fit, as previously described in the literature [188, 189]. We recorded the H/M ratio versus concentration for both the 100 nm thin films without any adhesion layer between the alloy and the Au QCM substrate and the 400 nm films with a 10 nm Cr layer between the substrate and the alloy. Both of these sets of samples follow similar linear relations within error bars. At 7 bar, our pure Pd samples had a hydrogen content of $H/M = 0.72 \pm 0.03$ and $H/M = 0.69 \pm 0.03$ for the 100 nm and 400 nm samples respectively, which are in good agreement with previous values found in literature [11, 57, 58]. Compared to previous gas-phase measurements on thin films, we have found higher hydrogen loading values for the alloys, especially for the lower Pd content alloys [188]. While previous measurements suggested no hydrogen reaction below $x \approx 0.55$ in Pd_xAu_{1-x}, we record measurable amounts of hydrogen entering the lattice down to $x = 0.34$ with a H/M value of 0.02 ± 0.01. Reasons for this higher measured loading could be contributed to different fabrication conditions of the alloys or different amounts of initial thin film stresses due to the film thickness, substrate, or the circular geometry of the film. These different intrinsic stresses can have a large effect on the material properties of the thin film system and should be characterized for each new experimental procedure.

We also performed the experiments at 0.25 bar H_2 at 1 bar of total pressure to test the effects of driving potential on the total loading amount, shown in Figure 6.11. These values are slightly lower than those taken at 7 bar, as expected due to

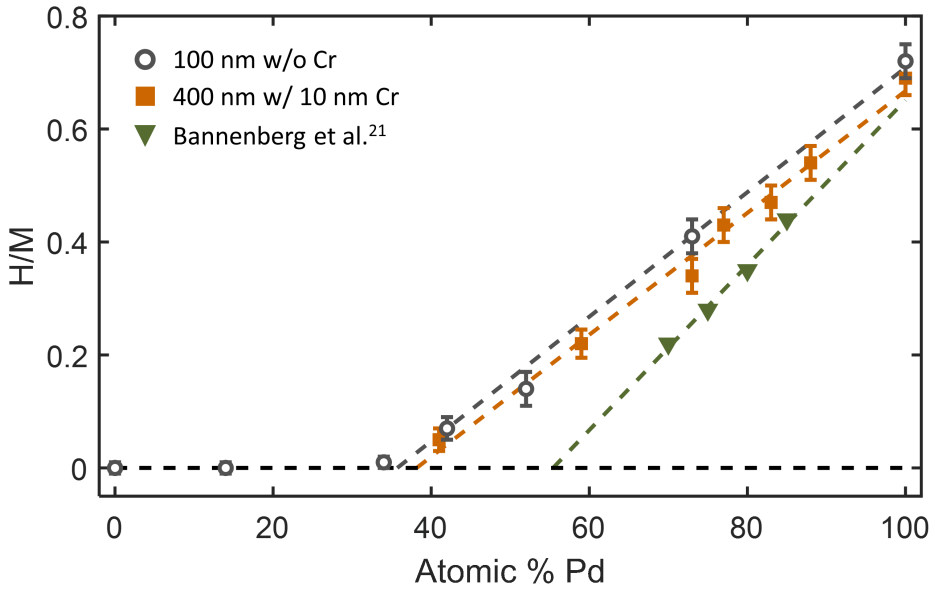

Figure 6.10: Total sorption data. The grey circles correspond to the 100 nm Pd_xAu_{1-x} alloy data. The grey dashed line is a linear fit of the five alloys that react with hydrogen. The solid orange squares correspond to 400 nm films that have a 10 nm Cr adhesion layer, and the orange dashed line refers to the linear fit. The measured values are compared to prior experiments from Bannenberg et al.[188] on 40 nm thick thin films at 10 bar H_2 partial pressure (green triangles and fit with green dashed line). The black dashed line is to guide the eye to the zero loading point.

the smaller driving potential of hydrogen in the lattice, but the same higher than previously observed loading trend with a shallower slope when compared to atomic Pd percent is still clearly present at these lower pressures. In the literature, gas-phase loading experiments have also been performed on Pd_xAu_{1-x} nanoparticles, which exhibit a loading curve with a similar slope but lower overall values than the thin films [188, 189]. Electrochemical loading experiments have also been performed on these alloys in the bulk with differing results, suggesting a range of potential mechanisms may be at play for these different samples [201, 202].

With these unexpectedly higher loading values, we suspect that differences

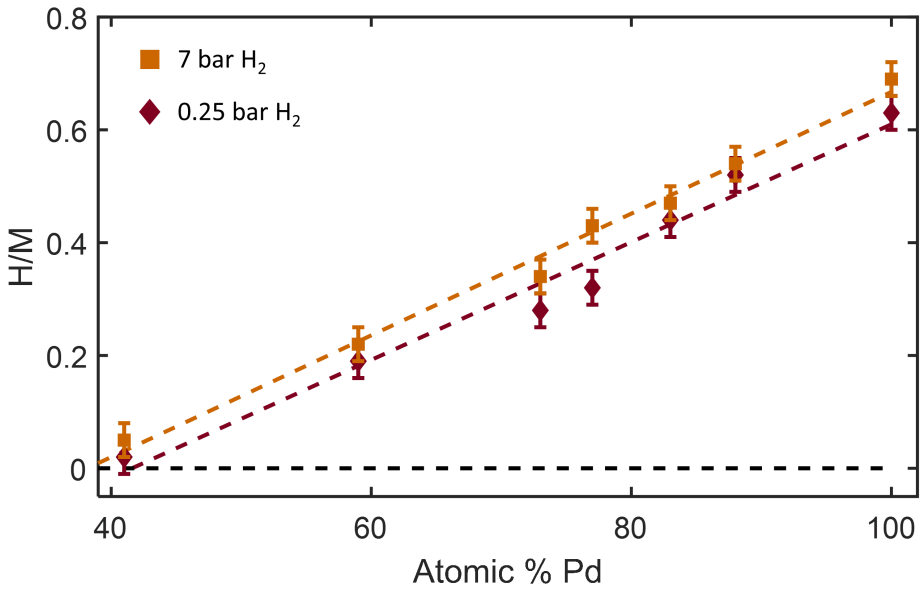

Figure 6.11: Comparison of total hydrogen content per metal atom at different hydrogen partial pressures. The ratio at 7 bar (orange squares) is slightly higher than that recorded at 0.25 bar (red diamonds). Even at lower pressures we have measurable loading down to alloys with 40 atomic percent Pd.

in film stress and microstructuring could be the cause. When thin metal films are hydrogenated, they undergo a compressive strain as the metal lattice expands to incorporate the hydrogen [12, 203, 204, 205]. This strain can affect how much hydrogen can be absorbed into the lattice and can have a significant impact on the sorption kinetics [57, 167, 206, 207, 208, 209]. Because of this effect, we investigated the amount of stress change upon hydrogenation for each of our films.

To determine the stress in our films, we measure the change in the curvature of the substrate (due to film stress) and then convert this curvature to stress using Equation 7.1 with inputs from the simultaneous QCM data. Figure 6.12a shows the raw curvature changes of the 100 nm and 400 nm alloy samples. The 400 nm samples clearly have a much higher curvature change than the 100 nm samples, as

we would expect due to there being a larger affected film mass to distribute the stress to the QCM. Once we convert this change in curvature into a change in stress (Figure 6.12b), we find that both the 100 nm and 400 nm samples have a similar relation between stress and hydrogen content.

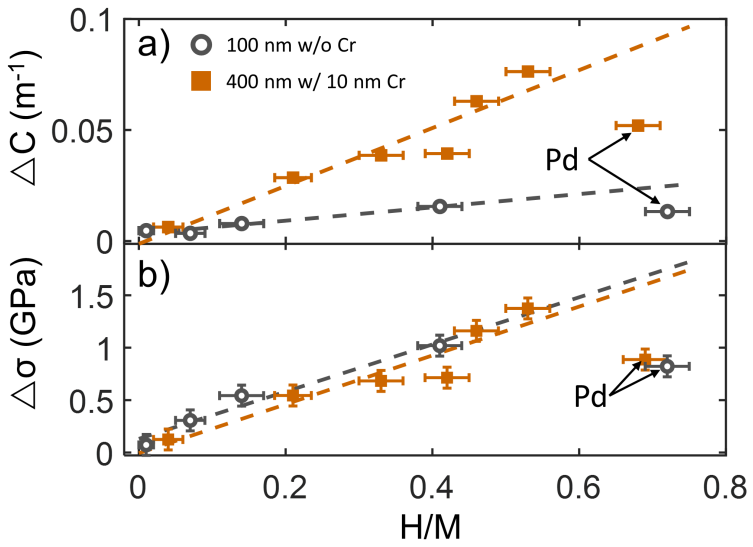

Figure 6.12: Stress characterization of Pd_xAu_{1-x} alloys. (a) Raw data of curvature change and (b) calculated stress values upon hydrogenation of each alloy versus the calculated final hydrogen per metal value under 7 bar H_2. For each plot, the grey dashed line is a linear fit of the 100 nm data (grey circles) and the orange dashed line is a linear fit of the 400 nm data (orange squares), with each linear fit excluding the pure Pd data points. The vertical error bars for the curvature in (a) are smaller than the marker size.

An interesting observation from this stress relation is that neither the 100 nm nor the 400 nm pure Pd samples fall upon the trend of the alloys (the Pd data points are excluded in the linear fits of each plot). The Pd values fall a full 0.9 GPa below the expected trend line of the stress of the alloys. An explanation for this difference could be attributed to the alloys having higher initial stresses than the pure Pd due to the intrinsic strain of alloying. By starting at a higher amount of initial stress,

the increase of stress per hydrogen atom is enhanced. This would cause the alloys to have a different response to hydrogen due to the different strains in the structure. This effect is an important factor in the design of future devices using Pd_xAu_{1-x} because unaccounted for stress could have deleterious effects on device performance. It is important to fully characterize the stress system down to the exact substrate and deposition temperatures, otherwise there may be different material responses in the system, such as the higher than expected loading observed in this work. See Figure 6.13 for the relationship of stress and Pd alloy composition.

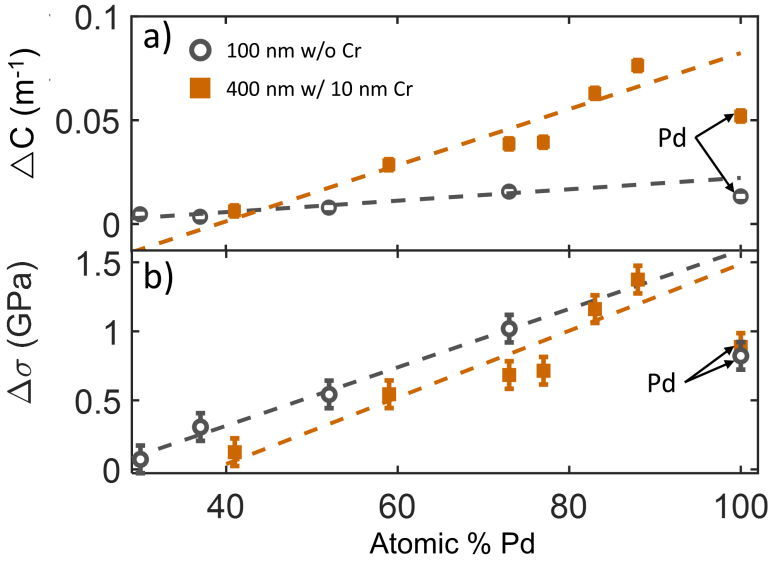

Figure 6.13: Stress dependence on atomic Pd %. The orange squares are 400 nm thick samples with a 10 nm Cr adhesion layer with the orange dashed line a linear fit of the data. The grey circles are 100 nm samples with no adhesion layer with the grey dashed line a linear fit of the data. In each plot, the pure Pd data points are excluded from the linear fits. a) Raw curvature data for each of the alloys upon hydrogenation. b) Calculated change in stress of the alloy thin films upon hydrogenation.

With these high film stresses present in the materials upon hydrogenation, we expect to see measurable changes in the surface morphology. We performed AFM

scans on the alloys immediately after fabrication (i.e. before H_2 introduction), after an initial H_2 exposure, and again after a second exposure. We expect an initial increase in the surface roughness of the films after the initial hydrogenation due to the hydrogen forming dislocations and vacancies in the lattice followed by lesser changes in roughness on subsequent cycles. Instead, we found that the H_2 exposures had no measurable effect on the surface roughness of any of the films, as seen in Figure 6.14. We measured Pd and $Pd_{0.73}Au_{0.27}$ films for the 100 nm samples without a Cr adhesion layer and for 400 nm samples with a 10 nm Cr layer. Both sets of samples were measured on the Au QCM electrode (initial electrode RMS roughness was 1.8 nm). We also evaporated, in contrast to the sputtered samples above, a 100 nm Pd film with a 5 nm Cr adhesion layer (required to prevent delamination) to test if the roughness change was dependent on the fabrication conditions for the thin films.

Both the distribution and RMS values of the roughness remain very consistent for all sample variations (sputtering vs. e-beam evaporation, 100 nm vs. 400 nm films, Cr adhesion layer vs. no adhesion layer). Figure 6.14a-e shows histograms of the topography data for all three scans of each material. The results are so consistent that it is difficult to distinguish between each histogram. Figure 6.14f-j shows the measured RMS roughnesses and Figure 6.14k-o shows the pristine metal topography image before the film was exposed to H_2. Figure 6.15 shows each separate histogram and the corresponding topography scan. The consistency of these roughness measurements is surprising due to pure Pd having a 12% volume increase upon hydrogenation, and $Pd_{0.73}Au_{0.27}$ having an expected 9% volume increase [12]. Note

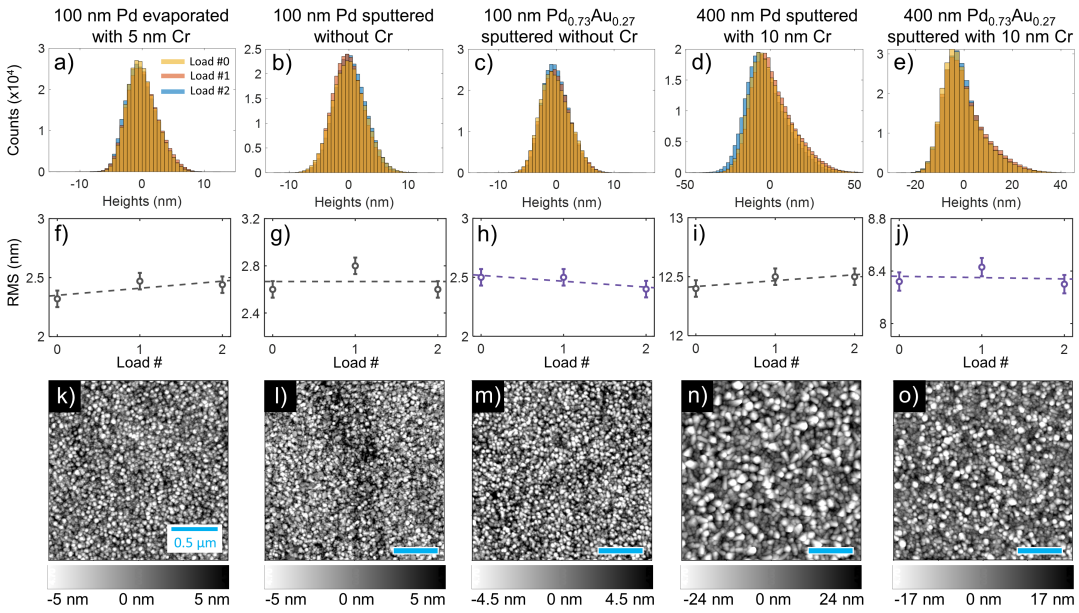

Figure 6.14: Pd_xAu_{1-x} thin film morphology characterization. (a-e) Histograms for each material before hydrogenation (yellow), after the first hydrogen load (red), and after the second hydrogen load (blue). Note: histograms for first and second loadings are barely visible due to similarities with the values obtained before loading. (f-j) Calculated RMS roughness values for each load. Dashed lines are a linear fit to the data showing no significant change upon each loading cycle. (k-o) Representative AFM topography scans of the alloys before any H_2 has been introduced.

that these measurements are not able to detect any vertical thickness changes, as the height set point is reset before each measurement. We do not see any difference in roughness change between the materials that are adhered directly to the QCM versus with the Cr adhesion layer, showing that in this case, the strength of the adhesion does not contribute to any roughness modification in this setup. A complete list of the measured RMS roughnesses for each of the other alloys can be found in Table 6.1. The data also suggest that the surface roughness of the film has no effect on the final loading amount in films of these thicknesses, as is expected. The 400 nm sputtered samples have significantly higher roughnesses than the others, yet all three Pd samples have the same total loading numbers within error bars. Similarly, the

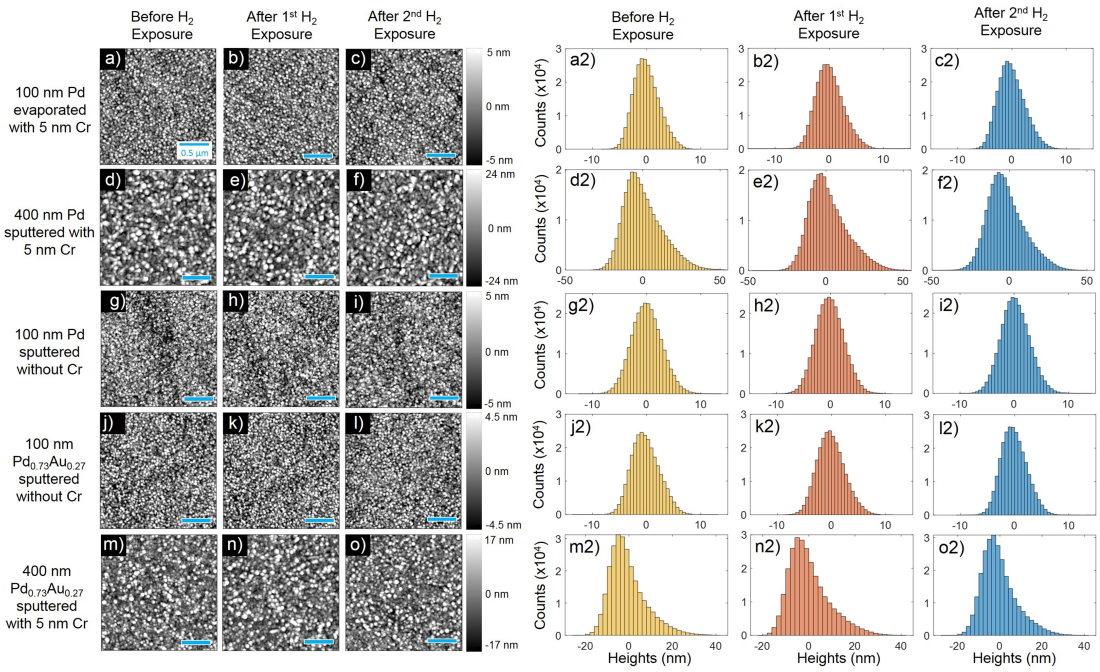

Figure 6.15: Roughness scans upon hydrogenation for five Pd_xAu_{1-x} samples prepared under different conditions. a-o) Topography images before H_2 exposure, after one H_2 exposure, and after a second H_2 exposure. a2-o2) Corresponding histograms for each topography image.

two $Pd_{0.73}Au_{0.27}$ samples also load to similar values despite differing roughnesses.

6.5 Simulations of optical switching

To apply these measured properties to an applicable optical switching system, we simulate (using FDTD) several grating structures to demonstrate the opportunity of using these alloys as devices. The measured optical properties for both the metals and hydrides presented in Figure 6.2 are used as inputs to the simulations. Figure 6.16 shows the results for two separate grating structures. Both structures consist of a grating with 100 nm width and height and a 65 nm SiO_2 spacer layer on a Au substrate. This spacer layer creates a cavity effect from the reflection off

Composition	Deposition type	t (nm)	Pristine (nm)	1st Load (nm)	2nd Load (nm)
Pd	Sputtered	100	2.6	2.8	2.6
$Pd_{0.73}Au_{0.27}$	Sputtered	100	2.5	2.5	2.4
$Pd_{0.52}Au_{0.48}$	Sputtered	100	2.5	2.5	2.4
$Pd_{0.42}Au_{0.58}$	Sputtered	100	-	-	-
$Pd_{0.34}Au_{0.66}$	Sputtered	100	2.7	2.3	2.4
$Pd_{0.14}Au_{0.86}$	Sputtered	100	2.7	2.5	2.7
Au	Sputtered	100	2.4	2.2	-
Pd	Sputtered	400	12.4	12.5	12.5
$Pd_{0.88}Au_{0.12}$	Sputtered	400	8.1	8.3	-
$Pd_{0.83}Au_{0.17}$	Sputtered	400	7.6	7.8	-
$Pd_{0.77}Au_{0.23}$	Sputtered	400	9.2	9.6	-
$Pd_{0.73}Au_{0.27}$	Sputtered	400	8.3	8.4	8.3
$Pd_{0.59}Au_{0.41}$	Sputtered	400	6.8	6.7	-
$Pd_{0.41}Au_{0.59}$	Sputtered	400	6.3	6.8	-
Pd	Evaporated	100	2.3	2.5	2.4

Table 6.1: Compiled RMS roughnesses of Pd_xAu_{1-x} upon hydrogenation. Table entries with the symbol '-' correspond to conditions where no data were not taken. t is thin film layer thickness. Pristine is the RMS roughness before H_2 exposure. 1st and 2nd loads are the RMS roughnesses after the 1st and 2nd full H_2 exposures respectively.

the Au substrate and enables increased sensitivity [115]. We simulated two different periodicities to show the tunability of the structure. First, a 550 nm periodicity is used to obtain large spikes in the relative reflectance, where the Pd structure shows an almost 200-fold increase. As we increase the amount of Au in the alloy, we see the peak of the reflectance ratio blue shift and decrease in magnitude, with the $Pd_{0.52}Au_{0.48}$ alloys still having over a 2-fold relative increase in reflectance. By changing the periodicity of the structure to 300 nm, we can achieve the opposite response to hydrogenation, where the relative reflectance dips to well below 1 for the same materials and exposures. This demonstrates the utility of these materials for a wide range of potential photonic device designs. We note that while Pd has a larger optical response than the alloys, the $Pd_{0.73}Au_{0.27}$ and $Pd_{0.52}Au_{0.48}$ both have

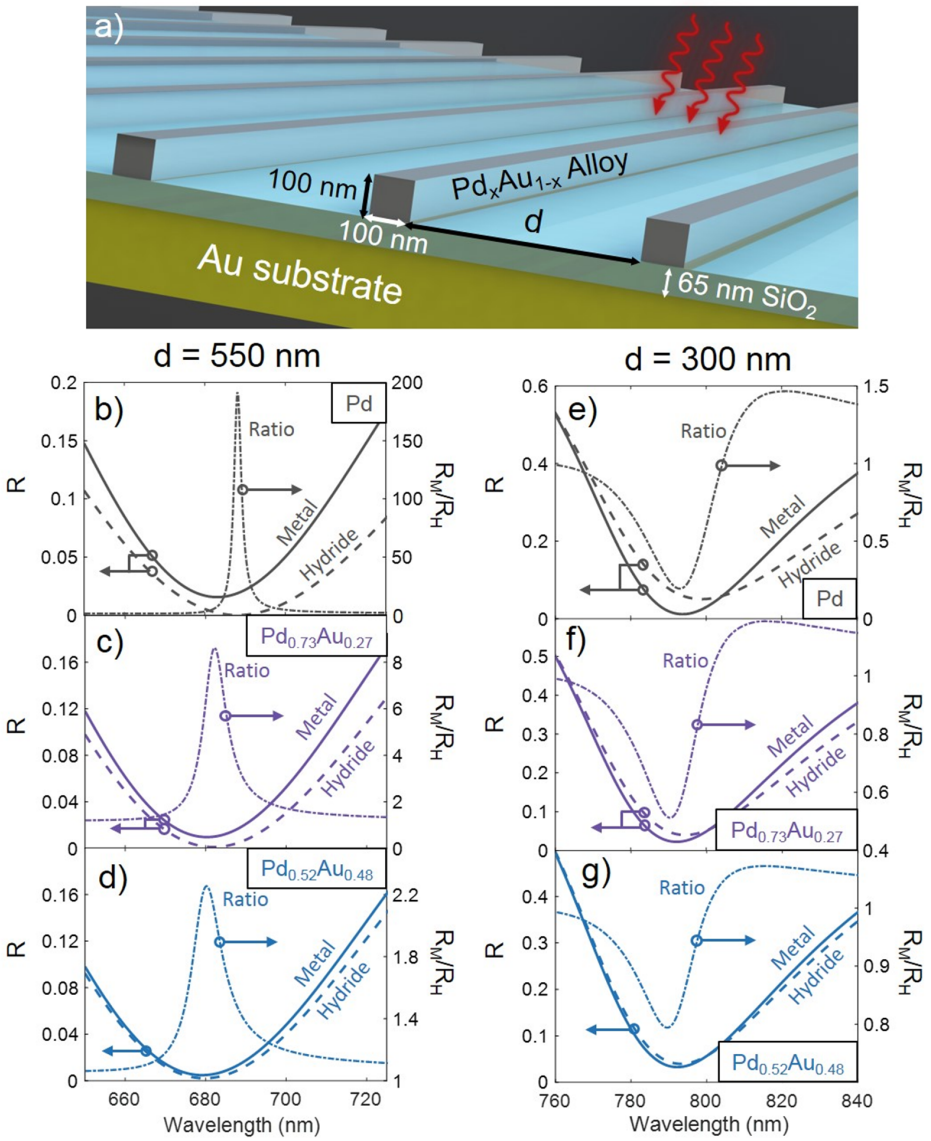

Figure 6.16: Simulated reflectance shifts upon hydrogenation. (a) Illustration of simulated grating structure. Gratings are 100 nm high and 100 nm wide with a spacing d between gratings. A 65 nm SiO_2 spacer layer separates the grating from a Au substrate. Light is incident normally on the grating with its polarization orthogonal to the grating direction. Reflection spectra for each of the alloys with grating periodicity of (b-d) 550 nm and (e-g) 300 nm plotted with the quotient of the metal (solid line) and hydride (dashed line) reflections showing the relative change in reflection with hydrogenation (dot dashed line).

significant optical responses in these structures. The tunable responses combined with the chemical resistance of the alloys will allow for improved sensor design. To

have an even higher sensitivity as an optical hydrogen sensor, the grating can be tuned for the resonance to occur in the NIR instead of the visible, because the largest optical changes upon hydrogenation occur at longer wavelengths. Figure 6.17 shows simulations with resonances in the NIR.

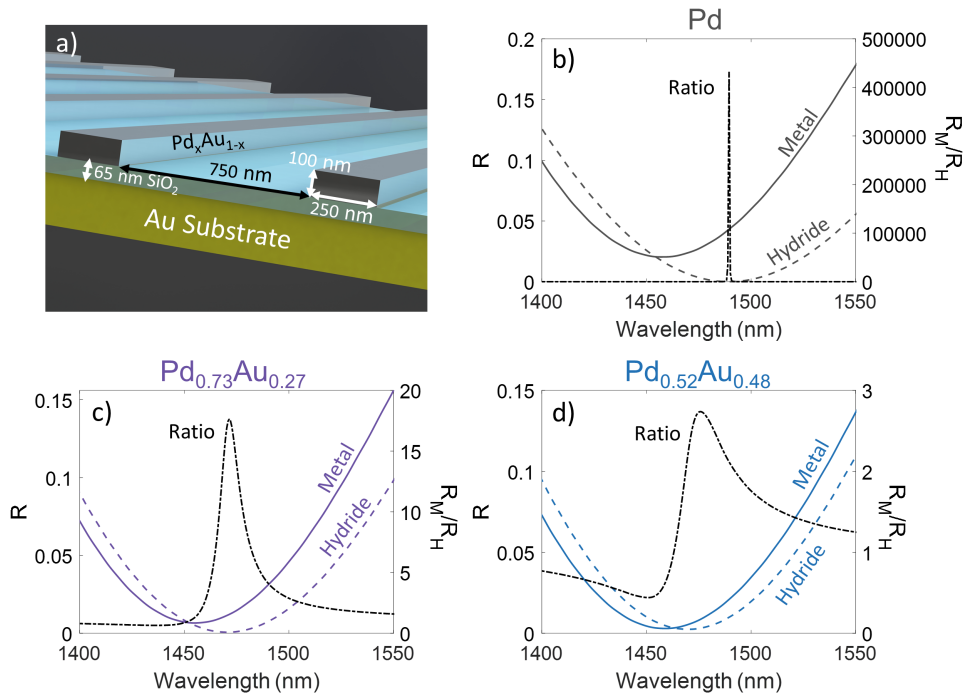

Figure 6.17: NIR simulations of the reflectivity of grating structures. (a) Schematic of grating structure. Gratings are 100 nm high and 250 nm wide with a 750 nm spacing between gratings. A 65 nm SiO_2 spacer layer separates the grating from an Au substrate. Light is incident normally on the grating with the polarization of the light orthogonal to the grating direction. (b-d) Reflection spectra for each of the alloys plotted with the quotient of the metal (solid line) and hydride (dashed line) reflections showing the relative change in reflection with hydrogenation (dot dashed line).

Finally, we show that these materials can be used for physical encryption and readout based on the gaseous H_2 in the environment. Previously, Mg nanostructures have been used for similar types of encryption schemes due to Mg's large optical change to H_2 [80, 210, 211]. In these works, e-beam lithography was used to create

small and intricate encryption images. In our example, we work with thin-film effects to make a macroscopic encryption scheme without the need for submicron nanostructuring. We do this by taking advantage of the similarities of the optical properties of Pd with $Pd_{0.42}Au_{0.58}$ in the non-hydrogenated state. By using the high optical sensitivity of Fabry-Perot-like resonances, we can amplify the difference in the optical responses of the two metals upon hydrogenation. Figure 6.18 outlines the encryption scheme of this setup. For the background of the image, there is an optically thick $Pd_{0.42}Au_{0.58}$ substrate with a 94 nm SiO_2 intermediate layer and a 5 nm $Pd_{0.42}Au_{0.58}$ capping layer. The lettering (encrypted message) is generated by using the same thickness of layers as the background structure but with Pd instead of the $Pd_{0.42}Au_{0.58}$ alloy for both the substrate and the cap. The multilayer resonance causes the coloring of the structure. Figure 6.18b shows the true-color image of the structure containing both the lettering and background before hydrogenation. These colors are found by calculating the reflection spectra with TMM simulations with the optical properties presented in Figure 6.2 as inputs. We then use the CIE XYZ color space to convert the reflection spectra to a color. See Appendix E for more details on the CIE color space. Note that all regions have indistinguishable colorings, hiding the message under ambient atmosphere. Once the structure is exposed to H_2, the Pd lettering has a large optical change as it hydrides, causing a shift in the resonance corresponding to an observed color shift. The $Pd_{0.42}Au_{0.58}$ background on the other hand has a limited response to the H_2 gas, causing a minimal color change of the substrate, as seen in Figure 6.18c. This allows for the lettering to become visible, revealing the message. Because these materials are fully

reversible as well, all one needs to do to re-encrypt the message is to remove the structure from the H_2 atmosphere. This allows for a full encryption scheme while only needing a small amount of H_2 gas to reveal the message with no other optical setup required. One note is that both sides of these structures would have to be exposed to hydrogen in order to fully hydride the Pd and $Pd_{0.42}Au_{0.58}$ layers. While the optical contrast between the two regions is relatively small, the planar nature of the structure (without the need for nanofabrication) is advantageous.

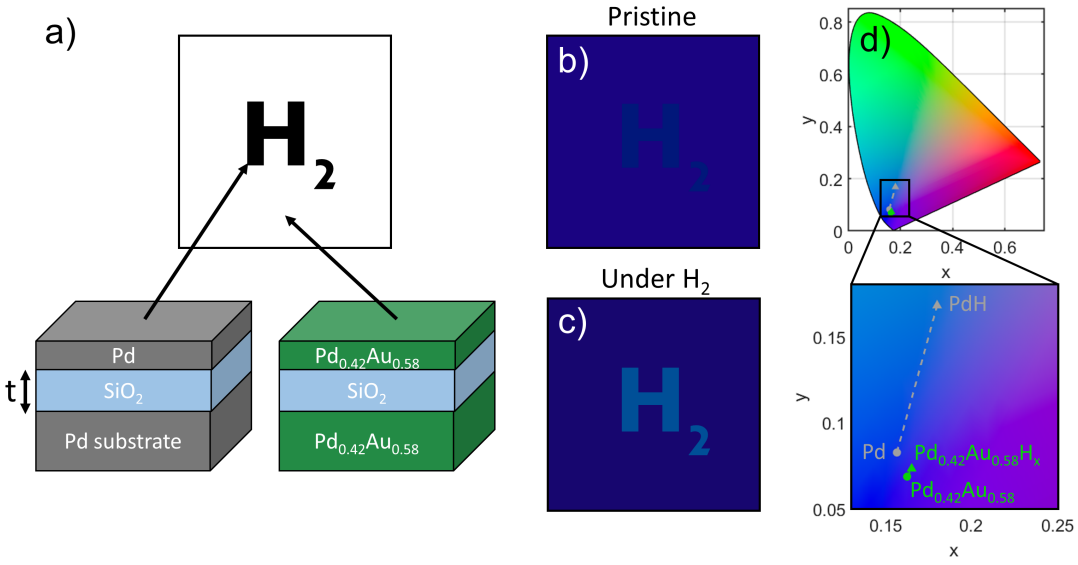

Figure 6.18: Physical encryption scheme. a) Design for using Pd_xAu_{1-x} alloys in a physical encryption scheme. The "H_2" message is created using a multilayer stack containing Pd while the background is created from a similar stack containing $Pd_{0.42}Au_{0.58}$. b) Simulated coloring of the design before exposure to H_2 and c) coloring of design after H_2 exposure. The SiO_2 thickness is t = 94 nm for these simulations with a 5 nm metal cap for both the active area and the background. d) Chromaticity diagram showing the change in coloring of the lettering versus the background.

6.6 Conclusions

In conclusion, we have directly measured the optical, sorption, and stress properties of a series of Pd_xAu_{1-x} alloys with controlled chemical composition upon hydrogenation. We implemented in situ spectroscopic ellipsometry from the mid-ultraviolet to the near-infrared regions and showed the consistency of these properties through multiple H_2 exposures after an initial hydrogenation cycle. We found that our alloys exhibited a linear relation between Pd composition and hydrogen loading amount, in agreement with previous reports. However, we measured a much smaller slope with respect to Pd composition than previously observed with higher loadings obtained in alloys with lower atomic percent Pd. We postulate that this difference is caused by different thin-film stresses present in our system. We characterized these stresses and found that the Pd_xAu_{1-x} alloys have a 0.9 GPa higher relative stress than measured for pure Pd which must be accounted for in device design. Surprisingly, even with these high stress amounts, there was no observed roughness (morphology) change in the alloys when hydrogenated. Using our measured optical properties, we showed the applicability of these alloys as grating devices, where the reflectivity can either be increased or decreased upon hydrogenation depending on the periodicity of the grating. Furthermore, we demonstrate their potential for use in a physical encryption scheme with no need for sub-micron nanostructuring.

Our results will further inform future sensor design, which must consider differences in fabrication methodology and the subsequent inherent stresses in the devices in order to accurately describe the sorption/optical response. We have shown that

different fabrication conditions and substrate choice can alter the stress of the system, which can be used to increase the response of new devices and allow for lower Pd composition alloys than previously expected to be utilized in the proper sensor design. We have also shown that moving to infrared sensing schemes could increase the sensitivity of these alloyed sensors when compared to the visible measurements. Future work will entail investigating new combinations of metals for potential improvements in sensing ability while maintaining chemical durability, potentially by moving from binary to ternary alloys.

Chapter 7: Optical Tunability Characterization of Mg-Ni, Mg-Ti, and Mg-Al Alloy Hydrides

In this chapter, we report the dynamically measured optical, loading, and stress properties of different compositions of three Mg alloy systems: Mg-Al, Mg-Ti, and Mg-Ni. By alloying Mg with secondary elements, it has been shown to increase the hydrogenation kinetics and improve the thermodynamics of the system. We find that these materials all have large optical changes when exposed to H_2 gas, with a wide range of potential properties in the hydride state. The magnitude and the sign of the optical properties change for each of the alloys is similar, but the differences have dramatic effects on device design. We find that Mg-Ti alloys in particular have applications for both switchable windows and broadband switchable light absorbers through TMM simulations.

7.1 Introduction to Mg alloys

As has been discussed previously in this dissertation in Chapter 3, Mg absorbs a large amount of hydrogen upon H_2 exposure and goes through dramatic changes in its optical properties. One issue with pure Mg is that the hydride state is too thermodynamically stable and must be unloaded at a high temperature [212].

The kinetics of both the absorption and the desorption are also slow, especially in bulk Mg, due MgH_2 being a poor proton conductor, which limits the diffusion of H through the material [213]. In order to improve upon the kinetic and thermodynamic properties of Mg, alloying has been extensively used to destabilize the hydride phase and increase H diffusion. This alloying has been attempted with many metals including Co [91, 214, 215, 216], Fe [91, 214, 217, 218], and Mn [91, 219] among others, but the most common secondary alloying elements used in the literature are Al [220, 221, 222, 223, 224], Ti [225, 226, 227, 228, 229, 230], and Ni [18, 183, 231, 232, 233, 234, 235, 236, 237, 238, 239]. These alloys have increased kinetics when compared to Mg [220, 240, 241, 242], and were each found to have interesting optical responses that are worth investigating further.

The Mg-Ni system in particular has been of interest in the optical community due to Mg_2Ni reportedly forming an intermediate optical "black state" during its loading process [18, 235, 236]. This black state is characterized by an intermediate loading state where the sample absorbs >75% of incident visible light when illuminated through a transparent substrate. The process has been investigated with ^{15}N nuclear reaction analysis hydrogen depth profiling [18] to determine the H atom vertical distribution in the sample. It was found that the black state formation is caused by preferential loading from the Mg_2Ni/substrate interface, as opposed to the hydride being seeded near the dissociation sites at the Mg_2Ni/Pd interface. A multi-layer interference effect occurs, where the bottom layer is fully hydrogenated Mg_2Ni and the top layer remains metallic Mg_2Ni, and this orientation creates the observed black state. In the fully hydrogenated state, some Mg-Ni alloys have also

been found to have good switchable window properties, switching from a reflecting state to a transparent state [183].

The Mg-Ti system has been investigated for switchable solar absorbers [228], switchable mirrors [243], and hydrogen sensor applications [24]. These materials have the advantage of having a reported high-absorbing state across the visible region for thick films ($>$ 200 nm) in their fully hydrogenated state, as opposed to Mg_2Ni which obtains this high-absorbing state only during intermediate loading [229]. This high-absorbing state occurs for y = 0.7 - 0.8 in Mg_yTi_{1-y}. This alloying system is also of interest due to a decrease in degradation over many hydrogenation cycles, along with faster kinetics during these cycles, when compared to pure Mg [229]. For very thin Mg-Ti films ($<$ 40 nm), the hydride state is more color-neutral than Mg-Ni alloys (which have a yellow tint), allowing for more aesthetically pleasing switchable windows, albeit with fairly low transmission amounts $\sim$20% [243].

Mg-Al alloys are of interest for their potential for high hydrogen weight percent (weight of hydrogen in a material divided by the total weight of the material) for hydrogen storage along with much faster hydrogenation kinetics at room temperature when compared to Mg [224]. These materials also have been suggested as switchable window devices, as Mg-Al alloys with $\sim$ 70% Mg have been demonstrated to have color-neutral transmission [220].

So far, all optical measurements reported in the literature of these alloys consist of normal incidence reflection and transmission measurements to determine the absorption coefficient of Mg-Ti alloys [229] and the absorption coefficient and optical bandgap of Mg-Ni alloys [234, 244] or fitting normal incidence reflection and

transmission measurements with a Drude-Lorentz model to determine the dielectric function of Mg-Ni alloys [18, 245]. As previously discussed in this thesis, this method of obtaining thin film optical properties is much less sensitive than variable-angle spectroscopic ellipsometry, especially for very thin films < 50 nm [246]. There have been no reports in the literature of the optical properties of Mg-Al alloys, or of any Mg-Ti, Mg-Ni, or Mg-Al alloys in intermediate loading states. Our system allows for in situ ellipsometry to dynamically investigate the optical properties of thin films (< 50 nm) of these materials with high sensitivity as they are hydrogenated. By using similar deposition parameters to fabricate the different alloy systems, these measurements will also allow us to quantitatively compare the responses of these systems.

In this chapter, we dynamically measure the optical properties of different atomic ratios of thin-film Mg-Al, Mg-Ti, and Mg-Ni alloys as they are exposed to H_2 gas. We also dynamically record the loading and stress values of these alloys during the loading. We find large optical changes for all of the alloys investigated, with $Mg_{0.85}Ti_{0.15}$ exhibiting the largest optical changes for any alloy. We confirm the optical black state in the Mg-Ni samples through TMM simulations using our found optical properties and observe the highest absorbing state for $Mg_{0.73}Ni_{0.27}$, as expected with that atomic composition being the closest to Mg_2Ni. We find that Mg-Ti alloys exhibit the best properties for both switchable windows and broad-band switchable light absorbers. We also find the loadings for the Mg-Ni alloys to be slightly lower than expected from the literature and hypothesize that different deposition parameters could affect the properties of the materials to cause different

loading amounts.

7.2 Experimental methods

Each of the thin-film samples is fabricated by room temperature physical vapor deposition cosputtering. For each deposition, two separate AT-cut 5 MHz QCMs, a glass slide, and a Si chip are included in the deposition chamber. Prior to deposition, each sample is cleaned with acetone, methanol, isopropanol, and water. The alloys were deposited through a 12.5 mm diameter shadow mask centered on the QCM substrate. The direct current powers of the sputtering tool ranged from 50 to 450 W to attain the different compositions of the different alloys. These minimum and maximum values are determined by the minimum voltage necessary to maintain a plasma and the voltage limit of the tool respectively. Each sample was capped with a 3 nm Pd layer without breaking vacuum to catalyze the hydrogenation reaction and prevent surface oxidation of the sample. The composition of each alloy was determined with EDX taken on the Si chip included in the deposition chamber, taking an average of 5 measurements at different points on the sample to ensure uniform alloying.

The optical properties of the materials were determined with in situ spectroscopic ellipsometry using the system outlined in Chapter 2. To determine the thickness of the Mg alloy films, the glass slide sample that was included in the deposition chamber was measured with ellipsometry and transmission measurements. The raw Ψ and Δ data were then fit with an optical model with the properties of

the Mg alloy and the thickness of that alloy as fit parameters. The optical properties of the glass substrate were taken before the metal deposition and were defined in the model. The properties of the sputtered Pd were measured separately and were defined in the model. The thickness of the Pd layer was set to be 3 nm for all samples. With the transmission measurements, this fitting procedure allows for unambiguous determination of the thickness of the Mg films. The thicknesses of the films we investigated ranged from 19 to 42 nm. As a consistency check for our thickness measurements, we used the same model properties and thickness on the data taken on the Au QCM electrode substrate and found good agreement without any refitting.

The dynamic optical fittings for these materials were done in a slightly different method than previous chapters. The volume expansion of these Mg-based alloys becomes important in these thin-film fittings. In previous measurements on metal hydrides, we have measured materials that are optically thick within the measurement regime (transmission across all measured wavelengths is zero). For these measurements, thickness expansion does not affect the fitting results as the materials are modeled as bulk. However, the Mg alloy thin films investigated in this chapter have appreciable transmission and the optical effect of the substrate must be taken into account. For these alloys, the volume expansion for each is found to be $\sim$15% over the atomic ratio region that we are investigating in this chapter [18, 247], and we use this value for all of our samples. To include this expansion in the model, we use the dynamic loading data to determine how much H is in the film at each optical time step and then scale the total thickness expansion by the same ratio as

the current loading to the final loading value (i.e if a film's final calculated loading value is 1 and at time step t we calculate the loading is H/M = 0.33, then we define the volume expansion at this time step to be 0.33*15% = 5%). We also define the loading amount of the Pd capping layer by this same ratio. At each time step, with the thicknesses and Pd cap properties defined, we then use a B-spline model with 0.3 eV node spacing to fit the optical properties of the Mg-alloy.

The hydrogen loading for each alloy was measured on the second QCM sample with the method outlined in Chapter 2. To convert from the QCM frequency to H/M loading ratio, the density of each sample must be input into the calculation. For Mg-Ti, both Mg and Ti have hexagonal close-packed lattice structures and no known intermetallic states form. Because of this, we believe that a linear weighting of the densities of Mg and Ti in the same ratio as their atomic percent in the alloy is a reasonable approximation of the density. As a check of this assumption, we compare densities calculated from linear weighting with densities calculated from lattice constant measurements using X-ray diffraction measurements and find good agreement $< 6\%$ difference. For the Mg-Al system, we also chose to use this linear weighting scheme because there are no other alloy phases found for this material when the atomic Mg percent $> 60\%$. For the Mg-Ni system, we use a slightly different method. Mg_2Ni is a known intermetallic with a density of 3.48 g/cm^3 and because this forms a separate phase within the Mg-Ni alloys, a linear combination of pure metal densities is not applicable. From Ref [244], we know for Mg_yNi_{1-y} if $0.67 < y < 0.89$, the alloy forms a varying mixture of crystalline Mg_2Ni and amorphous $Mg_{0.89}Ni_{0.11}$ but the lattice constant remains constant in this region. If $0.89 < y <$

0.95 the lattice constant begins to expand and the alloy is mainly nanocrystalline Mg_2Ni and crystalline Mg. Using this knowledge of the phases, we use the following equation to calculate the densities of the Mg-Ni alloys for $0.67 < y < 0.89$:

$$\rho = \rho_{Mg_2Ni} \frac{A_{Mg} y + A_{Ni}(1-y)}{0.67 * A_{Mg} + 0.33 * A_{Ni}} \tag{7.1}$$

where ρ_{Mg_2Ni} is the density of Mg_2Ni, A_{Mg} is the atomic mass of Mg, and A_{Ni} is the atomic mass of Ni. Here we calculate the density by multiplying the mass ratio of the alloy to Mg_2Ni with the known density of Mg_2Ni. This is using the fact that the volume of the lattice is not changing from the Mg_2Ni size, thus allowing us to only account for mass. For higher Mg percent with $0.89 < y < 0.95$:

$$\rho = \frac{1}{1 + \frac{y-0.89}{1-y}} \left(\rho_{Mg_2Ni} \frac{A_{Mg} y + A_{Ni}(1-y)}{0.67 * A_{Mg} + 0.33 * A_{Ni}} \right) + \frac{\frac{y-0.89}{1-y}}{1 + \frac{y-0.89}{1-y}} \rho_{Mg} \tag{7.2}$$

where ρ_{Mg} is the density of pure Mg. Here we linearly weight the density of $Mg_{0.89}Ni_{0.11}$ (calculated with Eq. 7.1) with the density of Mg. This rationale uses the fact that up to 89% Mg, there was no expansion in the lattice and with additional Mg added above this 89% point, we are adding crystalline Mg with the density ρ_{Mg}. Using these calculated densities and the thicknesses found from the optical fittings, we can then calculate the loadings and stresses in the same manner as Chapter 2.

7.3 Optical properties of Mg alloy hydrides

In the following sections, we report and discuss the dynamic optical properties of our fabricated Mg-Al, Mg-Ti, and Mg-Ni alloys as they are exposed to 1 atm H_2 gas.

7.3.1 Mg-Al hydrides

Figure 7.1 shows the measured optical properties $\tilde{n} = n + ik$ of four different compositions of Mg-Al alloys and how these properties change under complete hydrogenation under 1 bar H_2 pressure. For these materials, we observe a small spread in the initial and final properties of the materials, which is as expected due to all of the alloys being fairly close together in atomic composition. The reason for this proximity in composition is a relative lack of sensitivity of the different materials to different deposition voltages (i.e. 200 W Mg and 200 W Al powers compared to 450 W Mg and 50 W Al powers only give a 7% difference in atomic Mg percent). We find that both the real and imaginary parts of the index of refraction increase with longer wavelengths, as we expect from most lossy metals. Interestingly, we find that metallic $Mg_{0.77}Ni_{0.23}$ exhibits the largest n and k across the spectrum, as well as the largest optical change in k. We find that for all of the Mg-Al alloys, the change in the optical properties follow the same trend. For Δn, there is little variation from sample to sample. Each sample exhibits an increase in n for shorter wavelengths and a decrease for longer wavelengths, with the crossover point from positive to negative n occurring between 1100 - 1225 nm. All samples exhibit a decrease in k

across the measured spectrum, with the largest decreases occurring in the NIR and the smallest decreases in the visible. Despite having the largest Δk, fully loaded $Mg_{0.77}Ni_{0.23}H_x$ still has the largest k across the visible spectrum, although only by a small margin, and the second highest in the NIR. In the final hydride state, shown in Figure 7.1c, we find that each of the materials still has significant attenuation in the long-wavelength visible and into the NIR, with $k > 3$ after ~1000 nm for each alloy. This is despite the fact that the NIR optical properties saw the largest decreases in k. For the real part of the index of refraction, we find a minimum in the mid-visible spectrum, that increases to large values (> 3) in the NIR. The hydride samples are still somewhat optically metallic, not exhibiting a complete transition to a dielectric material.

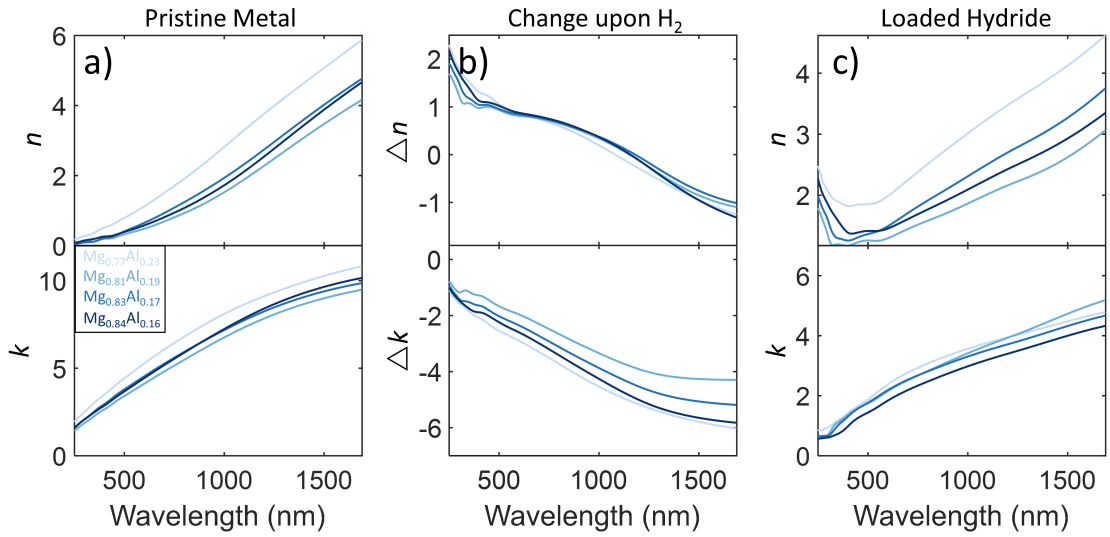

Figure 7.1: Optical properties $\tilde{n} = n + ik$ of four different Mg-Al alloy hydrides. a) Optical properties in the pristine metallic state before hydrogenation. b) Change in optical properties upon hydrogenation, defined here as the pure metal optical properties subtracted from the hydride optical properties. c) Optical properties in the fully hydrogenated hydride state. Each colored line on the plot represents a different atomic ratio of metal hydride, with darker shades representing higher atomic Mg percent ratios.

In Figure 7.2, we observe the intermediate states during the hydrogen loading. These plots show a smooth transition of the optical properties from the metallic (light colored curves) to the hydride states (darker colored curves). Note that the chosen optical curves on this plot are not linearly spaced with time, but are instead to show the range of properties of the intermediate states. Loading generally begins slowly as small amounts of H_2 are introduced to the chamber, then increases quickly during the beginning of the α to β phase transition, then slows down to a long tail for the final $\sim$10% of the load when most of the material is in the β phase. Most of our materials showed similar time dynamics, with the total time of loading ranging from 10 - 15 min for most samples.

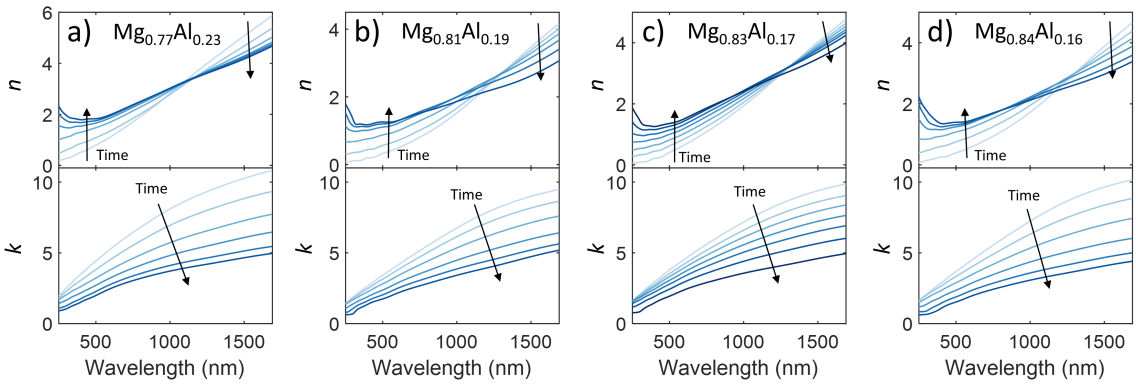

Figure 7.2: Optical properties of different Mg-Al alloys as they are exposed to H_2 gas. The lightest colored line depicts the alloy in the pristine metallic state. As H_2 is introduced to the system, the material begins to hydrogenate, denoted by the lines getting darker in the plot, with the darkest line indicating the full hydride state. Each line is not linearly spaced in time and is instead chosen to aesthetically show the range of possible intermediate states. The alloys shown here are a) $Mg_{0.77}Al_{0.23}$, b) $Mg_{0.81}Al_{0.19}$, c) $Mg_{0.83}Al_{0.17}$, d) $Mg_{0.84}Al_{0.16}$

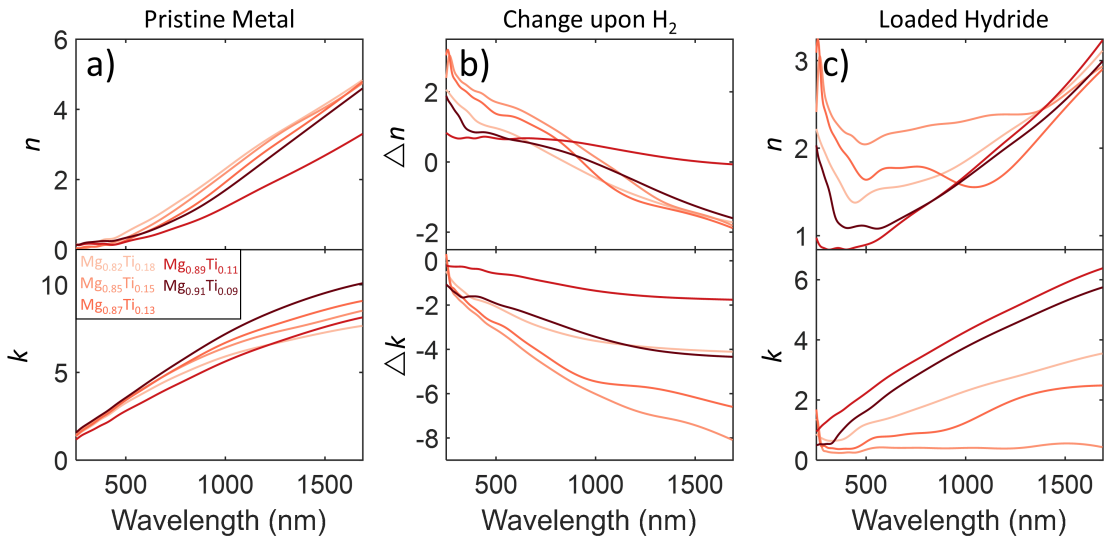

Figure 7.3: Optical properties $\tilde{n} = n + ik$ of five different Mg-Ti alloy hydrides. a) Optical properties in the pristine metallic state before hydrogenation. b) Change in optical properties upon hydrogenation, defined here as the pure metal optical properties subtracted from the hydride optical properties. c) Optical properties in the fully hydrogenated hydride state. Each colored line on the plot represents a different atomic ratio of metal hydride, with darker shades representing higher atomic Mg percent ratios.

7.3.2 Mg-Ti hydrides

Figure 7.3a shows the metallic optical properties of 5 different fabricated Mg-Ti alloys with the atomic Mg percent ranging from 82 - 91%. We find that the n values in the metallic state are fairly close together, with the exception of $Mg_{0.89}Ti_{0.11}$, which exhibits a lower n for the state. The higher Mg percent alloys exhibit higher k values, again with the exception of $Mg_{0.89}Ti_{0.11}$ (we will discuss the discrepancies of the $Mg_{0.89}Ti_{0.11}$ sample further down in the chapter). Higher attenuation for samples with more Mg is not unexpected, as Mg has much higher k values than Ti in their unalloyed form. The metallic properties of these Mg-Ti samples also align fairly closely with the metallic Mg-Al alloys investigated in the

previous section. As we hydrogenate these samples, we find similar types of changes in the optical properties when compared to the Mg-Al samples, with n increasing in the visible and decreasing the in the NIR, and with k decreasing for all wavelengths with larger decreases for longer wavelengths. There is a much broader range in the changes in properties for these alloys, and two alloys, $Mg_{0.85}Ti_{0.15}$ and $Mg_{0.87}Ti_{0.13}$, exhibit larger changes than the Mg-Al samples. Figure 7.3c shows the properties of the hydride states. The three lowest Mg percent samples show somewhat constant n in the visible spectrum, with peaks in the ultraviolet and then increasing with longer wavelengths into the NIR. The two highest Mg percent samples have smaller n values in the visible, with sharper minima that then monotonically increase with longer wavelengths, similar to the Mg-Al hydrides. These two samples also have the largest k by a significant margin. The lower Mg percent samples have relatively smaller k values, with $Mg_{0.85}Ti_{0.15}$ exhibiting almost no attenuation across the visible and NIR.

In Figure 7.4, we observe the intermediate states during the hydrogen loading. These plots mostly show smooth optical transitions, except for $Mg_{0.85}Ti_{0.15}$ and $Mg_{0.87}Ti_{0.13}$, which show a resonance like dip in n between 500-600 nm for high hydrogen content states. The $Mg_{0.82}Ti_{0.18}$ sample also slightly shows this effect. For the $Mg_{0.85}Ti_{0.15}$ sample, we also observe a decrease in n in the NIR until the almost fully hydrogenated state, and then a sharp increase in n when the hydrogenation is complete. Note that again the chosen optical curves on this plot are not linearly spaced with time but are instead shown to depict the range of properties of the intermediate states.

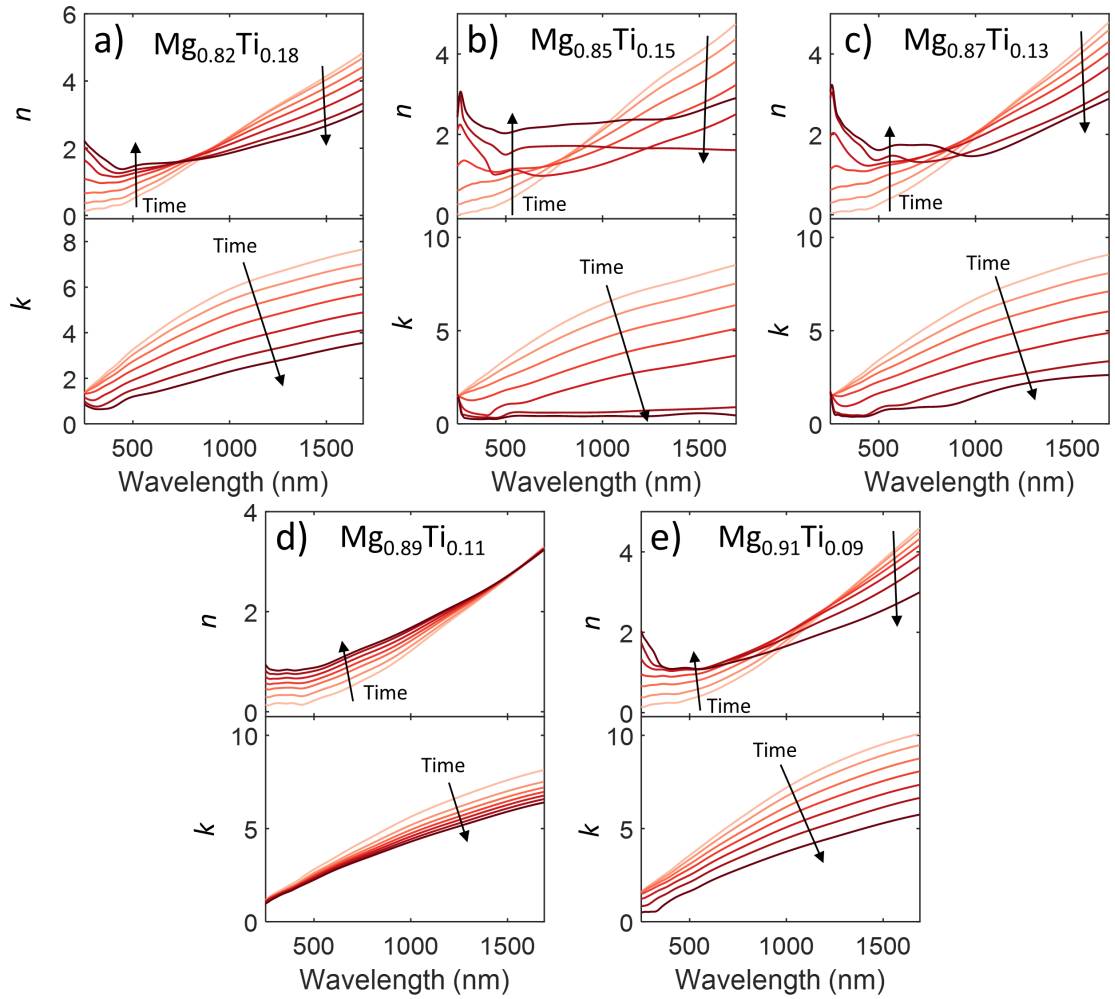

Figure 7.4: Optical properties of different Mg-Ti alloys as they are exposed to H_2 gas. The lightest colored line depicts the alloy in the pristine metallic state. As H_2 is introduced to the system, the material begins to hydrogenate, denoted by the lines getting darker in the plot, with the darkest line indicating the full hydride state. Each line is not linearly spaced in time and is instead chosen to aesthetically show the range of possible intermediate states. The alloys shown here are a) $Mg_{0.82}Ti_{0.18}$, b) $Mg_{0.85}Ti_{0.15}$, c) $Mg_{0.87}Ti_{0.13}$, d) $Mg_{0.89}Ti_{0.11}$, e) $Mg_{0.91}Ti_{0.09}$

7.3.3 Mg-Ni hydrides

Finally, we investigate the properties of Mg-Ni alloys. Figure 7.5a shows the properties in the metallic state, where we see a much larger spread in initial n values for these materials, but n and k still follow the same trend as was found with the

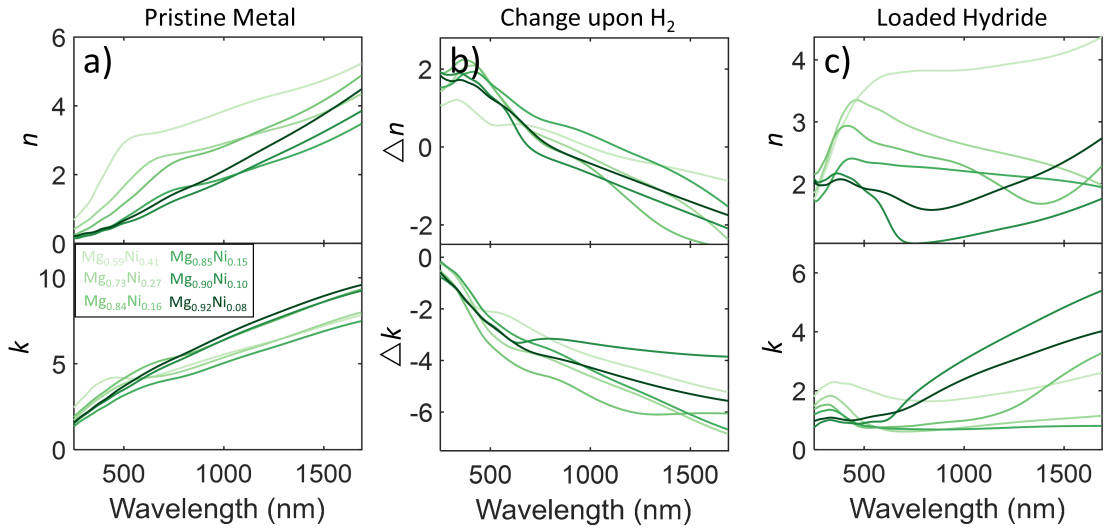

Figure 7.5: Optical properties $\tilde{n} = n + ik$ of siz different Mg-Ni alloy hydrides. a) Optical properties in the pristine metallic state before hydrogenation. b) Change in optical properties upon hydrogenation, defined here as the pure metal optical properties subtracted from the hydride optical properties. c) Optical properties in the fully hydrogenated hydride state. Each colored line on the plot represents a different atomic ratio of metal hydride, with darker shades representing higher atomic Mg percent ratios.

other Mg alloys (n and k generally increase with increasing wavelength). This larger spread in initial properties is expected, as we were able to obtain a larger range of atomic ratios for this alloy system compared to the other two, ranging from 59% - 92% Mg. In Figure 7.5b we see the same trends of optical properties change as Mg-Al and Mg-Ti with large decreases in k across the spectrum upon hydrogenation, and increases in n in the visible with decreases in the NIR. In the hydride state in Figure 7.5c, we see a large range of potential final properties. Generally, the lower Mg percent hydrides have a higher n across the spectrum, with the $Mg_{0.90}Ni_{0.10}$ sample demonstrating the lowest n across most of the spectrum and $Mg_{0.59}Ni_{0.41}$ the highest. Most of the hydrides have low attenuation in the visible, with $k < 2$. The higher Mg percent hydrides then have larger attenuation into the NIR, while the

lower Mg percent samples exhibit a more constant k across the measured spectrum.

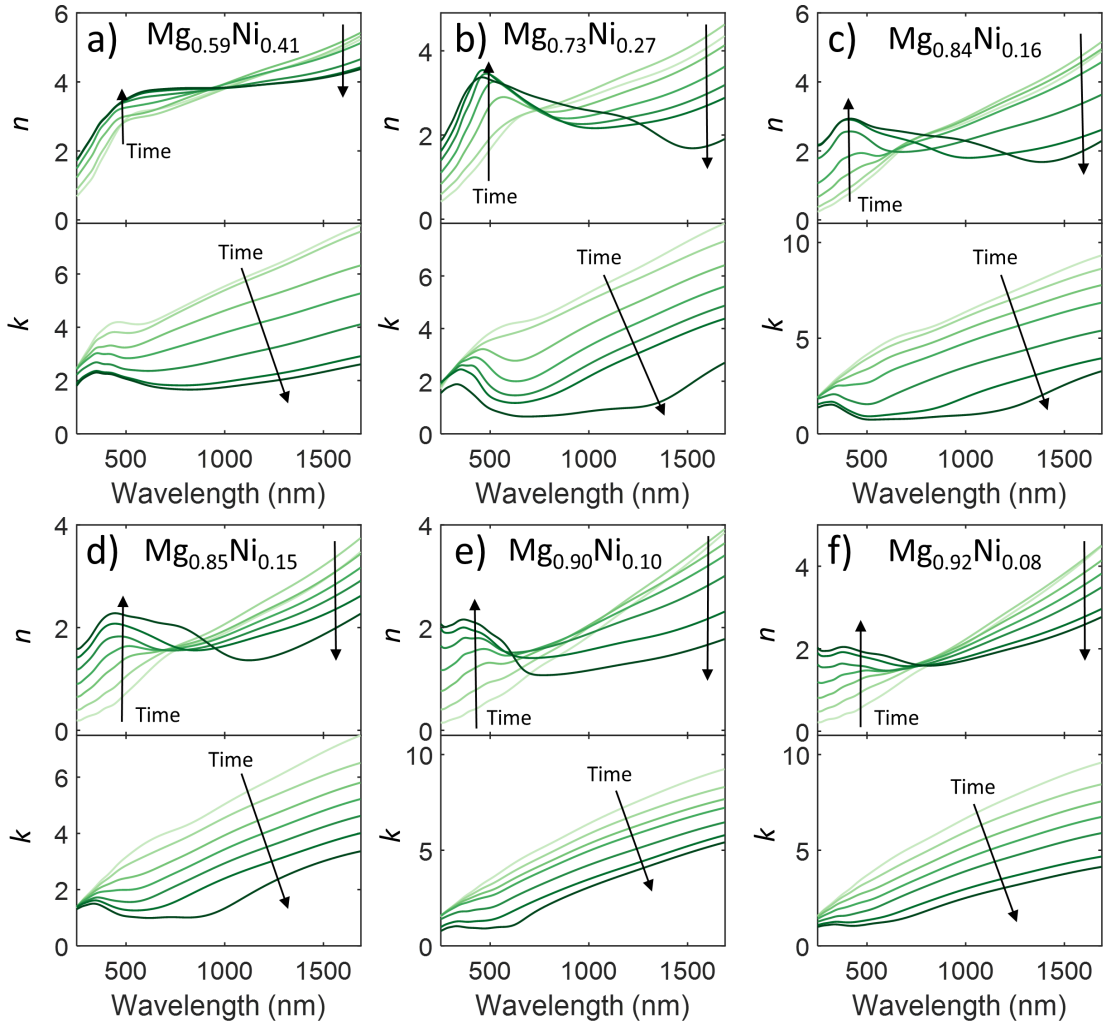

Figure 7.6: Optical properties of different Mg-Ni alloys as they are exposed to H_2 gas. The lightest colored line depicts the alloy in the pristine metallic state. As H_2 is introduced to the system, the material begins to hydrogenate, denoted by the lines getting darker in the plot, with the darkest line indicating the full hydride state. Each line is not linearly spaced in time and is instead chosen to aesthetically show the range of possible intermediate states. The alloys shown here are a) $Mg_{0.59}Ni_{0.41}$, b) $Mg_{0.73}Ni_{0.27}$, c) $Mg_{0.84}Ni_{0.16}$, d) $Mg_{0.85}Ni_{0.15}$, e) $Mg_{0.90}Ni_{0.10}$, f) $Mg_{0.92}Ni_{0.08}$

Figure 7.6 shows the dynamic transition state data for the Mg-Ni samples. For each of the samples, the transitions are mostly monotonic without any exotic features. For the intermediate loading states, here we are modeling the Mg-Ni

film as homogeneous throughout the thickness of the film. As was discussed in the introduction, it has been found that Mg-Ni films do not load homogeneously, but instead with preferential phase formation from the substrate of the film that propagates to the Pd cap. Our modeling process is not contradictory to this process and still allows for the bulk characterization of the properties of the film in this orientation with illumination through the Pd cap. The low MSE obtained in our optical fits indicate that our model accurately captures the optical properties of our samples. For our dynamic fits, the MSE for any individual fit was never greater than 10, indicating a good fit. However, for a different illumination orientation of the device (i.e. backside illumination through a transparent substrate), our intermediate model fits would not account for the layering effects of the loading. To model those bulk responses with our setup, the optical properties would have to be measured in that same orientation. Note that this layering effect would only affect the properties in the intermediate states, and have no effect on the modeling of the metallic or fully hydrogenated states shown in Figure 7.5.

To determine whether any of our materials would exhibit this black state with backside illumination, we modeled the multi-layer loading process with TMM simulations. Figure 7.7a shows the simulation architecture. The samples consist of illumination through a SiO_2 substrate. The layers proceed from the substrate with the fully hydrogenated Mg-Ni hydride, the fully metallic Mg-Ni alloy, and lastly a 3 nm PdH_2 capping layer. The hydrogenation of the material is simulated by beginning with the Mg-Ni-H layer equal to 0 nm, and then increasing this layer size while decreasing the Mg-Ni layer by the same rate, until the sample is completely

hydrogenated. We defined the alloy thickness to be 25 nm for these simulations. Using this method, we did find a high absorbing intermediate state for multiple samples, with the largest absorption occurring for the $Mg_{0.73}Ni_{0.27}$ sample, which is expected as this material is the closest composition to Mg_2Ni for which the black state was initially discovered. In Figure 7.7b, we show the absorption curves for different loading thicknesses for this alloy, where the peak absorption occurs at 12 nm loading, which is equal to half of the thin film being loaded.

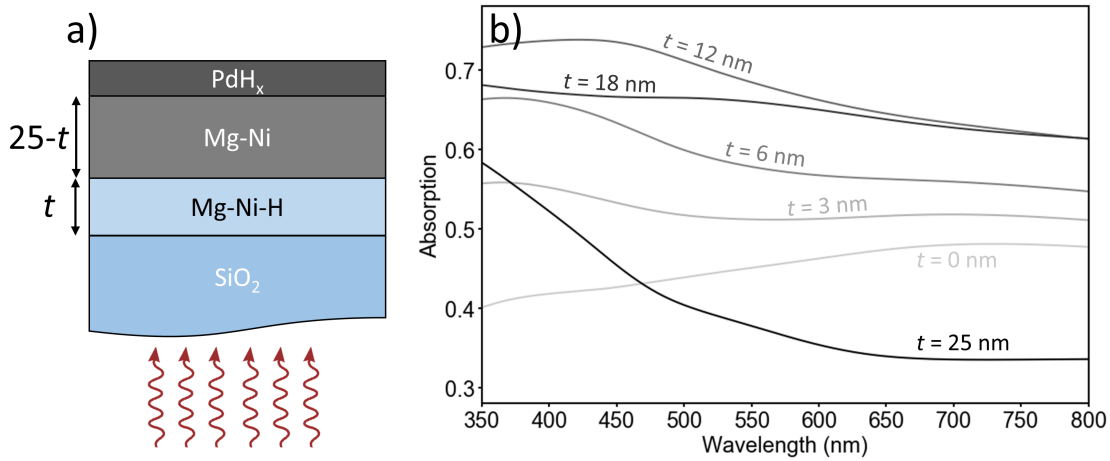

Figure 7.7: Modeled absorption from backside illumination of $Mg_{0.73}Ni_{0.27}$. a) Simulation architecture for sample loading. Sample consists of a SiO_2 substrate, followed by a fully hydrogenated Mg-Ni-H layer, then a fully metallic Mg-Ni layer, and finally a 3 nm Pd capping layer. The total Mg alloy thickness is defined to be 25 nm. Simulated hydrogenation is defined as an increase in the thickness of the hydride layer and a decrease of the same magnitude of the metal layer. b) Calculated absorption for different loading thicknesses using $Mg_{0.73}Ni_{0.27}$ optical properties.

7.4 Stress and loading properties

On the second QCM crystal included in the deposition chamber, we dynamically measured the loading and stress properties of the films. The loading values for

all of the samples are shown in Figure 7.8. Figure 7.8a shows the loading values of the Mg-Al samples. We can see that the samples have loadings near H/M = 1, with the highest measured loading at 1.28 for $Mg_{77}Al_{23}$ and the lowest loading at 0.75 for $Mg_{81}Al_{19}$. These values are at the low end of the range of hydrogen loading measurements reported in the literature for alloys in this composition range, which find loading values between H/M = 0.85 - 1.5 [220, 224]. The $Mg_{77}Al_{23}$ also exhibited the largest optical property change compared to the other Mg-Al samples. Future work looking at these samples should investigate fabrication of higher Al atomic percentages to determine if there is a correlation of higher loading for higher Al percent for any range of compositions and if the optical properties change is greater in this region.

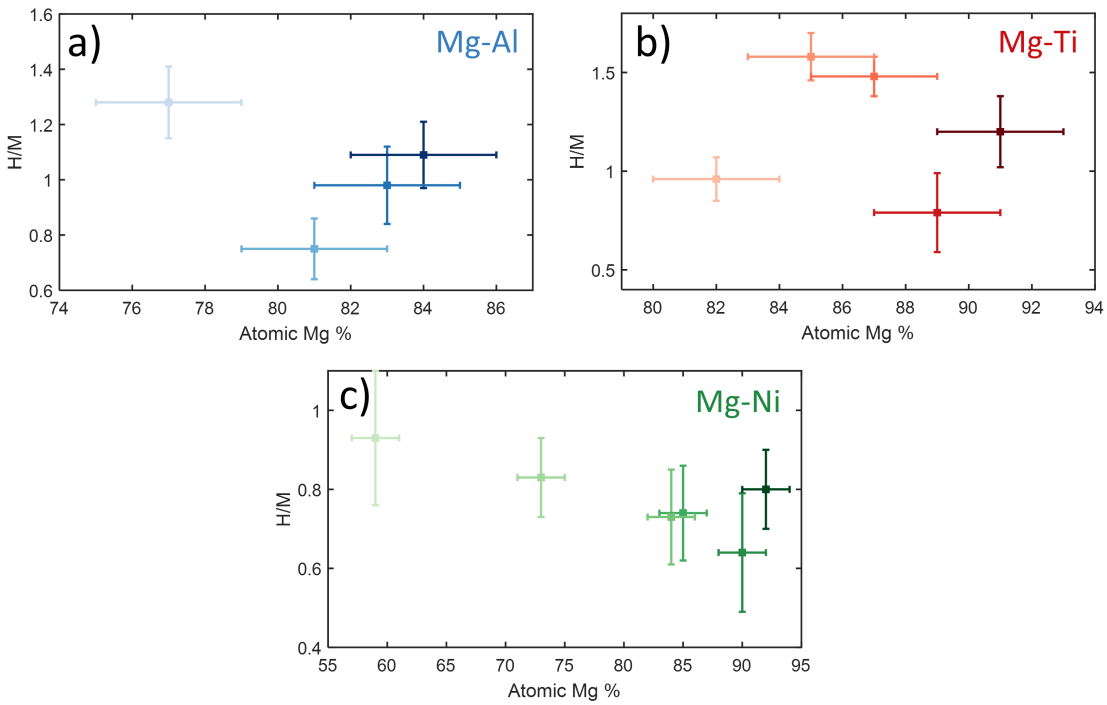

Figure 7.8: Measured maximum loading values for different thin film samples for a) Mg-Al, b) Mg-Ti, and c) Mg-Ni alloy samples.

The loading values of the Mg-Ti films are shown in Figure 7.8b. Three of these values are in general agreement in the literature, which finds that the average amount of loading of Mg-Ti alloys in this atomic composition range average H/M = 1.55 [229, 242]. We find two samples that fall measurably below this average, with $Mg_{0.82}Ti_{0.18}$ at 0.96 and $Mg_{0.89}Ti_{0.11}$ at 0.79. When we look at the optical data, we find that the $Mg_{0.89}Ti_{0.11}$ sample had the lowest optical change of any of the investigated alloys as well. We suspect that there was an issue with the fabrication of this sample that prevented a complete loading. This could have been caused by an incomplete Pd capping layer that did not fully encapsulate the sample, allowing for oxidation of the surface of the alloy, or potential alloying between the Pd capping layer and Mg near the surface of the Mg-Ni alloy.

For Mg-Ni alloys in Figure 7.8c, we see generally lower calculated loadings than for the other two alloys. We also find a slightly negative correlation between the loading amount and the atomic Mg percent. This does not agree with previously found data in the literature, which found that there should be a slightly positive correlation between these values and that the values should fall between 1.2 and 1.4 H/M [234]. This loading difference could be attributed to differences in sample preparation. Other thin-film Mg-Ni alloys have been fabricated with multi-layer metal deposition followed by a high temperature anneal, as opposed to our cosputtering method. These different fabrication conditions could potentially be forming different alloying phases within the metal, which would affect the total loading amount. Further studies on the crystal structures of Mg-Ni alloys fabricated with these two techniques should be done to determine if there is any difference.

In Figure 7.9, we show the total stress change of each of the measured Mg alloys upon full hydrogenation. These stress changes are compressive and are defined to be positive. We find the stresses for the samples to be fairly consistent within a material system. Taking the averages of the stresses in each system, the Mg-Al samples have the highest stresses with an average of 0.56 GPa, next is Mg-Ti with an average of 0.48 GPa, and finally the Mg-Ni alloys have the lowest measured stress with an average of 0.36 GPa.

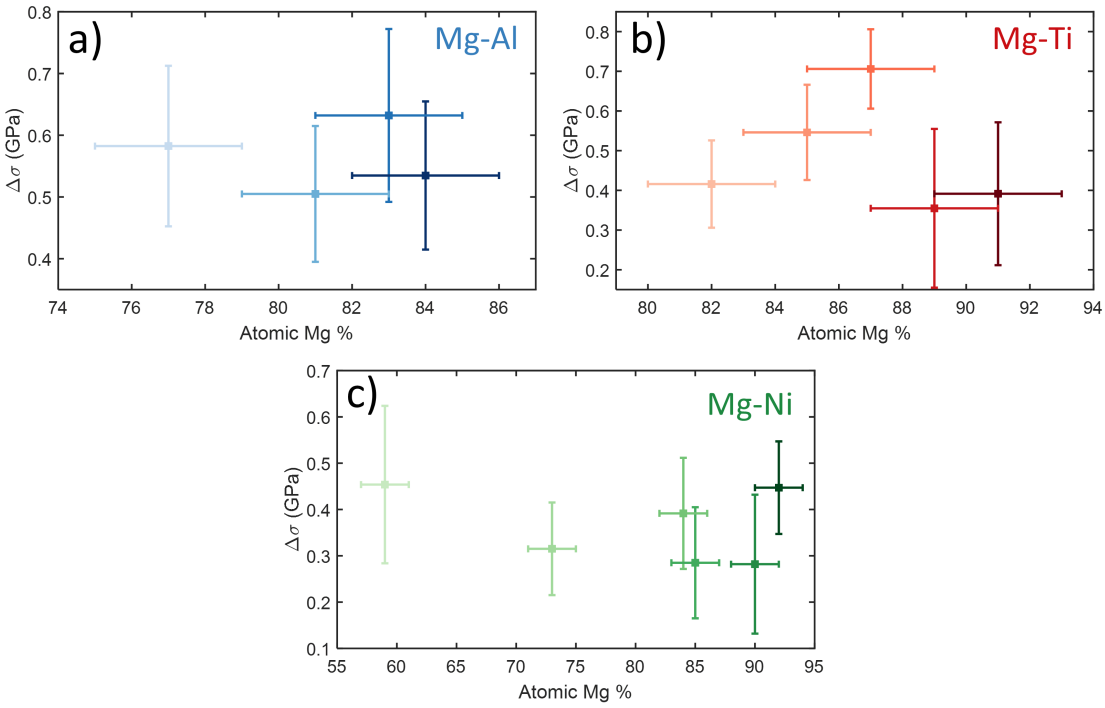

Figure 7.9: Measured total stress change values for different thin film samples for a) Mg-Al, b) Mg-Ti, and c) Mg-Ni alloy samples. The change in stress reported here is the stress change from the initial pristine metal mounted in the environmental chamber to the fully hydrogenated state (does not include intrinsic stress of initial pristine alloy).

7.5 Applications

In this section, we use our found optical properties of the alloys to simulate potential applications. We use the transfer-matrix method to simulate thin-film responses of these materials for different thicknesses and on different substrates. The first application of these alloys that has been suggested is for switchable window technologies. As a test of this application, we simulate the transmission through the alloys in their metallic and hydride states and compare transmission amounts. We use a metallic alloy thickness of 25 nm with a 3 nm Pd capping layer. We find that these thicknesses are in the ideal range for switchable window purposes because it has just thick enough in the metallic state to create high reflection, while remaining thin enough to allow appreciable transmission in the hydride state. These simulations also take into account the volume expansion of the alloys upon hydrogenation of 15%. Another important factor in window technologies is to have color-neutral transmission. Windows with non-neutral color transmission tint the light as it transmits through the window, which is not ideal when attempting to make a clear window. To model this color distortion, we use the CIE 1931 XYZ color space and plot the perceived colors of the transmitted spectra. Note that only x and y need to be plotted to fully characterize the color because $x + y + z = 1$. On these plots, color-neutral is the $x = y = 0.333$ data point, which creates the ideal window. We show these switchable window properties for all of the investigated alloys in Figure 7.10.

For the Mg-Al alloys, we see poor transmission in the hydride state, with the

$Mg_{0.84}Al_{0.16}$ alloy having the highest transmission through the visible with values $<$ 40% transmission for most of the spectrum. These materials generally only exhibit $\sim$20% absolute change in transmission upon hydrogenation. This is due to the materials still exhibiting a high attenuation in the visible, even in the hydride state. These windows are close to color neutral, even with their low transmission, adding a small blue-green tint to the transmitted light.

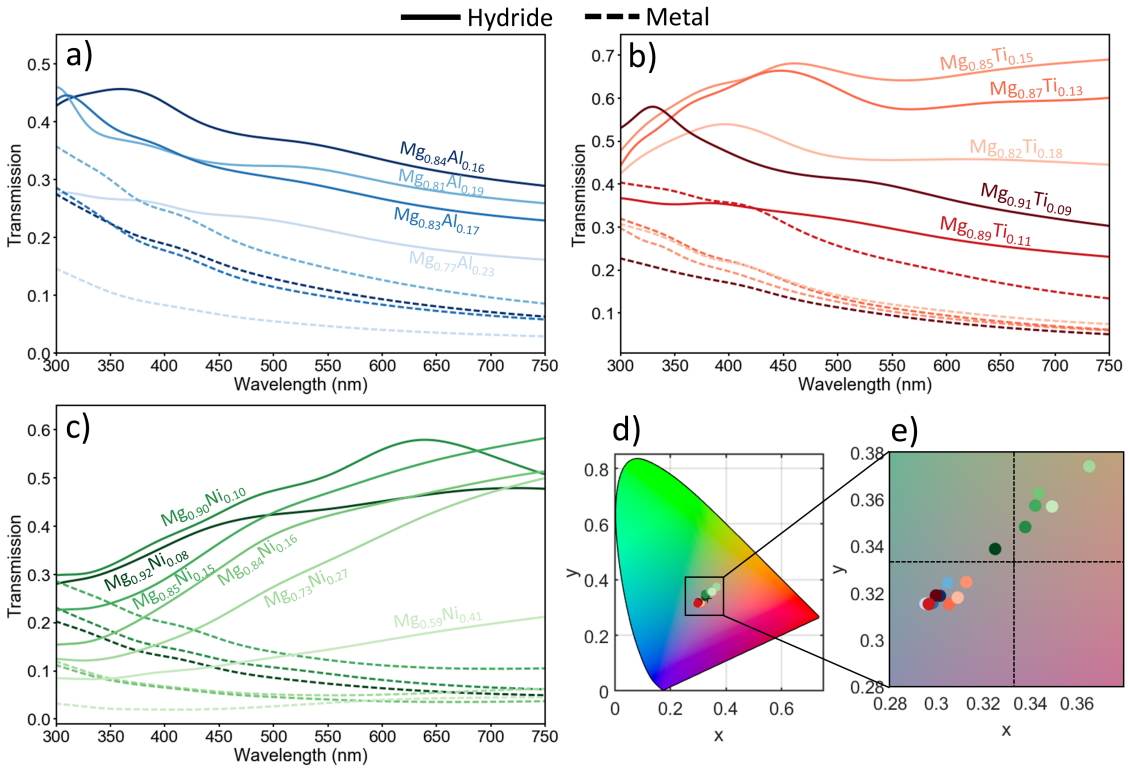

Figure 7.10: Simulated switchable window performance with Mg alloys. Simulated transmission values of thin film a) Mg-Al, b) Mg-Ti, and c) Mg-Ni alloys on SiO_2. The stack is defined as an SiO_2 substrate, a 25 nm Mg-Al film, and a 3 nm Pd capping layer. Transmission in the hydride (metal) state is represented by solid (dashed) lines. d) Chromaticity plot with the transmission color points for the different alloys. Colors of the points match with the colors in part a-c) along with the rest of the chapter. e) Zoom in of chromaticity plot. The intersection of the blacked dashed lines represents color neutral at x = y = 0.333.

Some of the Mg-Ti alloys perform much better as switchable window technolo-

gies with transmissions $> 60\%$ across most of the visible spectrum for $Mg_{0.85}Ti_{0.15}$ and $Mg_{0.87}Ti_{0.13}$. For these samples, we observe a transmission change of $\sim 40\%$. Higher transmission can be achieved in the hydride state by a thinning of the sample; however, this thinning causes the transmission in the metallic state to also become significantly higher. We find the transmission colors of these windows to be similar to those of the Mg-Al samples, being mostly color neutral with a slight blue-green tint. $Mg_{0.85}Ti_{0.15}$ is the most color neutral, in addition to having the highest transmission across most of the visible.

The Mg-Ni alloys measured in this chapter have poor switchable window characteristics, with low transmissions in the hydride state in the shorter wavelength visible region. For the longer wavelength visible, we see increased transmission but still only achieve values of $\sim 50\%$. However, we do see $\sim 40\%$ transmission changes in this region. Some Mg-Ni samples exhibit very good color neutrality, with $Mg_{0.92}Ni_{0.08}$ having a transmission color value of x = 0.325 and y = 0.338. The other alloys have a slight yellow tint, as opposed to the blue-green tint of the Mg-Al and Mg-Ti alloys.

As mentioned in the introduction, Mg-Ti alloys have also been investigated as broadband switchable light absorbers, with a highly reflecting state in the metallic form and a highly absorbing state when hydrogenated. The high absorption states for these materials have been found with thicker samples > 200 nm, much thicker than measured here, and it has been demonstrated that the total absorption of the film can be significantly tuned by just varying the thickness of the film [229, 248]. To see if our measured properties show any potential for switchable absorption, we

modeled a 300 nm Mg-Ti film on and SiO_2 substrate with a 10 nm Pd capping layer. The results of these simulations are shown in Figure 7.11. We see that for three of our measured Mg-Ti alloys, we achieve large amounts of switchable absorption throughout the visible, with absorption tailing off into the NIR. In the visible wavelength region, $Mg_{0.87}Ti_{0.13}$, $Mg_{0.85}Ti_{0.15}$, and $Mg_{0.82}Ti_{0.18}$ all achieve $>$ 80% absorption in the hydride state with $<$ 25% absorption in the metallic state (corresponding to high reflection in this state). This is a very large absorption change upon hydrogenation for these alloy compositions and shows their potential for broadband switchable light absorbers.

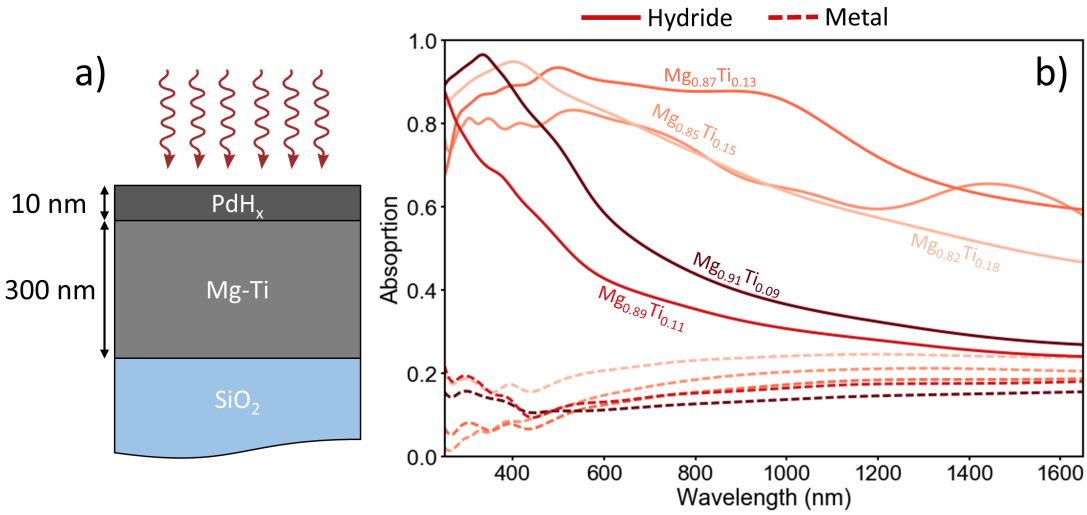

Figure 7.11: Broadband switchable light absorption with Mg-Ti alloys. a) Schematic of switchable light absorber consisting of a 300 nm Mg-Ti alloy with a 10 nm Pd cap on a SiO_2 substrate. b) Absorption plots for this structure for different alloy compositions. Solid (dashed) lines are absorption in the hydride (metallic) state. Colors represents different alloy compositions

Finally, as a last application, we determine whether these Mg alloy materials can be incorporated into the switchable absorber design demonstrated in Chapter 5. This architecture consisted of a Pd capped 25 nm Mg film deposited on an ITO

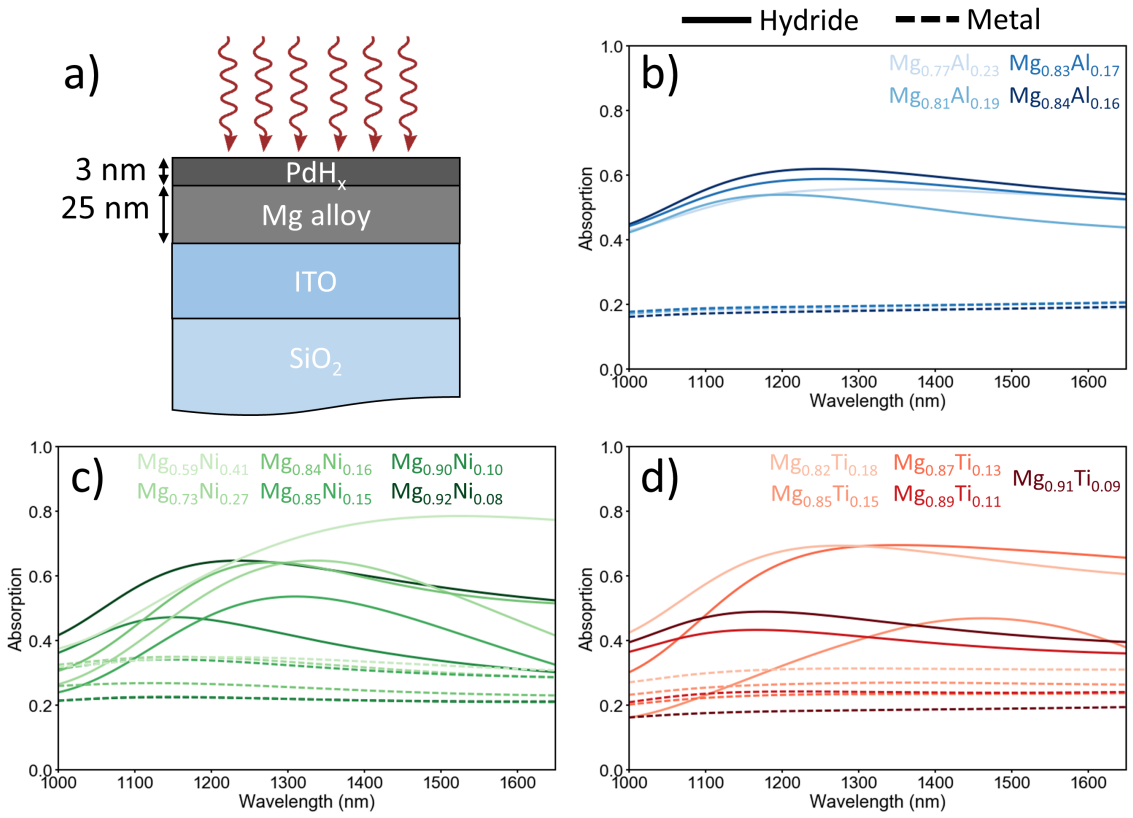

Figure 7.12: Simulation of Mg alloy/ITO switchable absorption device. a) Device architecture consisting of a SiO_2 substrate coated with a 350 nm ITO film, followed by 25 nm Mg, and a 3 nm Pd capping layer. b-d) Absorption plots of this system in the metallic (dashed lines) and hydrogenated (solid lines) states for Mg-Al, Mg-Ti, and Mg-Ni systems respectively.

substrate with an NZI resonance ~1250 nm. One issue with this setup was the time of hydrogenation and dehydrogenation were both long, around 30 min. With the faster kinetics of these Mg alloy samples, we ran simulations to determine whether a similar absorption change response could be obtained with any of these alloys. The results of our simulations are shown in Figure 7.12. We see from these plots that for any of the alloys we investigated here, we do not achieve as high of absorption as we attained with the pure Mg sample (93%). The largest absorption that we obtained was for $Mg_{0.59}Ni_{0.41}$ with a peak of 79% at 1524 nm. The Mg-Al samples

achieved final absorptions of ∼60% with two Mg-Ti samples achieving absorptions of 70% ($Mg_{0.87}Ti_{0.13}$ and $Mg_{0.82}Ti_{0.18}$). We conclude that although the kinetics may be improved with alloying in this system, the final absorption is not as high as it is for pure Mg.

7.6 Conclusions

In conclusion, we have for the first time experimentally measured the complex optical properties of different compositions of Mg-Al, Mg-Ti, and Mg-Ni alloys using spectroscopic ellipsometry. We have found a wide range in potential optical properties for the alloys in the final hydrogenated state, with most of the samples showing similar properties in the metallic state. We find mostly smooth optical transitions during the hydrogenation process when measured through the Pd capped side of the film, and showed that these measurements support previous observations of the Mg_2Ni "black state". We measured the loadings and stresses of all of these samples and found that the loadings of our materials are slightly less than those previously reported in the literature. Future experiments with this system will explore how different deposition parameters affect the properties of these alloys and how potential differences in alloy preparation could affect their final loadings and optical properties.

We also explored applications of these materials, showing that Mg-Ti alloys have potential as switchable windows and broadband switchable light absorbers. Further, we found that no alloys were able to outperform the high absorption of the

Mg/ITO device demonstrated in Chapter 5, indicating that more research needs to be done to find an alloy with increased kinetics to match the optical functionality of pure Mg for this structure.

Chapter 8: Conclusions and Future Experiments

This thesis provided details of our recent work utilizing metal hydrides as tunable plasmonic and nanophotonic materials. In Chapter 2, we described our custom-designed and fabricated measurement apparatus that simultaneously measures the optical, gravimetric, thermal, and stress properties of thin film and nanostructured samples. This apparatus allows us to quantify curvature changes of 0.001 m^{-1} and mass changes of 13 ng/cm^2 in material systems exhibiting large stress fluctuations. We also showed that our calorimetry model demonstrates a 150 μW calorimetric accuracy and 20 μW minimum detectable power and that we can obtain highly accurate optical property measurements by coupling our system with a spectroscopic ellipsometer. In Chapter 3, we used this apparatus to measure the optical properties of 5 different pure metals and demonstrated their potential use in various nanophotonic structures, showing 5 order of magnitude reflectivity changes and over 200 nm resonance shifts upon hydrogenation. In Chapter 4, we investigated a large variety of commercial NZI materials to identify the ranges of potential optical and electrical properties of different TCO materials. In Chapter 5, we then used one of those identified materials combined with a thin film metal hydride structure to experimentally demonstrate a switchable high absorption device, with a peak

absorption change of over 75%. Moving beyond pure metals, in Chapters 6 and 7 we introduced the benefits of alloying metals for added robustness to their optical responses. We investigated Pd-Au alloys and showed how measurable signals can be achieved with Pd atomic percentages as low as 34% and demonstrated hydrogen sensors with no surface poisoning or hysteresis, as well as a physical encryption scheme. We then showed the wide range of potential optical properties in the Mg alloy system, measuring and fitting the optical properties of different atomic compositions of Mg-Al, Mg-Ni, and Mg-Ti systems and showing potential uses of Mg-Ti alloys as broadband switchable light absorbers and switchable windows. Ultimately, this work has measured the properties of many types of metal hydrides and has opened up new avenues for the simulation and design of novel nanophotonic devices using our measured properties. In the following section, we will describe future directions of this research focusing on two potential material directions: using high-entropy alloys as metal hydrides to further explore the optical parameter space and by using plasmonic resonances in metal hydrides to lower the Coulomb barrier in nuclear reactions.

8.1 High entropy metal hydrides

In this thesis, we only investigated bi-metallic systems to improve the optical and structural properties of pure metal hydrides. These bi-metallic alloys open a wide parameter space, but to perfect certain designs, we can expand even further. Work is already being done using ternary metal alloy hydrides as hydrogen sensors,

specifically using a Pd-Au-Cu system to further improve chemical resistance and stability [22]. In these binary and ternary systems, generally there is a principal active element, with small additions of other secondary elements to adjust the material properties. In the case of Pd-Au-Cu, the Pd is the primary element with the secondary Au and Cu to enhance chemical resistance and cyclability. A new class of alloys has recently been investigated that uses many principal elements in high concentrations that exhibit properties that can far exceed those of traditional alloys [249]. These materials, named high entropy alloys (HEA), have become of particular interest in the hydrogen storage community since it has been demonstrated that a TiVZrNbHf HEA can absorb hydrogen to a much higher loading than normal transition metal hydrides (≤ 2) up to a loading of 2.5 H/M [250]. This large hydrogen storage capacity is due to increased lattice strains within the alloy, allowing hydrogen atoms to occupy both tetrahedral and octahedral interstitial sites. Many other combinations and different ratios of transition metals are currently being investigated to attempt to surpass this loading value [251, 252, 253].

Although HEAs have been studied for hydrogen storage applications, they have yet to be investigated for optical devices. One reason for this absence is that so far these materials have not been able to be fabricated at the nanoscale. The most common way of manufacturing the alloys is by arc melting specifically chosen ratios of the pure metals multiple times under an inert atmosphere. This method gives an ingot of the material so that the properties can be studied in bulk, but the method cannot be easily translated to thin films or nanostructures. As far as we know, there have been no attempts to use these ingots to deposit thin films through

a physical vapor deposition process such as electron beam evaporation or sputtering, but there is concern that there will be a separation of the individual metals during the cooling process. With this separation, the benefits of the HEA could be lost. Potentially combining a flash cooling method with this technique could yield positive results, which needs to be investigated. Other groups have been able to fabricate nanoparticles on carbon supports using flash heating and cooling, which has been demonstrated to be successful in fabricating HEAs with up to 8 elements [254]. This process would be very interesting to investigate with metal hydride HEAs to see if these nanoparticles can have exotic optical responses when exposed to H_2 gas. Unfortunately, this process only creates these particles on these specific supports and is not very versatile to other systems, thus more work is necessary to attempt to broaden the substrate choice. Lastly, co-sputtering has been shown to create non-energetically favorable alloys under certain conditions and could potentially be used to fabricate thin-film HEAs. The limitation is that most sputtering systems can only deposit 2-3 elements at a time. If a custom system was built that could co-deposit up to 5 elements, then thin-film and nanostructured devices could potentially be implemented. Using the apparatus described in this thesis, we could then measure the nanoscaled properties of these materials to determine whether further improvements to hydrogen sensors or other device designs could be implemented.

8.2 Nuclear plasmonics with metal hydrides

Moving beyond nanophotonic devices, we believe that metal hydrides can have future uses in increasing nuclear reaction rates. It has already been shown at Lawrence Berkeley National Laboratory and the National Aeronautics and Space Administration that when certain metal hydrides are loaded with a high density of deuterium atoms, the Coulomb barrier between deuterium ions is reduced due to the screening from the conduction electrons from the host metal [255, 256, 257]. This lowering of the Coulomb barrier allows for a greater probability of a deuterium ion tunneling through this barrier, causing a nuclear reaction. This effect is most prevalent at lower energies < 5 keV, as this is the energy region in which electron screening plays the largest part in nuclear reaction probabilities (at high energies, effects from screening become negligible). Schenkel et al. found that this screening effect from the metal hydride lattice was 1000 ± 250 eV, causing a significant increase in the fusion rates for ion energies < 5 keV [255]. These findings open up the door to potentially energetically favorable nuclear fusion reactions at much lower temperatures than previously thought.

We propose that this electron screening effect from the metal hydride lattice can be further enhanced by plasmonically exciting the target. Plasmonic excitations can increase the electric field on the edges of nanostructures by up to 1000x in ideal structures [258]. This large field enhancement could dramatically decrease the Coulomb barrier for deuterium atoms within this region. The plasmonic enhancements do not cause steady-state electric field enhancements at a specific point

on the structures, but the time scale of the plasmonic enhancement is still much great than that necessary for a nuclear reaction (10^{-9} s compared to 10^{-12} s [259]). This time scale difference allows for more than enough time to get a measurable enhancement of D-D fusion.

Our proposed experiment uses a nanoporous Pd membrane as our plasmonic metal hydride target. Nanoporous membranes have been well studied and can be fabricated using the process of dealloying. In this process, first, a bi-metallic alloy film is deposited onto a substrate, where one of the metals in the alloy is the metal of interest and the other is a sacrificial metal. This alloy is then wet etched until the sacrificial metal has completely dissolved and the remaining film is a nanoporous sheet of the desired metal. This process has been demonstrated to create Pd nanoporous membranes by using $Pd_{0.2}Co_{0.8}$ alloy and etching it in H_2SO_4 [260]. These membranes can have fairly strong plasmonic resonances, allowing for high field enhancements at ridges of the pores [261, 262]. We believe that these nanoporous materials are ideal for these experiments because they are robust to degradation from an incident ion beam. As the ion beam slowly breaks down the top of the target, the plasmonic resonance still stays intact because of the thick, random structure of the target. This is compared to other plasmonic targets, such as nanogratings or bowtie structures, that would stop exhibiting a strong plasmonic resonance after a small degradation in the structure.

To create the nuclear reactions on this target, we will use a variable energy deuterium ion gun, where the energy can be tuned from 0.5 - 5 keV. This range is ideal for these experiments because at the upper energy end we will be able to create

fusion reactions without any electron field enhancement, thus we can compare to literature values in this range. As we lower this ion gun energy, we then get into the energy regime where the greatest enhancements to the fusion rate will occur due to the reduction in the Coulomb barrier. We will then excite the nanoporous target with a visible laser set at the experimentally determined plasmonic resonance of the target. To find the effect of the plasmonic excitation on the nuclear reaction rate, we will compare the nuclear byproduct formation rate with the plasmonic excitation laser on and off. We will measure the neutron and proton formation from the nuclear reactions with the setup outlined in Schenkel et al. [255].

The results of these experiments will inform the possibilities to tailor nuclear reaction rates using visible light excitation. Structuring targets in nuclear reactors could significantly lower the necessary energy needed to spark nuclear fusion reactions. Beyond these experiments, there are many other applications of this nuclear plasmonics concept. One in particular would be to use plasmonic excitation to change the rates of nuclear decay of certain radioactive atoms. We know that the rate of α decay is dependent on the tunneling rate through the Coulomb barrier, thus if we lower this barrier through plasmonic excitation, we could speed up this decay process in a controlled way.

Appendix A: Curvature to frequency derivation

We know that there are no (DC) shear strains in this system, meaning $\epsilon_4 = \epsilon_5 = \epsilon_6 = 0$. Here and in what follows we use the standard contracted, Voigt notation and with ϵ's being strains, σ's being stresses, u's being displacements, and A's being stiffness elements. We can then multiply the strain by the stress tensor to get expressions for σ_1 and σ_2. The relationship between these two quantities is important in calculating wave propagation speeds in the crystal.

$$\begin{pmatrix} \sigma_1 \\ \sigma_2 \\ \sigma_3 \\ \sigma_4 \\ \sigma_5 \\ \sigma_6 \end{pmatrix} = \begin{pmatrix} A'_{11} & A'_{12} & A'_{13} & A'_{14} & A'_{15} & A'_{16} \\ A'_{21} & A'_{22} & A'_{23} & A'_{24} & A'_{25} & A'_{26} \\ A'_{31} & A'_{32} & A'_{33} & A'_{34} & A'_{35} & A'_{36} \\ A'_{41} & A'_{42} & A'_{43} & A'_{44} & A'_{45} & A'_{46} \\ A'_{51} & A'_{52} & A'_{53} & A'_{54} & A'_{55} & A'_{56} \\ A'_{61} & A'_{62} & A'_{63} & A'_{64} & A'_{65} & A'_{66} \end{pmatrix} \begin{pmatrix} \epsilon_1 \\ \epsilon_2 \\ \epsilon_3 \\ \epsilon_4 \\ \epsilon_5 \\ \epsilon_6 \end{pmatrix} \tag{A.1}$$

Thus, we have

$$\sigma_1 = A'_{11}\epsilon_1 + A'_{12}\epsilon_2 + A'_{13}\epsilon_3 \tag{A.2}$$

$$\sigma_2 = A'_{21}\epsilon_1 + A'_{22}\epsilon_2 + A'_{23}\epsilon_3 \tag{A.3}$$

Since the film is free to expand along x_3, we know that there is no stress σ_3. We can use this information to determine ϵ_3 as a function of ϵ_1 and ϵ_2.

$$\sigma_3 = 0 = A'_{31}\epsilon_1 + A'_{32}\epsilon_2 + A'_{33}\epsilon_3 \tag{A.4}$$

Solving for ϵ_3 yields

$$\epsilon_3 = \frac{A'_{31}\epsilon_1 + A'_{32}\epsilon_2}{A'_{33}} \tag{A.5}$$

We can also determine expressions for ϵ_1 and ϵ_2 if we make an assumption of the shape of the curved region. If the strained region has constant curvature, the displacement in that region can be written as

$$u_3 = \frac{\kappa_1}{2}x_1^2 + \frac{\kappa_2}{2}x_2^2 \tag{A.6}$$

Where $\kappa_1(\kappa_2)$ is the curvature in the x (y) direction. Earlier, we noted that there are no shear strains in this system. We can use this fact again to obtain expressions forϵ_1 and ϵ_2. We can write out the definition of strain to get

$$\epsilon_5 = 0 = \frac{1}{2}\left(\frac{\partial u_3}{\partial x_1} - \frac{\partial u_1}{\partial x_3}\right) \tag{A.7}$$

And thus,

$$\frac{\partial u_1}{\partial x_3} = -\frac{\partial u_3}{\partial x_1} \tag{A.8}$$

We know that u_3 is given by the expression above. Importantly, it does not depend on x_3, we can integrate with respect to x_3. We can then differentiate that expression with respect to x_1 to obtain an expression for the strain in the x_1 direction.

$$\frac{\partial u_1}{\partial x_1} = \epsilon_1 = -x_3 \frac{\partial^2 u_3}{\partial x_1^2} \tag{A.9}$$

Substituting in for u_3 yields

$$\epsilon_1 = -\kappa_1 x_3 \tag{A.10}$$

A similar analysis for ϵ_2 gives

$$\epsilon_2 = -\kappa_2 x_3 \tag{A.11}$$

We can insert these expressions for the strains along with the expression for ϵ_3 as a function of ϵ_1 and ϵ_2 into an above equation to yield

$$\sigma_1 = -A'_{11}\kappa_1 x_3 - A'_{12}\kappa_2 x_3 - \frac{A'_{13}A'_{31}}{A'_{33}}\kappa_1 x_3 - \frac{A'_{13}A'_{32}}{A'_{33}}\kappa_2 x_3 \tag{A.12}$$

$$\sigma_2 = -A'_{21}\kappa_1 x_3 - A'_{22}\kappa_2 x_3 - \frac{A'_{23}A'_{31}}{A'_{33}}\kappa_1 x_3 - \frac{A'_{23}A'_{32}}{A'_{33}}\kappa_2 x_3 \tag{A.13}$$

Now, if we assume that the curvatures must be identical along both axes due to sample clamping, we drop the κ direction distinction and find

$$\sigma_1 = -\kappa x_3 \left(-A'_{11} - A'_{12} - \frac{A'_{13}}{A'_{33}}(A'_{31} + A'_{32}) \right) \tag{A.14}$$

$$\sigma_2 = -\kappa x_3 \left(-A'_{11} - A'_{12} - \frac{A'_{13}}{A'_{33}}(A'_{31} + A'_{32}) \right) \tag{A.15}$$

As per EerNisse [46], the velocity of a shear wave through a crystal at zero stress, W_0, along a direction oriented at an angle θ relative to the x_3 axis, is given by

$$\rho_0 W_0^2 = C_{66} cos^2\theta + C_{44} sin^2\theta + 2C_{14} sin\theta cos\theta \tag{A.16}$$

Here, the stress tensor coefficients are in the crystal axes, not the lab axes. In the lab axes, the ratio of the stresses is $T'_2 = \sigma_2/\sigma_1$. Along the crystal axes, we have

$$\begin{aligned} T_2 &= cos^2\theta T'_2 \\ T_3 &= sin^2\theta T'_2 \\ T_4 &= sin\theta cos\theta T'_2 \end{aligned} \tag{A.17}$$

The expression relating the angle of propagation and curvature to the wave speed is then

$$W(\theta, x_3, \kappa) = \frac{1}{\sqrt{\rho_0}}(\rho_0 W_0^2 + \sigma(x_3, \kappa)(cos^2\theta(-0.08 + 1.38T_2 + 1.66T_3 + 0.49T_4) + sin^2\theta(0.55 + 0.20T_2 - 2.68T_3 - 5.75T_4) + 2sin\theta cos\theta(-1.81 + 0.28T_2 - 0.55T_3 - 0.04T_4))^{1/2} \tag{A.18}$$

Because the speed is a function of x_3, it changes as the wave propagates through the crystal. To calculate the total transit time, we need to take an integral. The transit time through the crystal and back to the starting point is given by

$$t(\kappa, \theta) = \int_{-h/3}^{2h/3} \frac{dx_3}{W(\theta, x_3, \kappa)} \tag{A.19}$$

The limits of the integral are referenced to the plane of no stress in the crystal, which is $h/3$ from the bottom of the crystal [263]. The change in oscillation frequency as a function of stress is then

$$\Delta f(\theta, \kappa) = \frac{1}{2t(\kappa, \theta)} - \frac{1}{2t(\kappa, 0)} \tag{A.20}$$

Thus, the change in frequency depends nearly linearly on curvature with a slope of approximately α = -777 Hz/m^{-1}.

Appendix B: Commercial NZI Materials Optical Properties

The individual optical properties of each of the TCO materials investigated in Chapter 4 are reported here. There properties were measured with spectroscopic ellipsometery combined with transmission measurements and fit with a Drude-Loretnz oscillator model. Figures B.1, B.2, and B.3 show the optical properties of the ITO samples, Figure B.4 shows the optical properties of the FTO samples, and Figure B.5 shows the optical properties of the AZO samples. The headers in each graph show the material, the company the sample was sourced from, and the nominal resistance quoted by that company.

We summarize the complete findings from these measurements in Table B.1 and Table B.2. In these tables, we report the minimum $|n|$ achieved for each sample, the location of the minimum, the NZI bandwidth, the measured thickness t of the TCO, and the measured resistance R.

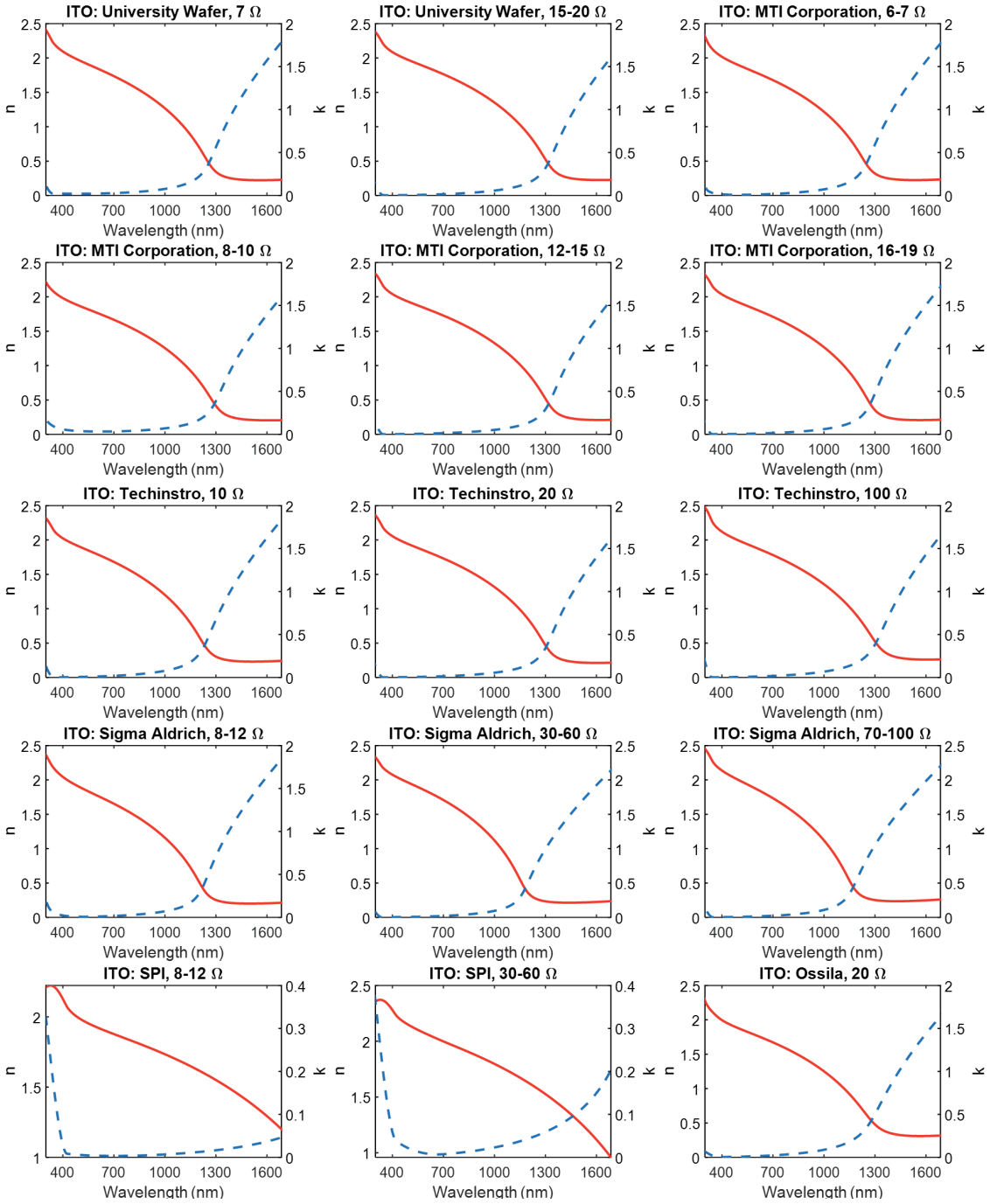

Figure B.1: Optical properties of commercially sourced ITO samples. Above each sample plot is the name of the company the sample was sourced from and the nominal resistance quoted for the sample.

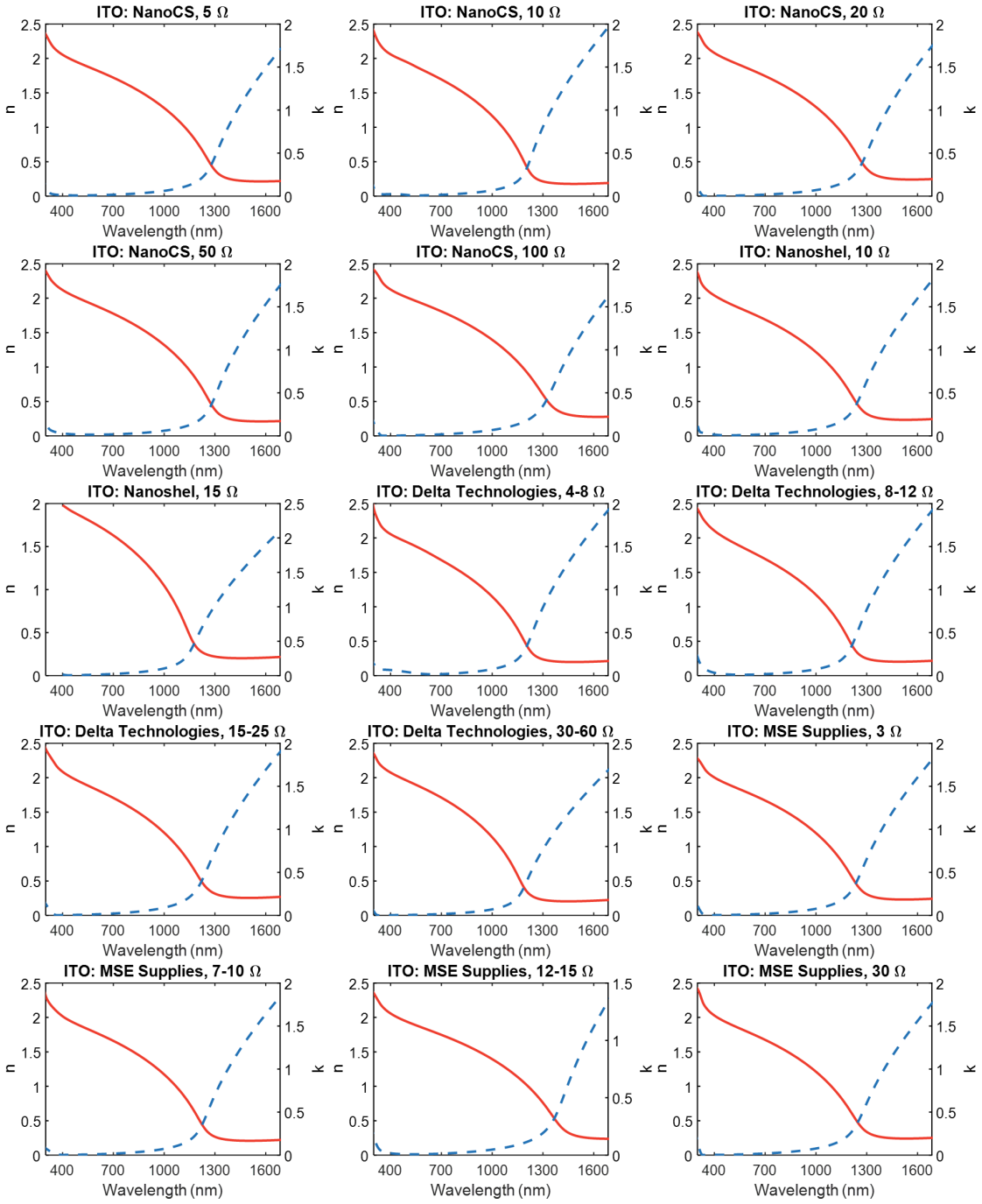

Figure B.2: Optical properties of commercially sourced ITO samples. Above each sample plot is the name of the company the sample was sourced from and the nominal resistance quoted for the sample.

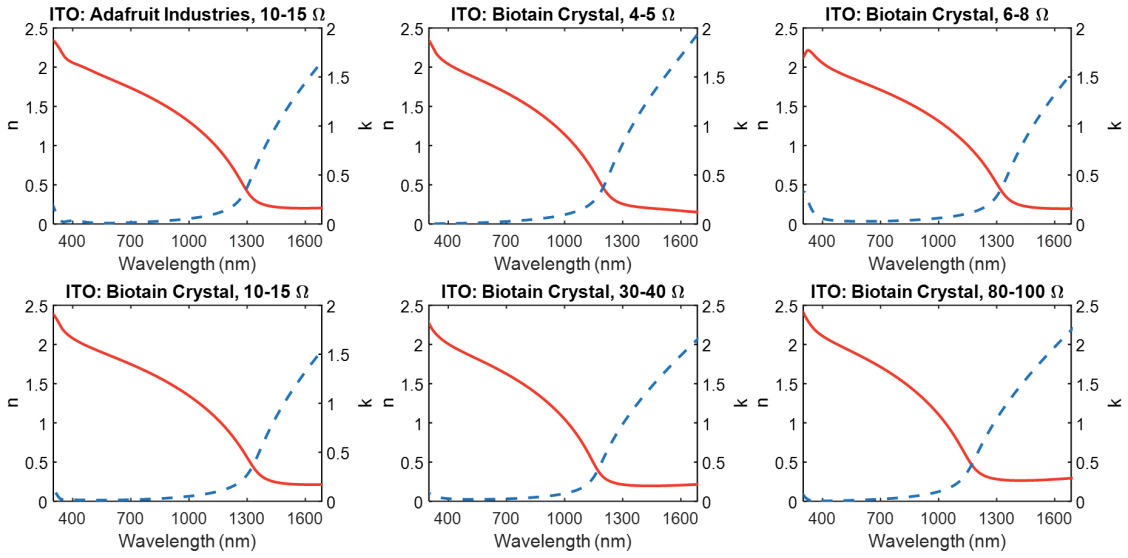

Figure B.3: Optical properties of commercially sourced ITO samples. Above each sample plot is the name of the company the sample was sourced from and the nominal resistance quoted for the sample.

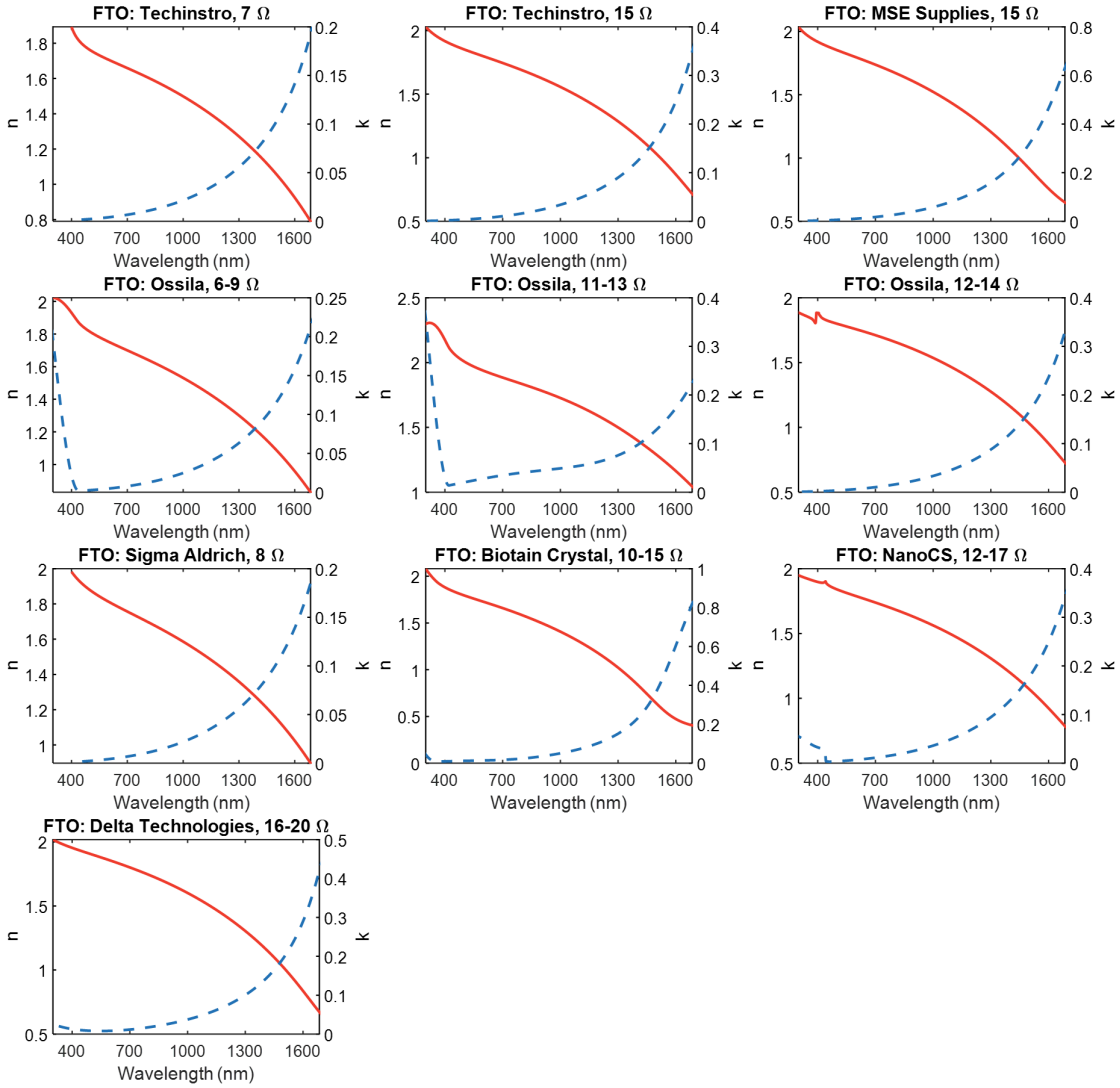

Figure B.4: Optical properties of commercially sourced FTO samples. Above each sample plot is the name of the company the sample was sourced from and the nominal resistance quoted for the sample.

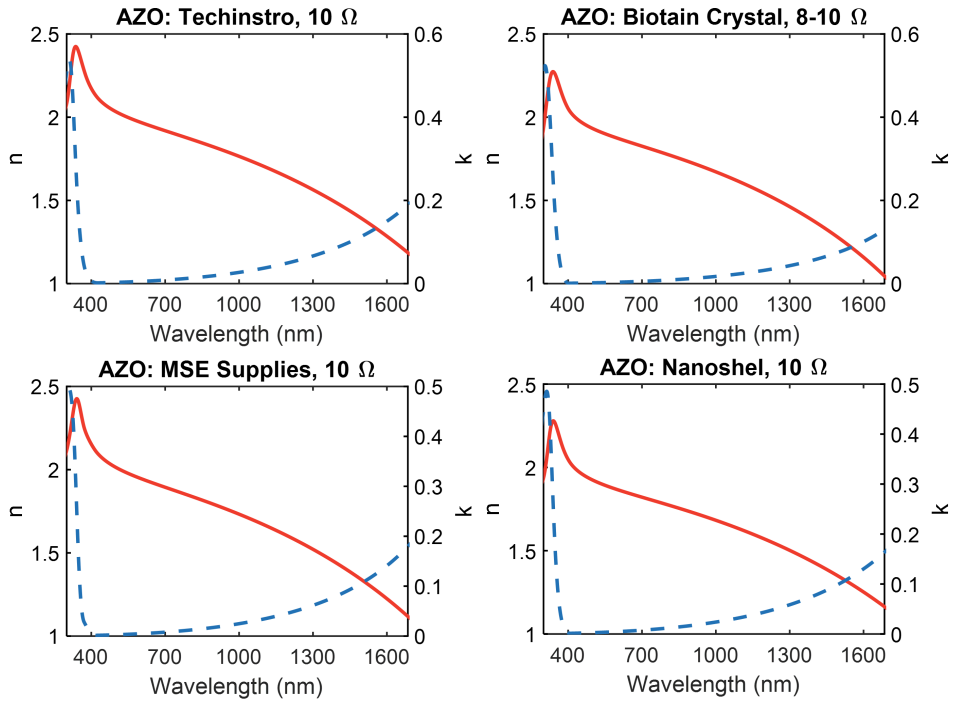

Figure B.5: Optical properties of commercially sourced AZO samples. Above each sample plot is the name of the company the sample was sourced from and the nominal resistance quoted for the sample.

Company	Material	Nominal R (Ω)	R (Ω)	t (nm)	$\|n\|_{min}$	λ_{center}	BW (nm)
Adafruit Industries	ITO	10-15	8.45	181.5	0.56	1300	303
Biotain Crystal	AZO	8-10	8.35	916.8	0.67	1984	492
Biotain Crystal	FTO	10-15	15.06	382.3	0.72	1536	406
Biotain Crystal	ITO	10-15	11.15	138	0.57	1333	314
Biotain Crystal	ITO	30-40	23.15	56.6	0.56	1166	279
Biotain Crystal	ITO	4-5	6.09	212.7	0.59	1205	284
Biotain Crystal	ITO	6-8	8.38	180.7	0.56	1326	326
Biotain Crystal	ITO	80-100	76.27	19.1	0.66	1162	237
Delta Technologies	FTO	16-20	19.96	234.8	0.78	1715	364
Delta Technologies	ITO	15-25	19.61	67.5	0.63	1225	273
Delta Technologies	ITO	30-60	44.29	29.2	0.57	1183	257
Delta Technologies	ITO	4-8	8.43	158.9	0.55	1211	288
Delta Technologies	ITO	8-12	11.55	121.2	0.56	1218	284
MSE Supplies	AZO	10	10.60	869	0.82	1993	390
MSE Supplies	FTO	15	20.72	307	0.88	1627	296
MSE Supplies	ITO	12-15	13.43	133.4	0.60	1392	344
MSE Supplies	ITO	30	34.28	46.3	0.61	1251	298
MSE Supplies	ITO	3	3.97	354	0.59	1241	295
MSE Supplies	ITO	7-10	5.99	227.1	0.57	1229	297
MTI Corporation	ITO	12-15	11.09	142.6	0.57	1325	315
MTI Corporation	ITO	16-19	14.22	106.9	0.57	1277	301
MTI Corporation	ITO	6-7	6.47	222.6	0.59	1254	300
MTI Corporation	ITO	8-10	9.37	186.1	0.57	1297	327
NanoCS	FTO	12-17	7.08	349.1	0.81	1774	393
NanoCS	ITO	100	78.09	21.6	0.67	1326	272
NanoCS	ITO	10	7.59	174.8	0.53	1211	281
NanoCS	ITO	20	15.69	94.2	0.62	1278	284
NanoCS	ITO	50	41.91	36.8	0.58	1285	282
NanoCS	ITO	5	3.91	354	0.58	1282	299

Table B.1: Summary of commercial NZI data#1. In this table we report the company, the nominal resistance, the measured sheet resistance R, the measured thickness t, the minimum possible magnitude of the index of refraction $|n|_{min}$, the location of that minimum λ_{center}, and the bandwidth BW of the resonance where $|n| < 1$

Company	Material	Nominal R (Ω)	R (Ω)	t (nm)	$\lvert n\rvert_{min}$	λ_{center}	BW (nm)
Nanoshel	AZO	10	10.10	891.3	0.85	2063	402
Nanoshel	ITO	10	8.38	185	0.60	1246	291
Nanoshel	ITO	15	25.06	61.7	0.58	1160	270
Ossila	FTO	11-13	11.33	437.9	0.85	1919	347
Ossila	FTO	12-14	13.22	355.5	0.75	1764	440
Ossila	FTO	6-9	7.80	625	0.69	1856	524
Ossila	ITO	20	17.34	111.5	0.68	1281	299
SPI	ITO	30-60	34.62	126.5	0.73	1864	363
Sigma Aldrich	FTO	8	8.20	603.1	0.69	1887	497
Sigma Aldrich	ITO	30-60	45.04	30.2	0.59	1174	251
Sigma Aldrich	ITO	70-100	85.31	18.1	0.62	1165	237
Sigma Aldrich	ITO	8-12	11.64	123.4	0.55	1225	302
Techinstro	AZO	10	11.03	838.6	0.90	2023	306
Techinstro	FTO	15	12.89	343	0.76	1754	419
Techinstro	FTO	7	7.03	574.4	0.64	1848	555
Techinstro	ITO	100	83.43	18.5	0.64	1311	281
Techinstro	ITO	10	8.05	183.5	0.60	1237	290
Techinstro	ITO	20	10.24	148.5	0.57	1311	308
University Wafer	ITO	15-20	15.42	101	0.60	1320	297
University Wafer	ITO	7	6.34	213.3	0.60	1264	284

Table B.2: Summary of commercial NZI data #2. In this table we report the company, the nominal resistance, the measured sheet resistance R, the measured thickness t, the minimum possible magnitude of the index of refraction $\lvert n\rvert_{min}$, the location of that minimum λ_{center}, and the bandwidth BW of the resonance where $\lvert n\rvert < 1$

Appendix C: H_2 Safety Protocols

When working with hydrogen gas, certain precautions must be taken to ensure safety in the laboratory. H_2 gas is colorless, odorless, and tasteless, so one cannot rely on their senses alone to detect a leak in their system. H_2 gas is flammable and is dangerous when it is in concentrations between 4% and 75% at atmospheric pressure. This is the combustion range for this gas. Below this range, there is not enough H_2 in the atmosphere for ignition, and above this range, there is not enough O_2. H_2 has a very low ignition energy, so even a small spark in this partial pressure range can set off an explosive reaction. Because of this, any room where hydrogen is being worked with should have good ventilation that is adequate enough to deal with the largest expected H_2 leak in the laboratory. Any hydrogen that is being used in an experiment and then discarded should be piped directly into this ventilation shaft.

Leaks when working with H_2 gas should be expected from time to time, as hydrogen can leak from very small gaps in the tubing connectors due to its small molecular size. It is recommended to use a hydrogen leak detector near any H_2 gas lines to alert of any leaks. Along with this, gas pressures should be periodically checked to make sure that they are depleting by the expected value of hydrogen

used in an experiment. To test the leak rate of the system, pressurize the system to the normal working pressure of an experiment, close off the input from the H_2 cylinder and output at the pressure controller, and measure the time it takes for the system to depressurize. If a leak is found, a common method to find the leak is the "soapy water method". Simply, soapy water is brushed onto any tubing connectors that are suspected to contain the leak. If soap bubbles begin to form around the connector, a leak has been identified and the fitting should be replaced. The leak rate test should then be performed again to ensure that the leak was properly fixed and that there are no more leaks in the system.

H_2 gas is known to cause embrittlement in certain materials. Make sure that all piping and gas connectors are rated to be compatible with H_2 and won't degrade over time. Only use regulators that have been specifically designed for hydrogen. For H_2 cylinder storage, the cylinders must be stored upright and should be secured to the wall. These cylinders should be kept away from any heating element, including direct sunlight. When moving the cylinders, be sure to completely close the valve, remove the regulator, fully screw on the safety cap, and chain the cylinder into the cart being used.

Appendix D: H_2 Sensors

Fast and reliable H_2 are becoming essential in the newly emerging hydrogen economy. H_2 gas can be created using the electrolysis of water, which can be driven with green electricity from sources like solar or wind power. When burned, H_2 gas gives off no greenhouse gasses, making it an ideal fuel for vehicles or as a method to store energy. In order to use it for any of these purposes, H_2 detectors are needed to locate any leaks quickly and efficiently, as H_2 is very combustible. There are five main components that must be accounted for to make an ideal H_2 gas sensor, as laid out by the United States Department of Energy [185]:

1. Reliable: Sensors must have unambiguous readings regardless of what the previous conditions were in the environment. This means that there can be no intracycle or intercycle hysteresis. Each value of the sensor signal must be mapped to a single hydrogen pressure value.

2. High Accuracy: Sensors must be able to measure H_2 pressure with precision in the range of 0.1 - 10% at atmospheric pressure.

3. Lifetime: Sensors must be able to run for many cycles of hydrogen gas, ideally reaching 10 years of successful operation. These sensors must also be

able to be resistant to poisoning gases in the atmosphere such as CO and sulfides. Additionally, the sensors must be able to perform in high humidity environments.

4. Speed: Sensor detection and recovery time should be < 1 second.

5. Cost: Sensor fabrication should be cheap enough to be feasibly made in bulk

There are many types of H_2 sensors that have been demonstrated in the literature or are currently on the market that have been attempting to reach these DOE goals. A summary of the current device types and how they operate follows:

1. Catalytic: A catalytic wire array is heated and introduced to the H_2 gas, which then reacts with O_2. This reaction releases heat, which is then measured and can be converted to H_2 pressure [264].

2. Electrical Conductivity: A metal hydride wire or thin film is exposed to H_2 gas and the change in the resistance of the metal hydride is measured and converted to the pressure of H_2 in the chamber [265, 266, 267, 268].

3. Thermal Conductivity: Heated gas is run through a pipe and changes in the thermal conductivity of the gas are used to calculate changes in gas composition [269].

4. Semiconductor Metal Oxides: Certain metal oxides have a large resistance change when exposed to H_2, such as SnO_2, and this resistance is used as a proxy for hydrogen concentration [270, 271]. Must be done at high temperatures.

5. Electrochemical: Electrodes are submerged in solution and gas is piped in through a porous membrane. Amount of H_2 in the gas changes the measured current [272, 273].

6. MOS/MOSFET/Schottky Diode: The top electrode is made of Pd or another hydrogen sensitive metal. As it hydrogenates, the work function of the structure changes and can be measured as a proxy for the H_2 concentration [274, 275, 276].

7. Surface Acoustic Wave Detector: As a material hydrogenates, the velocity of surface acoustic waves change due to conductivity changes in the Pd. This velocity change can be correlated with different H_2 amounts [277, 278].

8. Microelectromechanical: Structural changes in metal hydrides upon hydrogenation are used to determine the H_2 gas concentration. These designs include measuring the capacitance between a metal hydride cantilever and a plate, with the cantilevers bending at different angles with different H_2 concentrations [279] and using metal hydride nanoparticles that expand upon hydrogenation, completing an electrical circuit for a sharp drop in electrical resistance [280].

Another type of hydrogen sensor that is not yet commercially available, but is seeing significant attention in research and development, is optical hydrogen sensors. Optical hydrogen sensors are desirable for many reasons over some of the other

sensor types above. Optical sensors do not require for there to be any electrical connections in the region of detection, which eliminates any combustion risk from a spark from the detector. These sensors can also be designed to perform at room temperature, have a very fast sub-second response time, and can be highly selective to hydrogen compared with other methods. Within optical hydrogen sensors, many different designs can achieve effective readings. The most common design is to use nanoparticle arrays of metal hydrides. In these systems, a nanoparticle metal hydride array, typically Pd or a Pd-based alloy, is deposited on a glass substrate. The LSPR of this array is then measured with a spectrometer. By measuring the shift of the LSPR, the atmospheric H_2 percentage can be determined. By alloying the metal hydride with other transition metals, coating the array with a hydrogen-permeable polymer, or optimizing the nanoparticle shape and size, these sensors can have improved speed, sensitivity, and poisoning resistance. Demonstrations of these sensors have been widely shown in the literature [22, 23, 74, 77, 281, 282]. Other systems utilize thin film metal hydrides, using the reflectance of light off the thin film as a measure of the H_2 content in the atmosphere [17, 76, 283, 284]. Optical fibers are also frequently used as a base for optical H_2 sensors. These fibers can be coated with metal hydrides and can measure the H_2 pressure by either measuring the change in path length due to hydride expansion upon hydrogenation [25], measuring attenuation changes in the fiber [285, 286], measuring shifts in the Surface Plasmon Resonance within the fiber [287, 288], or using a metal hydride mirror at the end of the fiber and measuring changes in reflectivity [26, 247]. Finally, measuring shifts of the Surface Plasmon Resonance without coupling into a fiber have been used as

a sensing scheme [75, 289].

Appendix E: CIE 1931 Color Space Calcuations

In this thesis, we use the CIE 1931 color space to determine the colors of different structures under white light illumination. Our white light source is defined by the CIE Standard Illuminant D65 [290]. This color space is used to determine the color an average person would perceive under medium to bright illumination (at low brightness, the human perception becomes monochromatic). Color perception is determined by three types of cones in the average human eye that have different sensitivities at different wavelengths. This is why most color spaces can be determined with three values, with each value representing a level of stimulus for each of these different types of cones. The CIE 1931 color space is based off a "Standard Observer" where color matching functions $\bar{x}(\lambda)$, $\bar{y}(\lambda)$, and $\bar{z}(\lambda)$ describe the relative perception of red, green, and blue color for an average person. In this thesis, we use the analytical approximation to the CIE color tables from Ref [291]:

$$\bar{x}(\lambda) = 1.065 \exp\left(-0.5\left(\frac{\lambda - 595.8}{33.33}\right)^2\right) + 0.366 \exp\left(-0.5\left(\frac{\lambda - 446.8}{19.44}\right)^2\right) \quad \text{(E.1)}$$

$$\bar{y}(\lambda) = 1.014 \exp\left(-0.5\left(\frac{ln\lambda - ln556.3}{0.075}\right)^2\right) \tag{E.2}$$

$$\bar{z}(\lambda) = 1.839 \exp\left(-0.5\left(\frac{ln\lambda - ln449.8}{0.051}\right)^2\right) \tag{E.3}$$

With these analytical color matching functions, we can then calculate the CIE 1931 XYZ color values from a reflection or transmission spectrum using the following equations:

$$k = \int_0^\infty S_{D65}(\lambda)\bar{y}(\lambda)d\lambda \tag{E.4}$$

$$X = \frac{\int_0^\infty S_{D65}(\lambda)\bar{x}(\lambda)R(\lambda)d\lambda}{k} \tag{E.5}$$

$$Y = \frac{\int_0^\infty S_{D65}(\lambda)\bar{y}(\lambda)R(\lambda)d\lambda}{k} \tag{E.6}$$

$$Z = \frac{\int_0^\infty S_{D65}(\lambda)\bar{z}(\lambda)R(\lambda)d\lambda}{k} \tag{E.7}$$

Where k is a normalizing constant, X, Y, and Z are the tristimulus values, R is the reflection spectrum, and S_{D65} is the CIE D65 radiance spectrum. Note that transmission can be directly substituted for the reflection in these equations when determining colors of transmission through a material (such as the switchable windows in Chapter 7). To be able to plot these colors on a 2D diagram, we can

further convert these tristimulus values to the CIE xyY color space which divides the color into two parts: chromaticity and brightness. The brightness is determined by the Y value, while x and y are defined by:

$$x = \frac{X}{X + Y + Z} \tag{E.8}$$

$$y = \frac{Y}{X + Y + Z} \tag{E.9}$$

These two values determine the chromaticity of the spectra, with the value x = y = 0.33 representing the color neutral point. Note that chromaticity is not the same as a printing color, as the chromaticity is dependent on the spectrum of the illuminating light.

Appendix F: Useful Properties of Metal Hydrides and Hydrogen

Metal hydrides are classified as compounds containing a metal-hydrogen bond and can be classified into three categories: ionic, covalent, or metallic [292]. The alkali and alkaline earth metals generally form ionic hydrides, exhibiting properties similar to other salts formed from a combination of these elements and an element in the halogen group [292]. Metals to the right of group VII form covalent bonds with hydrogen, and generally can only form with complex chemical interactions, as opposed to a direct reaction with hydrogen gas [292]. Note that MgH_2 exhibits both ionic and covalent properties. For metallic hydrides, the hydrogen enters the interstitial sites of the lattice and forms a hydride phase within the metal. These compounds are still conductive, have metallic properties, and can be formed with a direct reaction with H_2 gas (although some elements require a catalyst such as Pd to aid in splitting the H_2 molecule). Many of the lighter metals from Group VI-VIII also require higher H_2 pressures ($>$1 atm) in order to form a metal hydride [292]. Ni is one example of this, requiring over 6000 atm for hydride formation [11]. For some of the rare earth metals, they are metal hydrides at low H contents but become semiconductors at high H contents [293]. In Figure F.1, we depict these classifications for each element on the periodic table.

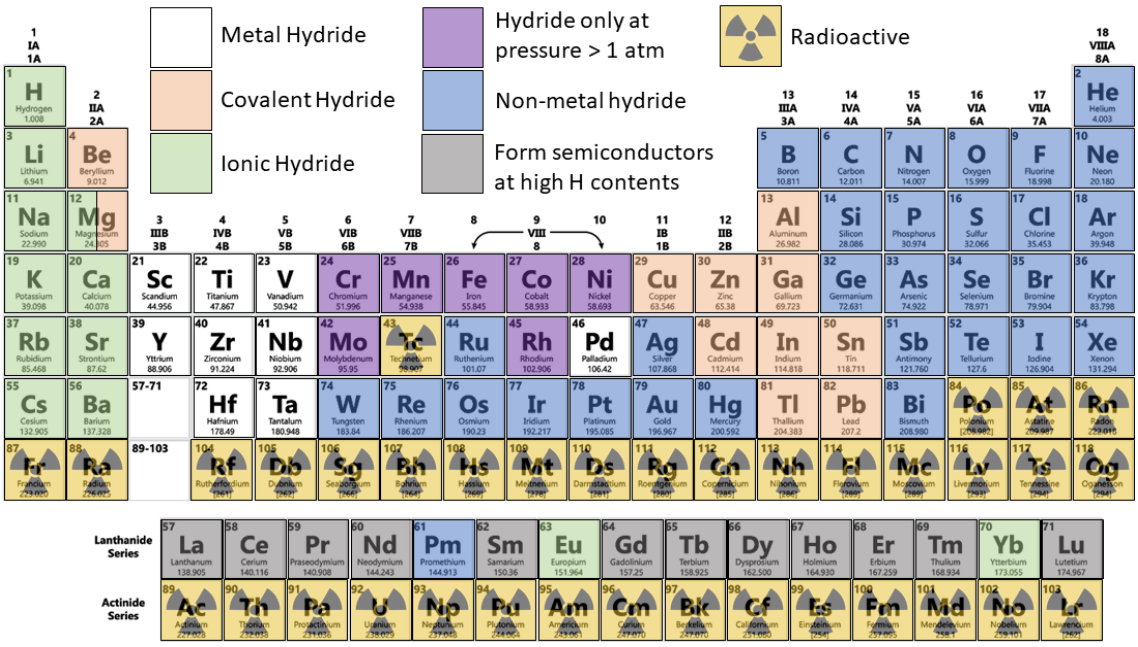

Figure F.1: Periodic table classification of metal hydrides. White box indicates the element forms a metal hydride under <1 atm hydrogen pressure, purple indicates elements with hydride formation >1 atm hydrogen pressure, red indicates covalent hydride formation, green indicates ionic hydride formation, blue indicates non-metals or no metal hydride formation, yellow indicates radioactive elements with no stable isotopes, and grey indicates metal hydride formation at low H content, but at high H contents the compound behaves as a semiconductor.

Another potentially important property of different metal hydrides is how close the H atoms are to each other within the metal lattice. This spacing is particularly important for potential fusion target designs, like the ones discussed in Chapter 8. In Figure F.2, we plot the different measured atomic spacings for hydrogen or deuterium in different forms, including muonic D_2 [294], molecular D_2 [295], the closest D spacing theoretically calculated in Pd [296], ZrV_2H_x at high pressures [297], TiH_2 [298], MgH_2 [298], VH [299], $PdH_{0.7}$ [10], and $PdD_{0.7}$ [60].

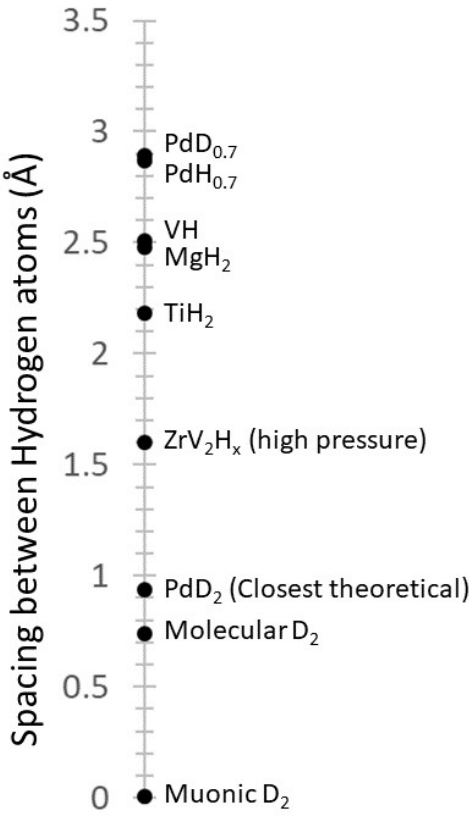

Figure F.2: H-H atom spacing in different materials. Values are the average distance between H atoms in different compounds.

Bibliography

[1] Thomas Graham. XVIII. On the absorption and dialytic separation of gases by colloid septa. *Philosophical Transactions of the Royal Society of London*, 156:399–439, January 1866. Publisher: Royal Society.

[2] Yu-Ming Lin, Guo-Lin Lee, and Min-Hon Rei. An integrated purification and production of hydrogen with a palladium membrane-catalytic reactor. *Catalysis Today*, 44(1):343–349, September 1998.

[3] Robert E. Buxbaum and Andrew B. Kinney. Hydrogen Transport through Tubular Membranes of Palladium-Coated Tantalum and Niobium. *Industrial & Engineering Chemistry Research*, 35(2):530–537, January 1996. Publisher: American Chemical Society.

[4] Lars J. Bannenberg, Christiaan Boelsma, Kohta Asano, Herman Schreuders, and Bernard Dam. Metal Hydride Based Optical Hydrogen Sensors. *Journal of the Physical Society of Japan*, 89(5):051003, February 2020. Publisher: The Physical Society of Japan.

[5] Carl Wadell, Svetlana Syrenova, and Christoph Langhammer. Plasmonic Hydrogen Sensing with Nanostructured Metal Hydrides. *ACS Nano*, 8(12):11925–11940, December 2014. Publisher: American Chemical Society.

[6] Xiangyu Zhao and Liqun Ma. Recent progress in hydrogen storage alloys for nickel/metal hydride secondary batteries. *International Journal of Hydrogen Energy*, 34(11):4788–4796, June 2009.

[7] Billur Sakintuna, Farida Lamari-Darkrim, and Michael Hirscher. Metal hydride materials for solid hydrogen storage: A review. *International Journal of Hydrogen Energy*, 32(9):1121–1140, June 2007.

[8] S. R. Ovshinsky, M. A. Fetcenko, and J. Ross. A Nickel Metal Hydride Battery for Electric Vehicles. *Science*, 260(5105):176–181, April 1993. Publisher: American Association for the Advancement of Science Section: Articles.

[9] Adolf Sieverts. Palladium und Wasserstoff. II. *Zeitschrift für Physikalische Chemie*, 88U(1):451–478, June 1914. Publisher: De Gruyter Oldenbourg Section: Zeitschrift für Physikalische Chemie.

[10] Jesse D. Benck, Ariel Jackson, David Young, Daniel Rettenwander, and Yet-Ming Chiang. Producing High Concentrations of Hydrogen in Palladium via Electrochemical Insertion from Aqueous and Solid Electrolytes. *Chemistry of Materials*, 31(11):4234–4245, June 2019. Publisher: American Chemical Society.

[11] G. Alefeld and J. Völkl, editors. *Hydrogen in Metals II: Application-Oriented Properties*. Topics in Applied Physics. Springer-Verlag, Berlin Heidelberg, 1978.

[12] G. Alefeld and J. Völkl, editors. *Hydrogen in Metals I: Basic Properties*. Topics in Applied Physics. Springer-Verlag, Berlin Heidelberg, 1978.

[13] Julian Karst, Florian Sterl, Heiko Linnenbank, Thomas Weiss, Mario Hentschel, and Harald Giessen. Watching in situ the hydrogen diffusion dynamics in magnesium on the nanoscale. *Science Advances*, 6(19):eaaz0566, May 2020. Publisher: American Association for the Advancement of Science Section: Research Article.

[14] J. N. Huiberts, R. Griessen, J. H. Rector, R. J. Wijngaarden, J. P. Dekker, D. G. de Groot, and N. J. Koeman. Yttrium and lanthanum hydride films with switchable optical properties. *Nature*, 380(6571):231–234, March 1996.

[15] K. Yoshimura, C. Langhammer, and B. Dam. Metal hydrides for smart window and sensor applications. *MRS Bulletin*, 38(6):495–503, June 2013.

[16] Maximilian Götz, Maren Lengert, Norbert Osterthun, Kai Gehrke, Martin Vehse, and Carsten Agert. Switchable Photocurrent Generation in an Ultrathin Resonant Cavity Solar Cell. *ACS Photonics*, 7(4):1022–1029, April 2020. Publisher: American Chemical Society.

[17] Mohamed ElKabbash, Kandammathe V. Sreekanth, Yunus Alapan, Myeongseop Kim, Jonathan Cole, Arwa Fraiwan, Theodore Letsou, Yandong Li, Chunlei Guo, R. Mohan Sankaran, Umut A. Gurkan, Michael Hinczewski, and Giuseppe Strangi. Hydrogen Sensing Using Thin-Film Perfect Light Absorber. *ACS Photonics*, 6(8):1889–1894, August 2019. Publisher: American Chemical Society.

[18] W. Lohstroh, R. J. Westerwaal, J. L. M. van Mechelen, C. Chacon, E. Johansson, B. Dam, and R. Griessen. Structural and optical properties of Mg2NiHx switchable mirrors upon hydrogen loading. *Physical Review B*, 70(16):165411, October 2004. Publisher: American Physical Society.

[19] Nikolai Strohfeldt, Andreas Tittl, Martin Schäferling, Frank Neubrech, Uwe Kreibig, Ronald Griessen, and Harald Giessen. Yttrium Hydride Nanoantennas for Active Plasmonics. *Nano Letters*, 14(3):1140–1147, March 2014. Publisher: American Chemical Society.

[20] Shahin Bagheri, Nikolai Strohfeldt, Monika Ubl, Audrey Berrier, Michael Merker, Gunther Richter, Michael Siegel, and Harald Giessen. Niobium as Alternative Material for Refractory and Active Plasmonics. *ACS Photonics*, 5(8):3298–3304, August 2018.

[21] Florian Sterl, Nikolai Strohfeldt, Ramon Walter, Ronald Griessen, Andreas Tittl, and Harald Giessen. Magnesium as Novel Material for Active Plasmonics in the Visible Wavelength Range. *Nano Letters*, 15(12):7949–7955, December 2015.

[22] Iwan Darmadi, Ferry Anggoro Ardy Nugroho, Shima Kadkhodazadeh, Jakob B. Wagner, and Christoph Langhammer. Rationally Designed PdAuCu Ternary Alloy Nanoparticles for Intrinsically Deactivation-Resistant Ultrafast Plasmonic Hydrogen Sensing. *ACS Sensors*, page acssensors.9b00610, May 2019.

[23] Ferry A. A. Nugroho, Iwan Darmadi, Lucy Cusinato, Arturo Susarrey-Arce, Herman Schreuders, Lars J. Bannenberg, Alice Bastos da Silva Fanta, Shima Kadkhodazadeh, Jakob B. Wagner, Tomasz J. Antosiewicz, Anders Hellman, Vladimir P. Zhdanov, Bernard Dam, and Christoph Langhammer. Metal–polymer hybrid nanomaterials for plasmonic ultrafast hydrogen detection. *Nature Materials*, 18(5):489–495, May 2019.

[24] M. Slaman, B. Dam, H. Schreuders, and R. Griessen. Optimization of Mg-based fiber optic hydrogen detectors by alloying the catalyst. *International Journal of Hydrogen Energy*, 33(3):1084–1089, February 2008.

[25] M. A. Butler. Optical fiber hydrogen sensor. *Applied Physics Letters*, 45(10):1007–1009, November 1984. Publisher: American Institute of Physics.

[26] Michael A. Butler. Micromirror optical-fiber hydrogen sensor. *Sensors and Actuators B: Chemical*, 22(2):155–163, November 1994.

[27] Casey P. O'Brien and Ivan C. Lee. The interaction of CO with PdCu hydrogen separation membranes: An operando infrared spectroscopy study. *Catalysis Today*, 336:216–222, October 2019.

[28] Shohei Ogura, Michio Okada, and Katsuyuki Fukutani. Near-Surface Accumulation of Hydrogen and CO Blocking Effects on a Pd–Au Alloy. *The Journal of Physical Chemistry C*, 117(18):9366–9371, May 2013. Publisher: American Chemical Society.

[29] G. Liang. Synthesis and hydrogen storage properties of Mg-based alloys. *Journal of Alloys and Compounds*, 370(1):123–128, May 2004.

[30] M. Zhu, H. Wang, L. Z. Ouyang, and M. Q. Zeng. Composite structure and hydrogen storage properties in Mg-base alloys. *International Journal of Hydrogen Energy*, 31(2):251–257, February 2006.

[31] C. Pistidda, N. Bergemann, J. Wurr, A. Rzeszutek, K. T. Møller, B. R. S. Hansen, S. Garroni, C. Horstmann, C. Milanese, A. Girella, O. Metz, K. Taube, T. R. Jensen, D. Thomas, H. P. Liermann, T. Klassen, and M. Dornheim. Hydrogen storage systems from waste Mg alloys. *Journal of Power Sources*, 270:554–563, December 2014.

[32] M. S. Wilson and S. Gottesfeld. Thin-film catalyst layers for polymer electrolyte fuel cell electrodes. *Journal of Applied Electrochemistry*, 22(1):1–7, January 1992.

[33] Jakob Kibsgaard, Zhebo Chen, Benjamin N. Reinecke, and Thomas F. Jaramillo. Engineering the surface structure of MoS_2 to preferentially expose active edge sites for electrocatalysis. *Nature Materials*, 11(11):963–969, November 2012.

[34] Peter Strasser, Shirlaine Koh, Toyli Anniyev, Jeff Greeley, Karren More, Chengfei Yu, Zengcai Liu, Sarp Kaya, Dennis Nordlund, Hirohito Ogasawara, Michael F. Toney, and Anders Nilsson. Lattice-strain control of the activity in dealloyed core–shell fuel cell catalysts. *Nature Chemistry*, 2(6):454–460, June 2010.

[35] J. B Bates, N. J Dudney, B Neudecker, A Ueda, and C. D Evans. Thin-film lithium and lithium-ion batteries. *Solid State Ionics*, 135(1):33–45, November 2000.

[36] Nian Liu, Hui Wu, Matthew T. McDowell, Yan Yao, Chongmin Wang, and Yi Cui. A Yolk-Shell Design for Stabilized and Scalable Li-Ion Battery Alloy Anodes. *Nano Letters*, 12(6):3315–3321, June 2012.

[37] Mark S. Gudiksen, Lincoln J. Lauhon, Jianfang Wang, David C. Smith, and Charles M. Lieber. Growth of nanowire superlattice structures for nanoscale photonics and electronics. *Nature*, 415(6872):617–620, February 2002.

[38] Kenji Nomura, Hiromichi Ohta, Kazushige Ueda, Toshio Kamiya, Masahiro Hirano, and Hideo Hosono. Thin-Film Transistor Fabricated in Single-Crystalline Transparent Oxide Semiconductor. *Science*, 300(5623):1269–1272, May 2003.

[39] Andrew N. Shipway, Eugenii Katz, and Itamar Willner. Nanoparticle Arrays on Surfaces for Electronic, Optical, and Sensor Applications. *ChemPhysChem*, 1(1):18–52, August 2000.

[40] Günter Sauerbrey. Verwendung von Schwingquarzen zur Wägung dünner Schichten und zur Mikrowägung. *Zeitschrift für Physik*, 155(2):206–222, April 1959.

[41] Claudia Steinem and Andreas Janshoff, editors. *Piezoelectric Sensors*. Springer Series on Chemical Sensors and Biosensors. Springer-Verlag, Berlin Heidelberg, 2007.

[42] Ilya Reviakine, Diethelm Johannsmann, and Ralf P. Richter. Hearing What You Cannot See and Visualizing What You Hear: Interpreting Quartz Crystal Microbalance Data from Solvated Interfaces. *Analytical Chemistry*, 83(23):8838–8848, December 2011.

[43] A. P. M. Glassford. Response of a quartz crystal microbalance to a liquid deposit. *Journal of Vacuum Science and Technology*, 15(6):1836–1843, November 1978.

[44] K. Keiji. Kanazawa and Joseph G. Gordon. Frequency of a quartz microbalance in contact with liquid. *Analytical Chemistry*, 57(8):1770–1771, July 1985.

[45] K Keiji Kanazawa and Joseph G Gordon. The oscillation frequency of a quartz resonator in contact with liquid. *Analytica Chimica Acta*, 175:99–105, January 1985.

[46] E. P. EerNisse. Simultaneous Thin-Film Stress and Mass-Change Measurements Using Quartz Resonators. *Journal of Applied Physics*, 43(4):1330–1337, April 1972.

[47] E. P. EerNisse. Extension of the double resonator technique. *Journal of Applied Physics*, 44(10):4482–4485, October 1973.

[48] T. P. Leervad Pedersen, C. Liesch, C. Salinga, T. Eleftheriadis, H. Weis, and M. Wuttig. Hydrogen-induced changes of mechanical stress and optical transmission in thin Pd films. *Thin Solid Films*, 458(1):299–303, June 2004.

[49] Vijay A. Sethuraman, Michael J. Chon, Maxwell Shimshak, Venkat Srinivasan, and Pradeep R. Guduru. In situ measurements of stress evolution in silicon thin films during electrochemical lithiation and delithiation. *Journal of Power Sources*, 195(15):5062–5066, August 2010.

[50] Markus Schwind, Saman Hosseinpour, Christoph Langhammer, Igor Zorić, Christofer Leygraf, and Bengt Kasemo. Nanoplasmonic Sensing for Monitoring the Initial Stages of Atmospheric Corrosion of Cu Nanodisks and Thin Films. *Journal of The Electrochemical Society*, 160(10):C487–C492, January 2013.

[51] Markus Schwind, Christoph Langhammer, Bengt Kasemo, and Igor Zorić. Nanoplasmonic sensing and QCM-D as ultrasensitive complementary techniques for kinetic corrosion studies of aluminum nanoparticles. *Applied Surface Science*, 257(13):5679–5687, April 2011.

[52] Allan L. Smith and Hamid. M. Shirazi. Principles of quartz crystal microbalance/heat conduction calorimetry: Measurement of the sorption enthalpy of hydrogen in palladium. *Thermochimica Acta*, 432(2):202–211, July 2005.

[53] Christoph Langhammer, Elin M. Larsson, Bengt Kasemo, and Igor Zorić. Indirect Nanoplasmonic Sensing: Ultrasensitive Experimental Platform for Nanomaterials Science and Optical Nanocalorimetry. *Nano Letters*, 10(9):3529–3538, September 2010.

[54] Stephen J. Martin, Victoria Edwards. Granstaff, and Gregory C. Frye. Characterization of a quartz crystal microbalance with simultaneous mass and liquid loading. *Analytical Chemistry*, 63(20):2272–2281, October 1991.

[55] J. Kestin, S. T. Ro, and W. A. Wakeham. Viscosity of the isotopes of hydrogen and their intermolecular force potentials. *Journal of the Chemical Society, Faraday Transactions 1: Physical Chemistry in Condensed Phases*, 68(0):2316–2323, January 1972.

[56] Liang Tan, Xue'en Jia, Xiangfu Jiang, Youyu Zhang, Hao Tang, Shouzhuo Yao, and Qingji Xie. In vitro study on the individual and synergistic cytotoxicity of adriamycin and selenium nanoparticles against Bel7402 cells with a quartz crystal microbalance. *Biosensors and Bioelectronics*, 24(7):2268–2272, March 2009.

[57] R. V. Bucur, V. Mecea, and T. B. Flanagan. The kinetics of hydrogen (deuterium) sorption by thin palladium layers studied with a piezoelectric quartz crystal microbalance. *Surface Science*, 54(2):477–488, February 1976.

[58] R. Feenstra, D. G. de Groot, J. H. Rector, E. Salomons, and R. Griessen. Gravimetrical determination of pressure-composition isotherms of thin PdH c films. *Journal of Physics F: Metal Physics*, 16(12):1953, 1986.

[59] George Sidebotham. *Heat Transfer Modeling: An Inductive Approach*. Springer International Publishing, 2015.

[60] J. E. Schirber and B. Morosin. Lattice constants of $\ensuremath{\beta}\ensuremath{-}\mathrm{P}\mathrm{d}{\mathrm{H}}_{x}$ and $\ensuremath{\beta}\ensuremath{-}\mathrm{P}\mathrm{d}{\mathrm{D}}_{x}$ with x near 1.0. *Physical Review B*, 12(1):117–118, July 1975.

[61] Long Ju, Baisong Geng, Jason Horng, Caglar Girit, Michael Martin, Zhao Hao, Hans A. Bechtel, Xiaogan Liang, Alex Zettl, Y. Ron Shen, and Feng Wang. Graphene plasmonics for tunable terahertz metamaterials. *Nature Nanotechnology*, 6(10):630–634, October 2011.

[62] A. V. Kabashin, P. Evans, S. Pastkovsky, W. Hendren, G. A. Wurtz, R. Atkinson, R. Pollard, V. A. Podolskiy, and A. V. Zayats. Plasmonic nanorod metamaterials for biosensing. *Nature Materials*, 8(11):867–871, November 2009.

[63] Zhichuan Xu, Yanglong Hou, and Shouheng Sun. Magnetic Core/Shell Fe3O4/Au and Fe3O4/Au/Ag Nanoparticles with Tunable Plasmonic Properties. *Journal of the American Chemical Society*, 129(28):8698–8699, July 2007.

[64] Andrea Tao, Prasert Sinsermsuksakul, and Peidong Yang. Tunable plasmonic lattices of silver nanocrystals. *Nature Nanotechnology*, 2(7):435–440, July 2007.

[65] F. J. Beck, A. Polman, and K. R. Catchpole. Tunable light trapping for solar cells using localized surface plasmons. *Journal of Applied Physics*, 105(11):114310, June 2009.

[66] A. T. M. van Gogh, D. G. Nagengast, E. S. Kooij, N. J. Koeman, J. H. Rector, R. Griessen, C. F. J. Flipse, and R. J. J. G. A. M. Smeets. Structural, electrical, and optical properties of ${\mathrm{La}}_{1\ensuremath{-}z}{\mathrm{Y}}_{z}{\mathrm{H}}_{x}$ switchable mirrors. *Physical Review B*, 63(19):195105, April 2001.

[67] Victor W. Brar, Min Seok Jang, Michelle Sherrott, Josue J. Lopez, and Harry A. Atwater. Highly Confined Tunable Mid-Infrared Plasmonics in Graphene Nanoresonators. *Nano Letters*, 13(6):2541–2547, June 2013.

[68] Ewald Veleckis and Russell Keith Edwards. Thermodynamic properties in the systems vanadium-hydrogen, niobium-hydrogen, and tantalum-hydrogen. *The Journal of Physical Chemistry*, 73(3):683–692, March 1969.

[69] Rebecca S. Sherbo, Marta Moreno-Gonzalez, Noah J. J. Johnson, David J. Dvorak, David K. Fork, and Curtis P. Berlinguette. Accurate Coulometric Quantification of Hydrogen Absorption in Palladium Nanoparticles and Thin Films. *Chemistry of Materials*, 30(12):3963–3970, June 2018.

[70] J Huot, G Liang, S Boily, A Van Neste, and R Schulz. Structural study and hydrogen sorption kinetics of ball-milled magnesium hydride. *Journal of Alloys and Compounds*, 293-295:495–500, December 1999.

[71] A. San-Martin and F. D. Manchester. The H-Ti (Hydrogen-Titanium) system. *Bulletin of Alloy Phase Diagrams*, 8(1):30–42, February 1987.

[72] Nikolai Strohfeldt, Jun Zhao, Andreas Tittl, and Harald Giessen. Sensitivity engineering in direct contact palladium-gold nano-sandwich hydrogen sensors [Invited]. *Optical Materials Express*, 5(11):2525–2535, November 2015.

[73] Murat Serhatlioglu, Sencer Ayas, Necmi Biyikli, Aykutlu Dana, and Mehmet E. Solmaz. Perfectly absorbing ultra thin interference coatings for hydrogen sensing. *Optics Letters*, 41(8):1724–1727, April 2016.

[74] Carl Wadell, Ferry Anggoro Ardy Nugroho, Emil Lidström, Beniamino Iandolo, Jakob B. Wagner, and Christoph Langhammer. Hysteresis-Free Nanoplasmonic Pd–Au Alloy Hydrogen Sensors. *Nano Letters*, 15(5):3563–3570, May 2015.

[75] Petr Tobiška, Olivier Hugon, Alain Trouillet, and Henri Gagnaire. An integrated optic hydrogen sensor based on SPR on palladium. *Sensors and Actuators B: Chemical*, 74(1):168–172, April 2001.

[76] Z. Zhao, M. A. Carpenter, H. Xia, and D. Welch. All-optical hydrogen sensor based on a high alloy content palladium thin film. *Sensors and Actuators B: Chemical*, 113(1):532–538, January 2006.

[77] Timur Shegai, Peter Johansson, Christoph Langhammer, and Mikael Käll. Directional Scattering and Hydrogen Sensing by Bimetallic Pd–Au Nanoantennas. *Nano Letters*, 12(5):2464–2469, May 2012.

[78] Joel Villatoro and David Monzón-Hernández. Fast detection of hydrogen with nano fiber tapers coated with ultra thin palladium layers. *Optics Express*, 13(13):5087–5092, June 2005.

[79] David Monzón-Hernández, Donato Luna-Moreno, and Dalia Martínez-Escobar. Fast response fiber optic hydrogen sensor based on palladium and gold nano-layers. *Sensors and Actuators B: Chemical*, 136(2):562–566, March 2009.

[80] Xiaoyang Duan, Simon Kamin, and Na Liu. Dynamic plasmonic colour display. *Nature Communications*, 8(1):1–9, February 2017.

[81] C. Boelsma, L. J. Bannenberg, M. J. van Setten, N.-J. Steinke, A. A. van Well, and B. Dam. Hafnium—an optical hydrogen sensor spanning six orders in pressure. *Nature Communications*, 8(1):1–8, June 2017.

[82] D. E. Azofeifa, N. Clark, W. E. Vargas, H. Solís, G. K. Pálsson, and B. Hjörvarsson. Hydrogen induced changes in the optical properties of Pd capped V thin films. *Journal of Alloys and Compounds*, 580:S114–S118, December 2013.

[83] M. J. van Setten, V. A. Popa, G. A. de Wijs, and G. Brocks. Electronic structure and optical properties of lightweight metal hydrides. *Physical Review B*, 75(3):035204, January 2007.

[84] J. Isidorsson, I. A. M. E. Giebels, H. Arwin, and R. Griessen. Optical properties of ${\mathrm{MgH}}_{2}$ measured in situ by ellipsometry and spectrophotometry. *Physical Review B*, 68(11):115112, September 2003.

[85] Daniel E. Azofeifa, Neville Clark, William E. Vargas, Hugo Solis, E. Avendano, Michael Cambronero, and Diana Valverde-Mendez. Dielectric function of palladium capped zirconium thin films as a function of absorbed hydrogen. *International Journal of Hydrogen Energy*, 42(35):22373–22378, August 2017.

[86] Y. Yamada, K. Tajima, S. Bao, M. Okada, and K. Yoshimura. Hydrogenation and dehydrogenation processes of palladium thin films measured in situ by spectroscopic ellipsometry. *Solar Energy Materials and Solar Cells*, 93(12):2143–2147, December 2009.

[87] William E. Vargas, Daniel E. Azofeifa, Neville Clark, Hugo Solis, Felipe Montealegre, and Michael Cambronero. Parametric formulation of the dielectric function of palladium and palladium hydride thin films. *Applied Optics*, 53(24):5294–5306, August 2014.

[88] Boyi Wang, Yong Zhu, Youping Chen, Han Song, Pengcheng Huang, and Dzung Viet Dao. Hydrogen sensor based on palladium-yttrium alloy nanosheet. *Materials Chemistry and Physics*, 194:231–235, June 2017.

[89] Yogendra K. Gautam, Amit Sanger, Ashwani Kumar, and Ramesh Chandra. A room temperature hydrogen sensor based on Pd–Mg alloy and multilayers prepared by magnetron sputtering. *International Journal of Hydrogen Energy*, 40(45):15549–15555, December 2015.

[90] S. Bao, K. Tajima, Y. Yamada, M. Okada, and K. Yoshimura. Color-neutral switchable mirrors based on magnesium-titanium thin films. *Applied Physics A*, 87(4):621–624, June 2007.

[91] T. J. Richardson, J. L. Slack, B. Farangis, and M. D. Rubin. Mixed metal films with switchable optical properties. *Applied Physics Letters*, 80(8):1349–1351, February 2002. Publisher: American Institute of Physics.

[92] K Yamamoto, K Higuchi, H Kajioka, H Sumida, S Orimo, and H Fujii. Optical transmission of magnesium hydride thin film with characteristic nanostructure. *Journal of Alloys and Compounds*, 330-332:352–356, January 2002.

[93] M. Singh, S. Srivastava, S. Agarwal, S. Kumar, and Y. K. Vijay. Optical properties of d.c. magneto sputtered tantalum and titanium nanostructure thin film metal hydrides. *Bulletin of Materials Science*, 33(5):569–573, October 2010.

[94] Setsuo Nakao, Kazuo Saitoh, Tatsuya Hirahara, Masami Ikeyama, Masato Tazawa, Ping Jin, Hiroaki Niwa, Seita Tanemura, Yoshiko Miyagawa, Soji Miyagawa, and Kyoichiro Yasuda. Preparation and optical transmittance of titanium hydride (deutende) films by rf reactive sputtering. *Thin Solid Films*, 343-344:195–198, April 1999.

[95] Joseph B. Murray, Kevin J. Palm, Tarun C. Narayan, David K. Fork, Seid Sadat, and Jeremy N. Munday. Apparatus for combined nanoscale gravimetric, stress, and thermal measurements. *Review of Scientific Instruments*, 89(8):085106, August 2018.

[96] Z Luz, J Genossar, and P. S Rudman. Identification of the diffusing atom in MgH2. *Journal of the Less Common Metals*, 73(1):113–118, September 1980.

[97] M. A. Pick, J. W. Davenport, Myron Strongin, and G. J. Dienes. Enhancement of Hydrogen Uptake Rates for Nb and Ta by Thin Surface Overlayers. *Physical Review Letters*, 43(4):286–289, July 1979.

[98] Roberto Machorro, Jesús M. Siqueiros, and Shu Wang. Optical properties of Mg, from UV to IR, using ellipsometry and reflectometry. *Thin Solid Films*, 269(1):1–5, November 1995.

[99] H.-J Hagemann, W Gudat, and C Kunz. Optical Constants from the Far Infrared to the X-Ray Region: Mg, Al, Cu, Ag, Au, Bi, C, and Al2O3. *Journal of the Optical Society of America*, 65(6):742–744, June 1975.

[100] P. Hjort, A. Krozer, and B. Kasemo. Resistivity and hydrogen uptake measurements in evaporated Mg films at 350 K. *Journal of Alloys and Compounds*, 234(2):L11–L15, February 1996.

[101] A. Baldi, M. Gonzalez-Silveira, V. Palmisano, B. Dam, and R. Griessen. Destabilization of the Mg-H System through Elastic Constraints. *Physical Review Letters*, 102(22):226102, June 2009.

[102] S. Singh, S. W. H. Eijt, M. W. Zandbergen, W. J. Legerstee, and V. L. Svetchnikov. Nanoscale structure and the hydrogenation of Pd-capped magnesium thin films prepared by plasma sputter and pulsed laser deposition. *Journal of Alloys and Compounds*, 441(1):344–351, August 2007.

[103] Marvin R. Querry. *Optical Constants of Minerals and Other Materials from the Millimeter to the Ultraviolet*. Chemical Research, Development & Engineering Center, U.S. Army Armament Munitions Chemical Command, 1987.

[104] P. B. Johnson and R. W. Christy. Optical constants of transition metals: Ti, V, Cr, Mn, Fe, Co, Ni, and Pd. *Physical Review B*, 9(12):5056–5070, June 1974.

[105] William E. Wall, M. W. Ribarsky, and J. R. Stevenson. Optical properties of titanium and titanium oxide surfaces. *Journal of Applied Physics*, 51(1):661–667, January 1980.

[106] Siham Mahmoud. Structure and optical properties of thin titanium films deposited on different substrates. *Journal of Materials Science*, 22(10):3693–3697, October 1987.

[107] Vitaliy Larionov, Shupeng Xu, and Maxim Syrtanov. Measurements of hydrogenated titanium by electric methods. *AIP Conference Proceedings*, 1772(1):040005, October 2016.

[108] J. H. Weaver, D. J. Peterman, D. T. Peterson, and A. Franciosi. Electronic structure of metal hydrides. IV. $\mathrm{Ti}{\mathrm{H}}_{x}$, $\mathrm{Zr}{\mathrm{H}}_{x}$, $\mathrm{Hf}{\mathrm{H}}_{x}$,

and the fcc-fct lattice distortion. *Physical Review B*, 23(4):1692–1698, February 1981.

[109] P. Romaniello, P. L. de Boeij, F. Carbone, and D. van der Marel. Optical properties of bcc transition metals in the range \$0–40\phantom{\rule{0.3em}{0ex}}\mathrm{eV}\$. *Physical Review B*, 73(7):075115, February 2006.

[110] D. G. Laurent, C. S. Wang, and J. Callaway. Energy bands, Compton profile, and optical conductivity of vanadium. *Physical Review B*, 17(2):455–461, January 1978.

[111] Lisa J. Krayer, Elizabeth M. Tennyson, Marina S. Leite, and Jeremy N. Munday. Near-IR Imaging Based on Hot Carrier Generation in Nanometer-Scale Optical Coatings. *ACS Photonics*, 5(2):306–311, February 2018.

[112] Igor Zoric´, Elin M. Larsson, Bengt Kasemo, and Christoph Langhammer. Localized Surface Plasmons Shed Light on Nanoscale Metal Hydrides. *Advanced Materials*, 22(41):4628–4633, 2010.

[113] Mariama Rebello Sousa Dias, Chen Gong, Zackery A. Benson, and Marina S. Leite. Lithography-Free, Omnidirectional, CMOS-Compatible AlCu Alloys for Thin-Film Superabsorbers. *Advanced Optical Materials*, 6(2):1700830, 2018.

[114] Ramon Walter, Andreas Tittl, Audrey Berrier, Florian Sterl, Thomas Weiss, and Harald Giessen. Large-Area Low-Cost Tunable Plasmonic Perfect Absorber in the Near Infrared by Colloidal Etching Lithography. *Advanced Optical Materials*, 3(3):398–403, 2015.

[115] Andreas Tittl, Patrick Mai, Richard Taubert, Daniel Dregely, Na Liu, and Harald Giessen. Palladium-Based Plasmonic Perfect Absorber in the Visible Wavelength Range and Its Application to Hydrogen Sensing. *Nano Letters*, 11(10):4366–4369, October 2011.

[116] Stefan Enoch, Gérard Tayeb, Pierre Sabouroux, Nicolas Guérin, and Patrick Vincent. A Metamaterial for Directive Emission. *Physical Review Letters*, 89(21):213902, November 2002. Publisher: American Physical Society.

[117] N. Garcia, E. V. Ponizovskaya, and John Q. Xiao. Zero permittivity materials: Band gaps at the visible. *Applied Physics Letters*, 80(7):1120–1122, February 2002. Publisher: American Institute of Physics.

[118] Richard W. Ziolkowski. Propagation in and scattering from a matched metamaterial having a zero index of refraction. *Physical Review E*, 70(4):046608, October 2004. Publisher: American Physical Society.

[119] Lisa J. Krayer, Jongbum Kim, Joseph L. Garrett, and Jeremy N. Munday. Optoelectronic Devices on Index-near-Zero Substrates. *ACS Photonics*, 6(9):2238–2244, September 2019. Publisher: American Chemical Society.

[120] Lisa J. Krayer, Jongbum Kim, and Jeremy N. Munday. Near-perfect absorption throughout the visible using ultra-thin metal films on index-near-zero substrates [Invited]. *Optical Materials Express*, 9(1):330–338, January 2019. Publisher: Optical Society of America.

[121] S. Vassant, A. Archambault, F. Marquier, F. Pardo, U. Gennser, A. Cavanna, J. L. Pelouard, and J. J. Greffet. Epsilon-Near-Zero Mode for Active Optoelectronic Devices. *Physical Review Letters*, 109(23):237401, December 2012. Publisher: American Physical Society.

[122] Viet Cuong Nguyen, Lang Chen, and Klaus Halterman. Total Transmission and Total Reflection by Zero Index Metamaterials with Defects. *Physical Review Letters*, 105(23):233908, December 2010. Publisher: American Physical Society.

[123] Jura Rensberg, You Zhou, Steffen Richter, Chenghao Wan, Shuyan Zhang, Philipp Schöppe, Rüdiger Schmidt-Grund, Shriram Ramanathan, Federico Capasso, Mikhail A. Kats, and Carsten Ronning. Epsilon-Near-Zero Substrate Engineering for Ultrathin-Film Perfect Absorbers. *Physical Review Applied*, 8(1):014009, July 2017. Publisher: American Physical Society.

[124] Simin Feng and Klaus Halterman. Coherent perfect absorption in epsilon-near-zero metamaterials. *Physical Review B*, 86(16):165103, October 2012. Publisher: American Physical Society.

[125] Klaus Halterman and Simin Feng. Resonant transmission of electromagnetic fields through subwavelength zero-epsilon slits. *Physical Review A*, 78(2):021805, August 2008. Publisher: American Physical Society.

[126] Andrea Alù, Mário G. Silveirinha, and Nader Engheta. Transmission-line analysis of $\ensuremath{\epsilon}$-near-zero–filled narrow channels. *Physical Review E*, 78(1):016604, July 2008. Publisher: American Physical Society.

[127] Brian Edwards, Andrea Alù, Michael E. Young, Mário Silveirinha, and Nader Engheta. Experimental Verification of Epsilon-Near-Zero Metamaterial Coupling and Energy Squeezing Using a Microwave Waveguide. *Physical Review Letters*, 100(3):033903, January 2008. Publisher: American Physical Society.

[128] D. C. Adams, S. Inampudi, T. Ribaudo, D. Slocum, S. Vangala, N. A. Kuhta, W. D. Goodhue, V. A. Podolskiy, and D. Wasserman. Funneling Light through a Subwavelength Aperture with Epsilon-Near-Zero Materials. *Physical Review Letters*, 107(13):133901, September 2011. Publisher: American Physical Society.

[129] Antonio Capretti, Yu Wang, Nader Engheta, and Luca Dal Negro. Enhanced third-harmonic generation in Si-compatible epsilon-near-zero indium tin oxide nanolayers. *Optics Letters*, 40(7):1500–1503, April 2015. Publisher: Optical Society of America.

[130] Christos Argyropoulos, Pai-Yen Chen, Giuseppe D'Aguanno, Nader Engheta, and Andrea Alù. Boosting optical nonlinearities in $\ensuremath{\epsilon}$-near-zero plasmonic channels. *Physical Review B*, 85(4):045129, January 2012. Publisher: American Physical Society.

[131] Haim Suchowski, Kevin O'Brien, Zi Jing Wong, Alessandro Salandrino, Xiaobo Yin, and Xiang Zhang. Phase Mismatch–Free Nonlinear Propagation in Optical Zero-Index Materials. *Science*, 342(6163):1223–1226, December 2013. Publisher: American Association for the Advancement of Science Section: Report.

[132] M. Zahirul Alam, Israel De Leon, and Robert W. Boyd. Large optical nonlinearity of indium tin oxide in its epsilon-near-zero region. *Science*, 352(6287):795–797, May 2016. Publisher: American Association for the Advancement of Science Section: Report.

[133] Daniel Traviss, Roman Bruck, Ben Mills, Martina Abb, and Otto L. Muskens. Ultrafast plasmonics using transparent conductive oxide hybrids in the epsilon-near-zero regime. *Applied Physics Letters*, 102(12):121112, March 2013. Publisher: American Institute of Physics.

[134] Jongbum Kim, Aveek Dutta, Gururaj V. Naik, Alexander J. Giles, Francisco J. Bezares, Chase T. Ellis, Joseph G. Tischler, Ahmed M. Mahmoud, Humeyra Caglayan, Orest J. Glembocki, Alexander V. Kildishev, Joshua D. Caldwell, Alexandra Boltasseva, and Nader Engheta. Role of epsilon-near-zero substrates in the optical response of plasmonic antennas. *Optica*, 3(3):339–346, March 2016. Publisher: Optical Society of America.

[135] Zhizhen Ma, Zhuoran Li, Ke Liu, Chenran Ye, and Volker J. Sorger. Indium-Tin-Oxide for High-performance Electro-optic Modulation. *Nanophotonics*, -1(open-issue):198–213, June 2015. Publisher: De Gruyter Section: Nanophotonics.

[136] Gururaj V. Naik, Jongbum Kim, and Alexandra Boltasseva. Oxides and nitrides as alternative plasmonic materials in the optical range [Invited]. *Optical Materials Express*, 1(6):1090–1099, October 2011. Publisher: Optical Society of America.

[137] Salvatore Campione, Iltai Kim, Domenico de Ceglia, Gordon A. Keeler, and Ting S. Luk. Experimental verification of epsilon-near-zero plasmon polariton modes in degenerately doped semiconductor nanolayers. *Optics Express*, 24(16):18782–18789, August 2016. Publisher: Optical Society of America.

[138] Salvatore Campione, Joel R. Wendt, Gordon A. Keeler, and Ting S. Luk. Near-Infrared Strong Coupling between Metamaterials and Epsilon-near-Zero Modes in Degenerately Doped Semiconductor Nanolayers. *ACS Photonics*, 3(2):293–297, February 2016. Publisher: American Chemical Society.

[139] N. Kinsey, C. DeVault, J. Kim, M. Ferrera, V. M. Shalaev, and A. Boltasseva. Epsilon-near-zero Al-doped ZnO for ultrafast switching at telecom wavelengths. *Optica*, 2(7):616–622, July 2015. Publisher: Optical Society of America.

[140] Francisco Javier Gonzalez, Robert E. Peale, Sepehr Benis, David Hagan, and Eric Van Stryland. Optical Limiter using Epsilon-Near-Zero Grating. In *2019 IEEE Research and Applications of Photonics in Defense Conference (RAPID)*, pages 1–3, August 2019.

[141] Farnood Khalilzadeh-Rezaie, Isaiah O. Oladeji, Justin W. Cleary, Nima Nader, Janardan Nath, Imen Rezadad, and Robert E. Peale. Fluorine-doped tin oxides for mid-infrared plasmonics. *Optical Materials Express*, 5(10):2184–2192, October 2015. Publisher: Optical Society of America.

[142] Hongwei Zhao, Yu Wang, Antonio Capretti, Luca Dal Negro, and Jonathan Klamkin. Broadband Electroabsorption Modulators Design Based on Epsilon-Near-Zero Indium Tin Oxide. *IEEE Journal of Selected Topics in Quantum Electronics*, 21(4):192–198, July 2015.

[143] Thomas E. Tiwald, Daniel W. Thompson, John A. Woollam, Wayne Paulson, and Robert Hance. Application of IR variable angle spectroscopic ellipsometry to the determination of free carrier concentration depth profiles. *Thin Solid Films*, 313-314:661–666, February 1998.

[144] G. E. Jellison and F. A. Modine. Parameterization of the optical functions of amorphous materials in the interband region. *Applied Physics Letters*, 69(3):371–373, July 1996. Publisher: American Institute of Physics.

[145] A. Baldi, D. M. Borsa, H. Schreuders, J. H. Rector, T. Atmakidis, M. Bakker, H. A. Zondag, W. G. J. van Helden, B. Dam, and R. Griessen. Mg–Ti–H thin films as switchable solar absorbers. *International Journal of Hydrogen Energy*, 33(12):3188–3192, June 2008.

[146] Andreas Tittl, Ann-Katrin U. Michel, Martin Schäferling, Xinghui Yin, Behrad Gholipour, Long Cui, Matthias Wuttig, Thomas Taubner, Frank Neubrech, and Harald Giessen. A Switchable Mid-Infrared Plasmonic Perfect Absorber with Multispectral Thermal Imaging Capability. *Advanced Materials*, 27(31):4597–4603, 2015. _eprint: https://onlinelibrary.wiley.com/doi/pdf/10.1002/adma.201502023.

[147] Soroosh Daqiqeh Rezaei, Zhaogang Dong, John You En Chan, Jonathan Trisno, Ray Jia Hong Ng, Qifeng Ruan, Cheng-Wei Qiu, N. Asger Mortensen, and Joel K.W. Yang. Nanophotonic Structural Colors. *ACS Photonics*, July 2020. Publisher: American Chemical Society.

[148] Carl Hägglund, S. Peter Apell, and Bengt Kasemo. Maximized Optical Absorption in Ultrathin Films and Its Application to Plasmon-Based Two-Dimensional Photovoltaics. *Nano Letters*, 10(8):3135–3141, August 2010. Publisher: American Chemical Society.

[149] N. Ahmad, J. Stokes, N. A. Fox, M. Teng, and M. J. Cryan. Ultra-thin metal films for enhanced solar absorption. *Nano Energy*, 1(6):777–782, November 2012.

[150] Mark L. Brongersma, Naomi J. Halas, and Peter Nordlander. Plasmon-induced hot carrier science and technology. *Nature Nanotechnology*, 10(1):25–34, January 2015. Number: 1 Publisher: Nature Publishing Group.

[151] Tao Gong and Jeremy N. Munday. Materials for hot carrier plasmonics [Invited]. *Optical Materials Express*, 5(11):2501–2512, November 2015. Publisher: Optical Society of America.

[152] Tao Gong and Jeremy N. Munday. Angle-Independent Hot Carrier Generation and Collection Using Transparent Conducting Oxides. *Nano Letters*, 15(1):147–152, January 2015. Publisher: American Chemical Society.

[153] Tao Gong and Jeremy N. Munday. Aluminum-based hot carrier plasmonics. *Applied Physics Letters*, 110(2):021117, January 2017. Publisher: American Institute of Physics.

[154] Joseph Murray, Dakang Ma, and Jeremy N. Munday. Electrically Controllable Light Trapping for Self-Powered Switchable Solar Windows. *ACS Photonics*, 4(1):1–7, January 2017. Publisher: American Chemical Society.

[155] Bo Zhu, Yijun Feng, Junming Zhao, Ci Huang, and Tian Jiang. Switchable metamaterial reflector/absorber for different polarized electromagnetic waves. *Applied Physics Letters*, 97(5):051906, August 2010. Publisher: American Institute of Physics.

[156] Dongju Lee, Heijun Jeong, and Sungjoon Lim. Electronically Switchable Broadband Metamaterial Absorber. *Scientific Reports*, 7(1):4891, July 2017. Number: 1 Publisher: Nature Publishing Group.

[157] David Shrekenhamer, Wen-Chen Chen, and Willie J. Padilla. Liquid Crystal Tunable Metamaterial Absorber. *Physical Review Letters*, 110(17):177403, April 2013. Publisher: American Physical Society.

[158] Prakash Pitchappa, Chong Pei Ho, Piotr Kropelnicki, Navab Singh, Dim-Lee Kwong, and Chengkuo Lee. Micro-electro-mechanically switchable near infrared complementary metamaterial absorber. *Applied Physics Letters*, 104(20):201114, May 2014. Publisher: American Institute of Physics.

[159] Sukosin Thongrattanasiri, Frank H. L. Koppens, and F. Javier García de Abajo. Complete Optical Absorption in Periodically Patterned Graphene. *Physical Review Letters*, 108(4):047401, January 2012. Publisher: American Physical Society.

[160] Mikhail A. Kats, Romain Blanchard, Patrice Genevet, Zheng Yang, M. Mumtaz Qazilbash, D. N. Basov, Shriram Ramanathan, and Federico Capasso. Thermal tuning of mid-infrared plasmonic antenna arrays using a phase change material. *Optics Letters*, 38(3):368–370, February 2013. Publisher: Optical Society of America.

[161] Hao Wang, Yue Yang, and Liping Wang. Switchable wavelength-selective and diffuse metamaterial absorber/emitter with a phase transition spacer layer. *Applied Physics Letters*, 105(7):071907, August 2014. Publisher: American Institute of Physics.

[162] Yi Zhao, Qiuping Huang, Honglei Cai, Xiaoxia Lin, and Yalin Lu. A broadband and switchable VO2-based perfect absorber at the THz frequency. *Optics Communications*, 426:443–449, November 2018.

[163] Tongling Wang, Yuping Zhang, Yuping Zhang, Huiyun Zhang, Maoyong Cao, and Maoyong Cao. Dual-controlled switchable broadband terahertz absorber based on a graphene-vanadium dioxide metamaterial. *Optical Materials Express*, 10(2):369–386, February 2020. Publisher: Optical Society of America.

[164] Kevin J. Palm, Joseph B. Murray, Tarun C. Narayan, and Jeremy N. Munday. Dynamic Optical Properties of Metal Hydrides. *ACS Photonics*, 5(11):4677–4686, November 2018.

[165] Kevin J. Palm, Joseph B. Murray, Joshua P. McClure, Marina S. Leite, and Jeremy N. Munday. In Situ Optical and Stress Characterization of Alloyed PdxAu1–x Hydrides. *ACS Applied Materials & Interfaces*, 11(48):45057–45067, December 2019. Publisher: American Chemical Society.

[166] Reginald M. Penner. A Nose for Hydrogen Gas: Fast, Sensitive H2 Sensors Using Electrodeposited Nanomaterials. *Accounts of Chemical Research*, 50(8):1902–1910, August 2017.

[167] Andrea Baldi, Lennard Mooij, Valerio Palmisano, Herman Schreuders, Gopi Krishnan, Bart J. Kooi, Bernard Dam, and Ronald Griessen. Elastic versus Alloying Effects in Mg-Based Hydride Films. *Physical Review Letters*, 121(25):255503, December 2018.

[168] Mikhail A. Kats, Romain Blanchard, Patrice Genevet, and Federico Capasso. Nanometre optical coatings based on strong interference effects in highly absorbing media. *Nature Materials*, 12(1):20–24, January 2013. Number: 1 Publisher: Nature Publishing Group.

[169] C. Hilsum. Infrared Absorption of Thin Metal Films. *JOSA*, 44(3):188–191, March 1954. Publisher: Optical Society of America.

[170] B. Edwards, A. Alù, M. G. Silveirinha, and N. Engheta. Reflectionless sharp bends and corners in waveguides using epsilon-near-zero effects. *Journal of Applied Physics*, 105(4):044905, February 2009. Publisher: American Institute of Physics.

[171] A. M. Vredenberg, E. M. B. Heller, and D. O. Boerma. Hydriding characteristics of FeTi/Pd films. *Journal of Alloys and Compounds*, 400(1):188–193, September 2005.

[172] P. Hjort, A. Krozer, and B. Kasemo. Hydrogen sorption kinetics in partly oxidized Mg films. *Journal of Alloys and Compounds*, 237(1):74–80, April 1996.

[173] Max Born and Emil Wolf. *Principles of Optics*. Cambridge University Press, 7th edition, 2005.

[174] P. B. Johnson and R. W. Christy. Optical Constants of the Noble Metals. *Physical Review B*, 6(12):4370–4379, December 1972.

[175] Lihong Gao, Fabien Lemarchand, and Michel Lequime. Exploitation of multiple incidences spectrometric measurements for thin film reverse engineering. *Optics Express*, 20(14):15734–15751, July 2012. Publisher: Optical Society of America.

[176] J. Rydén, B. Hjörvarsson, T. Ericsson, E. Karlsson, A. Krozer, and B. Kasemo. Unusual kinetics of hydride formation in Mg-Pd sandwiches, studied by hydrogen profiling and quartz crystal microbalance measurements. *Journal of the Less Common Metals*, 152(2):295–309, July 1989.

[177] I. R. Hooper and J. R. Sambles. Dispersion of surface plasmon polaritons on short-pitch metal gratings. *Physical Review B*, 65(16):165432, April 2002. Publisher: American Physical Society.

[178] Joshua P. McClure, Jonathan Boltersdorf, David R. Baker, Thomas G. Farinha, Nicholas Dzuricky, Cesar E. P. Villegas, Alexandre R. Rocha, and Marina S. Leite. Structure–Property-Performance Relationship of Ultrathin Pd–Au Alloy Catalyst Layers for Low-Temperature Ethanol Oxidation in Alkaline Media. *ACS Applied Materials & Interfaces*, May 2019.

[179] Chen Gong, Alan Kaplan, Zackery A. Benson, David R. Baker, Joshua P. McClure, Alexandre R. Rocha, and Marina S. Leite. Band Structure Engineering by Alloying for Photonics. *Advanced Optical Materials*, 6(17):1800218, 2018.

[180] Zhaoke Zheng, Takashi Tachikawa, and Tetsuro Majima. Plasmon-Enhanced Formic Acid Dehydrogenation Using Anisotropic Pd–Au Nanorods Studied

at the Single-Particle Level. *Journal of the American Chemical Society*, 137(2):948–957, January 2015.

[181] Mariama Rebello Sousa Dias and Marina S. Leite. Alloying: A Platform for Metallic Materials with On-Demand Optical Response. *Accounts of Chemical Research*, July 2019.

[182] Xiaoyang Duan, Simon Kamin, Florian Sterl, Harald Giessen, and Na Liu. Hydrogen-Regulated Chiral Nanoplasmonics. *Nano Letters*, 16(2):1462–1466, February 2016.

[183] T. J. Richardson, J. L. Slack, R. D. Armitage, R. Kostecki, B. Farangis, and M. D. Rubin. Switchable mirrors based on nickel–magnesium films. *Applied Physics Letters*, 78(20):3047–3049, May 2001.

[184] D. M. Borsa, A. Baldi, M. Pasturel, H. Schreuders, B. Dam, R. Griessen, P. Vermeulen, and P. H. L. Notten. Mg–Ti–H thin films for smart solar collectors. *Applied Physics Letters*, 88(24):241910, June 2006.

[185] U.S. Department of Energy, Fuel Cell Technologies Ofce., and Energy Efciency and Renewable Energy (EERE). Multi-Year Research, Development, and Demonstration Plan, 2011–2020. Section 3.7 Hydrogen Safety, Codes and Standards. 2015.

[186] Brian D. Adams and Aicheng Chen. The role of palladium in a hydrogen economy. *Materials Today*, 14(6):282–289, June 2011.

[187] R. B. Schwarz and A. G. Khachaturyan. Thermodynamics of open two-phase systems with coherent interfaces: Application to metal–hydrogen systems. *Acta Materialia*, 54(2):313–323, January 2006.

[188] Lars Johannes Bannenberg, Ferry Anggoro Ardy Nugroho, Herman Schreuders, Ben Norder, Thu Trang Trinh, Nina-Juliane Steinke, Ad A. van Well, Christoph Langhammer, and Bernard Dam. Direct Comparison of PdAu Alloy Thin Films and Nanoparticles upon Hydrogen Exposure. *ACS Applied Materials & Interfaces*, 11(17):15489–15497, May 2019.

[189] Ferry Anggoro Ardy Nugroho, Iwan Darmadi, Vladimir P. Zhdanov, and Christoph Langhammer. Universal Scaling and Design Rules of Hydrogen-Induced Optical Properties in Pd and Pd-Alloy Nanoparticles. *ACS Nano*, 12(10):9903–9912, October 2018.

[190] R. J. Westerwaal, J. S. A. Rooijmans, L. Leclercq, D. G. Gheorghe, T. Radeva, L. Mooij, T. Mak, L. Polak, M. Slaman, B. Dam, and Th. Rasing. Nanostructured Pd–Au based fiber optic sensors for probing hydrogen concentrations in gas mixtures. *International Journal of Hydrogen Energy*, 38(10):4201–4212, April 2013.

[191] Yoshiaki Nishijima, Shogo Shimizu, Keisuke Kurihara, Yoshikazu Hashimoto, Hajime Takahashi, Armandas Balčytis, Gediminas Seniutinas, Shinji Okazaki, Jurga Juodkazytė, Takeshi Iwasa, Tetsuya Taketsugu, Yoriko Tominaga, and Saulius Juodkazis. Optical readout of hydrogen storage in films of Au and Pd. *Optics Express*, 25(20):24081–24092, October 2017.

[192] Lulu Zhang, Qiaowan Chang, Huimei Chen, and Minhua Shao. Recent advances in palladium-based electrocatalysts for fuel cell reactions and hydrogen evolution reaction. *Nano Energy*, 29:198–219, November 2016.

[193] Bernard Coq and François Figueras. Bimetallic palladium catalysts: influence of the co-metal on the catalyst performance. *Journal of Molecular Catalysis A: Chemical*, 173(1):117–134, September 2001.

[194] Sarina Sarina, Huaiyong Zhu, Esa Jaatinen, Qi Xiao, Hongwei Liu, Jianfeng Jia, Chao Chen, and Jian Zhao. Enhancing Catalytic Performance of Palladium in Gold and Palladium Alloy Nanoparticles for Organic Synthesis Reactions through Visible Light Irradiation at Ambient Temperatures. *Journal of the American Chemical Society*, 135(15):5793–5801, April 2013.

[195] Kent E. Coulter, J. Douglas Way, Sabina K. Gade, Saurabh Chaudhari, Gökhan O. Alptekin, Sarah J. DeVoss, Stephen N. Paglieri, and Bill Pledger. Sulfur tolerant PdAu and PdAuPt alloy hydrogen separation membranes. *Journal of Membrane Science*, 405-406:11–19, July 2012.

[196] Anthony Knapton. Palladium Alloys for Hydrogen Diffusion Membranes. 1977.

[197] Stoney George Gerald and Parsons Charles Algernon. The tension of metallic films deposited by electrolysis. *Proceedings of the Royal Society of London. Series A, Containing Papers of a Mathematical and Physical Character*, 82(553):172–175, May 1909.

[198] Shima Kadkhodazadeh, Ferry Anggoro Ardy Nugroho, Christoph Langhammer, Marco Beleggia, and Jakob B. Wagner. Optical Property–Composition Correlation in Noble Metal Alloy Nanoparticles Studied with EELS. *ACS Photonics*, 6(3):779–786, March 2019.

[199] Yoshiaki Nishijima, Yoshikazu Hashimoto, Gediminas Seniutinas, Lorenzo Rosa, and Saulius Juodkazis. Engineering gold alloys for plasmonics. *Applied Physics A*, 117(2):641–645, November 2014.

[200] Arnulf Maeland and Ted B. Flanagan. X-Ray and Thermodynamic Studies of the Absorption of Hydrogen by Gold-Palladium Alloys. *The Journal of Physical Chemistry*, 69(10):3575–3581, October 1965.

[201] M. Łukaszewski, K. Kuśmierczyk, J. Kotowski, H. Siwek, and A. Czerwiński. Electrosorption of hydrogen into palladium-gold alloys. *Journal of Solid State Electrochemistry*, 7(2):69–76, February 2003.

[202] K. Hubkowska, M. Łukaszewski, and A. Czerwiński. Influence of temperature on hydrogen electrosorption into palladium–noble metal alloys. Part 1: Palladium–gold alloys. *Electrochimica Acta*, 56(1):235–242, December 2010.

[203] Y. Pivak, H. Schreuders, M. Slaman, R. Griessen, and B. Dam. Thermodynamics, stress release and hysteresis behavior in highly adhesive Pd–H films. *International Journal of Hydrogen Energy*, 36(6):4056–4067, March 2011.

[204] Stefan Wagner and Astrid Pundt. Quasi-thermodynamic model on hydride formation in palladium–hydrogen thin films: Impact of elastic and microstructural constraints. *International Journal of Hydrogen Energy*, 41(4):2727–2738, January 2016.

[205] R. Gremaud, M. Gonzalez-Silveira, Y. Pivak, S. de Man, M. Slaman, H. Schreuders, B. Dam, and R. Griessen. Hydrogenography of PdHx thin films: Influence of H-induced stress relaxation processes. *Acta Materialia*, 57(4):1209–1219, February 2009.

[206] B. Ham, A. Junkaew, R. Arróyave, J. Park, H. C. Zhou, D. Foley, S. Rios, H. Wang, and X. Zhang. Size and stress dependent hydrogen desorption in metastable Mg hydride films. *International Journal of Hydrogen Energy*, 39(6):2597–2607, February 2014.

[207] C.-J. Chung, Sang-Chul Lee, James R. Groves, Edwin N. Brower, Robert Sinclair, and Bruce M. Clemens. Interfacial Alloy Hydride Destabilization in Mg/Pd Thin Films. *Physical Review Letters*, 108(10):106102, March 2012.

[208] M. Dornheim, A. Pundt, R. Kirchheim, S. J. v. d. Molen, E. S. Kooij, J. Kerssemakers, R. Griessen, H. Harms, and U. Geyer. Stress development in thin yttrium films on hard substrates during hydrogen loading. *Journal of Applied Physics*, 93(11):8958–8965, May 2003.

[209] Stefan Wagner, Philipp Klose, Vladimir Burlaka, Kai Nörthemann, Magnus Hamm, and Astrid Pundt. Structural Phase Transitions in Niobium Hydrogen Thin Films: Mechanical Stress, Phase Equilibria and Critical Temperatures. *ChemPhysChem*, 20(14):1890–1904, 2019.

[210] Jianxiong Li, Simon Kamin, Guoxing Zheng, Frank Neubrech, Shuang Zhang, and Na Liu. Addressable metasurfaces for dynamic holography and optical information encryption. *Science Advances*, 4(6):eaar6768, June 2018.

[211] Thomas G. Farinha, Chen Gong, Zackery A. Benson, and Marina S. Leite. Magnesium for Transient Photonics. *ACS Photonics*, 6(2):272–278, February 2019.

[212] J. F. Stampfer, C. E. Holley, and J. F. Suttle. The Magnesium-Hydrogen System1-3. *Journal of the American Chemical Society*, 82(14):3504–3508, July 1960. Publisher: American Chemical Society.

[213] C. M. Stander. Kinetics of decomposition of magnesium hydride. *Journal of Inorganic and Nuclear Chemistry*, 39(2):221–223, January 1977.

[214] A Reiser, B Bogdanović, and K Schlichte. The application of Mg-based metal-hydrides as heat energy storage systems. *International Journal of Hydrogen Energy*, 25(5):425–430, May 2000.

[215] I. González Fernández, F. C. Gennari, and G. O. Meyer. Influence of sintering parameters on formation of Mg-Co hydrides based on their thermodynamic characterization. *Journal of Alloys and Compounds*, 462(1):119–124, August 2008.

[216] Huaiyu Shao, Tong Liu, Yuntao Wang, Hairuo Xu, and Xingguo Li. Preparation of Mg-based hydrogen storage materials from metal nanoparticles. *Journal of Alloys and Compounds*, 465(1):527–533, October 2008.

[217] G. F. Lima, A. M. Jorge, D. R. Leiva, C. S. Kiminami, C. Bolfarini, and W. J. Botta. Severe plastic deformation of Mg-Fe powders to produce bulk hydrides. *Journal of Physics: Conference Series*, 144:012015, January 2009. Publisher: IOP Publishing.

[218] L. E. A. Berlouis, E. Cabrera, E. Hall-Barientos, P. J. Hall, S. B. Dodd, S. Morris, and M. A. Imam. Thermal analysis investigation of hydriding properties of nanocrystalline Mg-Ni- and Mg-Fe-based alloys prepared by high-energy ball milling. *Journal of Materials Research*, 16(1):45–57, January 2001.

[219] Yanshan Lu, Hyunjeong Kim, Kouji Sakaki, Shigenobu Hayashi, Keiko Jimura, and Kohta Asano. Destabilizing the Dehydrogenation Thermodynamics of Magnesium Hydride by Utilizing the Immiscibility of Mn with Mg. *Inorganic Chemistry*, 58(21):14600–14607, November 2019. Publisher: American Chemical Society.

[220] R. Gremaud, A. Borgschulte, C. Chacon, J.L.M. van Mechelen, H. Schreuders, A. Züttel, B. Hjörvarsson, B. Dam, and R. Griessen. Structural and optical properties of MgxAl1-xHy gradient thin films: a combinatorial approach. *Applied Physics A*, 84(1):77–85, July 2006.

[221] A. Zaluska, L. Zaluski, and J.O. Ström-Olsen. Structure, catalysis and atomic reactions on the nano-scale: a systematic approach to metal hydrides for hydrogen storage. *Applied Physics A*, 72(2):157–165, February 2001.

[222] S. Bouaricha, J. P. Dodelet, D. Guay, J. Huot, S. Boily, and R. Schulz. Hydriding behavior of Mg-Al and leached Mg-Al compounds prepared by high-energy ball-milling. *Journal of Alloys and Compounds*, 297(1):282–293, February 2000.

[223] R. Gremaud, A. Borgschulte, W. Lohstroh, H. Schreuders, A. Züttel, B. Dam, and R. Griessen. Ti-catalyzed Mg(AlH4)2: A reversible hydrogen storage material. *Journal of Alloys and Compounds*, 404-406:775–778, December 2005.

[224] H. Fritzsche, M. Saoudi, J. Haagsma, C. Ophus, E. Luber, C. T. Harrower, and D. Mitlin. Neutron reflectometry study of hydrogen desorption in destabilized MgAl alloy thin films. *Applied Physics Letters*, 92(12):121917, March 2008. Publisher: American Institute of Physics.

[225] P. Vermeulen, P. C. J. Graat, H. J. Wondergem, and P. H. L. Notten. Crystal structures of MgyTi100-y thin film alloys in the as-deposited and hydrogenated state. *International Journal of Hydrogen Energy*, 33(20):5646–5650, October 2008.

[226] Hyunjeong Kim, Herman Schreuders, Kouji Sakaki, Kohta Asano, Yumiko Nakamura, Naoyuki Maejima, Akihiko Machida, Tetsu Watanuki, and Bernard Dam. Unveiling Nanoscale Compositional and Structural Heterogeneities of Highly Textured Mg0.7Ti0.3Hy Thin Films. *Inorganic Chemistry*, 59(10):6800–6807, May 2020. Publisher: American Chemical Society.

[227] A. Baldi, D. M. Borsa, H. Schreuders, J. H. Rector, T. Atmakidis, M. Bakker, H. A. Zondag, W. G. J. van Helden, B. Dam, and R. Griessen. Mg-Ti-H thin films as switchable solar absorbers. *International Journal of Hydrogen Energy*, 33(12):3188–3192, June 2008.

[228] D. M. Borsa, A. Baldi, M. Pasturel, H. Schreuders, B. Dam, R. Griessen, P. Vermeulen, and P. H. L. Notten. Mg-Ti-H thin films for smart solar collectors. *Applied Physics Letters*, 88(24):241910, June 2006. Publisher: American Institute of PhysicsAIP.

[229] D. M. Borsa, R. Gremaud, A. Baldi, H. Schreuders, J. H. Rector, B. Kooi, P. Vermeulen, P. H. L. Notten, B. Dam, and R. Griessen. Structural, optical, and electrical properties of MgyTi(1-y)Hx thin films. *Physical Review B*, 75(20):205408, May 2007. Publisher: American Physical Society.

[230] R. a. H. Niessen and P. H. L. Notten. Electrochemical Hydrogen Storage Characteristics of Thin Film MgX (X = Sc , Ti , V , Cr) Compounds. *Electrochemical and Solid-State Letters*, 8(10):A534, August 2005. Publisher: IOP Publishing.

[231] R. J. Westerwaal, A. Borgschulte, W. Lohstroh, B. Dam, B. Kooi, G. ten Brink, M. J. P. Hopstaken, and P. H. L. Notten. The growth-induced microstructural origin of the optical black state of Mg2NiHx thin films. *Journal of Alloys and Compounds*, 416(1):2–10, June 2006.

[232] S. Orimo and H. Fujii. Materials science of Mg-Ni-based new hydrides. *Applied Physics A*, 72(2):167–186, February 2001.

[233] A. Ludwig, J. Cao, B. Dam, and R. Gremaud. Opto-mechanical characterization of hydrogen storage properties of Mg–Ni thin film composition spreads. *Applied Surface Science*, 254(3):682–686, November 2007.

[234] Emil Johansson, Cyril Chacon, Claudia Zlotea, Yvonne Andersson, and Björgvin Hjörvarsson. Hydrogen uptake and optical properties of sputtered Mg-Ni thin films. *Journal of Physics: Condensed Matter*, 16(43):7649–7662, October 2004. Publisher: IOP Publishing.

[235] J. Isidorsson, I. a. M. E. Giebels, R. Griessen, and M. Di Vece. Tunable reflectance Mg-Ni-H films. *Applied Physics Letters*, 80(13):2305–2307, March 2002. Publisher: American Institute of Physics.

[236] W. Lohstroh, R. J. Westerwaal, B. Noheda, S. Enache, I. A. M. E. Giebels, B. Dam, and R. Griessen. Self-Organized Layered Hydrogenation in Black Mg2NiHxSwitchable Mirrors. *Physical Review Letters*, 93(19):197404, November 2004. Publisher: American Physical Society.

[237] R. Gremaud, C. P. Broedersz, A. Borgschulte, M. J. van Setten, H. Schreuders, M. Slaman, B. Dam, and R. Griessen. Hydrogenography of MgyNi1-yHx gradient thin films: Interplay between the thermodynamics and kinetics of hydrogenation. *Acta Materialia*, 58(2):658–668, January 2010.

[238] M. Pasturel, M. Slaman, D. M. Borsa, H. Schreuders, B. Dam, R. Griessen, W. Lohstroh, and A. Borgschulte. Stabilized switchable black state in Mg2NiH4-Ti-Pd thin films for optical hydrogen sensing. *Applied Physics Letters*, 89(2):021913, July 2006. Publisher: American Institute of Physics.

[239] Yevheniy Pivak, Valerio Palmisano, Herman Schreuders, and Bernard Dam. The clamping effect in the complex hydride Mg2NiH4 thin films. *Journal of Materials Chemistry A*, 1(36):10972–10978, August 2013. Publisher: The Royal Society of Chemistry.

[240] E. Akiba, K. Nomura, S. Ono, and S. Suda. Kinetics of the reaction between Mg-Ni alloys and H2. *International Journal of Hydrogen Energy*, 7(10):787–791, January 1982.

[241] Chengshang Zhou, Zhigang Zak Fang, Jun Lu, Xiangyi Luo, Chai Ren, Peng Fan, Yang Ren, and Xiaoyi Zhang. Thermodynamic Destabilization of Magnesium Hydride Using Mg-Based Solid Solution Alloys. *The Journal of Physical Chemistry C*, 118(22):11526–11535, June 2014. Publisher: American Chemical Society.

[242] P. Vermeulen, R. A. H. Niessen, and P. H. L. Notten. Hydrogen storage in metastable MgyTi(1-y) thin films. *Electrochemistry Communications*, 8(1):27–32, January 2006.

[243] S. Bao, K. Tajima, Y. Yamada, M. Okada, and K. Yoshimura. Magnesium-titanium alloy thin-film switchable mirrors. *Solar Energy Materials and Solar Cells*, 92(2):224–227, February 2008.

[244] R. Gremaud, J. L. M. van Mechelen, H. Schreuders, M. Slaman, B. Dam, and R. Griessen. Structural and optical properties of MgyNi1-yHx gradient thin films in relation to the as-deposited metallic state. *International Journal of Hydrogen Energy*, 34(21):8951–8957, November 2009.

[245] W. Lohstroh, R. J. Westerwaal, J. L. M. van Mechelen, H. Schreuders, B. Dam, and R. Griessen. The dielectric function of Mgy NiHx thin films (2<y<10). *Journal of Alloys and Compounds*, 430(1):13–18, March 2007.

[246] R. J. King and S. P. Talim. A Comparison of Thin Film Measurement by Guided Waves, Ellipsometry and Reflectometry. *Optica Acta: International Journal of Optics*, 28(8):1107–1123, August 1981. Publisher: Taylor & Francis _eprint: https://doi.org/10.1080/713820674.

[247] M. Slaman, B. Dam, M. Pasturel, D. M. Borsa, H. Schreuders, J. H. Rector, and R. Griessen. Fiber optic hydrogen detectors containing Mg-based metal hydrides. *Sensors and Actuators B: Chemical*, 123(1):538–545, April 2007.

[248] B Farangis, P Nachimuthu, T. J Richardson, J. L Slack, B. K Meyer, R. C. C Perera, and M. D Rubin. Structural and electronic properties of magnesium-3D transition metal switchable mirrors. *Solid State Ionics*, 165(1):309–314, December 2003.

[249] Easo P. George, Dierk Raabe, and Robert O. Ritchie. High-entropy alloys. *Nature Reviews Materials*, 4(8):515–534, August 2019. Number: 8 Publisher: Nature Publishing Group.

[250] Martin Sahlberg, Dennis Karlsson, Claudia Zlotea, and Ulf Jansson. Superior hydrogen storage in high entropy alloys. *Scientific Reports*, 6(1):36770, November 2016. Number: 1 Publisher: Nature Publishing Group.

[251] Magnus Moe Nygård, Gustav Ek, Dennis Karlsson, Martin Sahlberg, Magnus H. Sørby, and Bjørn C. Hauback. Hydrogen storage in high-entropy alloys with varying degree of local lattice strain. *International Journal of Hydrogen Energy*, 44(55):29140–29149, November 2019.

[252] R. B. Strozi, D. R. Leiva, J. Huot, W. J. Botta, and G. Zepon. Synthesis and hydrogen storage behavior of Mg–V–Al–Cr–Ni high entropy alloys. *International Journal of Hydrogen Energy*, 46(2):2351–2361, January 2021.

[253] Cheng Zhang, Anna Song, Yuan Yuan, Yuan Wu, Peilong Zhang, Zhaoping Lu, and Xiping Song. Study on the hydrogen storage properties of a TiZrNbTa high entropy alloy. *International Journal of Hydrogen Energy*, 45(8):5367–5374, February 2020.

[254] Yonggang Yao, Zhennan Huang, Pengfei Xie, Steven D. Lacey, Rohit Jiji Jacob, Hua Xie, Fengjuan Chen, Anmin Nie, Tiancheng Pu, Miles Rehwoldt, Daiwei Yu, Michael R. Zachariah, Chao Wang, Reza Shahbazian-Yassar,

Ju Li, and Liangbing Hu. Carbothermal shock synthesis of high-entropy-alloy nanoparticles. *Science*, 359(6383):1489–1494, March 2018. Publisher: American Association for the Advancement of Science Section: Research Article.

[255] T. Schenkel, A. Persaud, H. Wang, P. A. Seidl, R. MacFadyen, C. Nelson, W. L. Waldron, J.-L. Vay, G. Deblonde, B. Wen, Y.-M. Chiang, B. P. MacLeod, and Q. Ji. Investigation of light ion fusion reactions with plasma discharges. *Journal of Applied Physics*, 126(20):203302, November 2019. Publisher: American Institute of Physics.

[256] Vladimir Pines, Marianna Pines, Arnon Chait, Bruce M. Steinetz, Lawrence P. Forsley, Robert C. Hendricks, Gustave C. Fralick, Theresa L. Benyo, Bayarbadrakh Baramsai, Philip B. Ugorowski, Michael D. Becks, Richard E. Martin, Nicholas Penney, and Carl E. Sandifer. Nuclear fusion reactions in deuterated metals. *Physical Review C*, 101(4):044609, April 2020. Publisher: American Physical Society.

[257] Bruce M. Steinetz, Theresa L. Benyo, Arnon Chait, Robert C. Hendricks, Lawrence P. Forsley, Bayarbadrakh Baramsai, Philip B. Ugorowski, Michael D. Becks, Vladimir Pines, Marianna Pines, Richard E. Martin, Nicholas Penney, Gustave C. Fralick, and Carl E. Sandifer. Novel nuclear reactions observed in bremsstrahlung-irradiated deuterated metals. *Physical Review C*, 101(4):044610, April 2020. Publisher: American Physical Society.

[258] C. Ciracì, R. T. Hill, J. J. Mock, Y. Urzhumov, A. I. Fernández-Domínguez, S. A. Maier, J. B. Pendry, A. Chilkoti, and D. R. Smith. Probing the Ultimate Limits of Plasmonic Enhancement. *Science*, 337(6098):1072–1074, August 2012. Publisher: American Association for the Advancement of Science Section: Report.

[259] David K. Fork, Jeremy N. Munday, Tarun Narayan, and Joseph B. Murray. Target structure for enhanced electron screening, April 2019.

[260] Masataka Hakamada and Mamoru Mabuchi. Fabrication of nanoporous palladium by dealloying and its thermal coarsening. *Journal of Alloys and Compounds*, 479(1):326–329, June 2009.

[261] Xingyou Lang, Lihua Qian, Pengfei Guan, Jian Zi, and Mingwei Chen. Localized surface plasmon resonance of nanoporous gold. *Applied Physics Letters*, 98(9):093701, February 2011. Publisher: American Institute of Physics.

[262] Juergen Biener, Gregory W. Nyce, Andrea M. Hodge, Monika M. Biener, Alex V. Hamza, and Stefan A. Maier. Nanoporous Plasmonic Metamaterials. *Advanced Materials*, 20(6):1211–1217, 2008. _eprint: https://onlinelibrary.wiley.com/doi/pdf/10.1002/adma.200701899.

[263] G. C. A. M. Janssen, M. M. Abdalla, F. van Keulen, B. R. Pujada, and B. van Venrooy. Celebrating the 100th anniversary of the Stoney equation for film

stress: Developments from polycrystalline steel strips to single crystal silicon wafers. *Thin Solid Films*, 517(6):1858–1867, January 2009.

[264] Jianjun Chen, Judong Zhang, Mingming Wang, and Ye Li. High-temperature hydrogen sensor based on platinum nanoparticle-decorated SiC nanowire device. *Sensors and Actuators B: Chemical*, 201:402–406, October 2014.

[265] Syed Mubeen, Ting Zhang, Bongyoung Yoo, Marc A. Deshusses, and Nosang V. Myung. Palladium Nanoparticles Decorated Single-Walled Carbon Nanotube Hydrogen Sensor. *The Journal of Physical Chemistry C*, 111(17):6321–6327, May 2007. Publisher: American Chemical Society.

[266] Rakesh K. Joshi, Subramanian Krishnan, Mashamichi Yoshimura, and Ashok Kumar. Pd Nanoparticles and Thin Films for Room Temperature Hydrogen Sensor. *Nanoscale Research Letters*, 4(10):1191, July 2009.

[267] D. Gupta, D. Dutta, M. Kumar, P. B. Barman, C. K. Sarkar, S. Basu, and S. K. Hazra. A low temperature hydrogen sensor based on palladium nanoparticles. *Sensors and Actuators B: Chemical*, 196:215–222, June 2014.

[268] Juree Hong, Sanggeun Lee, Jungmok Seo, Soonjae Pyo, Jongbaeg Kim, and Taeyoon Lee. A Highly Sensitive Hydrogen Sensor with Gas Selectivity Using a PMMA Membrane-Coated Pd Nanoparticle/Single-Layer Graphene Hybrid. *ACS Applied Materials & Interfaces*, 7(6):3554–3561, February 2015. Publisher: American Chemical Society.

[269] Isolde Simon and Michael Arndt. Thermal and gas-sensing properties of a micromachined thermal conductivity sensor for the detection of hydrogen in automotive applications. *Sensors and Actuators A: Physical*, 97-98:104–108, April 2002.

[270] Sukon Phanichphant. Semiconductor Metal Oxides as Hydrogen Gas Sensors. *Procedia Engineering*, 87:795–802, January 2014.

[271] Ananya Dey. Semiconductor metal oxide gas sensors: A review. *Materials Science and Engineering: B*, 229:206–217, March 2018.

[272] L. P. Martin, A. Q. Pham, and R. S. Glass. Electrochemical hydrogen sensor for safety monitoring. *Solid State Ionics*, 175(1):527–530, November 2004.

[273] Ghenadii Korotcenkov, Sang Do Han, and Joseph R. Stetter. Review of Electrochemical Hydrogen Sensors. *Chemical Reviews*, 109(3):1402–1433, March 2009. Publisher: American Chemical Society.

[274] D. Dwivedi, R. Dwivedi, and S. K. Srivastava. Sensing properties of palladium-gate MOS (Pd-MOS) hydrogen sensor-based on plasma grown silicon dioxide. *Sensors and Actuators B: Chemical*, 71(3):161–168, December 2000.

[275] Danick Briand, Helena Wingbrant, Hans Sundgren, Bart van der Schoot, Lars-Gunnar Ekedahl, Ingemar Lundström, and Nicolaas F de Rooij. Modulated operating temperature for MOSFET gas sensors: hydrogen recovery time reduction and gas discrimination. *Sensors and Actuators B: Chemical*, 93(1):276–285, August 2003.

[276] Junghui Song, Wu Lu, Jeffrey S. Flynn, and George R. Brandes. AlGaN/GaN Schottky diode hydrogen sensor performance at high temperatures with different catalytic metals. *Solid-State Electronics*, 49(8):1330–1334, August 2005.

[277] Devika Sil, Jacqueline Hines, Uduak Udeoyo, and Eric Borguet. Palladium Nanoparticle-Based Surface Acoustic Wave Hydrogen Sensor. *ACS Applied Materials & Interfaces*, 7(10):5709–5714, March 2015. Publisher: American Chemical Society.

[278] A. D'Amico, A. Palma, and E. Verona. Surface acoustic wave hydrogen sensor. *Sensors and Actuators*, 3:31–39, January 1982.

[279] D. R. Baselt, B. Fruhberger, E. Klaassen, S. Cemalovic, C. L. Britton, S. V. Patel, T. E. Mlsna, D. McCorkle, and B. Warmack. Design and performance of a microcantilever-based hydrogen sensor. *Sensors and Actuators B: Chemical*, 88(2):120–131, January 2003.

[280] J. van Lith, A. Lassesson, S. A. Brown, M. Schulze, J. G. Partridge, and A. Ayesh. A hydrogen sensor based on tunneling between palladium clusters. *Applied Physics Letters*, 91(18):181910, October 2007. Publisher: American Institute of Physics.

[281] Ediz Herkert, Florian Sterl, Nikolai Strohfeldt, Ramon Walter, and Harald Giessen. Low-Cost Hydrogen Sensor in the ppm Range with Purely Optical Readout. *ACS Sensors*, 5(4):978–983, April 2020. Publisher: American Chemical Society.

[282] Iwan Darmadi, Ferry Anggoro Ardy Nugroho, and Christoph Langhammer. High-Performance Nanostructured Palladium-Based Hydrogen Sensors—Current Limitations and Strategies for Their Mitigation. *ACS Sensors*, November 2020. Publisher: American Chemical Society.

[283] V. Palmisano, M. Filippi, A. Baldi, M. Slaman, H. Schreuders, and B. Dam. An optical hydrogen sensor based on a Pd-capped Mg thin film wedge. *International Journal of Hydrogen Energy*, 35(22):12574–12578, November 2010.

[284] Donato Luna-Moreno and David Monzón-Hernández. Effect of the Pd–Au thin film thickness uniformity on the performance of an optical fiber hydrogen sensor. *Applied Surface Science*, 253(21):8615–8619, August 2007.

[285] Donato Luna-Moreno, David Monzón-Hernández, Joel Villatoro, and Gonçal Badenes. Optical fiber hydrogen sensor based on core diameter mismatch and

annealed Pd–Au thin films. *Sensors and Actuators B: Chemical*, 125(1):66–71, July 2007.

[286] Joel Villatoro, Donato Luna-Moreno, and David Monzón-Hernández. Optical fiber hydrogen sensor for concentrations below the lower explosive limit. *Sensors and Actuators B: Chemical*, 110(1):23–27, September 2005.

[287] Cédric Perrotton, Ruud J. Westerwaal, Nicolas Javahiraly, Martin Slaman, Herman Schreuders, Bernard Dam, and Patrick Meyrueis. A reliable, sensitive and fast optical fiber hydrogen sensor based on surface plasmon resonance. *Optics Express*, 21(1):382–390, January 2013. Publisher: Optical Society of America.

[288] X. Bévenot, A. Trouillet, C. Veillas, H. Gagnaire, and M. Clément. Surface plasmon resonance hydrogen sensor using an optical fibre\ast. *Measurement Science and Technology*, 13(1):118–124, December 2001. Publisher: IOP Publishing.

[289] Kaiqun Lin, Yonghua Lu, Junxue Chen, Rongsheng Zheng, Pei Wang, and Hai Ming. Surface plasmon resonance hydrogen sensor based on metallic grating with high sensitivity. *Optics Express*, 16(23):18599–18604, November 2008. Publisher: Optical Society of America.

[290] János Schanda. CIE Colorimetry. In *Colorimetry*, pages 25–78. John Wiley & Sons, Ltd, 2007. Section: 3 _eprint: https://onlinelibrary.wiley.com/doi/pdf/10.1002/9780470175637.ch3.

[291] Chris Wyman, Peter-Pike Sloan, and Peter Shirley. Simple Analytic Approximations to the CIE XYZ Color Matching Functions. *Journal of Computer Graphics Techniques*, 2(2):11, 2013.

[292] G. G. Libowitz. Metallic hydrides; fundamental properties and applications. *Journal of Physics and Chemistry of Solids*, 55(12):1461–1470, December 1994.

[293] G. G. Libowitz. Electronic properties of the rare earth hydrides. *Berichte der Bunsengesellschaft für physikalische Chemie*, 76(8):837–845, 1972. _eprint: https://onlinelibrary.wiley.com/doi/pdf/10.1002/bbpc.19720760854.

[294] Eugene V. Sheely. Theoretical Study of the Effects of Di-Muonic Molecules on Muon-Catalyzed Fusion. Technical report, AIR FORCE INST OF TECH WRIGHT-PATTERSON AFB OH GRADUATE SCHOOL OF ENGINEERING AND MANAGEMENT, March 2012. Section: Technical Reports.

[295] Russell D. Johnson. NIST Computational Chemistry Comparison and Benchmark Database, August 2020.

[296] Z. Sun and D. Tománek. Cold fusion: How close can deuterium atoms come inside palladium? *Physical Review Letters*, 63(1):59–61, July 1989. Publisher: American Physical Society.

[297] Andreas Borgschulte, Jasmin Terreni, Emanuel Billeter, Luke Daemen, Yongqiang Cheng, Anup Pandey, Zbigniew Łodziana, Russell J. Hemley, and Anibal J. Ramirez-Cuesta. Inelastic neutron scattering evidence for anomalous H–H distances in metal hydrides. *Proceedings of the National Academy of Sciences*, 117(8):4021–4026, February 2020. Publisher: National Academy of Sciences Section: Physical Sciences.

[298] Anubhav Jain, Shyue Ping Ong, Geoffroy Hautier, Wei Chen, William Davidson Richards, Stephen Dacek, Shreyas Cholia, Dan Gunter, David Skinner, Gerbrand Ceder, and Kristin A. Persson. Commentary: The Materials Project: A materials genome approach to accelerating materials innovation. *APL Materials*, 1(1):011002, July 2013. Publisher: American Institute of Physics.

[299] Arnulf J. Maeland. Investigation of the Vanadium—Hydrogen System by X-Ray Diffraction Techniques [1,2]. *The Journal of Physical Chemistry*, 68(8):2197–2200, August 1964.